BEHAVIOUR OF GROUT INFILLED STEEL TUBULAR MEMBERS AND JOINTS

SHEN WEI

(B.Eng, TJU)

(MSc, NUS)

A THESIS SUBMITTED

FOR THE DEGREE OF DOCTOR OF PHILOSOPHY

DEPARTMENT OF CIVIL ENGINEERING

NATIONAL UNIVERSITY OF SINGAPORE

March 2011

Acknowledgement

The research work reported in this thesis has been carried out at the Department of Civil Engineering, National University of Singapore (NUS).

Firstly, I would sincerely thank my supervisor Professor Choo Yoo Sang of National University of Singapore, for his excellent leadership, invaluable academic guidance and financial support in the PhD research work. I would specially thank Professor Stig Berge of Norwegian University of Science and Technology, for his unselfish and profound teaching and guidance on the fatigue knowledge during a memorable stay in the Norway. Thanks are also given to Professor J. Wardenier, Professor P.W. Marshall and Dr. Qian Xudong for their helpful discussions and valuable contributions.

I would also thank the technical staff of the structural Laboratory of NUS: Mr. Sit Beng Chiat, Mr. Lim Huay Bak, Mr. Koh Yian Kheng, Mr. Ang Beng Oon and Mdm. Annie Tan, and the key staff of DNV Singapore and Densit Asia Ltd: the late Mr. Chia Meng Teck, Mr. John Gronbech and Mr. Louren Woof, for their help of coordination and cooperation in conducting the experimental work.

My thanks also extend to my colleagues and friends at Centre for Offshore Research and Engineering (NUS), Dr. Wang Zhen (currently with DNV Norway) and Mr. Chen Zhuo for sharing and exchanging knowledge learnt.

Finally, I would thank my family. Without the support of family, every thing I do will become meaningless. This thesis is dedicated to my family.

Contents

List of figures

List of tables

Summary

There are potentially large demands for strengthening tubular structures in offshore engineering. Among the strengthening methods, the grout-infilling method has some significant advantages over other methods: such as flexibility and convenience in construction, no additional hydrodynamic drag force incurred, and cost effectiveness, etc. This thesis addresses two topics currently not fully understood but crucial for the application of infilled grouting method for strengthening tubular structures:

- Sectional capacity enhancement for partially grout infilled member; and
- Fatigue assessment of tubular joint with fully grout infilled chord

For the first topic, both experimental and numerical investigations were conducted. The specimens, designed to simulate typical leg members of jacket platform, were partially infilled with high strength grout with two interfacial schemes - with and without shear key, and tested under static axial compression load. The results showed that the proposed stiffening plates, as shear keys, effectively mobilize the bearing capacity of the high strength grout, demonstrating significant enhancement of sectional load carrying capacity achieved in partially grouted condition. In the subsequent refined finite element analyses, two complex effects: the grout damage and the interfacial bond-slip mechanism, under such confinement condition of partially infilled grouted member, were studied. The finite element (FE) results are found to be in good agreement with the experimental results and reveal that the strengthening effect relies on the effectiveness of contact mechanism for load transfer between the steel and grout. The FE results also indicate the plan interfacial shearing mechanism without shear key is ineffective for the member partially infilled with grout due to the relative Poisson's ratio effect. Shear keys, like the stiffening

plates, and high strength grout are indispensible for member strengthening using the partially infilled grout method. Simplified design model is proposed based on the results of subsequent FE parametric study.

For the second topic, systematic investigations were conducted on the reduction of stress concentration factor (SCF) and the variation of degree of bending (DOB) for tubular X joints with fully grouted chord. Both experimental measurements and finite element analyses are carried out for X joints in the loading conditions of in-plane bending and axial tension. The FE results are found to be in close agreement with the test results. FE parametric study is performed using the calibrated FE models. Based on the FE results simplified design charts are proposed to facilitate fatigue design of grouted joints.

In the following fatigue mechanism analysis, comprehensive fracture mechanics study was carried out for the reported fatigue tests of tubular T joints with grouted and un-grouted chord. The stress intensity factors (SIFs) of the two joints were determined by both numerical and empirical engineering methods. The SIF results are consistent and provide satisfactory justification for the fatigue test results. It confirms that for tubular joints with weld toe fatigue cracking, the hot spot stress with lower DOB is associated with larger SIF and is more damaging than that with higher DOB. For joints with grout-infilled chords, the presence of infilled grout in the chord not only reduces the SCF, but also lowers the DOB. Hence, for fatigue assessment of grouted tubular joints it is essential to include the effect of DOB.

Nomenclature

A	Material constant in fatigue S-N relationship
A_b	Area of cross section of brace
A_c	Current cross area of the cross section
A_i	Initial cross area of the cross section
A_g	effective bearing area of the grout
A_s	Cross section area of the structural steel
a	Depth of surface crack
a_i	Initial depth of crack
$[B]$	B matrix for each finite element
c	Half surface length of crack
C	Material constant for fatigue crack propagation in Paris law
Convexity	Weld leg convexity
d	Brace diameter
D	Chord diameter
D_p	Diameter of inserted pile in double skin grouting
$[D]$	Tangential stiffness matrix
$[D]_{ep}$	Elastic-plastic stiffness matrix
DOB	Degree of bending
e	Eccentricity
e	Engineering strain
E	Elastic modulus
F	Axial load in brace
$\{F\}$	Nodal force vector

$\{F\}_s$	Contact force vector
f_{gd}	Design strength of the grout
f_{yd}	Design strength of the steel
F_y	Yield function of damaged concrete plasticity
G	Plasticity flow potential
H_1	Weld leg length
H_2	Weld leg height
h	Plastic modulus
I	Unit vector
I_b	Second moment of initial of the cross section of brace
IPB	In plane bending
$\bar{J}$	Energy release rate for virtual crack extension
J	Energy release rate, J-integral
K	Stress intensity factor
$[K]$	Global stiffness matrix
ΔK	Range of stress intensity
K_I, K_{II}, K_{III}	Mode I, II, III stress intensity factors
K_{IC}	Material toughness
$[k]^e$	Element level stiffness matrix
l	Brace length
L	Chord length
L_{eb}	Half wave buckling length of cylindrical shell
M	Bending moment in the brace
m	Material constant in fatigue S-N relationship

m'	Material constant for fatigue crack propagation in Paris law
M_k	Notch magnification factor
M_{km},M_{kb}	Notch magnification factors on membrane and bending stresses due to the weld toe notch stress concentration
N	Fatigue life cycles
$[N]$	Shape function matrix for each finite element
N_i	Fatigue crack initiation life cycles
N_p	Design squash load capacity
OPB	Out plane bending
q	Effective contact-bearing factor
r	Weld toe radius
R	Stress ratio
SCF	Hot spot stress concentration factor
SCF_{corr}	Corrected hot spot stress concentration factor due to weld leg length
SCF_g	Stress concentration factor of grouted joint
SIF	Stress intensity factor
$SNCF$	Hot spot strain concentration factor
T	Chord thickness
T_e	Equivalent chord wall thickness
t	Brace thickness
T_g	Thickness of annulus grout in double skin grouting
t_o	Plain plate thickness
T_p	Thickness of inserted pile in double skin grouting
$\{U\}$	Displacement vector
v	Poisson ratio

Y	Dimensionless stress intensity factor, shape factor
Y_m, Y_b	Membrane and bending geometry shape factors based on the plain plate solution by Newman and Raju
Y_{hss}	Dimensionless stress intensity factor, normalized with hot spot stress
α	Ratio of chord length to outer diameter
β	Ratio of brace diameter to chord diameter
$\{\delta\}$	Nodal displacement vector
ε	True uni-axial strain
ε_{hs}	Hot spot strain in the normal direction
ε_y	The strain perpendicular to the normal hot spot strain ε_{hs}
$\{\varepsilon\}$	Strain vector
$\{\varepsilon_0\}$	Initial strain vector
$[\varepsilon^e]$	Elastic strain tensor
$[\varepsilon^p]$	Plastic strain tensor
ϕ	Angle along the crack front measured from the free surface
Ψ	Dilation angle
γ	Ratio of chord diameter to wall thickness
$\lambda(s)$	Virtual crack advance function
ρ	Notch radius
σ	Stress
$\{\sigma\}$	Stress vector
$[\sigma']$	Deviatoric stress tensor
σ_e	Effective (von Mises) stress
$\{\sigma_0\}$	Initial stress vector

$\Delta\sigma$	Stress range
σ_b	Bending stress
σ_b'	Effective bending stress considering load shedding effect
σ_{be}	Elastic cylindrical shell buckling stress
σ_{hs}	Hot spot stress
σ_g	Geometric stress
σ_l	Local notch stress
σ_m	Membrane stress
σ_n	Nominal stress
σ_y	Yeld stress
τ	Ratio of brace to chord wall thickness
τ_{eq}	Equivalent frictional stress
τ_1, τ_2	Direction 1 and 2 shear traction
τ_{crit}	Critical shear traction
$\tau_{\max}$	Maximum shear traction limit

Chapter 1

Introduction

1.1 Motivation

The potential of a large demand for strengthening tubular structures in offshore engineering has been noticed, as some aging platforms have remained in operation longer than their original estimations due to the forces of the global oil and gas market. Also, offshore structures are facing harsher loads than what was estimated decades ago. Still, although design codes, like RP2A (API, 2000), have been revised to account for larger environmental loads, certain crucial structural components in many aging platforms, like leg members and cross joints, have not been strengthened or retrofitted yet as a result of continuous operation of the platforms, with some of them more than 20 years old. The necessity of strengthening key structural components for old platforms to survive extreme conditions is indicated by recently published documents (Energo Engineering, 2006 ; 2007), which include abundant information of typical damaged structural components of existing jacket structures in Golf of Mexico caused by the hurricanes Katrina and Rita, as shown in Figure 1.1.

Figure 1.1 (a) shows a deformed leg member caused by local buckling near the weld connection. It suffices to indicate that the huge wave load in the hurricane led to excessive global overturning moment, which resulted in enormous axial compression beyond the sectional capacity of the tubular member and caused the local buckling

failure. Figure 1.1 (b) shows a fracture damage of an X joint, typical and crucial for cross bracing of jacket frame. For such a tubular joint in an old platform it is most possible to have fatigue crack initiated and growing under long time service load as a result of large stress concentration at hot spot region and cyclic wave load. In a storm condition, the cyclic wave load became extremely large and further tore apart the crack.

(a) (b)

Figure 1.1 Typical failures of components of existing jacket structure: (a) local buckling of leg member, (b) cracking and fracture of X joint. Extracted from Energo Engineering (2007)

In addition to the above mentioned, there are other needs for strengthening the existing platforms. For example, there is information recently received from the industry (DNV, 2006; DNV, 2008) that certain tubular members and tubular joints of an existing jacket structure need to be strengthened to sustain additional load from an added bridge, which will link an adjacent platform newly built with new facilities.

Even for new platforms, there are needs for strengthening certain particular members and joints. One such case is during the transport of jacket structures on barges (Boge et al., 2007). In the transit phase the dynamic load on tubular joints may become very large due to a combination of accelerations and dynamic amplification, and the stress cycles may be in the low cycle fatigue region, which is not considered

in the design stage. An appropriate way to overcome low cycle fatigue is reducing the stress range, which, in this case, means strengthening these particular joints.

Among the strengthening methods, the grout-infilling method has some significant advantages over others like flexibility and convenience in construction, having no additional hydrodynamic drag force incurred, and cost effectiveness, etc. Research related to grout infilled tubular members and joints started sometime ago and design codes, like RP2A (API, 2000) and CIDECT (Wardenier et al., 1991), provide certain design guidelines for fully grout-infilled tubular members and grouted joints based on some research conclusions. But the coverage of the codes for grouting method is not comprehensive. For example, in the case of Figure 1.1 (a), fully infilled grouting, meaning the grouted length equals to water depth, is unsuitable for a jacket leg member since the weight increase is significant, which may cause foundation failure and other detrimental dynamic effects. Partially infilling the leg member, in this case, is an attractive option. However, partial grouting is not covered in the design codes due to insufficient reliable information available in the literature. Similarly, for tubular joints with grouted chord, the information in the codes is also insufficient. Especially for fatigue assessment, there are doubts about what has been recommended in codes, such as:

- The linearity of hot spot stress of grouted tubular joints – if the hot spot stress is load dependent as indicated in ISO19902 (BSi, 2007), the recommended S-N approach together with the damage calculation for variable amplitude fatigue load (spectra load) may not be applicable;
- The accuracy of the determined hot spot stress of grouted joints using the equivalent chord thickness method; and

- The applicability of the same S-N curve of un-grouted (as-welded) joint for grouted joints.

In order to address the doubts as stated and provide more information for confident application of grouting technology in offshore engineering, a series of investigations about grouted tubular structures have been carried out in the National University of Singapore (NUS) since 2006 (Choo et al., 2007). The coverage of the investigation is quite broad. The structural components investigated include tubular members and tubular joints with different grouting schemes, single skin (infilling) grouting and double skin (annulus) grouting, and the loading modes include axial (both tension and compression) and in-plane bending under static loading condition. The author has been involved in most of these research activities. Due to the page limitations of a standard PhD thesis, the theme of this thesis is on the infilled grouting scheme based on two key investigations conducted by the author:

- the sectional compressive strength of partially infilled grouted tubular members, and
- the reduction of stress concentration for tubular X joints with chord with fully infilled grout and the associated fatigue mechanism according to fracture mechanics analysis.

1.2 Objectives and scope of work

The objectives of the study are to understand the behaviours of tubular member with grout infilling part of the member, and tubular X joints with fully grouted chords, and to quantify the strengthening effects for providing appropriate engineering proposals and design recommendations.

In detail, the following scope of works is expected to be accomplished for the PhD study:

For partially grout-infilled tubular member:

- Design specimens and then plan and carry out axial compression tests for partially grout-infilled tubular members, which are supposed to simulate typical jacket legs in both working and ultimate conditions;
- Conduct finite element analysis, and compare the results to calibrate FE models for further parametric study;
- Investigate the strengthening mechanism and quantify its effect; and
- Propose design recommendations based on the investigation results

For tubular X joints with fully grout-infilled chord:

- Carry out series of experimental measurements for hot spot stress/strain concentration factors (SNCF/SCF) in the static tests of in-plane bending and axial compression and tension for both un-grouted (as-welded) and grouted joints to determine stress reduction factors;
- Compare the experimental results with finite element results to calibrate the FE models and carry out further parametric study;
- Carry out fracture mechanics analysis for fatigue mechanism of grouted X tubular joints;
- Propose appropriate recommendations for practical fatigue assessment of chord grouted tubular joints.

1.3 Contents of thesis

This thesis reports the details of the research conducted, including major findings and recommendations. Chapters 3 to 4 are for partially grout-infilled tubular members, while Chapters 5 to 7 are on fatigue studies of tubular joints with emphasis on grouted X joints. Below is a brief summary of each chapter:

- Chapter 2 introduces the general background for the structural design and analysis of tubular structures in offshore engineering;
- Chapter 3 reports the experimental work carried out for three large scale tubular members subjected to axial compression under either un-grouted or partially infilling grouted conditions;
- Chapter 4 presents the refined finite element analyses and further parametric studies for the compression tests. Based on the FE results, simplified design model is proposed and additional verification tests using small scale column stubs were conducted;
- Chapter 5 presents the detailed study of the hot spot stress of tubular joints adopted in fatigue assessment in current design codes.
- Chapter 6 reports the details of the investigation for reduction of hot spot stress of grouted tubular X joints. The proposed design charts for determination of SCFs of chord grouted tubular X joints are presented.
- Chapter 7 shows the application of fracture mechanics method in fatigue assessment of grouted tubular joints with the recommendation for practical design. The design charts of DOB for grouted X joint are presented.
- Chapter 8 concludes the research findings and introduces proposals of future research work.

Chapter 2

Background of design and analysis for offshore tubular structures

2.1 Introduction

Circular hollow section (CHS) steel tubes are extensively used in offshore platforms like jackets and jack-ups, as shown in Figure 2.1, due to its excellent characteristics of low drag coefficient, high buoyancy and high strength-to-weight ratio. From structural mechanics point of view, the offshore platform, like the jacket structure, is a three dimensional space frame formed by connecting tubular members to tubular joints by the means of welding. The key structural components in such frame are tubular members and tubular joints.

(a) (b)

Figure 2.1 Typical offshore platforms: (a) jacket; (b) jack up

Current practice of structural design and analysis consists of global level frame analysis and component level design or assessment. The global frame analysis is usually performed using specifically programmed finite element software like SACS (HSE, 2000) and USFOS (Skallerud and Amdahl, 2002). These programs are capable of accounting for both dynamic load, like wave load, and dead load, like gravity in the frame analysis, and generate the nominal load for each component. The nominal load generally includes axial force, bending moment and shear force while torsional moment is usually neglected. At component level, static or quasi-static condition is assumed for design and analysis based on static strength and fatigue performance, either of which may be a governing factor.

The focus of this thesis is on structural analysis of components, i.e. for tubular member and tubular joint.

2.2 Tubular members

A tubular member is basically a cylindrical tube, which may experience axial tension, axial compression, bending, shearing and hydrostatic pressure, and the combination of all or part of the loads. Close form solutions for the response of the tubular member subjected to such loading conditions can be found in classic mechanics book (Timoshenko and Gere, 1963). Current design codes like RP2A (API, 2000), ISO 19902 (BSi, 2007), and CIDECT (Wardenier, 2002), etc. include detailed design guides for simple tubular members. The design guides are based on both close form solutions and experimental results. In terms of structural design and analysis, a tubular member is treated as a column or a beam column for global and local stability analyses, in which buckling strength and cross sectional capacity are two important criteria to determine the ultimate static strength. Buckling strength depends on the slenderness ratio of the member with the effect of eccentricity and end conditions.

Figure 2.2 shows a typical column buckling design chart of CIDECT (Wardenier, 2002). When slenderness ratio is small enough, the column capacity is controlled by cross sectional strength, i.e. either local buckling or squash load resistance capacity, and the diameter over thickness ratio (D/T) and material yield strength (σ_y) become the controlling parameters. For a tubular member, static strength governs the design. Fatigue is usually not a critical issue, provided the weld connection is properly treated without severe stress concentrations.

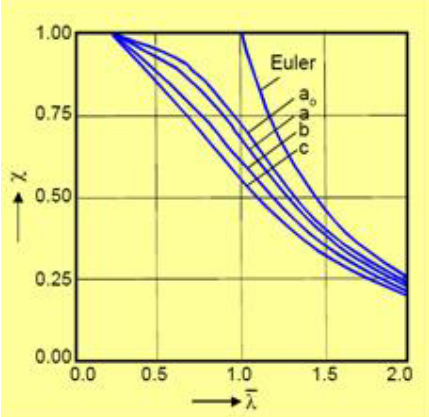

Figure 2.2 European column buckling curves, extracted from Wardenier (2002)

2.3 The state of the art grouted tubular members

Infilling a column with cementious grout or concrete provides a higher load carrying capacity without enlarging the outer diameter, so that in offshore application the drag force will not be increased. The technology has been applied in the offshore industry to repair or strengthen the damaged or un-damaged tubular members (Etterdal and Scherf, 2001). It is judged against other methods as convenient, flexible and economical (Harwood and Shuttleworth, 1988; Dier, 2004). Hence, since early sixties of last century, research programs for composite columns have been carried out (Wardenier, 2002). Some of the research conclusions have been recognized and

included in design codes. Figure 2.3 shows bending and compression interaction curves for fully grout-infilled columns.

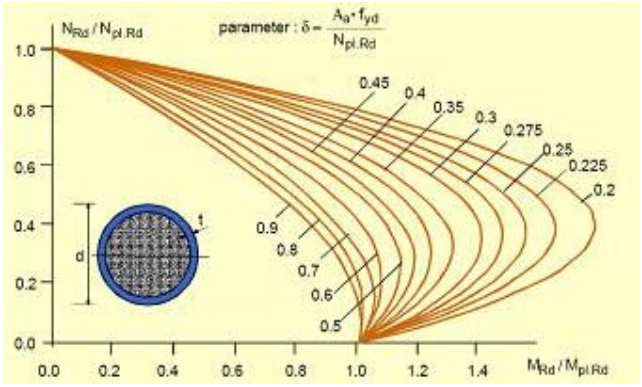

Figure 2.3 Bending and compression interaction curves for composite columns in CIDECT code (Wardenier, 2002)

Compared with full grouting, partial grouting has additional attractiveness like less weight increment. However, the provisions in current design codes are only applicable for fully grouted tubular member. Partial grouting is not covered yet due to insufficient knowledge about its behaviour at current stage (BSi, 2007), leading to limited usage of partial grouting method in offshore industry.

2.4 Tubular joints

Tubular joints are formed by welding the contoured end of the secondary tubular (brace member) onto the primary tubular (chord member). The geometry leads to complex stress/strain fields and high stress concentration at periphery of intersection of chord and brace. Figure 2.4 shows a typical T joint with basic geometry parameters. Customarily, dimensionless parameters as shown in the up-left corner of Figure 2.4 are preferred to facilitate design and analysis. The special mechanics of tubular joint is generally based on those dimensionless parameters, as described below, extracted from UEG (1985):

- Chord length parameter α, defined as the ratio of chord length L to chord radius D/2, gives an indication of chord beam bending characteristics.
- Diameter ratio β, the ratio of brace diameter (d) to the chord diameter (D), describes the compactness of the joint.
- Chord thinness ratio γ, the ratio of the chord radius to the chord wall thickness (D/2T), gives an indication of the thinness and radial stiffness of the chord.
- Wall thickness ratio τ, defined as the ratio of the wall thickness of the brace (t) to that of the chord (T), measures the likelihood that the chord wall will fail before the brace cross section.

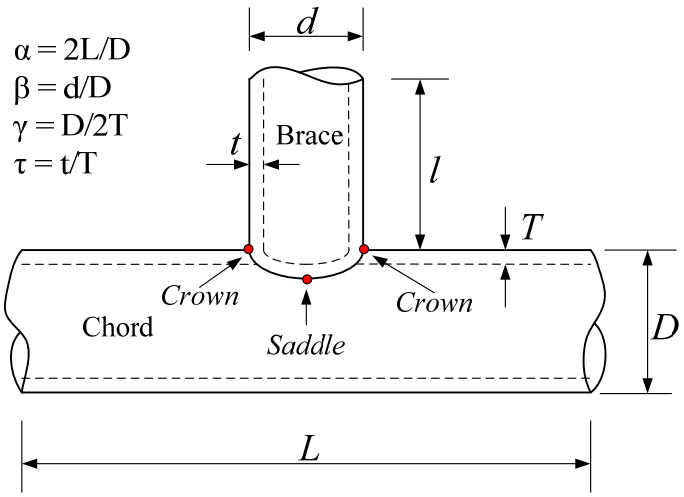

Figure 2.4 Typical tubular joint with terminology

The red dots in Figure 2.4 are the crown and saddle positions, where the largest stress, the so called 'hot spot stress', usually occurs.

Both static strength and fatigue strength need to be checked in design for tubular joints. The loading modes include axial load in brace, in-plane bending and out-plane bending in brace. For static strength, the stress induced by chord load is also included in most recent design codes (Wardenier, 2002).

2.4.1 Static strength of tubular joints

The design criteria of static strength are based on the interpretation of ultimate load test data. The failure mode of a tubular joint under static loading, as listed below, is dependent on material type, loading conditions and geometry parameters (UEG, 1985).

- Plastification of the chord;
- Chord punching shearing: cracking on the chord and gross separation of the chord and brace;
- Brace failure;
- Chord shear failure;
- Local buckling of chord and brace;

Since the examination of the failure modes under static loading shows that tubular joints have a tremendous reserve capacity beyond the point of first yield (UEG, 1985), the static strength is regarded to have little relationship with hot spot stress. It was observed in tests that the joint continued to deform to sustain increased loads beyond yielding. After approaching the peak load, the joint finally collapsed. The static strength could be characterized by various criteria, i.e. ultimate load resistance, deformation limit and fracture, etc.

Basic design formulae based on the concepts of chord plastification and punching shear have been well developed and can be found in current design codes, such as CIDECT (Wardenier et al., 1991), ISO19902 (BSi, 2007), RP2A (API, 2000), etc. Recently, further design considerations were extended to thick walled simple tubular joints (Choo et al., 2003; Qian, 2005); these thick walled joints are with small γ ratio, usually less than 10.

2.4.2 Fatigue strength of tubular joints

The fatigue performance of tubular joints is of primary importance to the integrity of offshore structures. High stress concentration makes tubular joints prone to fatigue damage. Wave loadings cause fluctuations in the stress levels at the joints, leading to fatigue crack initiation and propagation and eventual failure.

There are two basic approaches to assess the fatigue life of tubular joints. The first is S-N approach, which relies on empirically derived relationship between applied stress range and fatigue life (BSi, 2007) as shown in equation (2.1)

$$N \cdot \Delta\sigma^{m} = A \qquad (2.1)$$

where, N is fatigue life, $\Delta\sigma$ is the range of reference stress and m and A are material constants obtained from experimental investigation.

The second is fracture mechanics method, which is based on linear elastic fracture mechanics and considers the growth rate of an existing crack at each stage in its propagation. The basic fracture mechanics formula is Paris Law (Paris and Erdogan, 1960) as shown in Eq.(2.2):

$$\frac{da}{dN} = C(\Delta K)^{m'} \qquad (2.2)$$

where, a is crack depth, N is fatigue crack propagation life, ΔK is the range of stress intensity factor (SIF), and m' and C are material constants. C is sometimes called Paris coefficient.

The S-N approach is recommended in current design codes like RP2A (API, 2000), ISO 19902 (BSi, 2007), DNV RP C203 (DNV, 2005), UEG (UEG, 1985), CIDECT (Wardenier, 2002), and BS7608 (BSI, 1993), etc, which provide detailed design guides and recommendations for fatigue assessment of tubular joints in un-grouted (as-welded) condition. It is important to note that the reference stress in

different design codes varies, so that the parameters, *m* and *A* in Eq. (2.1) also varies. The reference stress can be *nominal stress* in the brace, *hot spot stress*, *notch stress* and *effective notch stress*. Even with the same reference stress like *hot spot stress*, the definition can be significantly different. Great care is needed when applying those S-N curves in actual design practice.

Compared with S-N approach, the fracture mechanics method is not so popular due to scarce accurate solutions of SIF for tubular joints, but recommendations can still be found in BS7910 (BSI, 2005). Detailed discussion and application of both *hot spot stress* S-N approach and fracture mechanics method have been presented in this thesis from Chapter 5 to Chapter 7.

2.5 The state of the art grouted tubular joints

Grouted tubular joints are also referred as composite joints. Initially, it was a by-product occurred in jacket structure as a connection between leg member and pile, the so called double-skin grouting. In a re-analysis of such grouted joints, it was found the static strength significantly improved and maximum stress much reduced. Similarly, infilling the chord of a tubular joint with cementitious material, the single skin grouting, can also achieve such enhancement effect. It was realized that the grouting method is an effective, flexible and economical way of strengthening and retrofitting. Figure 2.5 illustrates the grouted tubular joint schematically.

Effective or equivalent chord wall thickness concept has been adopted in the design codes, like ISO 19902(BSi, 2007) and DNV RP-C203 (DNV, 2008). For static strength calculation, ISO 19902 (BSi, 2007) recommends Eq. (2.3) for double skin grouting.

$$T_e = (T^2 + T_p^2)^{0.5} \qquad (2.3)$$

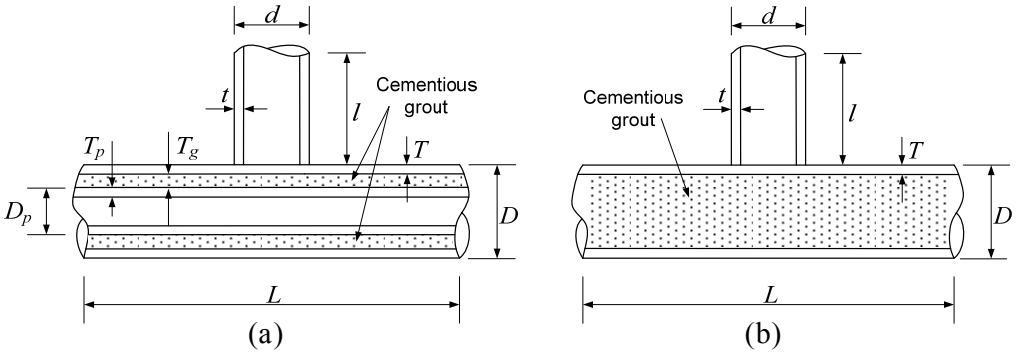

Figure 2.5 Grouted tubular joints: (a) double skin; (b) single skin (UEG, 1985)

No recommendation for single skin grouting is available in design codes currently.

For fatigue assessment, Eq. (2.4) is recommended in ISO 19902 (BSi, 2007) and DNV RP-C203 (DNV, 2008) for hot spot stress computation for grouted tubular joints.

$$T_e = (5D + 134T)/144 \qquad (2.4)$$

ISO 19902 (BSi, 2007) and DNV RP-C203 (DNV, 2008) qualitatively suggest that the S-N curve approach using the same hot spot stress S-N curve of as-welded joints is also applicable for fatigue assessment for grouted tubular joints. However, through literature review (UEG, 1985; BOMEL, 1995,a), it is found there are insufficient experimental results to support this claim. Fatigue tests of two infill grouted tubular T joints conducted in UK (HSE, 1993; BOMEL, 1995,a) shows this approach can be un-conservative for T joints with fully grouted chords.

2.6 Methodologies

Generally, from the structural and/or solid mechanics point of view, three methodologies have been adopted to analyse and understand the behaviours of tubular members and tubular joints. They are:

- Simplified analytical model,
- Numerical method, and

- Physical model test.

The three methodologies are closely related and co-exist with each other. If consistent agreements can be achieved, more simplified design procedures can be formed for routine design. Simplified analytical model is preferred by the designer, as it usually reveals the dominant mechanism from the viewpoint of physics or mechanics. Simplified analytical model needs supporting evidence from experiments. However, physical model test may be expensive and time consuming. A good replacement of physical model testing is a calibrated numerical model. In addition, numerical simulation can provide some insights that are difficult to capture in the physical model test. These insight quantities may be important to explain the dominant mechanism to support the simplified analytical model. The following sub-sections provide some very brief descriptions of how the tubular member and tubular joints are analysed in current practice.

2.6.1 Simplified analytical model

As mentioned above, the simplified model for a tubular member is a column or beam-column, so the classic buckling and beam solution can be applied with consideration of boundary conditions and eccentricities. The local buckling can be dealt with by controlling the D/t ratio for an un-reinforced member.

For a tubular joint, frequently used models for static strength analysis include (Wardenier et al., 1991):

- Ring model for chord plastification;
- Punching shear model for chord punching shear;
- Chord shear model,

based on which the basic design formula for static strength is formed in design codes.

For fatigue analysis, both the S-N approach and the fracture mechanics method may be considered as simplified analytical model.

For tubular joints using S-N approach, the nominal load is determined from global frame analysis, and nominal stress can be determined following equations (2.5) and (2.6).

for axial load in brace:

$$\sigma_n = N / A_b \qquad (2.5)$$

where, σ_n is the nominal stress, N is the axial load in brace, A_b is the cross sectional area of brace.

for bending in brace:

$$\sigma_n = M / I_b \cdot d / 2 \qquad (2.6)$$

where, M is the moment load in brace, I_b is the second moment of initial of the cross section of brace.

The nominal stress can be used directly as reference stress or multiplied by stress concentration factors to obtain hot spot stress or notch stress to check the fatigue life according to correspondent S-N curve (Wardenier et al., 1991).

The stress due to chord loading is ignored for fatigue assessment. The fatigue life of the tubular joint is correlated to the reference stress range in the S-N curve, which is determined from fatigue test. The scatter band using nominal stress is larger than using hot spot stress. Major modern design codes (Wardenier et al., 1991; API, 2000; BSi, 2007) adopt the latter as reference stress for tubular joint.

For fracture mechanics method, with the nominal load determined, the stress intensity factor can be found by either empirical solution or numerical method, and then the fatigue life can be decided according crack propagation law as discussed in section 2.4.

2.6.2 Numerical method

Finite element method is currently the most widely used and recommended numerical method. In the absence of closed form solution for complex problem like tubular joint, FE solution is the most accurate approximation to-date. General approach of finite element method for structural analysis consists of the following procedures according to the references (Zienkiewicz, 1971; Bathe, 1996).

At first, the complex structure is discretized into many substructures, the finite elements. The elements are interconnected at the boundaries by sharing the common nodes. A set of functions, the shape function, $[N]$, is chosen to describe the displacement within each element, $\{U\}$, in terms of its nodal displacements, $\{\delta\}$.

$$\{U\} = [N]\{\delta\} \tag{2.7}$$

The strain, $\{\varepsilon\}$, within each element is defined by differentiation of the displacement. The so called B matrix is determined from differentiating shape function, so that

$$\{\varepsilon\} = [B]\{\delta\} \tag{2.8}$$

The stress-strain relationship is realized by imposing Eq. (2.9):

$$\{\sigma\} = [D](\{\varepsilon\} - \{\varepsilon_0\}) + \{\sigma_0\} \tag{2.9}$$

where, $\{\sigma\}$ is the stress vector. $\{\sigma_0\}$ and $\{\varepsilon_0\}$ are the initial stress and initial strain. $[D]$ is called the tangential stiffness matrix, which represents the constitutive modelling and depend on the element type and material property.

The element level stiffness matrix, $[k]^e$, can then be obtained by using virtual work principle, and becomes:

$$[k]^e = \int [B]^T [D][B] d(vol) \tag{2.10}$$

where, $[B]^T$ is the transpose form of B matrix. (*vol)* denotes the volume integration.

Then the global stiffness matrix, $[K]$, is obtained by assembling all the element level stiffness matrixes:

$$[K] = \Sigma[k]^e \qquad (2.11)$$

With the global stiffness, the force-displacement equation can be formed:

$$[K]\{\delta\} = \{F\} \qquad (2.12)$$

where, $\{F\}$ is the nodal force vector, including the contribution from initial strain and stress, and external surface traction.

If there is only one object, the summation of the nodal force for an internal node is zero for equilibrium, and equation. (2.12) can be applied directly. If there are N objects in contact in the system, the formulation of (2.13) needs to include the contact forces on the contact surfaces, and the equation in summation form is

$$\sum_{i=1}^{N}[K]\{\delta\} = \sum_{i=1}^{N}\{F\} + \sum_{i=1}^{N}\{F\}_s \qquad (2.13)$$

where, $\{F\}_s$ is the contact force vector for the respective object, and $\sum_{i=1}^{N}\{F\}_s$ is the summation. $\{F\}_s$ is obtained through integration on the contact surfaces S_{ij}.

Note contact surfaces must appear in pair, called contact surface pair, for which the distance in between is controlled by imposing constraints. The constraints are special functions, and can be solved by using either a penalty approach or a Lagrange multiplier method for approximation (Bathe, 1996). Contact problem is frequently encountered in simulation of grouted cases. Particular concerns of contact problem are the convergence and accuracy when complex geometries, like tubular structures, are analysed. A few practical issues in dealing with contact problem like meshing, treatment of deformed shape and element selection in application for grouted tubular structures are briefly presented in this thesis in the following chapters.

Finally, through solving equations (2.12) or (2.13), the displacements vector, $\{\delta\}$, can be obtained. Once the nodal displacements have been determined, the strain and stress can be determined by equations (2.9) and (2.10) respectively.

In general, the accuracy of finite element analysis result will depend on the choice of mesh, element and boundary conditions. If the non-linearity of the analysis is significant, the iteration algorithm and imposed constraint may influence the accuracy. Even when using already matured popular commercial FE software like Abaqus (SIMULIA, 2007), attentions need to be paid for these aspects in practical application. Sensitivity study is essential, and calibration of FE results is a must for using it as a tool.

2.6.3 Physical model test

As mentioned, either simplified analytical model or numerical analysis result needs to be supported by proof from model test. Experimental work is indispensible in any engineering disciplines. However, there are concerns for model test in offshore engineering. Firstly, the scale of offshore structure is large as compared with normal onshore structure. As design proof, large scale specimen is preferred, this leads to high expenditure. Secondly, the boundary condition of the real structure is difficult to simulate. For component level testing, the boundary restraint is normally set sufficiently far away from the critical region, usually at distance of certain times of diameter for tubular structure, so that the influence of boundary conditions can be ignored according to Saint-Venant's Principle (Timoshenko and Gere, 1963).

Modern design codes like ISO19902 (BSi, 2007) and CIDECT (Wardenier et al., 1991), are based on interpretation of available data, both experimentally and numerically, while RP2A (API, 2000) is largely based on experimental data.

2.7 Conclusion

Sections 2.2 to 2.5 of this chapter review generally the code provisions for deign of tubular member and tubular joint. For as-welded (un-grouted) tubular members and joints, current design codes are becoming mature. However, for grouted tubular members and joints, reliable information for some important aspects is insufficient at current stage. For grouted tubular member, the partial grouting and local buckling are not covered. For grouted tubular joints, the design calculation for static strength and fatigue assessment are incomplete. This thesis is an attempt to address some of the uncovered topics using the three methodologies mentioned in the above section 2.6.

Chapter 3

Experimental investigation for partially grout infilled tubular members subjected to axial compression

3.1 Introduction

Tubular members of offshore platforms - especially existing aging jacket platforms, may need to be strengthened to extend the service life or sustain additional load. Among the strengthening technologies, infill grouting method has favorable advantages over the others, such as no additional hydrodynamic drag force incurred, convenience in construction and cost effectiveness, etc. Based on the research results conducted in recent decades, major offshore codes, like API RP2A (2000), ISO19902 (BSi, 2007) and CIDECT (Wardenier, 2002), have incorporated some engineering equations for design calculations for fully grout-infilled tubular members with the assumption of full composite action. The industry has also adopted the fully grout-infilling construction as one of repairing and strengthening methods for tubular members (Harwood and Shuttleworth, 1988; MSL, 2004). However, in certain situations, grout infilling along part of a member will be a good solution. For example, in case part of a leg member of a platform needs to be strengthened, partial infilled grouting of the leg member together with the tubular joint, as illustrated in

Figure 3.1, is rational in the sense of structural mechanics, since the additional weight due to partial infilling is insignificant. Yet, it is found that information in the open literature about partial grouting is insufficient for reference in structural analysis and design. The understanding and confidence for application of partially grouted method significantly lags behind that of fully grouted method at current stage.

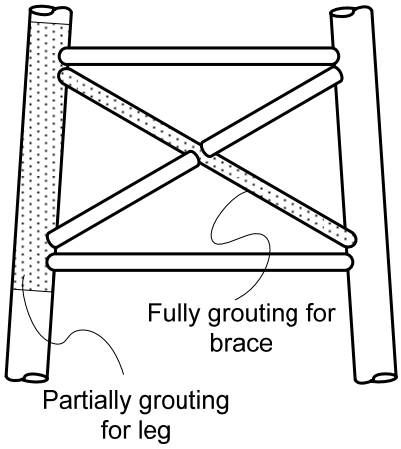

Figure 3.1 Illustration of grouting schemes for typical tubular frame

From structural analysis point of view, the fundamental mechanisms for a grout-infilled tubular member to achieve composite effect under axial compression load is either end bearing or interfacial shearing, or a combination of the two. In fully grouted condition, if the end bearing mechanism is active, the sectional load carrying capacity may be calculated based on full composite assumption, as illustrated in Figure 3.2 (a), where the grout and steel have same displacement Δ. Sufficient ductility for both steel and grout ensures plastic analysis and design is valid. Design codes, like CIDECT (Wardenier, 2002), contain detailed design guides for this case. The interfacial action concerned is mainly on the normal direction for the confinement effect of enhanced grout strength due to tri-axial stress condition. If the end bearing is inactive or ambiguously defined, then the interfacial shearing is considered as governing

mechanism. Offshore code ISO19902 (BSi, 2007) includes the design equations for this case based on experimental results. It is noted that a similar case based on interfacial shearing mechanism is the grouted connection of double-skin pile and sleeve, where the annulus between the pile and sleeve is infilled with grout. This type of connection together with shear key, as illustrated in Figure 3.2 (b), is extensively used for pile head connection with the jacket platform. Offshore code API RP2A (2000) considers this type of *load transfer mechanism as a combination of bond and confinement friction between the grout and the steel surfaces and the bearing of grout against mechanical aids such as shear keys*. The design equation for API RP2A was derived based on such understanding of the mechanism (Krahl and Karsan, 1985). For the case of plain connection without shear key, the limiting transfer stress on the interface is also specified in the code (API, 2000) based on experimental evidence.

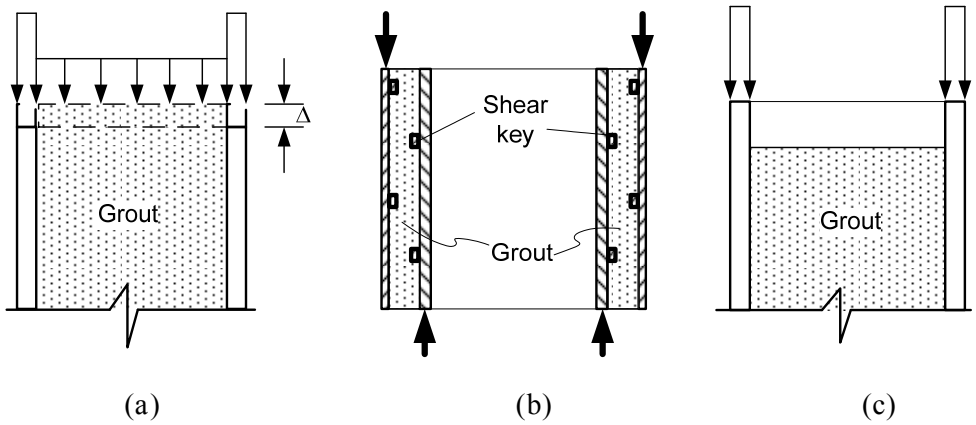

Figure 3.2 Illustrations of grouted tubular members: (a) fully grouting with end bearing active; (b) pile-sleeve grouted connection (double skin) with shear keys on the interface; (c) partially infilled grouting

In contrast to the research for full grouting, the study for partial grouting, as illustrated in Figure 3.2 (c), is rarely reported in the open literature. Only Parsanejad and Gusheh (1992) proposes a conservative solution for partially grout-filled damaged

and undamaged tubular members, in which the interfacial shearing action is totally ignored in sectional capacity calculation for axial load. They mentioned *that the behavior of grouting in partially grouted tubes is somewhat unpredictable*. But the composite effect is still assumed in their equation derivation. The function of the grout is considered to prevent the dent, or the wall at critical location, from deforming inwards, so that the member buckling capacity, or bending modulus, could be improved with the partially infilled grout.

Obviously, if the tangential interfacial shearing mechanism is effective for a partially grout-infilled member, its sectional axial load carrying capacity can be improved also. However, even in fully grouted condition, the information about the tangential shearing mechanism for grout-steel interface reported in the literature is neither consistent nor conclusive. The most arguable issue is the interfacial bond (adhesive shearing resistance).

Dier (2004) emphasized the essentiality for active bearing mechanism in fully infilled grouting condition that *this is the only way that load can be transferred to the grout by direct bearing on the grout column*.

Elnashai and Aritenang (1991) conducted nonlinear FE modeling for the bond-slip action on the grout-steel interface of double-skin grouted connection. They used the term '*intrinsic shear strength*' to express the interfacial bond and postulated it is related to the normal confinement pressure.

Shakir-Khalil and Hassan (1994) found that the interfacial transferring stress is generally low and with large scatter in the push out tests. They indicated the bond between the steel and concrete seems to be related to the shrinkage of the concrete.

Sele and Skjolde (1993) performed statistical analysis for 750 test results on the ultimate strength of double-skin grouted connections. For the plain grouted

connections, they indicated the interfacial bond is closely related to the surface unevenness of the steel and the shrinkage of the grout, which is further related to the tensile stress in the grout and the radial stiffness of the steel pile.

Etterdal et al. (2001) published the experimental results for push out tests for grout-infilled columns with high strength grout Ducorit S5. They claimed the steel-grout interfacial bond/friction stress to be 0.33 MPa from slip test in low confinement condition.

From the brief review above, it can be found that the interfacial bond is related to multiple factors, in which the confinement condition of the grout is an important one. Comparing the confinement conditions of the grout, the double-skin pile-sleeve connection has the best confinement condition and the partially infill grouting has the lowest. As such, it is essential to point out that the limiting transfer stress in the design code (API, 2000; BSI, 2007) for plain steel-grout interface corresponds to sufficient confinement condition, and is not supposed to be applied for partially infilling case.

Therefore, in order to have a better understanding for the behavior of partially grout-infilled tubular members and find a solution for enhancing the axial load carrying capacity of the cross section with partial grouting method, a series of investigations were carried out. Preliminary finite element analyses for a partially grouted tubular member simulating part of a leg member of offshore jacket structure were conducted firstly. Then, based on the results of preliminary FE results, three tubular members with same sizes were designed and fabricated and finally tested under static axial compression loads. The first specimen was in an un-grouted condition serving as a control specimen. The other two specimens G1 and G2 were partially grouted with high strength grout Ducorit D4. G1 was with proposed stiffening plates as the shear keys and G2 was with plain grout-steel interface to exam

the strengthening effects of the two interfacial mechanisms. G1 shows the highest strength and eliminates local member buckling problem which occurred in the un-grouted control specimen, and G2 in the monotonic loading tests. In the subsequent cyclic loading test for G1, its performance was encouraging: it did not exhibit observable signs of degradation even under large amplitude load cycles. The experimental results strongly demonstrated that with the high strength grout and the proposed stiffening plate, significant strengthening effect could be achieved for partial infilled grouting. The details of the research are presented in the following sections in the sequence of preliminary FE analysis, experimental investigation and discussion of the results and conclusion.

3.2 Preliminary finite element analysis

Preliminary finite element analysis was carried out first with the computed results serving as basis for specimen design. The general finite element software package Abaqus6.7-1 (SIMULIA, 2007) was utilized in the study. In the following sub-sections, the equations related to the computational aspects are referenced from Abaqus manuals.

3.2.1 Modeling a jacket platform leg in reduced scale

The specimen was supposed to simulate an idealized jacket platform leg member with reduced scale. The initial size of the preliminary FE model was based on simple hand calculation, and the following considerations were taken into account:

- The diameter-to-thickness(D/t) ratio and the slenderness (L/D) were controlled around 50 and 10 respectively, so that plastic/compact section, which is typical for offshore platform leg member, can be achieved;

- To simulate the leg member of offshore platform in actual condition, the working stress and failure mode of the specimen should be similar to real situation;
- Joint can should be included to simulate the actual connection between joint can and leg member;
- The maximum load to crush the specimen to be within the capacity of test rig.

After a few iterations, the geometry of the preliminary FE model was determined as shown in Figure 3.3 (a). Three-dimensional model was built and meshed. The model consisted of three parts, the leg, the grout and the joint can. Two orthogonal lateral stubs were attached to the joint can perpendicularly to simulate brace members. Due to the symmetry of loading and geometry, one-eighth model was analyzed in preliminary FE work.

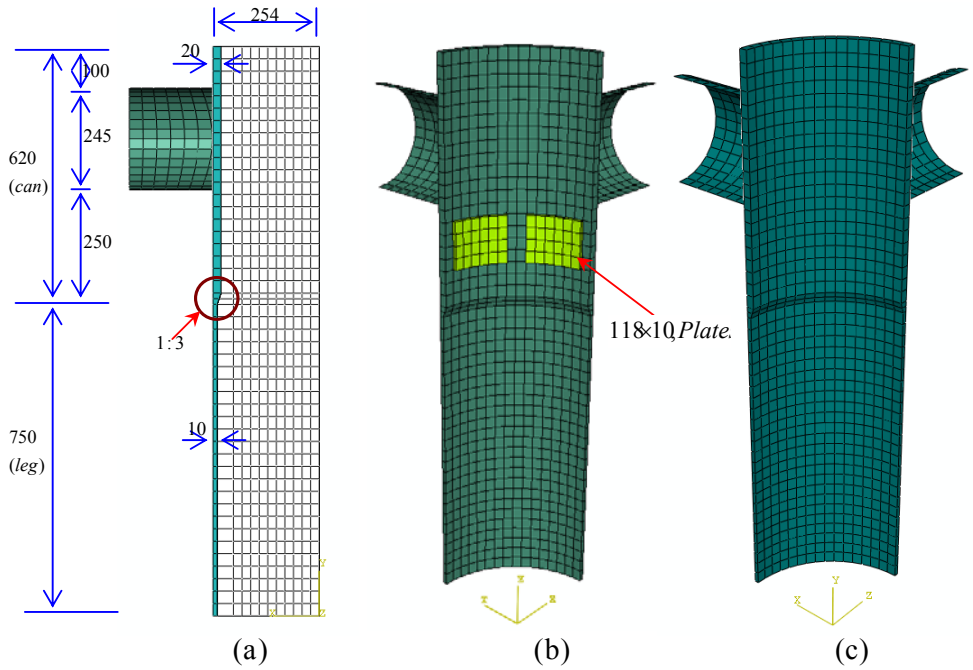

Figure 3.3 Models of preliminary FEA: (a) over view of one-eighth model; (b) model I (with stiffening plates); (c) control specimen and model II

3.2.2 Interfacial mechanisms

The grout-steel interfacial mechanism and its strengthening effect was the focus of the research work. If the two materials are in fully bonded condition, the mesh of two parts in finite element analysis can be tied up, as there is no relative sliding. However, this full composite effect is very difficult to achieve for plain pipe connection in real situation, even for grout in fully confined condition. Dier (2004) indicated that *for infill grout method sufficient load cannot be relied upon to be transferred in bond between the tube inner wall and grout - tests show that a progressive mode of failure acts*. On the other hand, there are references recognizing the adhesive bonding effect on the interface. RP2A (API, 2000) specifies that for confined grout in plain pipe connection, the limits for interface bond/shear stress around 0.1MPa~0.2MPa. As mentioned above, Etterdal et al. (2001) claimed that for unconfined grout the measured value is 0.33 MPa from the interface slip test.

In this study, the interfacial bonding stress is deemed as the resistance strength against shearing caused by external loading. Only tangential shear resistance is recognized as the bond strength. If the interfacial shear stress reaches a certain value, the bond will fail and the bond shear strength decreases to zero. Then, the frictional shear becomes effective, provided the two materials are in contact, i.e. there is contact pressure on the interface. The frictional shear mechanism will continue to transfer the load after the bond break.

However, the interfacial mechanism is rather complex as considered above. For simplification for initial estimation, only frictional shear stress was recognized in the preliminary FE analysis, ignoring the initial adhesive bond effect. The interfacial action between the steel and grout was specified as normal “hard contact”, which means that the nodes of two materials are not allowed to penetrate with each other.

The tangential frictional shear effect is included according to the standard Coulomb friction model. It assumes that no relative motion occurs if the equivalent frictional stress, τ_{eq} , Eq. (3.1),

$$\tau_{eq} = \sqrt{\tau_1^2 + \tau_2^2} \qquad (3.1)$$

is less than the critical stress, τ_{crit}, which is proportional to the contact pressure, p, in the form of Eq. (3.2)

$$\tau_{crit} = \mu \cdot p \qquad (3.2)$$

where, μ is the friction coefficient.

In Abaqus it is possible to put a limit on the critical stress, Eq. (3.3):

$$\tau_{crit} = \min(\mu p, \tau_{\max}) \qquad (3.3)$$

It can be reasonably postulated that this is a conservative way to consider the interfacial mechanism from the point of view of design. The preliminary FE solution was lower bound estimation for initial sizing of specimen. In fact, more sophisticated bond analysis was performed later in the refined FE back analysis in Chapter 4.

In the preliminary FE analysis, two 3D models, Model I and Model II, as shown in Figure 3.3, were adopted to compare the different strengthening effects of two suggested interfacial mechanisms. Model I was with proposed shear keys - the 10mm thick stiffening plates, while Model II was based on plain grout-steel interface. The coefficient of friction was 0.3 and the maximum shear stress was limited to 1 MPa.

3.2.3 Element types

The element type in Abaqus (SIMULIA, 2007) for the leg (including the thick wall part simulating the joint can) and grout was C3D8R, the 8 node brick element with reduced integration. In order to reduce the total number of elements for efficient computation, incompatible shell element SR4 was adopted for the lateral stubs, which

was coupled to the leg using shell-to-solid coupling function, i.e. multi-point constraint in Abaqus (SIMULIA, 2007). This was because the major concern of the analysis was on the global performance of the composite member, and the local stress-strain information of the joint connection was a secondary concern.

3.2.4 Material properties

The steel used in the preliminary FE had minimum yield strength of 355 MPa, and ultimate strength of 500 MPa. The grout material was high strength cementious grout, Ducorit D4, with a nominal compressive strength 200 MPa. The Young's moduli were 205GPa and 70 GPa, and the Poison' ratios were 0.3 and 0.19 for the steel and grout respectively. The stress-strain curves used in preliminary FE work are shown in Figure 3.4. The classic Von – Mises plastic constitutive model was assigned for both materials.

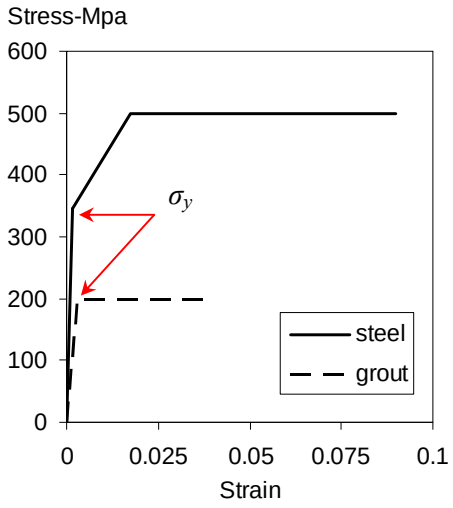

Figure 3.4 Uni-axial stress-strain curves used in preliminary FEA

It has been mentioned in Chapter 2 that the material stress-strain relationship, also called as constitutive modeling in finite element analysis, is represented in the tangential stiffness $[D]$. For an elastic material, the material's response to loading

obeys the generalized Hook's law, so that for a 3 dimensional isotropic solid element, the tangential stiffness matrix is:

$$[D]=\frac{E(1-\nu)}{(1+\nu)(1-2\nu)}\begin{bmatrix} 1 & \nu/(1-\nu) & \nu/(1-\nu) & 0 & 0 & 0 \\ & 1 & \nu/(1-\nu) & 0 & 0 & 0 \\ & & 1 & 0 & 0 & 0 \\ & \textit{symmetric} & & \frac{(1-2\nu)}{2(1-\nu)} & 0 & 0 \\ & & & & \frac{(1-2\nu)}{2(1-\nu)} & 0 \\ & & & & & \frac{(1-2\nu)}{2(1-\nu)} \end{bmatrix} \quad (3.4)$$

where, E is the Young's modulus and υ is the Poisson's ratio.

When the loading continues to increase, the material will yield and go into plastic stage. The yield criteria adopted in this study is von Mises criteria using the effective stress, also called von Mises stress, which is a scalar and can be expressed in terms of principal stress as equation (3.5):

$$\sigma_e=\frac{1}{\sqrt{2}}[(\sigma_1-\sigma_2)^2+(\sigma_2-\sigma_3)^2+(\sigma_3-\sigma_1)^2]^{1/2} \quad (3.5)$$

or in terms of direct and shear stresses as equation (3.6):

$$\sigma_e=[\frac{3}{2}(\sigma_{11}{}^2+\sigma_{22}{}^2+\sigma_{33}{}^2+2\sigma_{12}{}^2+2\sigma_{23}{}^2+2\sigma_{13}{}^2)]^{1/2} \quad (3.6)$$

Comparing the effective stress with the yield stress σ_y, the turning points of the curves in Figure 3.4, indicate that,

- if $\sigma_e<\sigma_y$, then the material is elastic,
- if $\sigma_e\geq\sigma_y$, then the material has yielded.

The stress-strain relationship in plastic stage follows incremental plasticity model incorporated in Abaqus (SIMULIA, 2007) , which decomposes every total strain increment into two parts, (3.7):

$$d[\varepsilon]=d[\varepsilon^e]+d[\varepsilon^p] \quad (3.7)$$

$d[\varepsilon^e]$ is the elastic strain increment and $d[\varepsilon^p]$ is the plastic strain increment.

The increment of elastic strain follows Hook's law, while the increment of plastic strain follows flow rule and hardening multiplier taken from uniaxial stress-strain data. In simple expression, the stress-strain relationship can be written as (3.8):

$$d[\sigma] = [D](d[\varepsilon] - d[\varepsilon^p]) = [D](d[\varepsilon] - d\lambda[n]) \qquad (3.8)$$

where, $d[\sigma]$and $d[\varepsilon]$ are the increments of total stress and total strain. $[n]$ is the stress tensor normal, which determines the direction of plastic strain increment and is derived from plastic normality hypothesis.

$$[n] = \frac{3}{2}\frac{[\sigma']}{\sigma_e} \qquad (3.9)$$

where, $[\sigma']$ is the deviatoric stress tensor, (3.10):

$$[\sigma'] = \begin{bmatrix} \sigma_{11} & \sigma_{12} & \sigma_{13} \\ \sigma_{21} & \sigma_{22} & \sigma_{23} \\ \sigma_{31} & \sigma_{32} & \sigma_{33} \end{bmatrix} - \begin{bmatrix} \sigma_{11} & & \\ & \sigma_{22} & \\ & & \sigma_{33} \end{bmatrix} \qquad (3.10)$$

$d\lambda$ is the plastic multiplier, determined from uniaxial stress-strain curve. For a von Mises material with linear hardening, $d\lambda$ is determined from equation (3.11) (Dunne and Petrinic, 2005):

$$d\lambda = \frac{[n]\cdot[D]d[\varepsilon]}{[n]\cdot[D][n] + h} \qquad (3.11)$$

where, h is the plastic modulus, the slope of uniaxial stress-strain curve in plastic stage. In Figure 3.4, h has two magnitudes.

With the $[n]$ and $d\lambda$ incorporated into equation (3.8), the stress-strain relationship can be written as (3.12):

$$d[\sigma] = [D]_{ep}\, d[\varepsilon] \qquad (3.12)$$

in terms of total stress strain increments and general elasto-plastic stiffness $[D]_{ep}$.

In Abaqus/standard (SIMULIA, 2007) backward Euler method is used for iterative solution.

3.2.5 Boundary conditions

The boundary conditions of the models are shown in Figure 3.5, in which, two symmetric planes were specified for the one eighth models, so that the nodes on the symmetric plane could not move perpendicular to its reference plane. Vertically, the displacement is restrained at bottom.

To simulate a partial infilled grout situation, the loads were imposed on steel only, without direct bearing load on the grout, as shown in Figure 3.5. In this case, the load resistance capacity of the grout would only be mobilized through interface load transfer mechanism. Two steps of pressure loads were imposed first, then in step 3 displacement was imposed to crush the member. Step 1 and step 2 corresponded to working condition and extreme condition respectively, as listed in Table 3.1, and step 3 was to obtain the ultimate strength. Different combinations of the loads in first two steps were specified as different load cases, and are listed in the following sub-section.

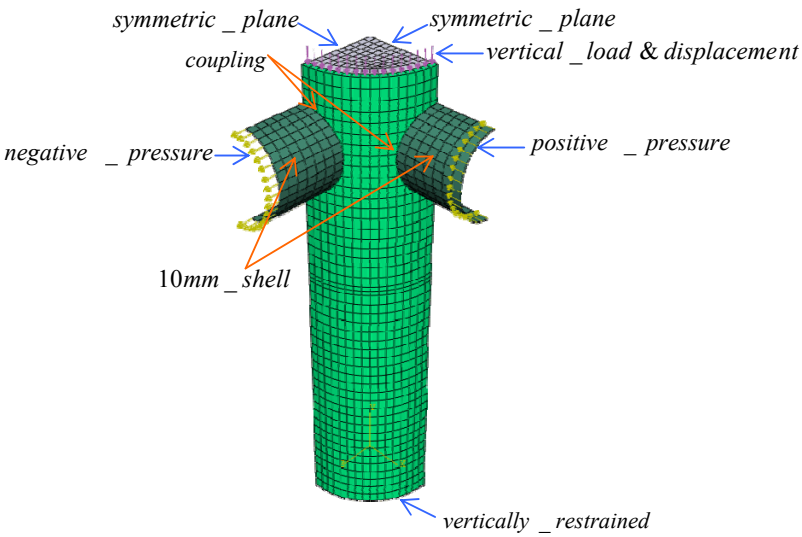

Figure 3.5 Illustration of loads and boundary conditions

Table 3.1 Loads imposed in step 1 and step 2

	Vertical load	Proportional lateral load on brace stubs
Step 1	1670kN	No
Step 2	2041kN	Tension = 354 kN (refer to load cases)
		Compression = -565 kN (refer to load cases)

3.2.6 Load Cases

For concise presentation, the following load cases are selected for reporting. The contact effect kicked in from 1st step is to simulate a newly built member, while the contact effect kicked in from 2nd step is to simulate an existing member which undergoes strengthening operation in working condition. For the latter case, the 1st step load is termed as pre-load.

Base case, steel member with vertical load only, no contact effect;

Load case I, the corresponding model is Model I with stiffening plates welded in the internal surface, considering bearing effect with different lateral load combinations:

- ***I-a***, steel/grout contact effective from beginning with lateral compressive loads on both stubs effective from 2nd step;
- ***I-b***, steel/grout contact effective from beginning with lateral tensile and compressive loads effective from 2nd step;
- ***I-c***, steel/grout contact with lateral compressive loads on both stubs effective from 2nd step;
- ***I-d***, steel/grout contact with lateral tensile and compressive loads effective from 2nd step;
- ***I-e,*** steel/grout contact effective from beginning with only one lateral compressive load from 2nd step;
- ***I-f***, steel/grout contact with the only one compression lateral load effective from 2nd step.

Load Case II, this corresponds with Model II, based on As-is condition but considering the reinforcing infilled grout frictional effect, while varying the lateral load combinations:

- ***II-a***, steel/grout contact effective from beginning with lateral tensile and compressive loads effective from 2nd step;
- ***II-b***, steel/grout contact effective from 2nd step with lateral tensile and compressive loads effective from 2nd step;
- ***II-c,*** steel/grout contact effective from beginning with lateral compression load only effective from 2nd step;
- ***II-d,*** steel/grout contact effective from 2nd step with lateral compression load only effective from 2nd step;

3.2.7 Analyses and results

The analysis was performed on HP workstation HPXW6200. In order to have efficient and accurate computational analyses, matching mesh for different parts at contact area was adopted. However, convergence was still a main obstacle frequently encountered, especially for the contact effect starting from 2nd step. Deformed grout mesh for the step when contact effect kicks in was used to solve the convergence problem. The following operations were performed to achieve a good matching deformed mesh for the grout:

- Specify the grout as purely linear elastic with very small Young's modulus;
- Tie the grout mesh to the steel member mesh, so that the two mesh deform simultaneously with the negligible stiffness contribution from the grout mesh;
- Start another contact analysis with deformed grout mesh. The deformed grout mesh can be imported from previous analysis result file (.odb file)

The preliminary FEA results are summarized in the Table 3.2 and Figure 3.6 and

Figure 3.7. The analysis results reveal significant difference between the two considered interfacial mechanisms.

For the base case, the most critical region is the chamfered transition zone of the cross section, where stress concentration occurred, leading to first yield as the load is increased, and the thin wall part finally buckled causing failure. Figure 3.6 (a) shows the failure mode for the base case.

For Model I, the infilled grout with additional stiffening plates, the strength was significantly improved as compared with the base case. The stress level at chamfer transition zone was greatly relieved, and the ultimate strength was much higher. However, the grout under direct contact with the stiffening plate experienced high stress, which will cause crushing before reaching the global yield point. It was noted that the grout in preliminary FE analysis was assumed to be elastic-plastic perfect without failure; the local failure of the grout was thus not captured.

For Model II, the infilled grout in plain connection, the strengthening effect was not as significant, and the failure mode is similar to the base case. Compared with base case, there was minor stress relief for the chamfer transition zone, and the ultimate strength was slightly improved. Due to the Poisson's ratio effect: the steel member expands radially under axial compressive load, so that there was no contact pressure between the grout and internal surface of the steel, which leads to zero interfacial skin friction for most area. The contact pressure only exists in the chamfer transition zone.

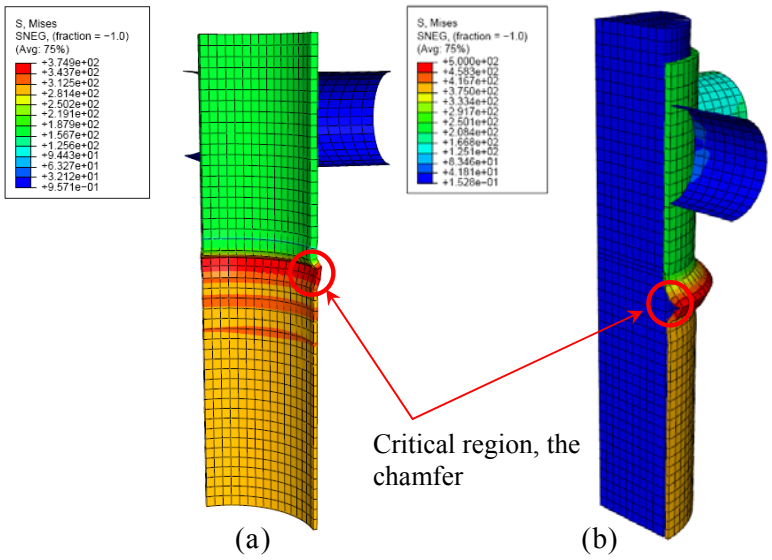

Figure 3.6 Predicted failure modes: (a) base case, (b) Model II

Table 3.2 Summary of preliminary FEA results

Model	Analysis no.	Two Steps				Load at onset of first yield - N	Displacement at onset of first yield - mm
		Step 1		Step 2			
		Axial	Lateral	Axial	Lateral		
Base	Base	Yes (without contact)	no	Yes (without contact)	yes	3.86E+06*	1.44
I	I-a	yes(with contact)	no	yes(with contact)	c&c	5.90E+06**	0.88
	I-b					5.46E+06**	0.84
	I-c	yes(without contact)				7.21E+06**	1.45
	I-d					6.77E+06**	1.42
	I-e	yes(with contact)			c	5.90E+06**	0.89
	I-f	yes(without contact)				7.21E+06**	1.46
II	II-a	yes(with contact)	no	yes(with contact)	c&t	4.00E+06*	1.24
	II-b	yes(without contact)				4.00E+06*	1.28
	II-c	yes(with contact)			c	4.00E+06*	1.28
	II-d	yes(without contact)				4.00E+06*	1.33

*: governed by yielding of steel;
** governed by yielding of grout;
Model I: As-is with two brace stubs and internal stiffening plates;
Model II: As-is with two brace stubs; **c&c**: Both brace stubs in compression; **c&t**: One brace stub in compression and another in tension; **c**: One brace stub in compression and another free

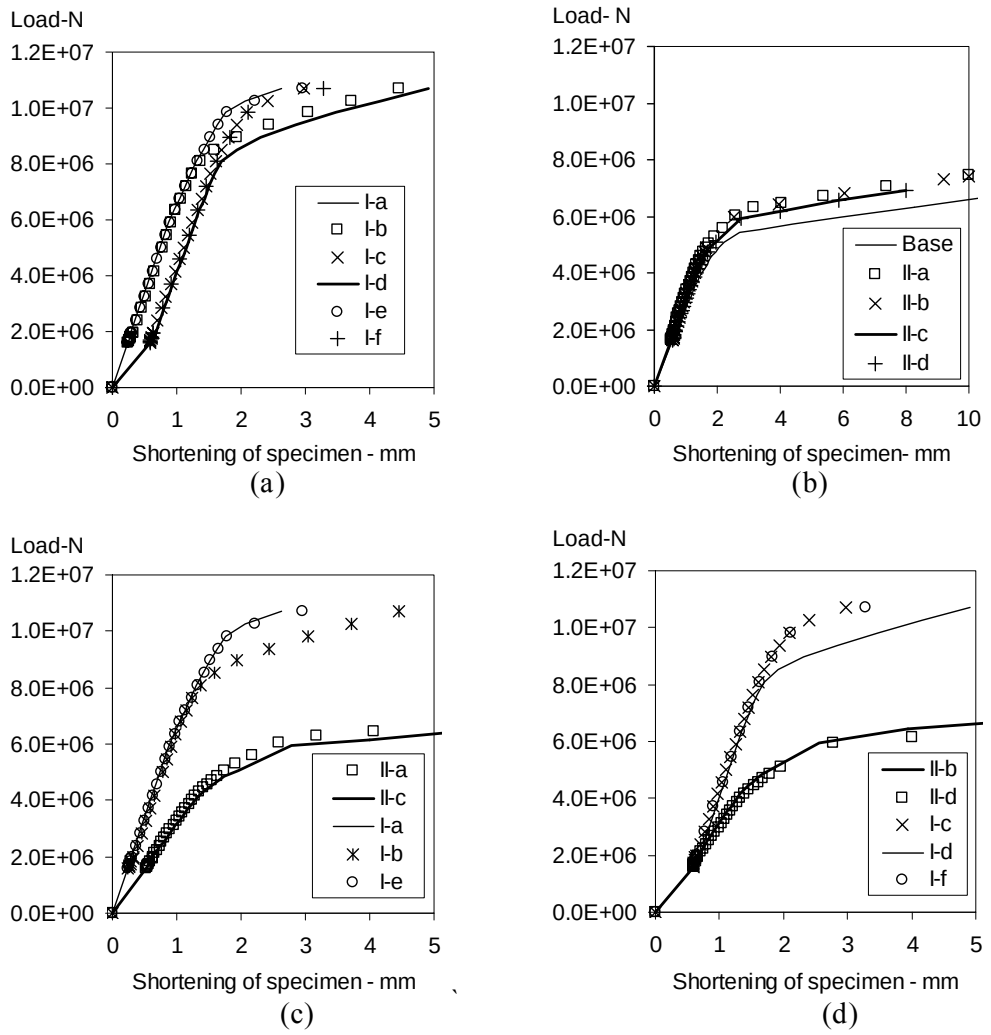

Figure 3.7 Predicted load-displacement curves: (a) model I; (b) model II; (c) contact effect from beginning; (d) contact effect from 2nd step

From the summary of results and plots it was further noted that:

For Model I:

- The effect of pre-stress is significant. However, the difference is constant irrespective of the lateral loading combination up to the yield load.
- For both with and without grout-steel contact from step 1, the mixed lateral load (c&t) cases show lower axial load at yield; however the difference is constant.
- All other load cases produce similar axial load at yield.

For Model II:

- Axial loads at the onset of yield at the chamfer cross section transition zone are the same irrespective of lateral loading combination, while the corresponding displacements are slightly different showing the minor changes in stiffness.

3.3 Experimental investigation

3.3.1 Specification of specimen

Based on preliminary finite element analysis results, a steel tubular member was designed according to the preliminary FE model with the additional features as follows:

- Including a special feature - stiffening rings, which are very often used in existing jacket platforms;
- Since the influence of lateral loads is insignificant, it was proposed to apply only the compressive load on one pair of opposing stubs instead of applying tensile and compressive loads on two pairs of stubs. This simplification avoided the difficulties faced in setting up for tensile load at the specimen end;
- Extending grout length with the thick wall portion to exam the bond effect, this was not included in preliminary FEA. If the bond effect was significant, the strengthening effect of grouted specimen should be higher than the preliminary FEA prediction;
- Stiffening plates were proposed in grouted specimen according to preliminary FE Model I, but the position was shifted up slightly for easy fabrication.

The geometry of the specimen is shown in the Figure 3.8, and Table 3.3. The construction drawing with detailed dimensions is attached in Appendix 1. In addition,

a 75mm diameter tensioner bar was designed as shown in Figure 3.8 to impose lateral load onto the stubs. During the tests, the 75mm bar will be post-tensioned progressively by a hydraulic pump from one end of the lateral stub. The post tension pressure would be converted to compressive load.

Table 3.3 Geometric parameters for the specimens

	Joint can section	Leg member section	Brace
Diameter (D)-mm	508	508	273
Thickness (t)-mm	20	10	7.1
D/t	25.4	50.8	39
Length-mm	1330	1300	300
L/D	2.6	26	1.1

The chamfer profile of transition of cross section was 1:3 following the preliminary FE model. Welds were over-match butt weld for the tube connection, and three side-welded fillet weld for the stiffening plates of G1 to ensure a direct flush bearing contact with the infill grout.

The steel material used had minimum yield strength of 355 MPa and complied with API 5 L specifications (API, 2000). The grout material was high strength cementitious grout Ducorit D4 with nominal compressive strength 200 MPa. A summary of the mechanical properties (nominal values) of the materials is presented in Table 3.4. The notations of the specimens are listed in Table 3.5.

Table 3.4 Mechanical properties of materials

	Young's modulus -MPa	Poisson ratio	Yield strength - MPa	Ultimate strength-MPa
Steel (API 5L)	205000	0.3	345	500
Grout (Ducorit D4)	70000	0.19	200	200

Table 3.5 Notation of the specimens

Specimens	Control	G1	G2
Grouting	no	yes	yes
Stiffener plates	no	yes	no
Preliminary FE model	Base	Model I	Model II

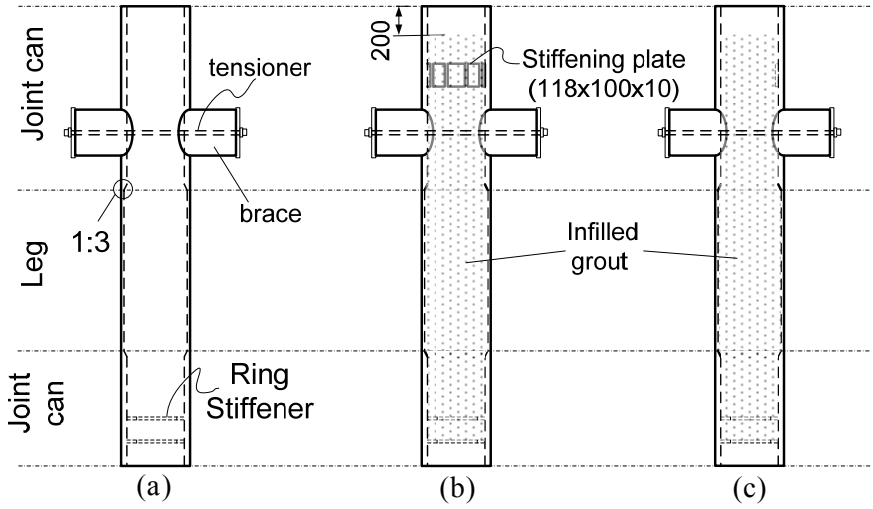

Figure 3.8 Details of the specimens: (a) control; (b) G1; (c) G2

3.3.2 Fabrication and grouting

The tubular members were fabricated by the contractor, WY Ltd, according to the above specifications. Welding quality was inspected by DNV Singapore, using NDT technology. General dimensional tolerance was later measured in the lab before testing and was found to be within acceptable range.

Grouting was carried out in the Structural Engineering Laboratories of NUS. In order to ensure a smooth casting operation, accurate weighing and pre-batching was done beforehand, as Ducorit D4 is a fast setting cementitious grout (the mix rate and setting time is shown in the Appendix 2). The bottom of the tubes was sealed with timber formwork. Tremie method was used for grouting with the specimen in upright position, shown in Figure 3.9. During casting the outlet of the tremie hose was always

kept below the grout surface level to minimize trapped air bubble. Mechanical vibration was not employed to simulate the worst offshore construction condition, thus the compactness relied fully on gravity. Curing was in natural condition. The load tests were carried out 30 days after casting. Both cylindrical and cube grout samples were taken during casting.

Figure 3.9 Grouting the specimen: keeping the trimie hose out-let below the grout surface

3.3.3 Experimental equipment

3.3.3.1 Test rig and set up

The axial load tests were conducted in the Structural Engineering Laboratory of NUS. A custom built test rig with Instron actuator, Figure 3.10, was employed to load the specimens in axial direction. The computerized servo-controlled electro-hydraulic actuator has a capacity of 1,000T. Progressive lateral loads were imposed by post tensioning the tensioner using a manual hydraulic pump. One UPM 100 data logger and two extension boxes, with PC connected, were used to record the data.

Two thick bearing plates were attached to the specimen to eliminate the influence

of eccentricity. For safety considerations, the specimen was chain blocked during tests. Details are shown in Figure 3.10.

Figure 3.10 Set up of the test rig

3.3.3.2 Instrumentation

Post-yield rosette strain gauges, Figure 3.11, (c), were applied on the external surface of the steel. The strain gauges were classified at 7 levels for easy notation, as shown in Figure 3.11 (a). Level 5 and level 3 correspond to the chamfer transition zone of the section. Level 4 was at the middle of the thin section, where the nominal stress/strain value was supposed to be measured. At each level, there were 4 rosette gauges.

3 pairs of displacement transducers (Figure 3.11, d) were mounted on the two thick bearing plates to measure the shortening of the whole specimen. In order to make a direct comparison with the preliminary FEA results, 2 pairs were mounted on the middle part of the specimen following the length of preliminary FE model. Each pair of the transducers stood on the same ground, so that the difference of the readings

of each pair represented the actual deformation under compression.

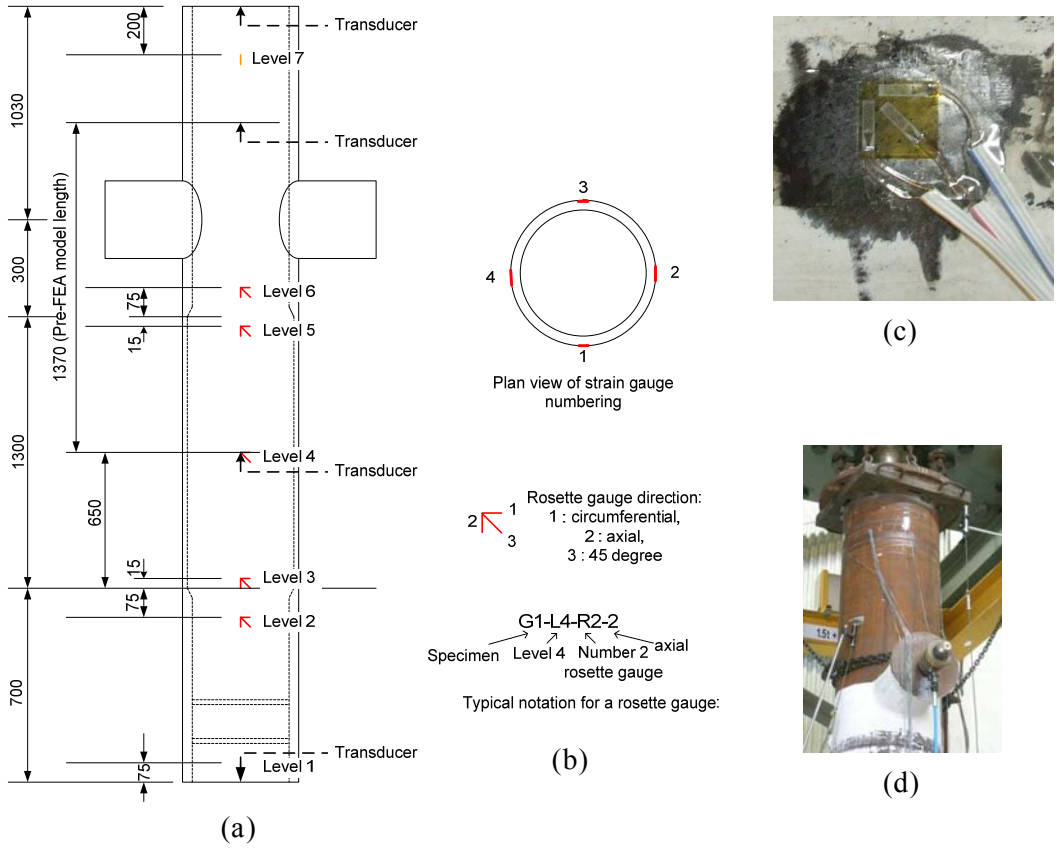

Figure 3.11 Illustrations of the instrumentation: (a) layout; (b) notations; (c) typical post yield rosette gauge; (d) typical transducer

3.3.4 Test procedures

3.3.4.1 Monotonic loading

For axial capacity, the preliminary FEA result indicated the difference in the yield load was a constant between with and without pre-stress. Hence, the pre-stress stage was not tested to reduce the complexity of the specimen preparation and avoid the difficulties in applying consistent pre-stress. The axial compressive load in the tests was applied from beginning.

With respect to the lateral load, only compressive load was applied on the stubs. This simplification avoided the difficulties faced in setting up for tensile load and

ensured a better control to applied load and hence the test results. Corresponding to the load case notation in Table 3.2, three load cases were tested: II-base, II-c and I-e. Two runs of pre-load were performed beforehand in each test to minimize the residual stress in strain gauges incurred in installation. Lateral load was applied progressively by manually controlling the hydraulic pump as shown in Table 3.6.

Table 3.6 Loads applied in monotonic load tests

Step Number	Loading		Cycles
	Axial	Lateral	
1	743 kN (20%)	0	1
2	1671 kN (45%)	0	1
3	2229 kN (60%)	141 kN (7600psi)	3
4	2972 kN (80%)	283 kN (15500psi)	3
6	3715 kN (100%)	480 kN (25000psi)	3
7	Displacement control to failure	480 kN (25000psi)	1

Table 3.6 shows the loading sequence. Axial loading rate was kept at 0.2mm/min initially, and gradually increased to 0.5mm/min after significant yield was detected. The percentage for axial load in the bracket in Table 3.6 is the percentage of an assumed design working load, while the psi number for lateral load is the post tensioning pressure on the hydraulic pump, equivalent to the lateral force. The control specimen and G2 were loaded until failure in step 7. However, G1 was loaded up to 9500kN, the maximum capacity of the test rig without failure, and was unloaded afterwards.

3.3.4.2 Cyclic loading for G1

It is understood that under repeated loadings, a structure may have elastic shakedown, plastic shakedown, or ratcheting response. The limit states corresponding to elastic shakedown and plastic shakedown are high cycle fatigue and low cycle fatigue

respectively; the limit state corresponding to ratcheting is incremental collapse, which should be avoided for plastic limit state design. Grundy (1994) and Kwong and Grundy (1994) addressed the problem of incremental collapse for tubular members and tubular joints of offshore jacket structures.

As mentioned, it was unexpected but without surprise that the capacity of G1 was beyond the limit of test rig; the G1 was subsequently loaded cyclically after 9 months to check whether there was incremental plastic collapse due to either degrading of grout or local ratcheting of steel at the chamfered region. The cyclic load was imposed in axial direction only, and the loading pattern is shown in Table 3.7.

Table 3.7 Cyclic load applied on G1

Step Number	Load range	Cycles
1	0~3000 kN	5
2	0~4500 kN	5
3	0~7000 kN	10
4	0~9500 kN	100

3.4 Test results

The test results are shown from Figure 3.13 to Figure 3.21, and discussed below.

3.4.1 Ultimate strength and failure mode

Table 3.8 shows the test results of the specimen strengths. The control specimen and G2 failed at axial load level 6900 kN and 7900 kN respectively. G1 did not show observable failure at axial load level of 9500 kN, the ultimate capacity of the test rig. The failure modes of the control specimen and G2, as shown in Figure 3.12 were similar: local buckling. For the control specimen, local buckling occurred at thinner section slightly away from the transition zone. For G2, local buckling was regularly and evenly distributed around the transition zone, at almost exactly the same position

predicted by the preliminary FE. The failure mode of G2 showed that infill grouted tubular member is more tolerant in accommodating imperfection than the control specimen.

Table 3.8 Experimental results

	Control	G1	G2
Yield strength	6000 kN	>9500 kN	7000 kN
Ultimate strength	6800 kN	>9500 kN	8000 kN
Enhancement	-	>50%	20%

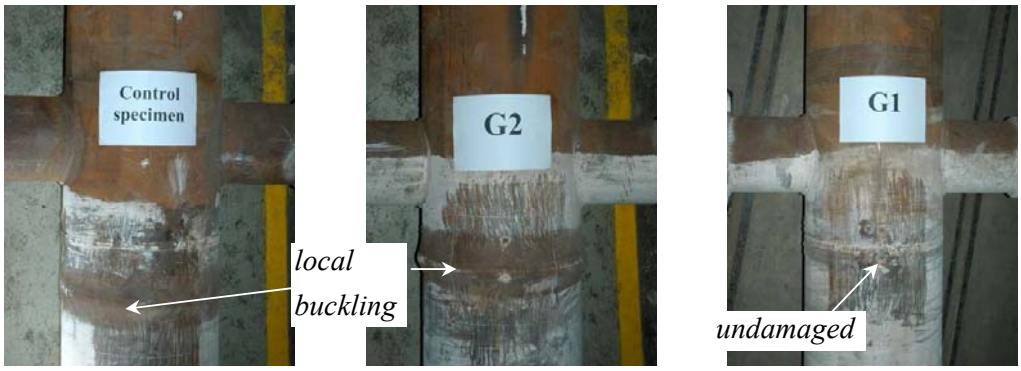

(a) (b) (c)

Figure 3.12 Tested specimens: (a) control specimen; (b) G2; (c) G1

Table 3.8 shows that G1 is significantly stronger than G2. Note G1 was with additional stiffening plates, one side of which was directly in contact with the grout, so that the bearing capacity of the small part of grout under contact was mobilized. This contact-bearing mechanism is more effective than interfacial bond-friction mechanism, consistent with the MSL report (Dier, 2004) as mentioned previously.

3.4.2 Global behavior subjected to monotonic loading

Figure 3.13 shows the load-displacement curves of the test specimens and Figure 3.14 (a) is the corresponding prediction by preliminary FE analysis. It can be seen that the predicted trend is very close to those of test results. The stiffness of G1 is significantly

larger than that of the control specimen and G2, while the control specimen and G2 have similar stiffness in initial stage and G2 becomes slightly stiffer after 2500 kN load level. Comparing the ultimate capacities of test results with prediction, G2 was slightly under-predicted as shown in Figure 3.14 (b) both in terms of stiffness and ultimate strength.

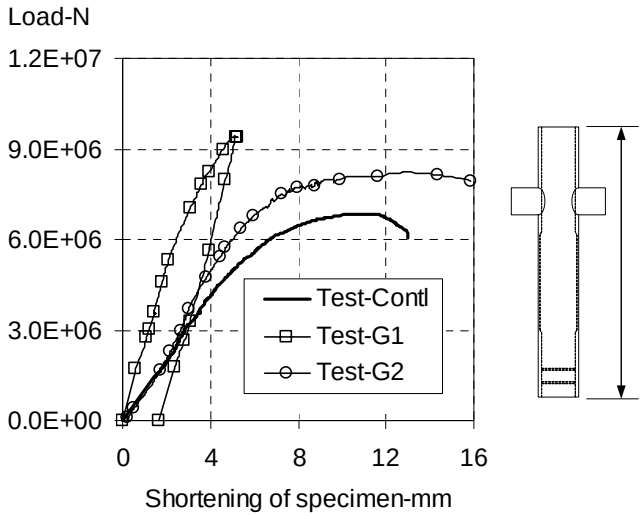

Figure 3.13 Load-displacement curves for monotonic load tests (measurement based on total length)

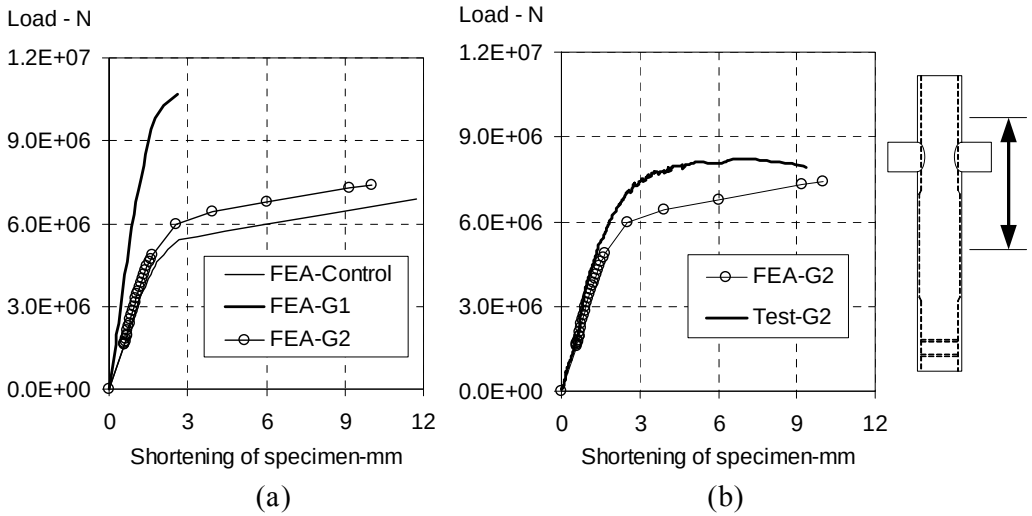

Figure 3.14 Result comparisons: (a) prediction by Preliminary FE; (b) comparison for G2 (measurement based on the length of preliminary FEA model)

3.4.3 Local behavior subjected to monotonic loading

Figure 3.15 to Figure 3.20 show the test results of vertical load versus surface strain values. The strain values were the average of 4 strain gauge readings at the same level, as indicated in Figure 3.11 (b). The average strain values at three levels (Level 3, Level 4, and Level 5) were plotted with different combinations for comparison as described below. It was noted that the symmetry was true only for the control specimen and not the grout-infilled specimens.

3.4.3.1 Comparison of three levels' strains for control specimen

Figure 3.15 shows the strain comparison for the control specimen. It can be seen both circumferential and axial strains at Level 3 and Level 5 are very close to each other, indicating the symmetric model in preliminary FE work is reasonable. Due to stress concentration, circumferential expansion at chamfer transition zone is more critical. In the axial direction, the tensile bending stress induced by local bending in the chamfer transition region offset the axial compressive stress on the external surface, as interpreted in Figure 3.16. The internal surface at level 5 is more critical, but not detectable in the experiment.

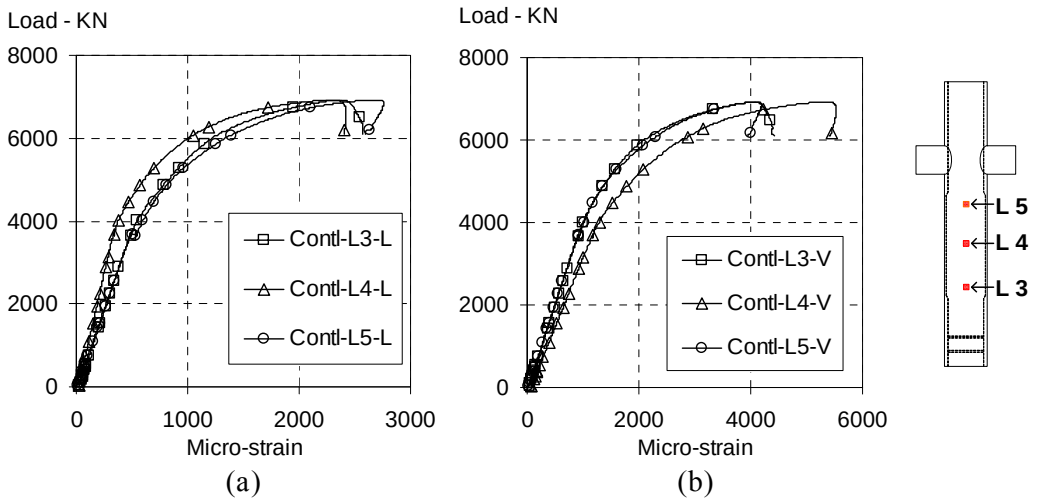

Figure 3.15 Strain readings for the control specimen: (a) circumferential tensile strain; (b) axial compressive strain

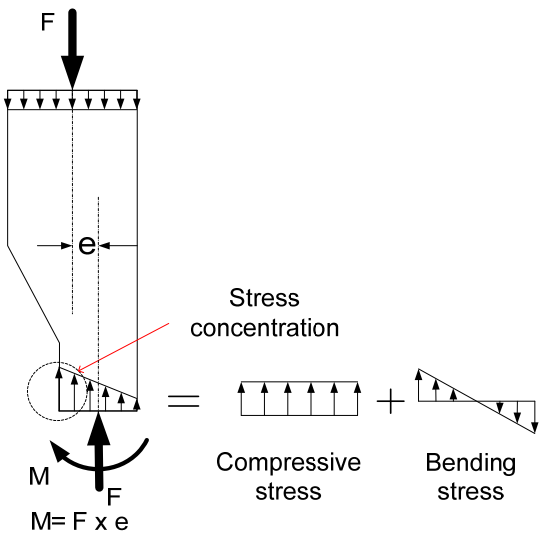

Figure 3.16 Illustration of axial compressive stress distribution at chamfer transition for the control specimen

3.4.3.2 Comparison of three levels' strains for G1

Figure 3.17 shows the strain readings for G1. In the circumferential direction, the expansion at Level 5 is the most critical; showing the contact action at the chamfer transition zone did not help to reduce the expansion trend. However, in the axial direction the dominant compressive stresses at the three levels were relived with the mid-section experiencing slightly higher stress similar to the control specimen.

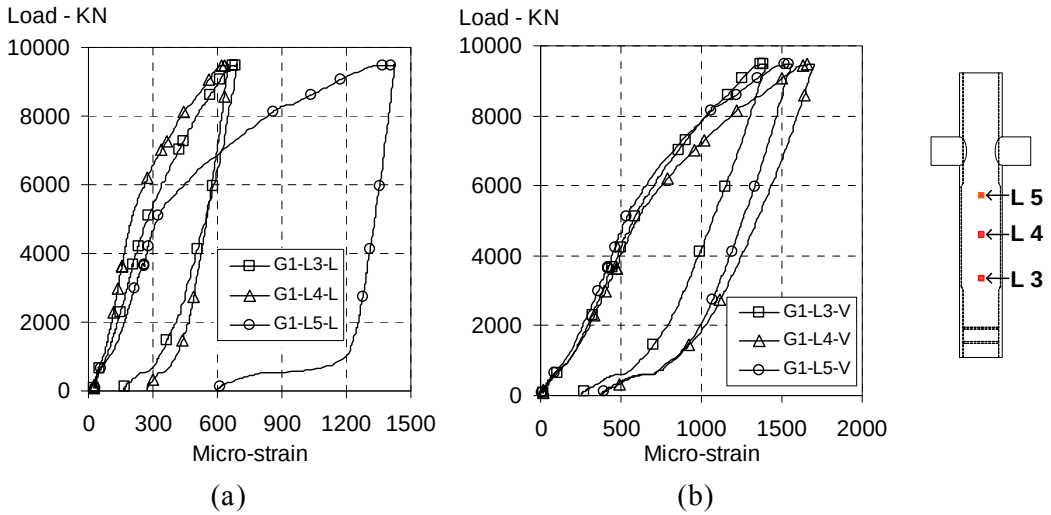

Figure 3.17 Strain readings for G1: (a) circumferential tensile strain; (b) axial compressive strain

3.4.3.3 Comparison of three levels' strains for G2

Figure 3.18 shows that strains for G2 Level 5 is the most critical in both circumferential and axial directions.

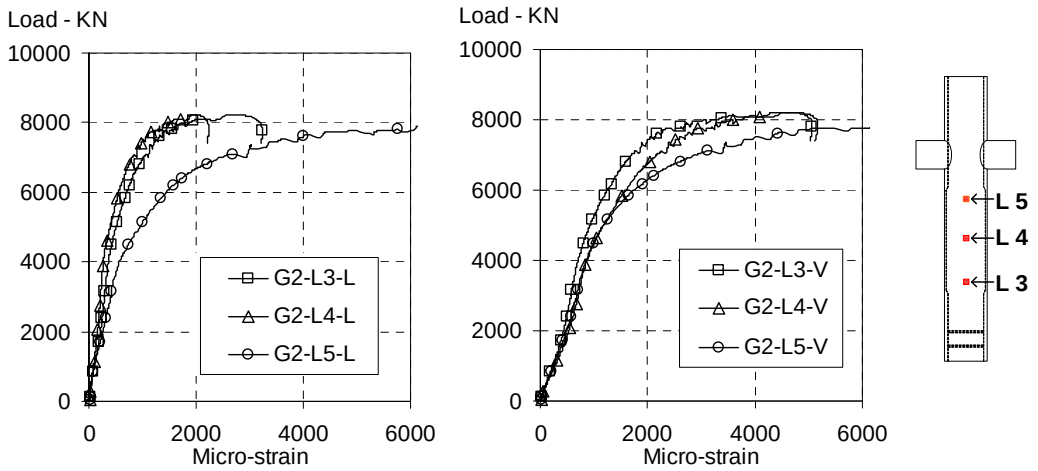

Figure 3.18 Strain readings for G2: (a) circumferential tensile strain; (b) axial compressive strain

3.4.3.4 Comparison of circumferential tensile strains for three specimens

Figure 3.19 shows the comparisons for the circumferential expansive strains. The circumferential expansion for G1 was the smallest. G2 and the control specimen experienced similar expansions at level 5 where local buckling occurred. The comparison shows the strengthening effect of G2 is insignificant.

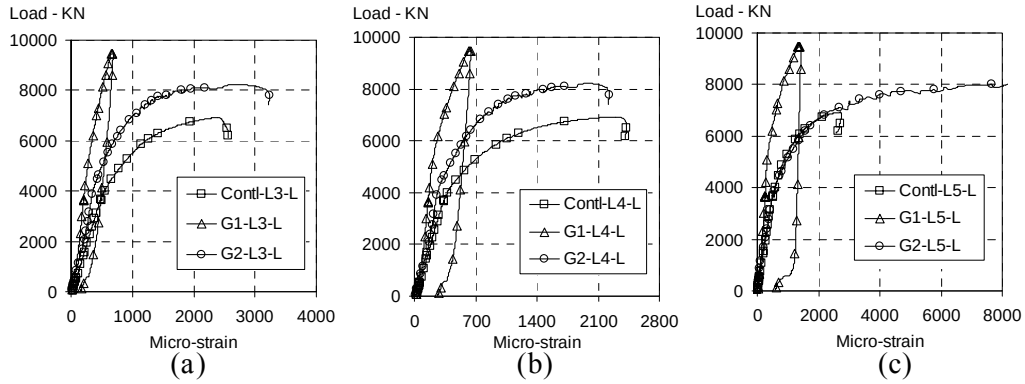

Figure 3.19 Comparisons of circumferential tensile strain: (a) level 3; (b) level 4; (c) level 5

3.4.3.5 Comparison of axial compressive strains for three specimens

Figure 3.20 shows comparisons for the axial compressive strain values of the three specimens. The trend and pattern are similar to that of lateral strain comparison. G1 exhibits the stiffest behavior all the way, while G2 and the control specimen show similar stiffness at initial stage and G2 became stiffer after 1500kN load level. All the three levels are consistent showing the same pattern.

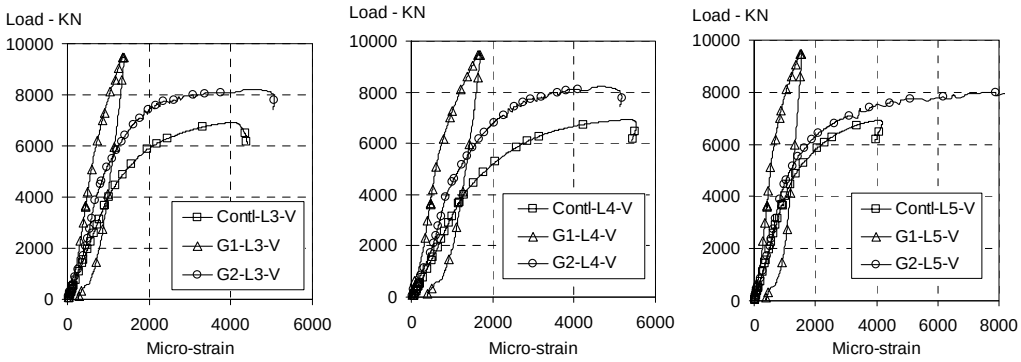

(a) (b) (c)

Figure 3.20 Comparisons of axial compressive strain: (a) level 3; (b) level 4; (c) level 5

3.4.4 Response of G1 subjected to cyclic loading

Figure 3.21 shows the response of G1 subjected to cyclic loading. When the peak load was lower than 7000 kN, the cyclic response was steady, and nonlinearity was insignificant. When peak load was increased to 9500 kN, transient drifting phenomenon appeared in the first few cycles; the drifting is significant for strain at level 5. After about 30 cycles, the hysteresis curves became steady again, but the nonlinearity was slightly more severe than before. The cyclic test stopped at 120 cycles, because there was no change in the steady response. The above-mentioned plastic shakedown state was considered achieved for the steel, which should lead to low cycle fatigue. The maximum strain range measured was about 0.1%, as shown in Figure 3.21, not large enough to make low cycle fatigue failure within 10^6 cycles, in reference to the experimental S-N curve from (Gotoh and Berge, 2004).

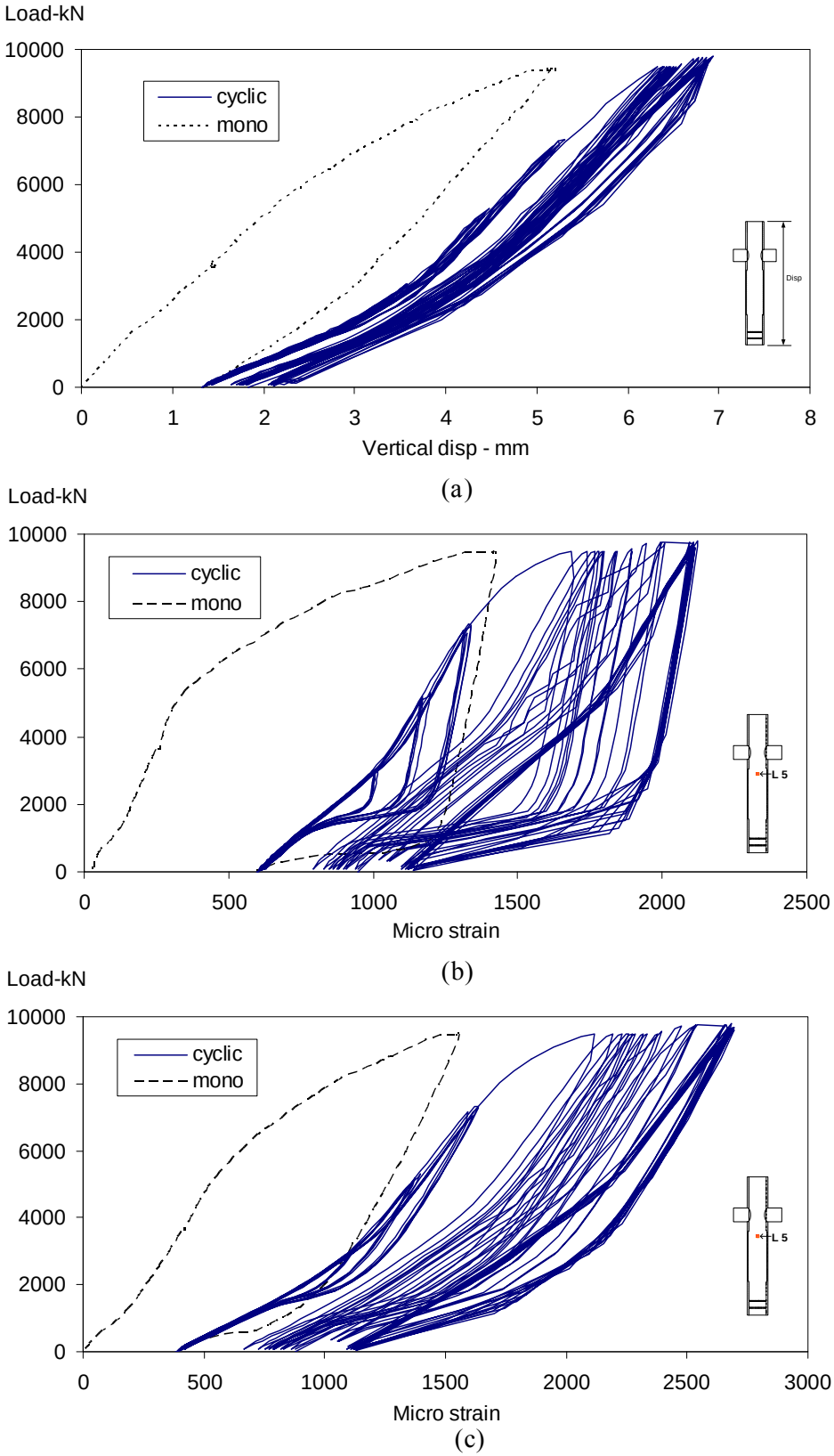

Figure 3.21 Cyclic response of G1: (a) load vs displacement; (b) axial compressive strain at level 5; (c) circumferential expansive strain at level 5

3.5 Discussion and conclusion

Based on the above observations for the three tested specimens, it can be confidently concluded that the strengthening effect of G1 are significantly better than G2 due to the addition of stiffening plates. In G1, the contact-bearing mechanism between the stiffening plates and grout effectively transferred part of the load to the grout. This relieved the stress level of the thin wall portion adjacent to the chamfered transition region, where local buckling occurred for the control specimen and G2. Figure 3.22 illustrates the internal force flow of G1. It could reasonably be postulated that the effectiveness of the contact action and the strength of grout would govern the strengthening effect.

For the behavior of G1 subjected to cyclic loading, the response is favorable, showing the shakedown state had been reached at maximum load range that the test rig could generate. It was noticed that the slope of beginning part of the hysteresis loop was slightly smaller than that of monotonic load-displacement curve. This would probably be due to grout shrinkage and/or localized degradation resulting from partial crushing under severe contact pressure, which caused a delayed contact effect and minor redistribution of the stress. The transient drifting recorded also supports this inference. However, such effect can be seen is insignificant. The most important evidence is that the steady state had been achieved, demonstrating the incremental collapse limit was not yet reached and definitely higher than 9500kN.

Generally, it can be concluded as follows:

- Under partial grouting condition, the proposed shear key-stiffening plate scheme, can be used effectively;
- The strengthening effect of using stiffening plates was much more significant than that of plain steel-grout interface.

- The grout strength would govern the strengthening effect based on contact-bearing mechanism;
- When it was re-tested after 9 month and subjected to cyclic loading, the performance of G1 is reliable, showing the influence of degradation and creep of grout to be insignificant.

Comparing the monotonic loading test results with preliminary FE predictions, the predicted global behavior was generally satisfactory; but in terms of local measurements, like the surface strain at the transition region, the prediction was not good enough to fit the strain measurements. This might be attributed to the preliminary FE analysis which used single layer coarse mesh and linear elements, which was too stiff to model a section under bending (Cook, 1994).

Figure 3.14 shows that the tested strength of G2 was higher than the prediction; the possible reasons could be:

- The bond effect, which was ignored in preliminary FEA, or
- Inaccurate material property - the real material may be stronger than the assumed in the preliminary FE analysis;

In order to clarify the doubts, fully understand the grout-steel interaction mechanism and further capture more characteristic details, a more refined finite element analysis was carried out, and reported in the following chapter.

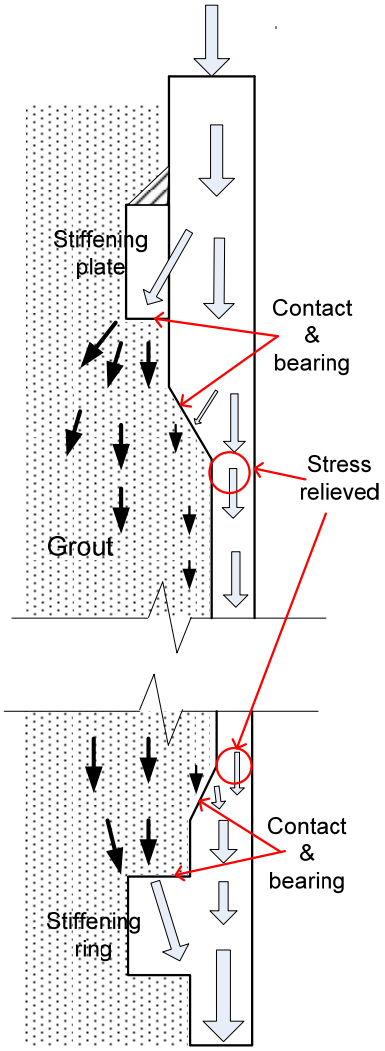

Figure 3.22 Illustration of internal force flow of G1

Chapter 4

Refined FE analysis and proposed design model for partially infilled tubular member under axial compression

4.1 Introduction

The responses of partially grouted specimens G1 and G2 as detailed in Chapter 3 were predicted in general trends by the preliminary FE analysis, as shown in Figure 3.7 and Figure 3.14. However, two major simplifications were made in the preliminary FEA: the von Mises plasticity assumed for both steel and grout without damage modeling, and the assumption of no interfacial bond. The two simplifications may be used to explain the differences presented in the comparison of preliminary FE results with test results that

- Neglecting local crushing of grout leads to over-prediction for G1, and
- Neglecting bonding effect results in under-prediction for G2.

It is realized that with detailed experimental measurements, refined FE models with the two effects included can be calibrated, and should provide an opportunity for exploring and better understanding of such complex and complicated effects associated with grouted tubular members. In fact, the performance of grout infilled tubular members has been studied for decades (H.Shakir-Khalil and Hassan 1994; O'Shea and Bridge 2000; Shanmugam and Lakshmi 2001; O'Shea and Bridge 2002;

Han, Yao et al. 2005; Liew and Xiong 2009; Zhao, Tong et al. 2010). But almost all the investigations reported in the literature are for fully grouted member with effective end bearing mechanism for loading the infilled grout. There has been no detailed study reported yet for partially grouted condition. To provide confident application of partial grouting method in practice, it is vital to have basic understanding of the two effects. With such concerns, the monotonic tests are therefore back analyzed with much more refined FE models including the grout damage modeling and interfacial bond-slip simulation. The FE results are calibrated with test results for parametric studies to generate a simplified design model, which is further verified by testing a series of small scale specimens. This chapter reports the details of the study by first investigating the material property tests.

4.2 Material property

4.2.1 Tests for uni-axial stress-strain behaviors

The material property used in preliminary FE study in Chapter 3 was assumed to be elasto-plastic perfect based on von Mises model. It may be considered as over-simplification for cemetitious grout. In order to eliminate the influence of inaccurate assumption for material property in the refined FE analysis, standard steel coupon tests and grout cube and cylinder tests were carried out. The measured material property parameters were used in the refined FE analysis.

Three pieces of steel coupons (two from the thin section 10mm and one from the thick section 20mm) underwent tensile tests to fracture and final failure. Six pieces of grout sample (three cubes and three cylinders taken during the casting) underwent compressive test to final failure. The tests were performed on INSTRON 500kN test rig as shown in Figure 4.1.

The steel coupon samples, as shown in Figure 4.2, (a) were cut from the actual

specimens after test at those areas away from critical region, while the grout samples were taken during casting. Special attention was paid when making grout samples, as shown in Figure 4.2 (b), that the test cubes or cylinders were not machine vibrated but only manually blended by throes and steel robs to simulate the real self compact condition during the casting and avoid making too 'good' test samples. The tested strength of the grout exhibited certain scatter as listed in the Table 4.1 and was slightly below the nominal value of 200 MPa.

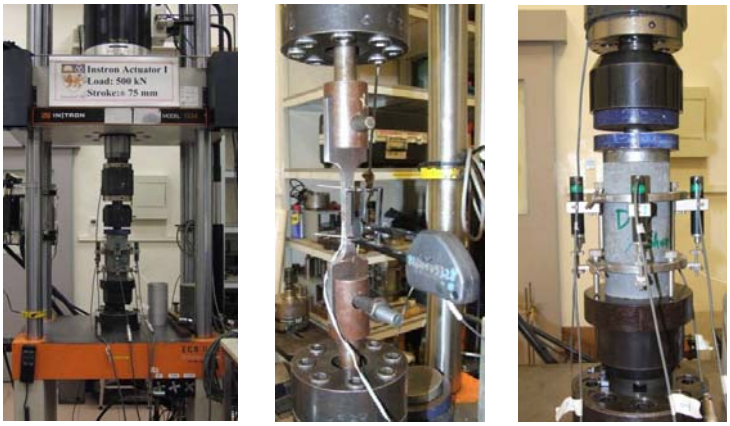

(a) (b) (c)

Figure 4.1 Instron test rig for material property tests: (a) overview of test rig; (b) steel coupon tensile test; (c) grout cylinder compressive test

(a) (b)

Figure 4.2 Material test samples: (a) failed steel coupons; (b) grout cylinder ready for test

Table 4.1 Ultimate compressive strength for the grout (specimen dimensions in mm)

	Cube 50x50	Cube 50x50	Cube 100x100	Cube 100x100	Cylinder 100x200	Cylinder 100x200
Strength (MPa)	163.4	172.3	186.4	185	200.9	157

Engineering strain was measured using both strain gauges and displacement gauges in the material property tests, as shown in Figure 4.1. In the linear elastic stage the strain reading was taken from strain gauge readings. After yielding it was from displacement gauges, because the strain gauge readings became unstable and some strain gauges even broke up. The engineering strain was converted to true strain value using equations (4.1) and (4.2) below.

$$\varepsilon = \ln(1+e) \qquad (4.1)$$

where, ε is true strain;

e is engineering strain

$$\varepsilon = \ln\frac{A_i}{A_c} \qquad (4.2)$$

where, A_i: initial cross section area;

A_c: current cross section area

For steel coupon test, when necking is about to occur, equation Eq. (4.1) is not applicable; the true value was then calculated through the ratio of cross section by Eq. (4.2). The stress-strain curves for the steel and grout used in refined FE back analysis are shown in Figure 4.3. Table 4.2 and Table 4.4 present the corresponding magnitudes in linearly piecewise representation used in Abaqus input file.

4.2.2 Material constitutive modeling in the refined FE analysis

As shown in Figure 4.3 (a) and Table 4.2, the post yield stress/strain values of steel used in refined FE study are in between the two test result curves. Classical von Mises plasticity model was employed for steel. The model uses Mises yield surfaces with associated plastic flow for isotropic yield and hardening. The Mises yield surface

is defined by giving the value of the uni-axial yield stress as a function of both effective stress and equivalent plastic strain. For isotropic hardening, the yield surface changes size uniformly in all directions such that the yield stress increases in all stress directions as plastic strain occurs. The three-dimensional stress increment and corresponding strain increment after yielding at a given state is linked to uni-axial stress and strain increments by using a plastic multiplier. Detailed mathematical formulae can be found in Chapter 2. The references like Abaqus manual (SIMULIA 2007), Dunne and Petrinic (2005) and Chakrabarty (2006) include similar information.

Table 4.2 Material parameters for steel used in refined FEA

stress	plastic strain	total strain	Youngs' modulus - MPa	Poison ratio
300	0	0.001765	180000	0.3
370	0.0007	0.002876		
380	0.0009	0.003135		
390	0.0012	0.003494		
400	0.0015	0.003853		
430	0.003	0.005529		
460	0.018	0.020706		
580	0.116588	0.12		
800	0.695294	0.7		

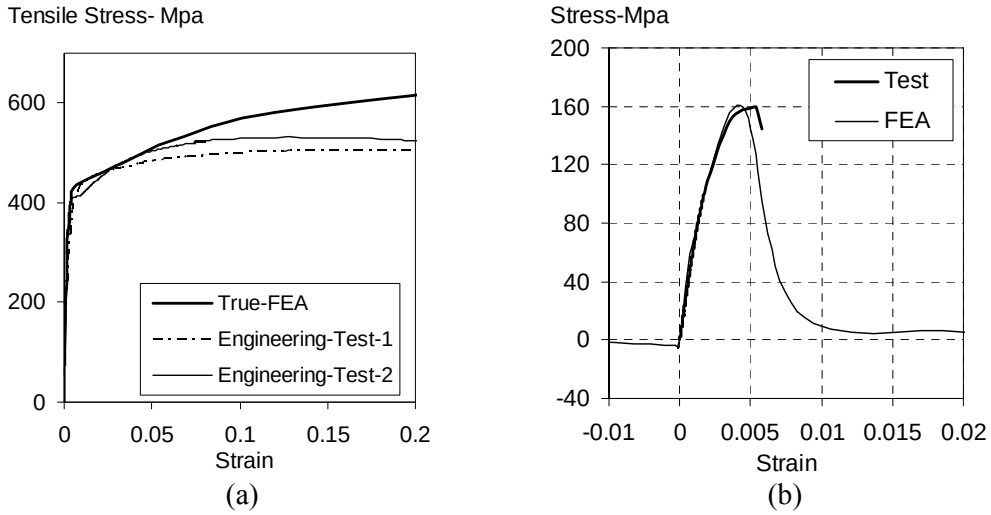

Figure 4.3 Stress-strain curves: (a) steel; (b) grout

Figure 4.3 (b) shows the uni-axial stress-strain curve for grout in the refined FE simulation with the concrete damaged plasticity material model of Abaqus (SIMULIA 2007). The concrete damaged plasticity model provides a general capability for modeling concrete and other quasi-brittle materials in structures. The theoretical basis of the concrete damaged plasticity model is from Lubliner et al (1989). Its constitutive model uses concepts of isotropic damaged elasticity in combination with isotropic tensile and compressive plasticity to represent the inelastic behavior of concrete. The model assumes that the main two failure mechanisms are tensile cracking and compressive crushing. The main features of this material model including the yield condition, flow rule and stiffness degradation are presented below.

The damaged concrete plasticity model uses a yield condition based on the yield function proposed by Lubliner et al. (1989). In terms of effective stresses the yield function takes the form of equation (4.3)

$$F_y = \frac{1}{1-\alpha_y}(\sigma_e - 3\alpha_y\sigma_m + \beta_y\langle\sigma_{\max}\rangle - \gamma_y\langle-\sigma_{\max}\rangle) - \overline{\sigma_c} \qquad (4.3)$$

where, σ_e is the effective von Mises stress,

σ_m is the effective hydrostatic pressure, $\sigma_m = \frac{1}{3}(\sigma_{11} + \sigma_{22} + \sigma_{33})$;

$\sigma_{\max}$ is the maximum eigen value of initial elastic stress tensor $[\overline{\sigma}]$:

$$[\overline{\sigma}] = [D_0]^{el}([\varepsilon] - [\varepsilon]^{pl}) \qquad (4.4)$$

$[D_0]^{el}$ is the initial (undamaged) elastic stiffness of the grout.

$\langle\ \rangle$ is defined as $\langle x\rangle = 0.5(|x| + x)$.

α_y is defined as:

$$\alpha_y = \frac{(\sigma_{b0}/\sigma_{c0})-1}{2(\sigma_{b0}/\sigma_{c0})-1};\ 0 \le \alpha_y \le 0.5; \qquad (4.5)$$

where, σ_{b0}/σ_{c0} is the ratio of initial equi-biaxial compressive yield stress to initial uni-axial compressive yield stress (the default value is 1.16),

β_y is defined as:

$$\beta_y = \frac{\overline{\sigma_c}}{\overline{\sigma_t}}(1-\alpha_y)-(1+\alpha_y); \qquad (4.6)$$

where, $\overline{\sigma_t}$ is the effective tensile cohesion stress, and $\overline{\sigma_c}$ is the effective compressive cohesion stress. They are determined from uni-axial stress-strain curve by integration. The physical meaning can be found in Lubliner et al (1989).

γ_y is defined as:

$$\gamma_y = \frac{3(1-K_c)}{2K_c-1} \qquad (4.7)$$

where, K_c is the ratio of the second stress invariant on the tensile meridian, the default value is 2/3.

If $F_y < 0$, the grout is in elastic stage;

If $F_y = 0$, the grout is in plastic stage, and the stress tensor is maintained on the surface of $F_y = 0$.

The concrete damaged plasticity model assumes non-associated potential plastic flow. The flow potential G used for this model is the Drucker-Prager hyperbolic function:

$$G = \sqrt{(\xi\sigma_{t0}\tan\psi)^2 + \sigma_e{}^2} - \sigma_m \tan\psi \qquad (4.8)$$

where, Ψ is the dilation angle, in this simulation it took 45^0 obtained by try and error

tests and result fitting; the value is also consistent with the value in the benchmark study by Famiglietti and Prevost introduced in Abaqus manual (SIMULIA 2007);

σ_{t0} is the uni-axial tensile stress at failure, taken from the user-specified tension stiffening data; and

ξ is a parameter, referred to as the eccentricity, defining the rate at which the function approaches the asymptote (the flow potential tends to a straight line as the eccentricity tends to zero). The default value of ξ is 0.1 in Abaqus.

The strain softening part of the uni-axial stress-strain curve, as shown in Figure 4.3, is fictitious due to the difficulties in obtaining from the material tests. This is considered acceptable according to Lubilner et al (1989) that the strain-softening branch of the stress-strain curves of glandular material cannot represent a local physical property of the material, but just provides physical grounds for achieving stable FE solutions with appropriately defined damage parameter that is related to the mesh size. The damage parameter, *d*, was defined in tabular form as shown in Table 4.4. This parameter determines the stiffness degradation for the grout after yield occurs during simulation. Damage associated with the failure mechanisms of the grout (cracking and crushing) results in a reduction in the elastic stiffness, Eq (4.9):

$$[D]^{el} = (1-d)[D]_0^{el} \qquad (4.9)$$

where, $[D]^{el}$ is the degraded elastic stiffness,

$[D]_0^{el}$ is the initial undamaged elastic stiffness.

The damage parameter *d* is the scalar stiffness degradation variable, which can take values in the range from zero (undamaged material) to one (fully damaged material). However, numerical instability will cause convergence problem, when *d*

approaches one. In this study, the maximum value of d is limited to 0.98. The stress-strain relationship in plastic stage is then taking the form, Eq. (4.10):

$$[\sigma] = [D]^{el}([\varepsilon] - [\varepsilon]^{pl}) \qquad (4.10)$$

For concrete damaged plasticity model, the stiffness and strength of compression and tension are treated separately; therefore the damage parameter d is also noted as d_c and d_t respectively as shown in Table 4.4.

For comparison and sensitivity study, the model without damage parameter d, but using the same elasto-plastic stress-strain curve in Figure 4.3 (b), was also analyzed. In this case, the stress-strain relationship took the form of equation (4.10), but the degraded tangential matrix $[D]^{el}$ was substituted by $[D_0]^{el}$.

The parameters, biaxial stress ratio σ_{b0}/σ_{c0}, K_c, and eccentricity ξ to describe the tri-axial behavior of the grout, were specified using default values in Abaqus (SIMULIA 2007), Table 4.3. As introduced (SIMULIA 2007), the default values are suitable for normal concrete in low confinement condition. The viscosity parameter was for numerical stability as recommended (SIMULIA 2007).

Table 4.3 Parameters used in concrete damaged plasticity

Dilation angle	Eccentricity	F_{b0}/f_{c0}	K	Viscosity parameter
45	0.1	1.16	0.667	0.0001

Table 4.4 Material parameters for grout used in FEA

	Stress	Damage parameter- d_t / d_c	Plastic-Strain[a]	Inelastic Strain[a]	Total Strain[a]	Young's modulus-MPa	Poisson ratio
Tension	-0.1	0.98	0.010073	0.01	-0.01	67000	0.19
	-4	0.7	0.000439	0.0003	-0.00036		
	-6	0	0	0	-9E-05		
Origin	0	0	0	0	0		
Compression	80	0	0	0	0.001231		
	160	0.4	0.000408	0.002	0.004462		
	20	0.95	0.002328	0.008	0.008308		
	5	0.98	0.016343	0.02	0.020077		

[a] Inelastic strain =Total strain – Stress/Young's modulus (Abaqus (SIMULAI, 2007))

4.3 Finite element modeling

4.3.1 Three-dimensional (3D) models

In order to simulate the testing conditions and capture the characteristics as much as possible, 3D FE models using brick elements were built up first according to the general geometries of real specimens. The only difference was that the two ring stiffeners at the lower part of the real member were simplified as one thick ring in FE models. Quarter FE model was adopted due to the symmetry of the structure and loads. Typical geometries of 3D models are shown in Figure 4.4.

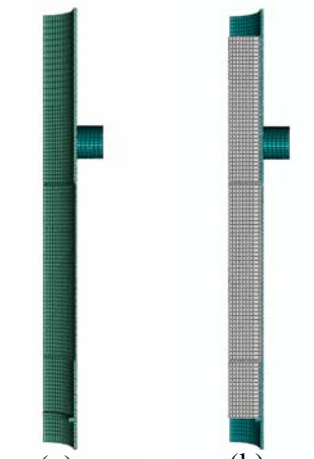

Figure 4.4 Geometry of the FE models: (a) control specimen (b) grouted specimen

For sensitivity study, two types of brick elements, C3D20R (20 node quadratic element with reduced integration) and C3D8R(8 node linear element with reduced integration), were tested with different mesh densities. It was found the global FE results were insensitive to the element type, if the shapes of solid elements were close to regular cubic with appropriate density of mesh. In order to achieve such 'good' element shape for the whole leg portion of the specimen, the lateral stub was modeled as incompatible mesh part using 4 node shell element S4R, and attached to the steel tube using shell-to-solid coupling function in Abaqus (SIMULIA 2007), the same

technical treatment as used in the preliminary FE works.

The boundary conditions were also the same as those in the preliminary FE analysis, but the sequences of loading followed the real test condition with the lateral load varied simultaneously. With no surprise, the computed global results were found insensitive to the lateral loads within the loading range applied in the tests.

4.3.2 Axisymmetric models

Since the results were insensitive to the influence of imposed lateral loads, the lateral load and stubs could be reasonably ignored in the FE simulation. Thus, axisymmetric models could be adopted for its equivalence to 3D model due to symmetry of geometry and loading. Figure 4.5 shows the axisymmetric models built accordingly. Compared with 3 D models, axisymmetric models reduced total number of element significantly, but much denser mesh can be deployed, which greatly improved the computation efficiency and effectiveness.

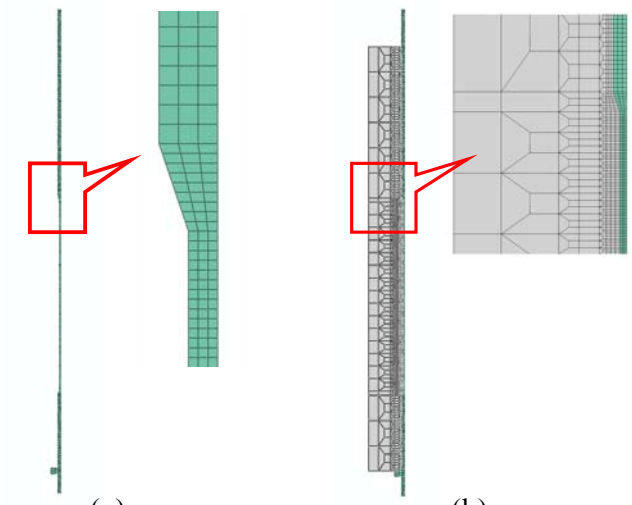

Figure 4.5 Axisymmetric models: (a) control specimen; (b) grouted specimen G2

Both linear and quadratic axisymmetric elements with reduce integration, CAX4R and CAX8R, were tested for sensitivity study. It was found that when mesh density

reached about 3mm for steel tube, the difference of computed results between linear and quadratic elements was negligible.

4.4 Comparison and discussion of FE results

It was noted in Chapter 3 that FE analysis would generate unstable results for the same problem with different approaches related to iteration algorithms, element type and mesh density. For this refined FE study Abaqus/standard 6.7-1 (SIMULIA 2007) that uses Euler backward iteration algorithm was employed for all the cases. For all the three specimens, the boundary conditions were same: the bottom end was pin constrained in vertical direction and the top end was imposed with displacement load in vertical downwards direction to simulate the monotonic loading test conditions. The FE results reported herein include the sensitivity studies for element type and mesh density for the control specimen.

In order to observe the grout condition and compare the buckling deformations, the three tested specimen were cut open, so that the FE results can be compared with test results in insightful details. Figure 4.6 shows how the tested G1 was cut open.

(a) (b)

Figure 4.6 Open the tested G1: (a) manual saw cutting; (b) opening up

4.4.1 Control specimen

For the control specimen, the FE results of both 3D models and axisymmetric models with different mesh schemes were compared for sensitivity study. The load-

displacement and load-strain curves were plotted in Figure 4.7 together with the test results. Figure 4.8 show the comparison for buckled shapes.

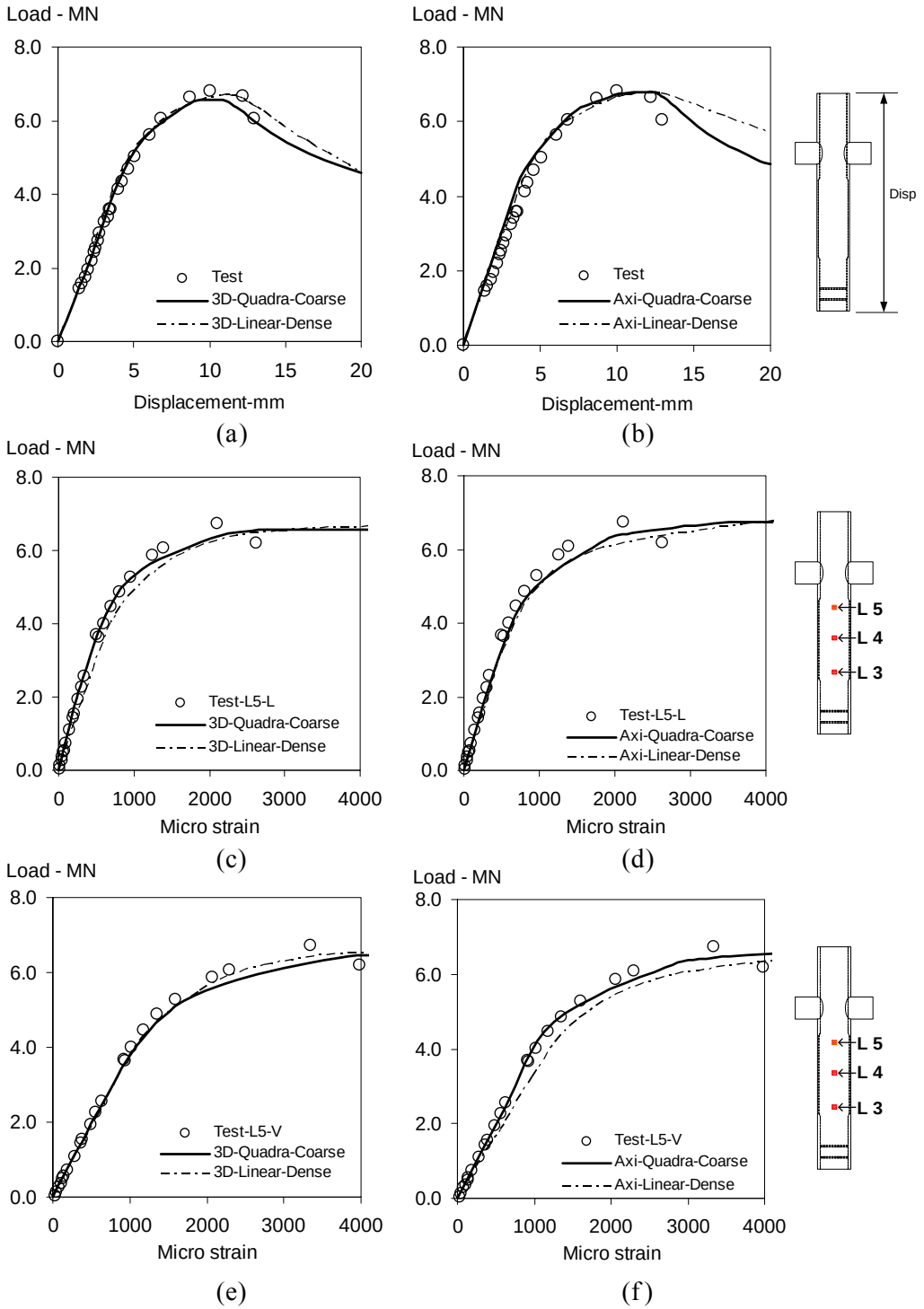

Figure 4.7 Result comparison for the control specimen of load-displacement curves: (a) 3D (b) axisymmetric; and circumferential tensile strain at level 5: (c) 3D; (d) axisymmetric; and axial compressive strain at level 5: (e) 3D; (f) axisymmetric

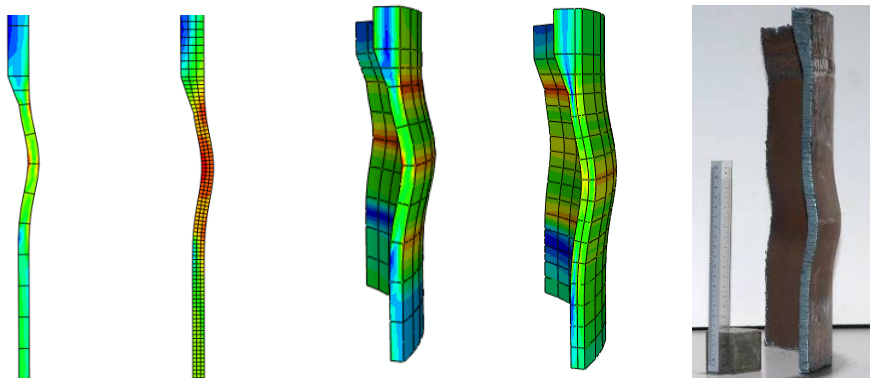

(a) (b) (c) (d) (e)

Figure 4.8 Comparison of buckling shape for control specimen: (a)&(b) axisymmetric modes; (c)&(d) 3D models; (e) cut-out from real specimen

Table 4.5 summarizes the comparison of buckling stress and half wave length. The analytical solutions for elastic buckling stress σ_{eb} and half wave buckling length L_{eb}, equations (4.10) and (4.11), are from the solution for buckling of cylindrical shell (Timoshenko and Gere 1963):

$$\sigma_{eb} = \frac{Et}{D\sqrt{3(1-\nu^2)}} \qquad (4.10)$$

where, E is the Young's modulus,

D is the center to center diameter of the cylinder,

t is the wall thickness, and ν is the Poisson's ratio;

$$L_{eb} \approx 1.72\sqrt{Dt} \qquad (4.11)$$

It could be seen in Table 4.5 that the elastic buckling stress is much higher than yield stress, indicating the local buckling is controlled by yield strength.

Table 4.5 Comparison of local buckling for control specimen

	Refined FE	Experimental	Analytical
Buckling stress - MPa	428	447	2430
Half wave buckling length - mm	118	120	121.3

From the comparison of Figure 4.7 and Figure 4.8, it could be seen that the FEA results of control specimen fit closely with the test results in terms of global behavior,

local response and failure mode. The following can be concluded:

- The uni-axial elasto-plastic stress-strain curve of steel obtained from steel coupon tests was calibrated; and the non-linear algorithm with the classic von Mises plasticity model in Abaqus (SIMULIA 2007) was validated.
- In terms of measures of interest, like global displacement, local surface strains near the chamfer region and at the mid section, the effect of lateral load was insignificant, and the axisymmetric model is valid.
- For axisymmetric model with linear elements, when the element size was less than 3.5 mm, the difference of results from quadratic elements was insignificant.
- The dense axisymmetric mesh with linear elements and the coarse 3D mesh with quadratic elements (size around 20mm), together with the steel property would be appropriate for the computation for grouted specimens.

4.4.2 G1, the grouted specimen with stiffening plates

G1 was with specially designed stiffening plates as shown in Figure 4.9 and Figure 4.10, to test the degree of contribution of mechanical shear keys to the enhancement of static strength. Test results of G1 have shown the strengthening effect is significant and consistent with the preliminary FE prediction in general trends. In the refined back analyses, the concern was to find out the grout behavior subject to severe contact pressure. Grout damage simulation using the concrete damaged plasticity model embedded in Abaqus (SIMULIA 2007) was the focal point.

Based on the analyses results of G2 (reported in the following sub-section), the interfacial bond effect was ignored and the frictional shear stress was set unlimited in contact analysis. Both 3D model, Figure 4.9, and axisymmetric model, Figure 4.10, were built up according to real specimen and analyzed.

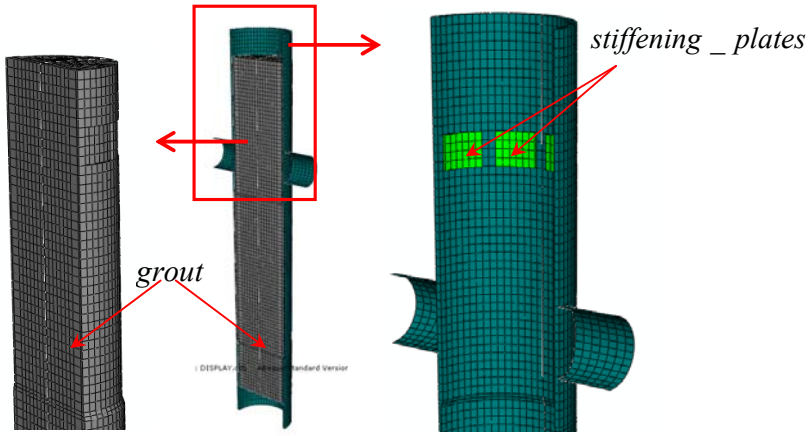

Figure 4.9 3D model for G1

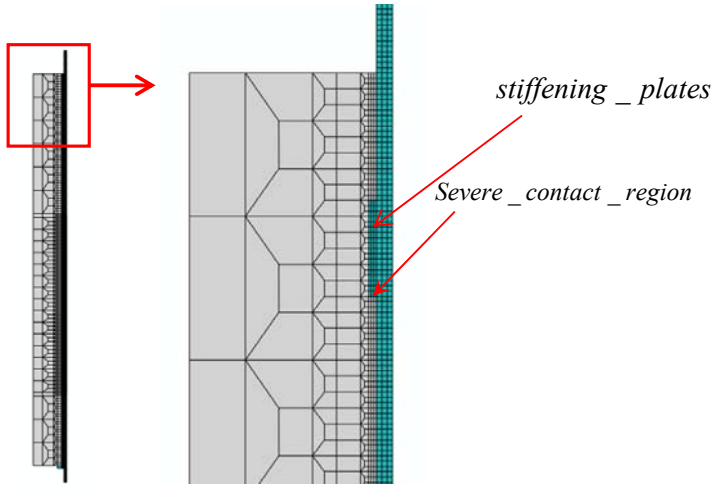

Figure 4.10 Axisymmetric model for G1

Based on the concrete damaged plasticity model (SIMULIA, 2007) as introduced at beginning of this chapter, extensive sensitivity studies were performed on the axisymmetric models to determine the damage parameter *d* for Ducorit D4 grout, because there was no reference information for this parameter together with the stress-strain curve in such confinement condition. The values shown in Table 4.4 were the best fit data. The corresponding FEA results are shown in the Figure 4.11 to Figure 4.18.

Figure 4.11 shows the comparison of load-displacement curves. It can be seen both axisymmetric and 3D models using the damaged plasticity model with damage parameter *d* are in very close agreement with the test result, while the two without damage parameter *d* show stiffer responses after load level 6000 kN. A small kink at that load level on the load-displacement curves with damage parameter *d* in Figure 4.11 indicates the numerical difficulties due to the onset of local damage of the grout. As reported in Section 3.3.4, the specimen was unloaded at 9500 kN (at close to the maximum capacity of the test rig).

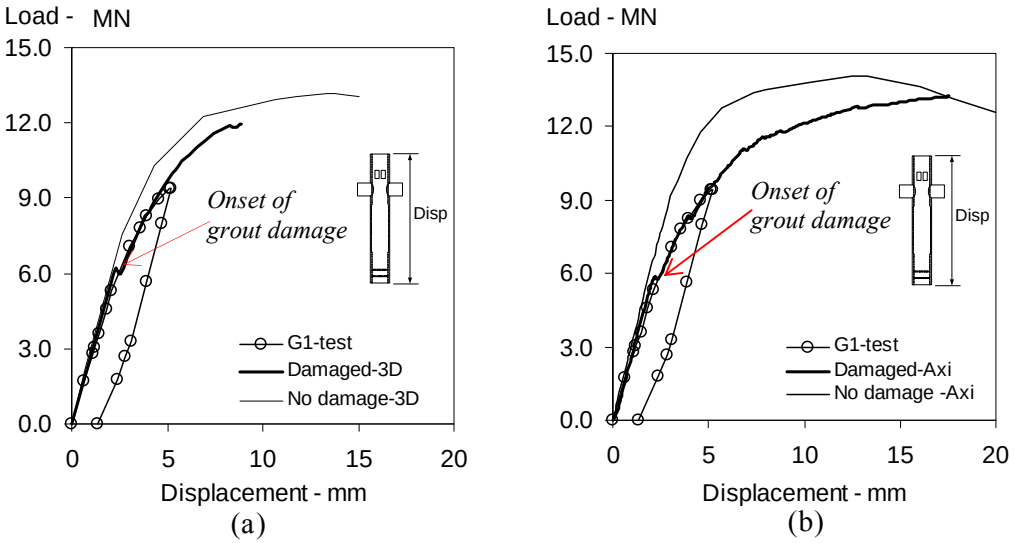

Figure 4.11 Load-displacement curves for G1: (a) 3D; (b) axisymmetric

The models with damage parameter *d* indicate the grout under high contact pressure at critical region actually started unloading from 6000 kN. Figure 4.12 to Figure 4.14 show the stress contours at load levels of 6000 kN and 9500 kN respectively. The stress level for the grout predicted by 3D model was lower than that for the axisymmetric model due to the effect of mesh refinement: denser mesh predicts higher stress at locations with stress concentration. However, the coarser mesh is still considered acceptable in terms of averaged values, and the global behavior was found not to be affected significantly by such local effect.

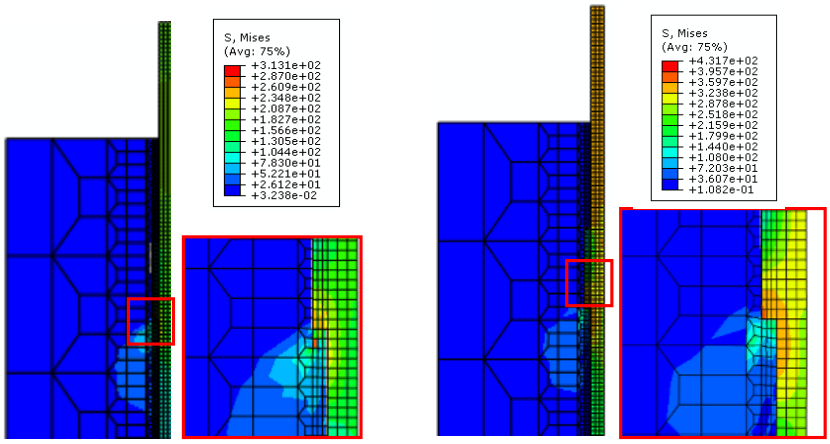

(a) (b)

Figure 4.12 Critical stress level at load levels of: (a) 6000kN and (b) 9600kN for G1, axisymmetric model

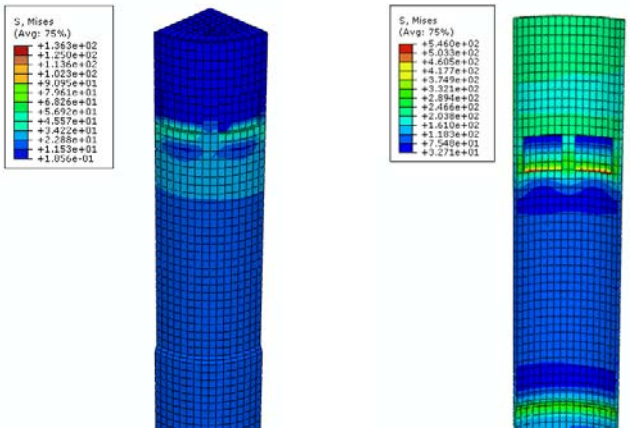

(a) (b)

Figure 4.13 Critical stress level at load level of 6000kNfor G1: (a) grout (b) steel, 3D model

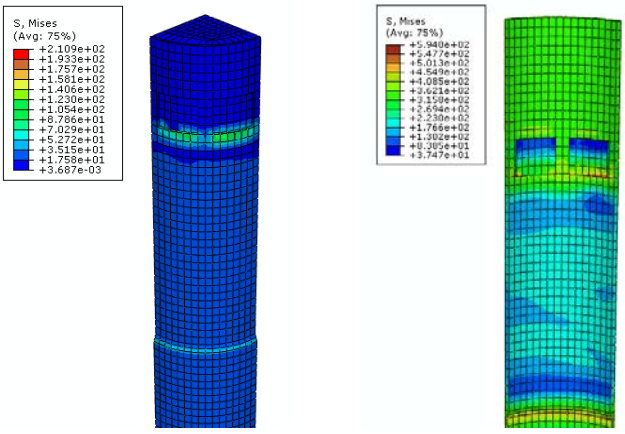

(a) (b)

Figure 4.14 Critical stress level at load level of 9500kN for G1: (a) grout (b) steel, 3D model

Consistent with the global load-displacement behavior, the damage parameters of both FE models at load level 6000kN indicate the onset of local failure of the grout. Tensile crack appeared first, and at load level of 9500kN the grout under critical contact region was partially crushed as shown in Figure 4.15 to Figure 4.18. Figure 4.19 shows the grout condition when the specimen was cut open. It can be seen the actual grout condition strongly supports the damage simulation. Figure 4.19 (a) shows the undisturbed grout at the moment when the specimen was just opened up corresponding to Figure 4.6 (b). Some loose grout debris can be found adjacent to the stiffening plates. Figure 4.19 (b) shows the loose (crushed) grout debris is removed with the fresh grout underneath exposed. It can be seen that the damage of grout was localized as in the FE prediction of Figure 4.16 and Figure 4.18.

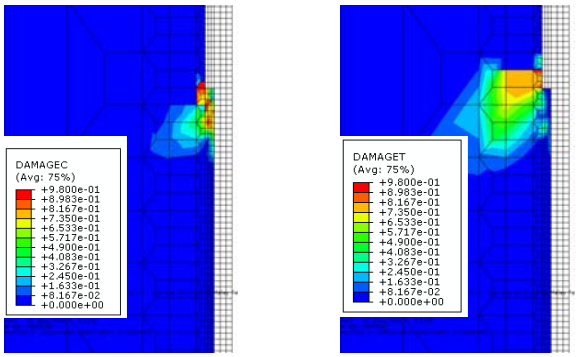

(a) (b)

Figure 4.15 Damage parameters at load level 6000kN, G1, axiaymmetric model:(a) compression damage parameter d_c ; (b) tension damage parameter d_t

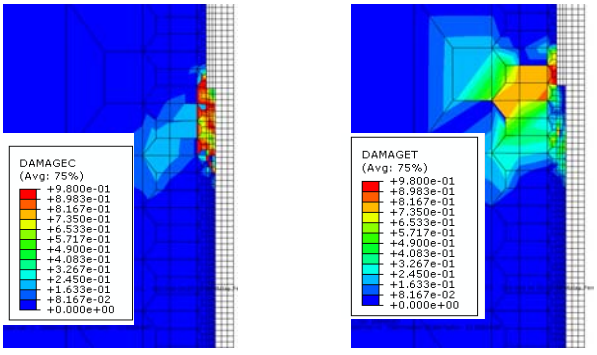

(a) (b)

Figure 4.16 Damage parameters at load level 9500kN, G1, axiaymmetric model: (a) compression damage parameter d_c ; (b) tension damage parameter d_t

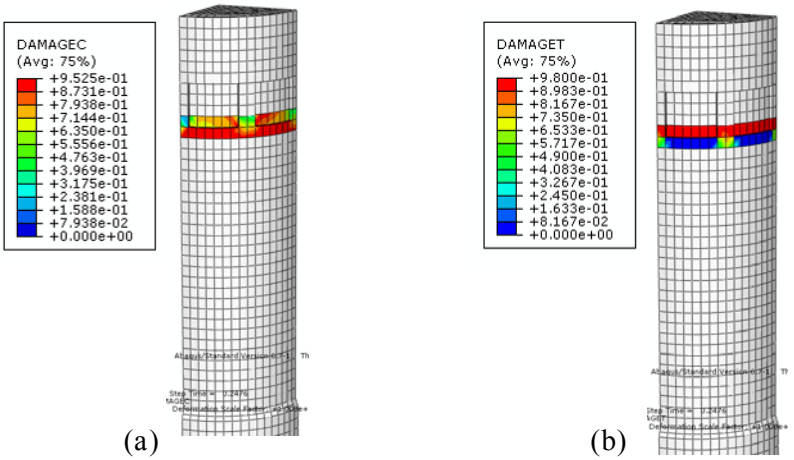

(a) (b)

Figure 4.17 Damage parameters at load level 6000kN, G1, 3D model: (a) compression damage parameter d_c ; (b) tension damage parameter d_t

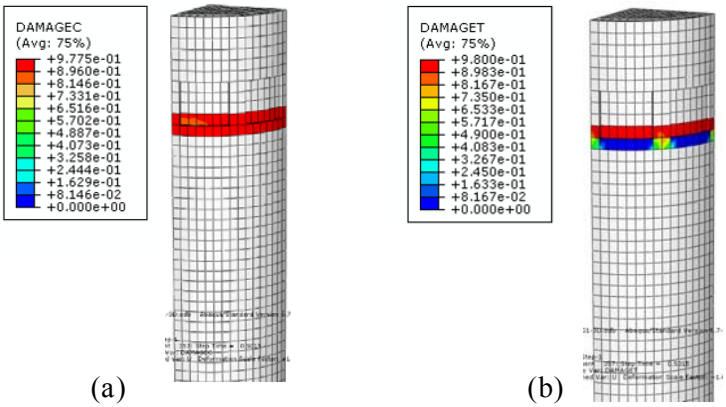

(a) (b)

Figure 4.18 Damage parameters at load level 9500kN, G1, 3D model: (a) compression damage parameter d_c ; (b) tension damage parameter d_t

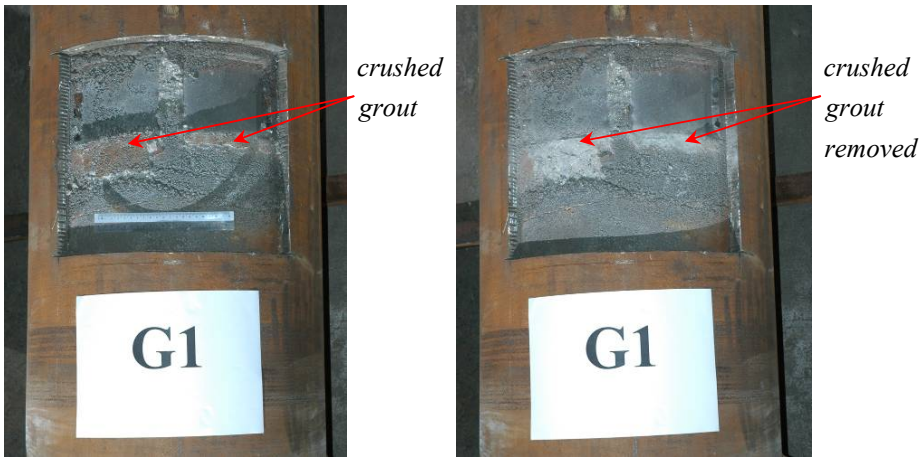

(a) (b)

Figure 4.19 Opening up of G1 after tests: (a) with loose damaged grout in original position; (b) with loose damaged grout removed

From the detailed comparison of the FEA results with test results for G1, the following findings can be summarized:

- The FE results using the proposed damage parameters coupled with the assumed descending stress-strain curve was in close agreement with the test results, indicating the applicability of the concrete damaged plasticity model in Abaqus (SIMULIA 2007) to the Ducorit D4 grout in such confinement condition.
- The local stress level for the grout at critical region computed by different models with different mesh densities shows certain degree of mesh sensitivity, probably due to stress concentration. However, the results for global behavior and the damage simulation were consistent and close to test results;
- Both 3D and axisymmetric FE models show the grout damage starts at load level 6000kN, and at load level 9500kN, the damage has spread to certain area as simulated. However, the static capacity would further develop up to at least 12000kN in such a confinement condition, indicating good ductility and alternative load path exists for D4 grout.

4.4.3 G2, grouted specimen without stiffening plate

As mentioned previously, the possible existence of unaccounted bond on the grout-steel interface might contribute to the strengthening effect of G2. However, the related information in the literature shows such kind of bond is not reliable (Dier 2004) even for plain pipe-grout connection, which is with better confinement condition as compared with partially infilled grouting condition. From fracture mechanics point of view, the bond-slip failure shown in the test for G2 is a mode II fracture procedure. The crack starts to propagate, when the loading stress intensity factor K_{II} reaches the mode II toughness K_{IIc}, the interfacial resistance stress intensity factor. However, at

current stage there is no reliable test data of K_{IIc} for D4 grout-steel interface.

In this study, a mechanism-based failure approach, which has been frequently used in fiber push out study (Liang and Hutchinson 1993; Tandon and Pagano 1998), was employed to simulate the interfacial bond-slip behavior. An apparent reason was that the empirical interfacial transferring shear limits in the literature may be used for reference. The offshore code, RP2A (API 2000), specifies the limiting transferring shear stress on the interface for plain concrete-steel connection at the range of 0.138 MPa to 0.184 MPa for design, while (Etterdal, Askheim et al. 2001) indicates the interfacial shear strength for S5 grout is 0.33MPa. Although these empirical transferring shear strengths are not specified clearly whether they are critical bonding shear stress or critical frictional shear stress, and are meaningful only in terms of average value, they may be considered as lower bond reference values for the failure criteria based on traction separation law, which is simulated using **debond** function in Abaqus (SIMULIA 2007). The process is illustrated in Figure 4.20 (a). The debonding was assumed to be only related to the shearing traction, and the magnitude of normal traction has no effect on debonding. The two key parameters of the procedure are:

- initial crack size, and
- fracture criterion.

In the analyses, the initial crack size was fixed at 13mm at top, which was based on visual inspection of the specimen as shown in Figure 4.21. For fracture criterion, critical shear traction was used. The stress singularity at crack tip requires the critical shear traction for bond break to be specified for the location at certain 'distance' behind the crack tip, as illustrated in Figure 4.20 (b). The critical shear traction and critical distance were treated as variables for sensitivity study, as there is no reliable

reference currently. After bond break, surface-to-surface contact was assigned for debonded nodes using 'hard contact' with Coulomb friction model, as used in Chapter 3 in preliminary FEA. The same frictional coefficient of 0.3 was adopted. It was noticed the limiting frictional shear stress in contact may affect the redistribution of stress field and was varied for sensitivity study also. Table 4.6 shows the cases run for sensitivity study.

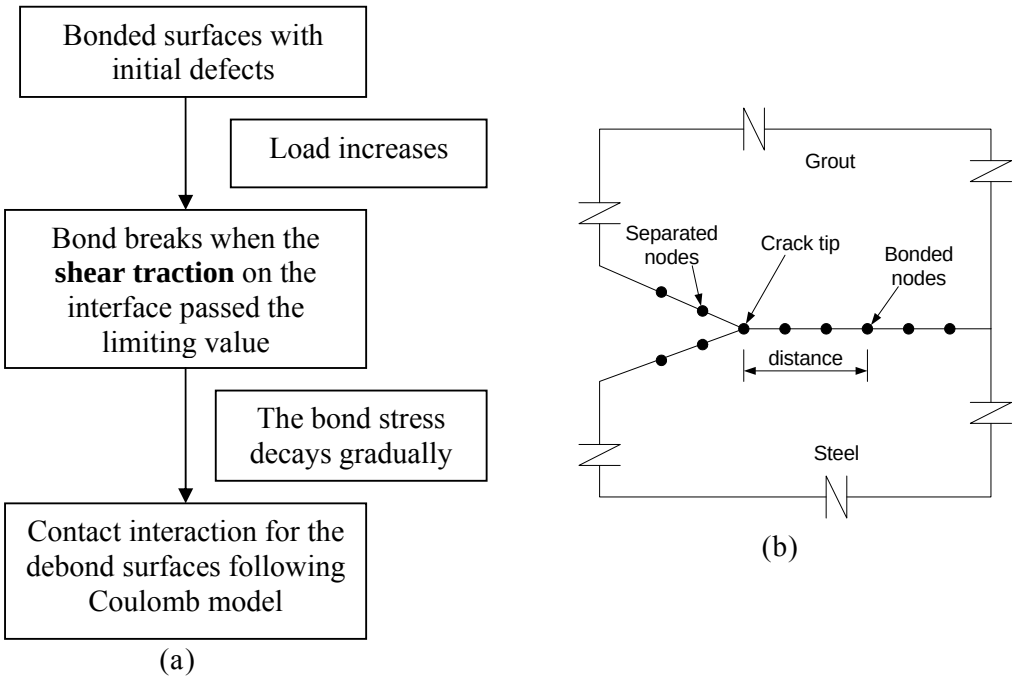

Figure 4.20 Illustration of debond procedure in FEA simulation: (a) computational flow chat; (b) critical distance in front of crack tip

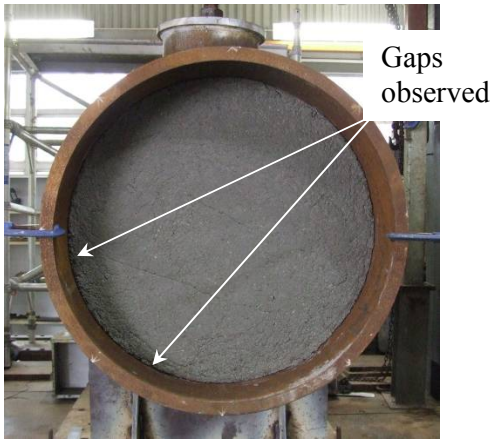

Figure 4.21 Observed shrinkage gaps, G2

The analyses for the bond-debond-contact procedure were conducted using axisymmetric models with linear elements. 20 cases in Table 4.6 were analyzed. In four cases, RUN - 6,9,15,18, analyses stopped half way, when the crack ceased to propagate at same location, the chamfered transition. In six cases, RUN 1to 3, 10 to 12, all with critical distance equal to 12 mm, the crack propagated to a very short length, less than 200mm, and no local buckling was developed. For the rest of the cases with initial bond, local buckling was developed and the crack traveled up to 1.1m, just below the location of local buckling. In short, for all the initially bonded cases, the simulation shows crack will be arrested around the chamfer region. For the two un-bonded cases, local buckling was developed like the experimental failure mode.

Table 4.6 FEA runs for adhesive bond effect study for G2

Case	Critical shear traction - MPa	Critical distance - mm	Limit for frictional shear
RUN-1	1	12	unlimited
RUN-2	0.1		
RUN-3	0.01		
RUN-4	1	6	unlimited
RUN-5	0.1		
RUN-6	0.01		
RUN-7	1	3	unlimited
RUN-8	0.1		
RUN-9	0.01		
RUN-10	1	12	1
RUN-11	0.1		
RUN-12	0.01		
RUN-13	1	6	1
RUN-14	0.1		
RUN-15	0.01		
RUN-16	1	3	1
RUN-17	0.1		
RUN-18	0.01		
RUN-19	unbonded		unlimited
RUN-20	unbonded		1

Figure 4.22 and Figure 4.23 show the load-displacement curves of the simulation results and comparison with the test result, it could be seen that none of the initially bonded model matched the test result, only the two initially un-bonded models, RUN-19 and RUN-20, were close to the test result. RUN-19, the case with unlimited frictional shear, fit experimental result best. This strongly suggested that the bond effect should be omitted in such confinement condition. The initially bonded cases were with steeper slope of the elastic range than the test results, which means if there was initial bond on the interface, whether the bond will break or not, the strengthening effect as simulated should be better than tested.

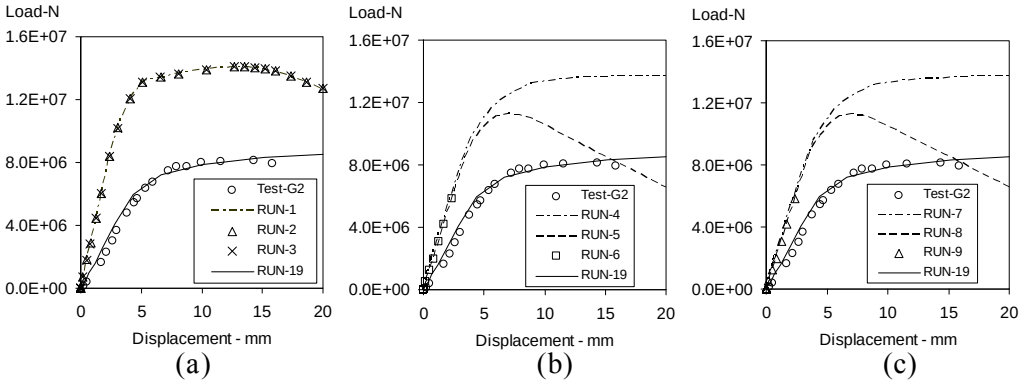

Figure 4.22 Comparison of load-displacement curves for G2 for adhesive bond study with frictional shear set unlimited: (a) critical distance 12mm; (b) critical distance 6mm; (c) critical distance 3mm

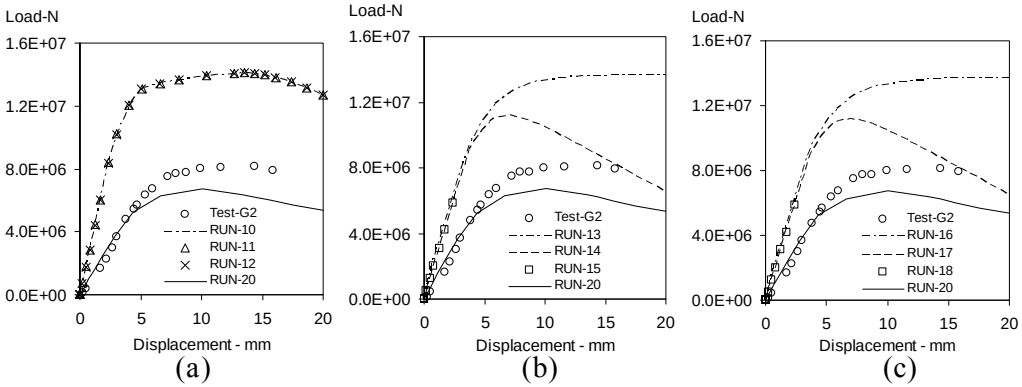

Figure 4.23 Comparison of load-displacement curves for G2 for adhesive bond study with frictional shear limited to 1 Mpa: (a) critical distance 12mm; (b) critical distance 6mm; (c) critical distance 3mm

With regards to the effect of limiting frictional shear stress, for initially bonded cases, the limiting frictional shear did not have significant influence. However, for initially un-bonded cases, the limiting shear showed influence on the post yield stage. Hence, for FE simulation, the shear stress was suggested to be unlimited, as the shear distribution on the critical region is not uniform. The values as specified in design codes and recommendations have average meaning and are probably on the conservative side.

RUN-19, 20 were slightly stiffer in the beginning part than the test result. This small difference was probably due to the grout shrinkage in the axial direction, which caused the separation of the two surfaces at the chamfer, leading to delayed contact effect. This phenomenon could be more clearly observed from the test results comparison in Chapter 3, where the control specimen and G2 have almost the same slope in the initial part of the load-displacement curves. To simulate the case with grout shrinkage in axial direction, both axisymmetric model and 3D model with shrunken grout geometry (2mm shorter than original grout length) were analyzed. The models excluded the adhesive bond effect. For 3D model, the lateral compressive load was imposed according to the test condition. Figure 4.24 shows the results and comparison with the test result. It could be seen that the agreement is very good. 3D model was with slightly lower strength, probably due to the more flexible response of quadratic elements of 3D model with relatively coarse mesh unlike the axisymmetric model with linear elements and dense mesh. Figure 4.25 shows the comparison of the opened up of G2 with FE simulation. Excellent consistency and agreement can be seen. Unlike G1, the grout of G2 is not damaged at all. It could also be seen that the shrinkage of grout in radial direction is insignificant: the grout still tightly fit into the steel tube even after significant slip in the test.

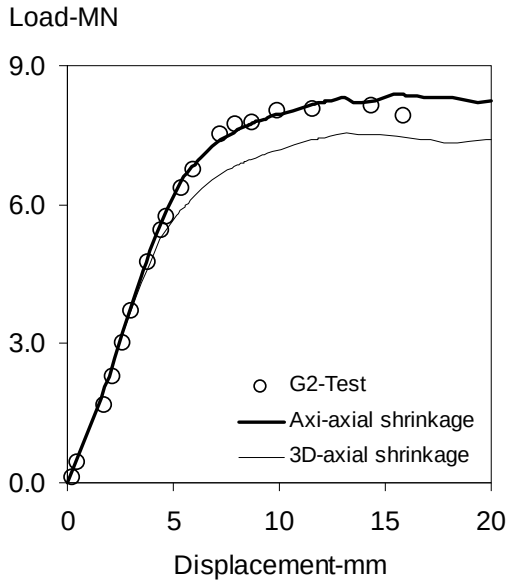

Figure 4.24 Comparison of FE results for G2 with axial shrinkage of grout, the FE models were without initial bond and frictional shear was unlimited

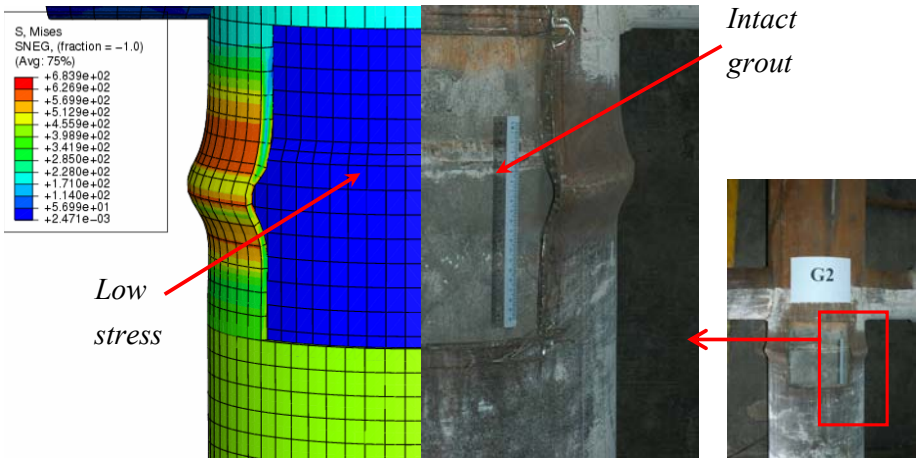

Figure 4.25 Deformed shape comparison of G2 with 3D FEA - no bond, but with axial shrinkage of grout

4.4.4 Discussion

It has already been shown the effect of mesh density for local stress/strain prediction for the grout in G1, however, in terms of global behavior and damage simulation the difference is insignificant. For G2, whatever the variation of fracture criterion is, the

bonded case will have crack arrest and stiffer response in the elastic range, which is inconsistent with the test result. Hence, further FE sensitivity study is deemed unnecessary, the justification of FE results are based on comparison with experimental results. As shown above, by using the same mesh scheme for G1 and G2, systematic difference in FE results analogous to the experimental results were observed due to different interfacial mechanism. Therefore, in a comparative sense, the mechanisms simulated in the FE models were considered close to those in the actual specimens.

For grouted cases, it was obvious that the adhesive bond effect on the interface should be ignored in the design; the tangential interaction was frictional shear only. However, similar to the findings in preliminary FE analysis, the friction on most area of interface was zero due to expansion of steel tube under axial compression. Hence, it can be concluded that the interfacial shear transfer mechanism was ineffective for plain grout-steel interface, consistent with the literature (Parsanejad and Gusheh 1992; MSL and Dier 2004). Shear keys are indispensible, especially for partially grouted condition with ineffective end bearing mechanism.

Generally, for G1, load transfer between steel and grout was mainly realized by contact action between the stiffening plates and the grout underneath, the so called contact-bearing mechanism. For G2, the load transfer was also by contact action at the chamfer region, based on the so called contact-sliding mechanism, which shed part of the load from steel tube to the grout and led to the change in buckling length and shape, as shown in Figure 4.26. The two load transfer mechanisms originated from the same contact action between the steel and grout. However, the strengthening effect of G2 was lower than that of G1, because:

- For G1, almost no relative slide for the contact action between the stiffening

plates and the grout, and the normal of the interface was in line with the contact movement, so that the grout was loaded by contact pressure directly. The grout bearing capacity is mobilized. In short, the effectiveness of contact for load transfer was high.

- For G2, the relative sliding between steel and grout was significant due to the normal of contact interface inclined with the contact movement, so that contact pressure and tangential frictional shear for load transfer was small; the stress level that the grout experienced is low. In short, the effectiveness of contact for load transfer was low.

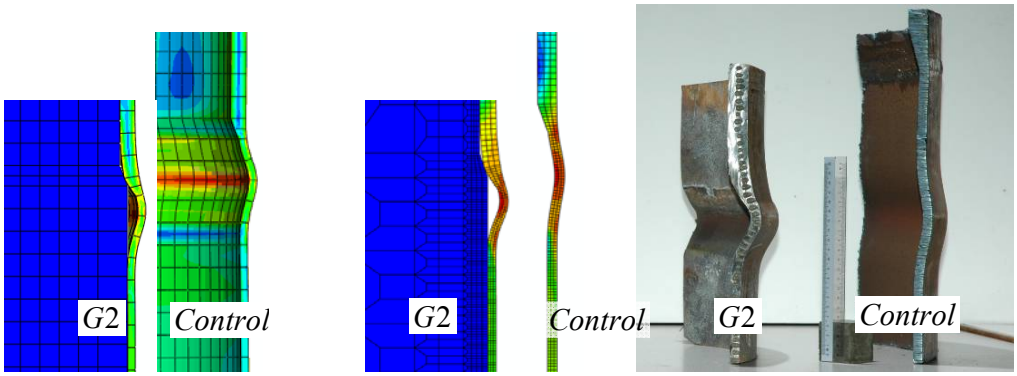

(a) (b) (c)

Figure 4.26 Buckling shape comparison for the control specimen and G2: (a) 3 D models; (b) axisymmetric models, (c) tested real specimens

4.5 Parametric study

Based on the refined FEA results, it was found that the strengthening mechanisms for G1 and G2 were similar: they originated from the dominant steel-grout contact action. The difference between them was due to the difference of the effectiveness of contact. The effectiveness of contact for G1 was significantly higher than that for G2, due to the adoption of stiffening plates in G1. G2 is purely based on the 'jam' effect. The 'jam' effect shown in G2 is complex and could be further related to the radial stiffness

of the steel tube for confinement effect. In order to evaluate the effectiveness of contact, a parametric study was carried out using the calibrated FE models above. Three parameters, listed below, were singled out and assigned with consistently varying values to test their influences to the effectiveness of contact:

- the thickness of stiffening plates for G1;
- the chamfer angle for G2;
- the grout strength for G1.

4.5.1 The effect of the thickness of stiffening plate

Based on the geometry of G1, four different thicknesses of the stiffening plates, 3.3mm, 6.7mm, 10mm (G1), and 20 mm, were modeled and meshed using axisymmetric model. The material properties were the same as in the refined FE work using tested steel and Ducorit D4 grout stress/strain curves as shown above. The FEA results of global load-displacement curves were plotted in Figure 4.27 below for comparison.

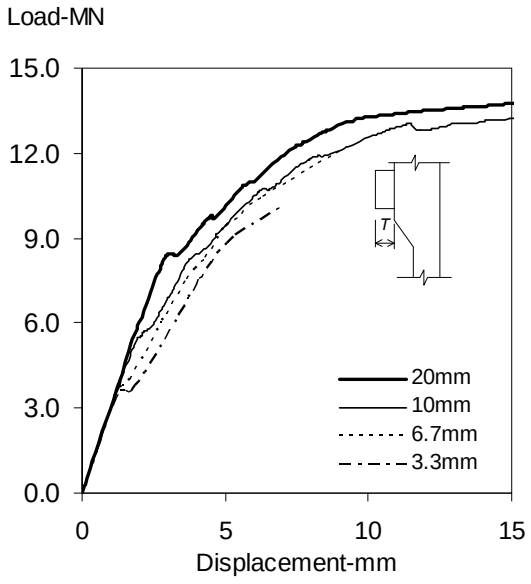

Figure 4.27 Load-displacement curves for different thicknesses of stiffening plates based on G1 model using Ducorit D4 grout

It could be clearly seen that thicker stiffening plate leads to larger static strength. The zigzags of the curves indicate the progressive failures of the grout at different loading stages. For 3.3mm and 6.7mm plate's models, the program stopped due to large strains incurred for the grout at load levels 10 MN and 11.9 MN respectively, which could be interpreted as grout crushed, and the values of damage parameters *dc* also indicated consistent results.

4.5.2 The effect of the chamfer angle

Four chamfer angles, 1:1, 1:2, 1:3(G2), and 1:4, for the transition zone of cross section based on G2 model were analyzed. The load-displacement curves were plotted in Figure 4.28. It can be seen that steeper transition angle lead to larger static strength, although the projections for the contact area were the same. With steeper angles, the failure modes changed from steel yielding to the combination and steel yielding and grout crushing. The kink appears on the load-displacement curve for 1:1 model at the load level about 7 MN, indicating the change of failure mode from steel buckling to grout crushing.

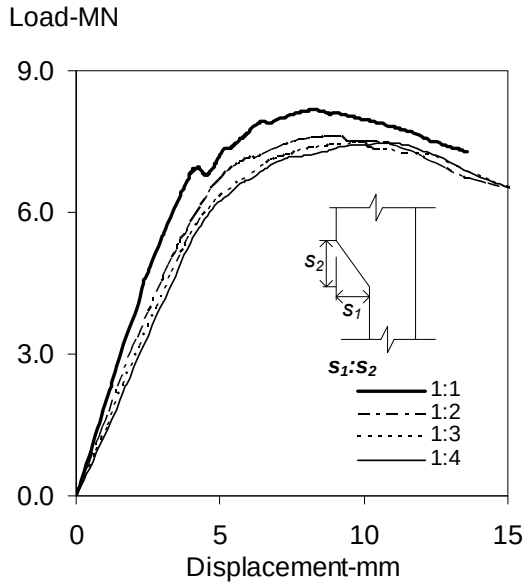

Figure 4.28 Load-displacement curves for different chamfer angles based on G2 model.

4.5.3 The effect of grout strength

According to the contact-bearing mechanism, the grout strength will be mobilized for those areas under effective contact, and will determine the ultimate strength of the composite member. Three types of the grout material were tested using G1 mesh in the FE parametric study. The grouts were Ducorit D4, Ducorit S5, and normal Grade 40 concrete. The material property of Ducorit D4 was based on the material test results as shown in Figure 4.3 and Table 4.4; the latter two were based on nominal values as shown in Figure 4.29, Table 4.7 and Table 4.8 below. The concrete damage parameters d_c and d_t were also assigned to the S5 and G40 concrete similar to that of D4. The FEA results of load-displacement curves were plotted together for comparison presented in Figure 4.30.

Table 4.7 Material property of Ducorit S5 used in FE parametric study

Stress	Inelastic strain	Total strain	Damage parameter	Plastic strain
-0.1	0.01	-0.010002381	0.98	0.010117
-3.5	0.0003	-0.000383333	0.7	0.000494
-5	0	-0.000119048	0	0
0	0	0	0	0
60	0	0.001428571	0	0
115	0.002	0.004738095	0.35	0.000526
20	0.01	0.01047619	0.93	0.003673
5	0.02	0.020119048	0.98	0.014167

Table 4.8 Material property of normal G40 concrete used in FE parametric study

Stress	Inelastic strain	Total strain	Damage parameter	Plastic strain
-0.1	0.01	-0.010003333	0.98	0.010163
-2	0.0003	-0.000366667	0.7	0.000456
-3	0	-0.0001	0	0
0	0	0	0	0
20	0	0.000666667	0	0
40	0.002	0.003333333	0.3	0.002571
5	0.008	0.008166667	0.95	0.011167
1	0.02	0.020033333	0.98	0.021633

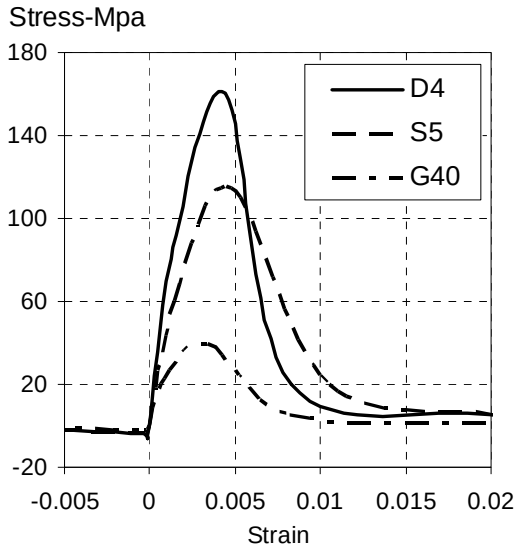

Figure 4.29 Stress-strain curves for the three grouts used in FE parametric study

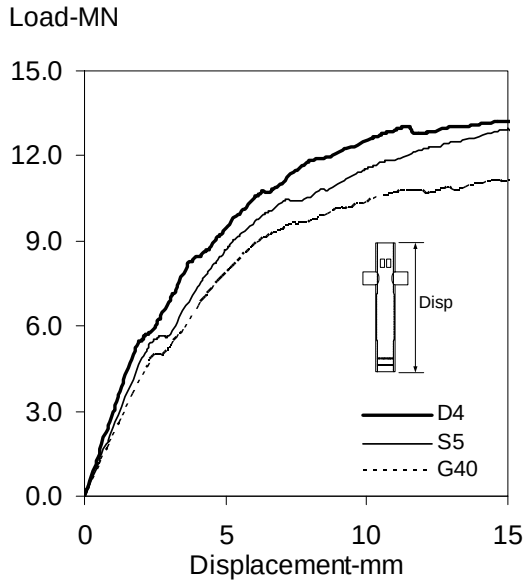

Figure 4.30 Load-displacement curves for different grout materials based on G1 model

4.5.4 Conclusion for FE parametric study

From the FE parametric study results, it could be concluded that:

- Larger effective contact area leads to larger static strength;
- Steeper chamfer angle make more effective contact-bearing effect;
- Higher grout strength leads to stiffer and stronger composite member.

4.6 Simplified model for design

Based on the FE parametric study as reported above, the following equation, (4.12), is proposed for calculating the sectional capacity of a partial infilling grouted circular tubular member subjected to axial compression based on plastic design:

$$N_p = A_s f_{yd} + qA_g f_{gd} \qquad (4.12)$$

where, N_p is the design squash load capacity;

A_s is the cross section of the steel tube;

f_{yd} is the design strength of the steel;

q is the effective contact-bearing factor;

A_g is the effective bearing area of the grout;

f_{gd} is the design strength of the grout.

The effective contact-bearing factor, q, is proposed to be related to the angle θ, which is the angle of the normal direction of contact interface with the direction of axial load. A linearly decreasing q from one to zero with the angle α increasing from zero to 90 degree can be used, as shown in Figure 4.31 below.

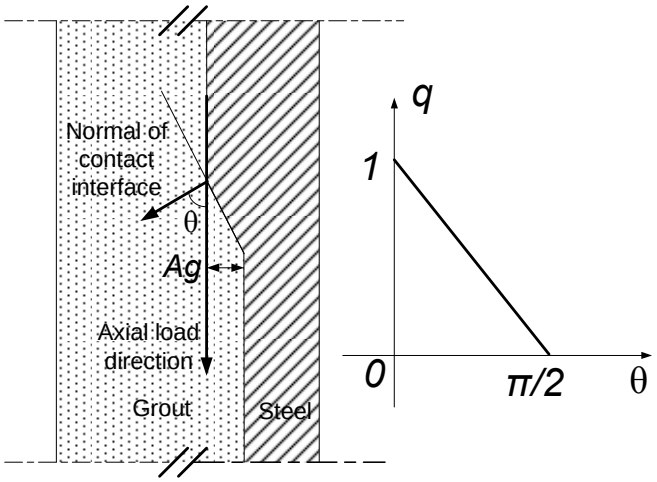

Figure 4.31 Determination of effective contact-bearing factor q

It should be noted that the study is performed on the tubular member with class I cross section. The diameter to thickness ratio of the thinner portion (member segment) is around 50, which is popular in the real offshore jacket structure. The q factor in nature could be loosely related to the radial stiffness of the thinner section. Hence, the validity range of Eq. (4.12) should be limited to plastic (class I) cross section. With regards to design of stiffening plates, a tentative recommendation is to keep H/T around 10 following the design of G1, as illustrated in Figure 4.32. The height, H, of each stiffening plate can be calculated from fillet weld strength check. Note only three fillet weld sides are allowed for the fillet weld to ensure a 90 degree contact interface.

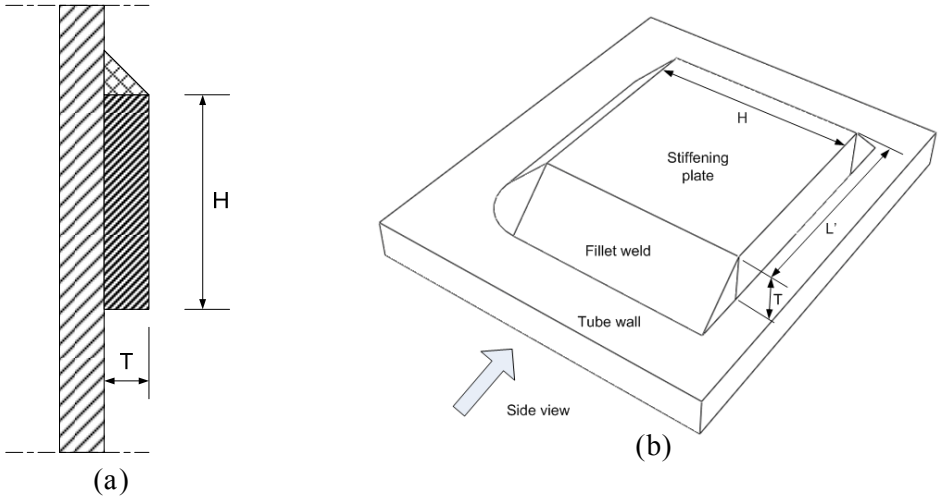

Figure 4.32 Details of stiffening plate: (a) side view (b) 3D view

As shown in the Figure 4.32 above, the effective contact-bearing area can be calculated as, equation (4.13):

$$A_g = L'T \qquad (4.13)$$

The following calculations demonstrate the strength check for G1 and G2. The design values of the materials are shown in Table 4.9, and the material safety factors are 1.1 and 1.5 for steel and grout respectively.

Table 4.9 Material properties used in design hand calculation

	Steel -MPa	Grout-MPa
Design value	355/1.1	200/1.5

Figure 4.33 shows the force flow for the grouted members G1 and G2, the upper portion is critical and used as free body diagram for calculation as follows.

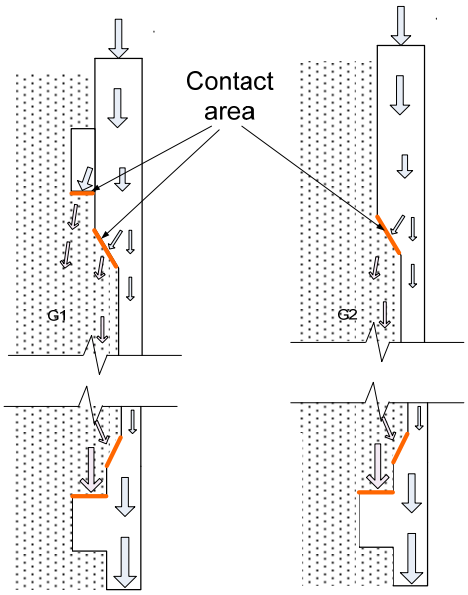

Figure 4.33 Force flow for the grouted members

For the control specimen:

$$N_p = A_s f_{yd}$$
$$= 3.14 \times (254^2 - 244^2) \times 355/1.1$$
$$= 5047 kN$$

For G1:

$$N_p = A_s f_{yd} + (q_1 A_{g1} + q_2 A_{g2}) f_{gd}$$
$$= 5047 + (1 \times 8 \times 118 \times 10 + (1 - 71.6/90) \times 3.14 \times (244^2 - 234^2)) \times 200/1.5$$
$$= 6717 kN$$

For G2:

$$N_p = A_s f_{yd} + q_2 A_{g2} f_{gd}$$
$$= 5047 + (1 - 71.6/90) \times 3.14 \times (244^2 - 234^2) \times 200/1.5$$
$$= 5458 kN$$

Table 4.10 shows the enhancement percentage and actual safety factors for the design calculation. The safety factors are within satisfactory range.

Table 4.10 Safety margins for the proposed equation (4.13)

	Actual results		Design values		Safety factor
	Strength-kN	Enhancement	Strength-kN	Enhancement	
Control	6732	-	5047	-	1.3
G1	11924(FE)	77%	6717	33%	1.8
G2	8006	18.9%	54558	8.1%	1.5

4.7 Further verification tests of small scaled specimens

In order to further verify the proposed simplified design equation (4.12) and check whether there is significant size effect, a series of axial compression tests for small scale column stub, which were partially infilled with D4 grout, was carried out.

4.7.1 Specimens

The design of small scale specimen maintained the major features of large specimen: two thickness, chamfer and infill grouted with D4. Totally there were 5 types of specimen: one was the empty control specimen and one was purely partially infilled. The other 3 of them were with slightly different mechanical aids to load the infilled grout. Figure 4.34 shows the geometry and notation of the specimens.

The specimens were fabricated using seamless hot finished carbon steel pipe. The nominal strength of the steel is 355 MPa. Overmatch butt weld with chamfer profile was employed for connecting the pipes as shown in Figure 4.34, and fillet weld was used to attach the stiffening plates to the internal surface. The specimens were infilling grouted with high strength grout Ducorit D4, Figure 4.35 (b). The inspection before casting revealed that actual the chamfer slope was about 1:10, much flatter than the specification, 1:3, as shown in Figure 4.35, (c).

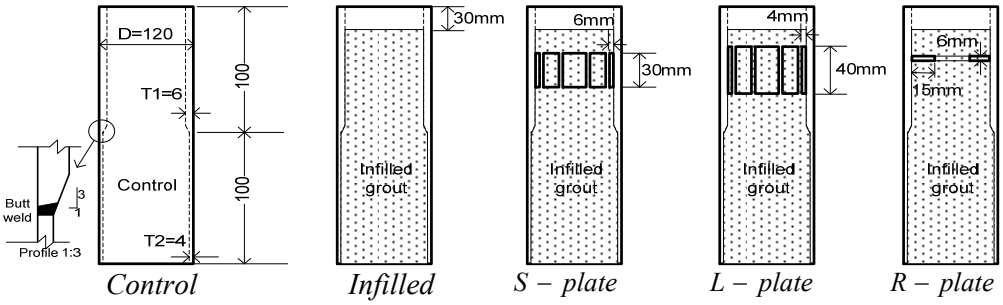

Figure 4.34 Geometry and notation of the small scale column stubs

(a)

(b)

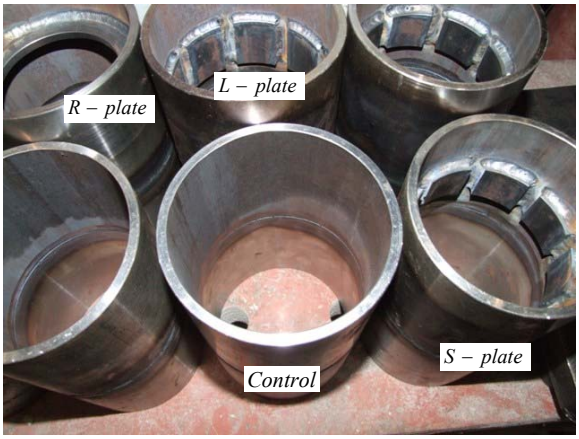

(c)

Figure 4.35 Small scale column stubs: (a) external view of un-grouted specimens; (b) infill grouted specimens with grout samples; (c) internal view of un-grouted specimens

4.7.2 Test procedures

The tests were performed in the Structural Engineering Laboratories of NUS using the 200 Ton Instron test rig. A thick plate with 5mm recess was attached to the top and bottom of the specimen respectively for positioning purpose (detailed design drawings are attached in the Appendix). Similar instrumentation scheme to the large specimens were carried out during testing. Pre-load was conducted to monitor the severity of eccentricity. Adjustment of the position was carried out until the eccentricity is within a satisfactory tolerance during pre-load stage. Axial compressive load was applied by displacement control with loading rate kept at 0.1~0.2 mm/minute before yield. After yield the loading rate was increased gradually up to 0.8mm/minute to final failure.

4.7.3 Test results

The load displacement curves are plotted in Figure 4.36. Figure 4.37 shows the final failure modes. Figure 4.38 shows the comparison of averaged load–displacement curves. From Figure 4.36, it can be seen the scatters of test results for each type of specimen is very small, the quality control of the test is satisfactory and the results are consistent and reliable. Generally, it can be seen that with the mechanical aids the strength of partial grouted specimen was improved significantly, while the change of stiffness in linear elastic range is insignificant.

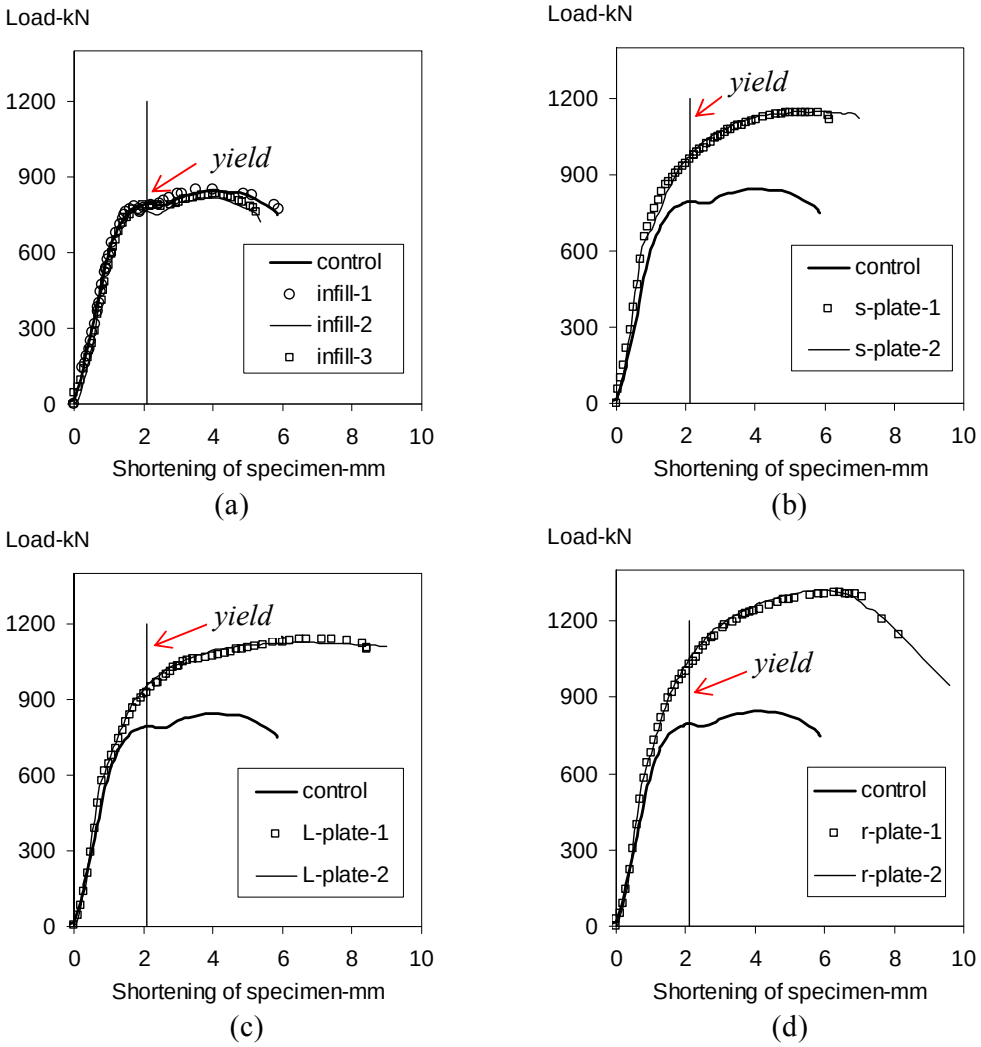

Figure 4.36 Load-displacement curves for small scale column stubs: (a) Infilled; (b) S-plate; (c) L-plate; (d) R-plate

(a)

(b)

(c)

(d)

(e)

Figure 4.37 Failure modes of column stubs: (a) Control specimen; (b) Infilled; (c) S-plate; (d) L-plate; (e) R-plate

From the comparison of load-displacement curves shown in Figure 4.36 (a) and the failure modes in Figure 4.37 (a) (b), it is apparent that there is no difference in terms of mechanical behavior between the control specimen and simply partially infilled specimens. No strengthening effect has been gained based on simple steel-grout interface mechanism. The adhesive bond was clearly proved to be insignificant again. Certain mechanical aids must be introduced to divert the load from steel to

grout. In contrast, the strengthening effects with proposed shear keys and ring can be seen quite significant from Figure 4.36 (b) to (d).

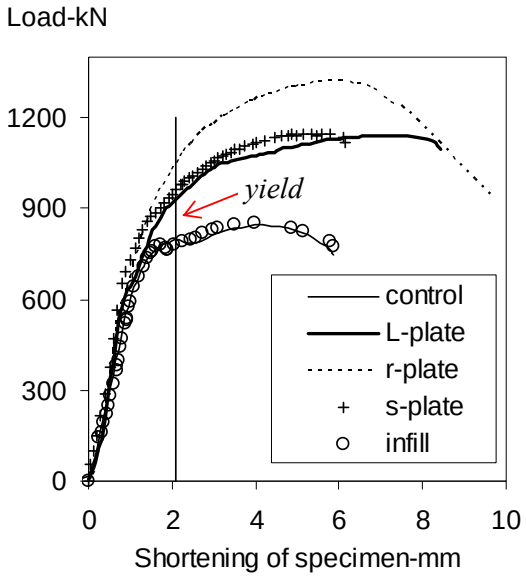

Figure 4.38 Comparison of averaged load-displacement curves

As expected, the predictions by Eq. (4.12) for infilled with stiffening plate type of specimens are good. For the infilled type the chamfer was taken as the actual 1:10 and the q, the effective contact-bearing factor in Eq. (4.12) is less than 0.1, so that the strength enhancement is less than 2%. For the S-plate specimen, the over prediction is expected, because the strength was governed by the thick wall portion, where the local buckling happens, as shown in Figure 4.37 (c). The best prediction is from L-plate specimen, in which the thickness of the stiffening plate was intentionally controlled in the design to just crush the grout beneath, and the capacity of the composite section is close to that of the thick wall section. From Figure 4.37 (d), it can be seen that both chamfer region and upper thick wall were buckled. For the ring stiffener specimen, the over prediction is also expected, because the bearing mechanism for ring stiffener was based on bending not shearing. Equation (4.12) is derived based on shearing plate. However, the test results of ring stiffener are

encouraging: it shows the stiffening effect based on bending is also significant. In reality, the ring stiffener is widely used in large diameter jacket leg member.

The tested strength of the specimens are summarized in the Table 4.11 together with the prediction by proposed equation (4.12). The yield strength is defined from load-displacement curve with the corresponding displacement equal to 2.5mm as shown in Figure 4.36 and Figure 4.38, while the ultimate strength is the peak load tested for each case. It was noted that the actual steel strength was higher than the nominal value 355 MPpa, so that when applying equation (4.12) the yield strength and ultimate strength for steel were taken as 530 MPa and 580 MPa respectively, which were from the fitting the prediction result to test result of control specimen. The yield strength of D4 was taken 180 MPa and ultimate strength 200 MPa.

It has been shown that the results of the small scale column stubs are consistent with those of large scale tubular member tests. The scale effect for the proposed simple design equation (4.12) is insignificant within its validity. The adhesive bond on plain steel-grout interface was proved again ineffective under partially infilling grouting condition.

Table 4.11 Comparison of results for column stubs

Specimens		Control	Infill	S-plate	L-plate	R-plate
Test results	Yield-kN	770	781 768 771	999 1019	991 1002	1058 1119
	Average-kN	770	773	1009	996	1088
	Improve-%	-	0.40%	31%	29%	41%
	Ultimate-kN	844	852 816 831	1139 1141	1138 1125	1313 1317
	Average-kN	844	833	1140	1131	1315
	Improve-%	-	1.30%	35%	34%	55%
Predicted results	Yield-kN	772	784	1082	979	1594
	Improve-%	-	1.60%	40%	27%	108%
	Ultimate- kN	845	859	1190	1075	1758
	Improve-%	-	1.60%	40%	26%	106%

4.8 Conclusions

Both experimental and numerical investigations for partial infilled grouted tubular member subjected to axial load were conducted. The results are consistent and indicative. The following conclusions can be drawn:

- For the large scale tubular member tests, the refined FE analysis using accurate material properties and finer mesh improved the simulation results significantly; the comparison with experimental results was in close agreement.
- The damaged plasticity model (Lubliner, Oliver et al. 1989; SIMULIA 2007) could be applied to simulate the behavior of Ducorit D4 in such low confinement condition as partial infilled grouting. Compared with experimental results, satisfactory FE results have been achieved using the material model with suggested parameters and uni-axial stress-strain curve.
- When subjected to axial load, the interfacial action between grout and steel was ineffective for partial infilled grouted tubular member in plain grout-steel interface. Both adhesive bond effect and frictional shear are ineffective. The mechanical aid, like the stiffening plate as shear keys, are indispensable for partial infilled grouting method. The proposed stiffening plate has been demonstrated with significant strengthening effect.
- A simplified design method was proposed based on plastic design formation to calculate the sectional capacity of the partial infilled grouted member under axial compression loads. Compared with experimental results, the design values were conservative.
- Small scale column stubs with partial infilled grout were tested under axial compression. The results were consistent with the large scale tubular member.

The adhesive bond on the interface of steel and grout was proved again ineffective. The proposed simple design equation gave good prediction compared with test results. The scale effect was found to be insignificant.

Chapter 5

Hot spot stress for tubular joints

5.1 Introduction

Fatigue of welded tubular joint is an important aspect for structural design and integrity assessment due to the combined effects of its severe stress concentration and the environmental cyclic loads. Current offshore codes (API, 2000; Hobbacher, 2005; BSi, 2007; DNV, 2008) recommend the hot spot stress S-N approach for estimating the fatigue life of welded tubular joint. The methodology uses the range of hot spot stress to characterize the fluctuation of the stress/strain field of hot spot region, where fatigue crack is likely to initiate. The link between the hot spot stress and the global load (represented by nominal stress) is the hot spot stress concentration factor (SCF) as defined in Eq. (5.1) (Wardenier, 2002):

$$SCF = \frac{\sigma_{hss}}{\sigma_n} \qquad (5.1)$$

where, σ_{hss} can be either the geometric stress σ_g or the hot spot stress σ_l, as discussed in **5.2**; σ_n is the nominal stress in the brace, computed according to simple beam theory, as introduced in Chapter 2, **2.6.1**.

The SCF reflects stiffness distribution of a particular joint and quantifies the local stress amplification effect. In practice, reliable and accurate prediction of SCF is fundamental for application of S-N approach. The determination of SCF depends mainly on the overall geometry of the tubular joint and the detailed geometry of its

weld (HSE, 1997). In recent decades, many researchers have focused on the effect of overall joint configuration, resulting in successful development of a few sets of empirical formulae to predict SCFs based on global non-dimensional geometric parameters, as defined in Chapter 2. The HSE report prepared by Lloyd's Register (HSE, 1997) summarizes some of these formulae and assesses the accuracy of the predicted SCFs. In contrast, it is found through literature review (Dijkstra and Noordhoek, 1985; Back, 1987; Marshall, 1992; HSE, 1997; HSE, 1999; BSI, 2009) that the research for the effect of detailed weld geometry parameters, as defined in Figure 5.1, has not been carried out adequately and only limited experimental investigations have been conducted. In certain cases the measured SCFs have been reported with very large fluctuations (Wylde, 1983; Wordsworth, 1987).

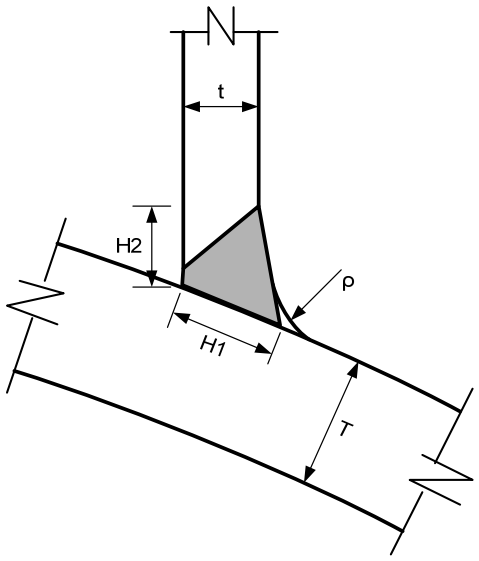

Figure 5.1 Weld geometry parameters notations for typical tubular joint

In fact, the effect of weld geometry is indispensible for an accurate prediction of SCF. One typical example is the Efthymiou formulae (Efthymiou, 1988), which generate the most accurate SCF predictions among all the empirical formulae due to incorporation of weld geometry, using solid elements, in the finite element models of derivation (Marshall, 1992).

In the practice of design and fabrication of tubular joints, full penetration butt weld is normally specified according to AWS (1994), which indicates the range or minimum weld size required. The actual weld geometry for each joint configuration is with large variation due to different fabrication and welding procedures, which is without doubt a major contribution to the large scatter of measured SCFs. Wylde (1983) reports that the measured SCFs of T joints with similar global parameters γ, τ and β =1 have difference more than 100% due to the variation of weld leg length. Wordsworth (1987) studies the problem experimentally with acrylic model and concluded that the largest differences between measured SCFs and predicted SCFs occur when the brace diameter approaches the chord diameter.

In order to reduce the uncertainties associated with SCFs, since early 1980s researchers like de Back (1987) and Dijkstra and Noordhoek (1985) have started studying the weld geometry effects by experimental investigation (mainly on the variable position of the actual weld toe). This is in accordance with the experimental nature of hot spot stress. Recently Marshall (2005) proposes an empirical correction, $SCF_{corr,}$ for SCFs determined by Efthymiou formulae.

However, further systematic numerical investigation has not been found in the literature. The FE study for SCF of K-joints by Gibstein (1987) used shell element without weld modeling. It is felt that the effect of detailed weld geometry to SCF could, or should, be addressed more analytically by numerical method with the advancement of computer technology nowadays. As compared to experimental investigation, numerical study is not only inexpensive, but also more convenient and straight forward for revelation of the mechanism, as by precisely modeling and imposing boundary conditions, the uncertainties of physical tests can be eliminated.

Based on such considerations and with the main concern for the effect of detailed weld geometry, two tubular joints in the open literature are selected for finite element analysis by the author. One is a tubular T-joint with diameter ratio β=0.5, the other is a tubular X-joint with diameter ratio β=1. For the former, it is due to the fact that T-joint is a simple and typical representation of tubular joint without loss of generality, and the information with the variation of weld geometry of this joint in the literature (Dijkstra and Noordhoek, 1985; Bowness and Lee, 1995; Bowness and Lee, 1998) is sufficient for FE model calibration. For the latter, it is because the mechanism associated with joints with β=1 are postulated to be different – the experimental results reported are with much larger uncertainties as compared with other β ratios (Wordsworth, 1987; API, 2000). Meanwhile X-joint is considered as the simplest tubular joint (without global beam mechanism), so that the focus can be on the joint mechanism with the effect of weld geometry only. In addition, it is with practical significance that in existing offshore tubular frames a large number of X-joints are with β=1. The selected X-joint contains the properly documented information of various weld geometry (MSL, 1997). The global geometry parameters of the two joints are shown in Table 5.1 below.

Table 5.1 Geometric parameters of the tubular joints studied

Joint	α	β	γ	τ	D-mm	T-mm	d-mm	t-mm
T joint [a]	8.53	0.5	14.29	0.5	914.4	32	457.2	16
X joint [b]	12	1	12.7	1	406.4	16	406.4	16

[a] referred from (Dijkstra and Noordhoek, 1985)

[b] referred from (MSL, 1997)

In this chapter, the definitions of various hot spot stresses are first reviewed. Then in the finite element analyses, the convergence study of mesh density is performed on the T-joint, and the FE results are calibrated with the experimental results. Based on

the optimized mesh scheme, parametric study for weld geometry is carried out for both joints. The FE results are discussed and compared with the prediction of the proposed correction formula by Marshall (2005).

5.2 Various definitions of hot spot stress

There are considerable differences in the definitions of hot spot stress. It is important to ensure that the particular hot spot stress is applied with its correct S-N curve in practical fatigue assessment. In Figure 5.2 an idealized weld geometry at chord saddle is plotted to illustrate the concepts and definitions of hot spot stress accepted in current offshore codes (API, 2000; Hobbacher, 2005; BSi, 2007; DNV, 2008). The hot spot stress can be defined according to the following:

- ECSC definition – linear extrapolation of maximum principal stresses from two points at some distances from the weld toe, the σ_g in Figure 5.2. ECSC hot spot stress is adopted in ISO19902 (BSi, 2007) and RP C-203 (DNV, 2008) and the corresponding S-N curves are T and T'.
- IIW definition – same linear extrapolation of maximum principal stresses as ECSC definition but the distances are a bit different, also illustrated as the σ_g in Figure 5.2. IIW hot spot stress is adopted in IIW (Hobbacher, 2005; Niemi et al., 2007), CIDECT (Wardenier, 2002) and Eurocode 3 (BSI, 2008; BSI, 2009) and the corresponding S-N curves are the basic S-N curves for different wall thickness.
- API and AWS definition - the direct stress (normal to the weld toe) in the immediate vicinity of a structural discontinuity, the σ_l in Figure 5.2. API (AWS) hot spot stress is adopted in American codes (AWS, 1994; API, 2000), the corresponding S-N curves are X and X'.

The stress sampling positions are summarized in Table 5.2. As illustrated in Figure 5.2, the magnitudes of both σ_g and σ_l are obviously smaller than the true notch stress σ_{notch}, which is highly dependent on the local microscopic geometry parameters, e.g. ρ, with large scatters (Engesvik and Moan, 1983; Berge, 1985). The intention of extrapolation for σ_g is to eliminate the influence of microscopic notch effect with assumption of linear variation of structural stress (to be discussed later) in the notch sensitive zone. On the other hand, σ_l is a more localized stress, which includes some notch effects of weld profile shape and size (Marshall, 1992). In the latest ISO19902 (BSi, 2007), σ_g is formally termed as geometric stress to be differentiated from σ_l. The Efthymiou formulae (Efthymiou, 1988) are derived based on ECSC definition.

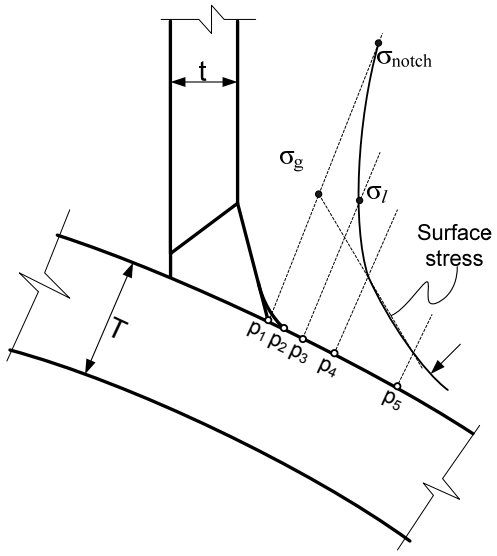

Figure 5.2 Idealized weld geometry with surface transverse stress distribution

Table 5.2 Stress sampling points for calculation of hot spot stress following Figure 5.2

Sampling positions	Distance from weld toe		
	API (AWS) [a]	IIW [b]	ECSC [a]
p_3	$0.1\sqrt{rt}$ (p_2 to p_3)	-	-
p_4	-	0.4 T (p_1 to p_4)	$0.2\sqrt{rt}$ (p_1 to p_4)
p_5	-	T (p_1 to p_5)	$0.4\sqrt[4]{rtRT}$ or 5^0 (p_1 to p_5)

[a] referred from (Radaj et al., 2006)

[b] referred from (Wardenier et al., 1991)

5.3 The effect of residual stress and shake down

For welded structures, the residual stress due to welding is large: it can be up to the magnitude of yield stress (Gurney, 1968). However, when a structure is subjected to cyclic loading, the residual stress will be partially released through permanent plastic deformation. This is the so called shake down effect. Generally, the response of a structure under cyclic loading can be categorized into three scenarios depending on the load levels (Skallerud and Amdahl, 2002):

- Steady shake down to linear elastic state, Figure 5.3, (a);
- Steady shake down to elasto-plastic state with closed hysteresis loop; Figure 5.3, (b)
- Steady shake down not achieved-incremental collapse. Figure 5.3, (c).

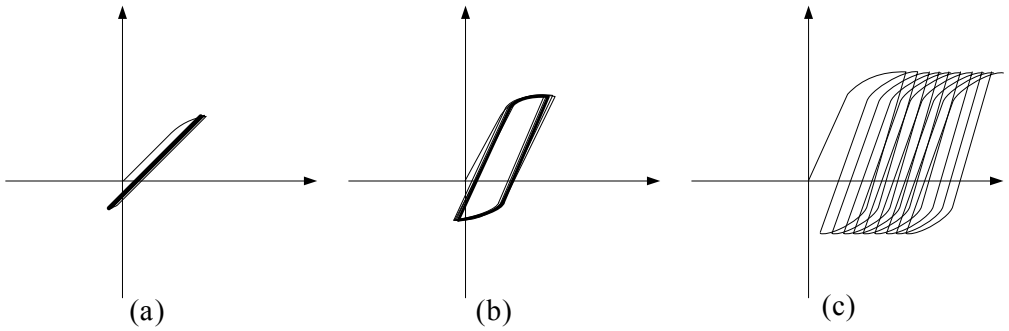

Figure 5.3 Illustration of the response of structure subjected to cyclic loading: (a) elastic shake down; (b) elasto-plastic shake down; (c) ratcheting

For offshore platform under service load, elastic shake down state need to be achieved from global structure analysis (Skallerud and Amdahl, 2002). However, at component level for tubular joints, the steady shake down limit, which should become the maximum design load, is not defined clearly due to the complexity of the problem. Grundy and Kwong (Grundy and Kwong, 1994; Kwong and Grundy, 1994) find the steady shake down limit depends not only on the load level but also the constraints

(the boundary condition) for tubular joints. In current design practice for fatigue of tubular joints, steady elastic shake down state is assumed implicitly. Waalen and Berge (2005) reported the observed steady elastic shake down in low cycle fatigue tests for tubular T-joint with strain gauge measurement located 6.1 mm away from weld toe, as shown in Figure 5.4. The cyclic loading is associated with linear variation of the hot spot stress (ECSC definition) range at two times the yield stress of the material with stress ratio R = -1. In such conditions, as illustrated in Figure 5.2, the true notch stress is much higher than the hot spot stress. When the hot spot stress reaches yield point, the notch stress is surely beyond yield, but the macroscopic global structural response as represented by the strain measures is still linear in most fatigue life span. In other words, the plasticity is well confined in a small volume. The influence due to microscopic plastic deformation and material softening, including the change of geometry from initial configuration, can be neglected in fatigue analysis using hot spot stress approach. Such linearity of hot spot stress is consistent with the assumption in fatigue damage calculation using Miners rule (BSi, 2007) for variable amplitude fatigue (actual service load) for offshore structure. (The topic of variable amplitude fatigue is beyond the scope of the thesis and will not be covered here.)

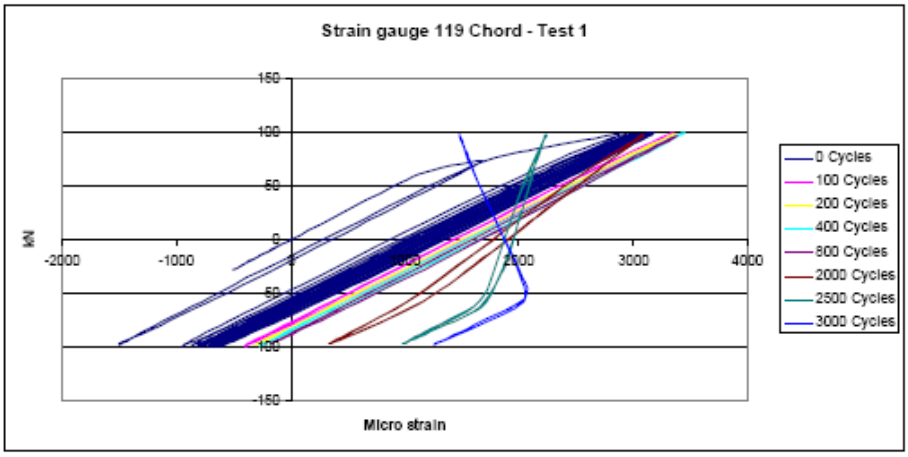

Figure 5.4 Load – strain curve, extracted from Waalen and Berge (2005)

5.4 Stress distribution through thickness and degree of bending

All the hot spot stresses adopted in the design codes are experimentally measurable, consistent with the experimental nature of S-N curve, but the extrapolation stress σ_g is more close to the analytical definition of structural stress, which refers to the shell bending stress σ_b and membrane stress σ_m through the shell wall thickness, determined as (Niemi et al., 2007):

$$\sigma_m = 1/T \cdot \int_{x=0}^{x=T} \sigma(x)dx \qquad (5.2)$$

$$\sigma_b = 6/T^2 \cdot \int_{x=0}^{x=T} \sigma(x) \cdot (T/2 - x)dx \qquad (5.3)$$

where, $\sigma(x)$ is the stress distribution through thickness as shown in Figure 5.5

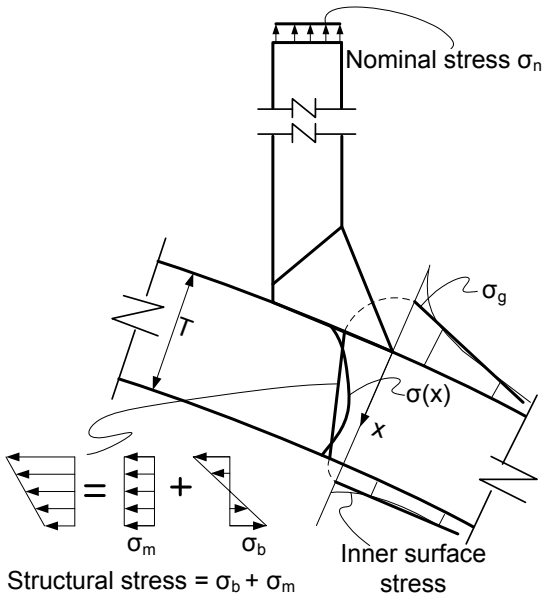

Figure 5.5 Structural stress through thickness

In IIW documents (Niemi, 1995; Hobbacher, 2005; Niemi et al., 2007), σ_g is called structural hot spot stress, assuming Eq.(5.4) is valid at the hot spot:

$$\sigma_g = \sigma_b + \sigma_m \quad (5.4)$$

Recent research (Berge et al., 1994; Boge et al., 2007) shows that the fatigue strength of tubular joint is significantly influenced by the parameter degree of bending (DOB), as defined in Eq. (5.5) (BSI, 2005):

$$DOB = \sigma_b / (\sigma_b + \sigma_m) \quad (5.5)$$

Based on Eq. (5.5) the DOB can also be determined as Eq.(5.6).

$$DOB = 0.5 \cdot (1 - SCF_{in} / SCF) \quad (5.6)$$

where, SCF_{in} is the stress concentration factor on the inner surface at the hot spot as shown in Figure 5.5 and equals to σ_b - σ_m.

The influence of DOB to fatigue life can be explained by fracture mechanics analysis. Newman-Raju solution (Newman and Raju, 1981) indicates the contributions of σ_b and σ_m to stress intensity factor (the fatigue crack driving force) are different, so that the resulting effect is dependent on the weights of bending and membrane stresses, which is characterized by DOB. Generally, for the same magnitude of hot spot (geometric) stress range, lower DOB will lead to shorter fatigue life and higher DOB will have longer fatigue life. However, the DOB effect is ignored in current design codes for S-N approach for simplification (HSE, 1999; Hobbacher, 2005; BSi, 2007). In this study for the purpose of research, both the structural stress and DOB are determined together with the hot spot stress for comparison.

5.5 Finite element analysis for the variations of SCFs of tubular joints due to weld geometry

This section reports the full details of the investigation for the variation of SCFs of tubular joints due to the expected variation of weld geometry by finite element method. Two case studies as mentioned in **5.1** above are conducted. The FE models

are built with pre-processing software Patran (MSC, 2005) and then analyzed with general FE software Abaqus/standard 6.7 (SIMULIA, 2007), finally the FE results are post processed with Abaqus CAE 6.7.

5.5.1 Case study I: T-joint with β=0.5

The stress/strain field in the hot spot region of tubular joint is highly three dimensional. Computation of hot spot stress and SCF using FE method is recommended by current design codes and literature (Marshall, 1992; HSE, 1997; BSi, 2007; DNV, 2008), in which the weld geometry is suggested to be included for accuracy. However, due to the geometrical complexity of tubular joint, especially at intersection of brace member and chord member, the weld toe has always been simplified as sharp notch in 3D FE modeling practice. This simplification leads to geometric discontinuity at the weld toe and causes singularity in linear elastic analysis. Inherently, if sharp notch weld toe model is adopted, the notch stress result will be mesh size sensitive. The question is whether and how it affects the SCF results. It is interesting and important to compare the application and computed results of various hot spot stresses, and observe how the local weld geometric parameters, as defined in Figure 5.2, influence the SCF results.

What has been selected for FE study is a T-joint configuration, which appeared in a series of classic fatigue tests conducted in Delft (Dijkstra and Noordhoek, 1985). In the tests, different weld toe conditions including as-welded, ground and improved weld profile of T-joints with one geometrical configuration underwent fatigue tests in different environmental condition. It was found ground weld toe in lab air condition improved fatigue life by a factor of 1.5, and no improvement under sea water condition. The hot spot stress SCF measured and adopted to correlate the fatigue lives was using ECSC definition.

5.5.1.1 Modeling

The T-joint configuration is following the description in Dijkstra and Noordhoek (1985), shown in Table 5.1, and weld profile parameters is taken from Bowness and Lee (1995; 1998) and shown in Table 5.3.

Table 5.3 Weld profile corresponding to Figure 5.2

	H1	H2	Weld toe radius, ρ
Sharp weld toe-As-welded	24	20	0
Ground weld toe	24	20	4.8

Brace axial tensile loading was applied according to test condition. Boundary condition is pin. Due to the symmetry, only quarter 3 D model was built up and analyzed, as shown in Figure 5.6.

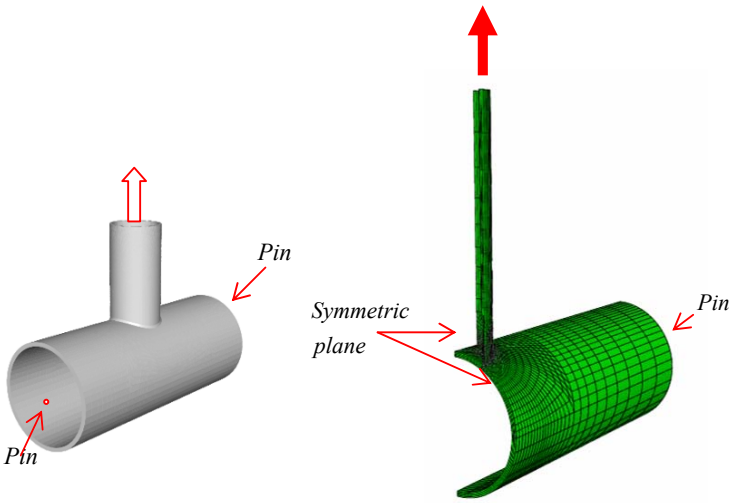

Figure 5.6 Quarter model of T joint used in FE study

Based on recommendations in current design codes and literature (Marshall, 1992; Vanwingerde et al., 1995; vanWingerde et al., 1996; HSE, 1997; Lee, 1999; Tveiten and Moan, 2000; HSE, 2001; Niemi et al., 2007; DNV, 2008; Radaj et al., 2009), quadratic solid element with reduced integration was adopted for hot spot stress

computation, as it can satisfactorily describe high stress/strain gradient in hot spot region. In Abaqus library, the element code is C3D20R. Initial preliminary study shows there is very little difference in the result between full and reduced integration for the element. However, it is generally understood that the element shape and aspect ratio would be influential to the computed result in critical region with high stress/strain gradient like the hot spot region for tubular joints. In the models built, the element aspect ratio is controlled within 1:5, and great efforts have been put in to make the brick element as cubic as possible in hot spot region. In addition, the two edges of each element are intentionally built to be perpendicular to the weld toe as shown in the Figure 5.7, so that the nodal value can be used for extrapolation without any further interpolation. Four meshes with different density for each model were analyzed for sensitivity study.

For sharp weld toe model (to simulate as-welded condition), as shown in Figure 5.7, the meshes are:

- **t-base**: coarse mesh, smallest element size at weld toe is about 6.5 mm
- **t1**: medium mesh, smallest element size at weld toe is about 3.3 mm
- **t2**: dense mesh, smallest element size at weld toe is about 0.9 mm, 8 layers for the chord
- **t3**: very dense mesh, smallest element size at weld toe is about 0.9 mm, 12 layers for the chord

For ground weld toe model, as shown in Figure 5.8, the grinding profile is smoothly merged to weld and chord surface. The meshes are:

- **tr-base**: coarse mesh, smallest element size at weld toe is about 2 mm
- **tr1**: medium mesh, smallest element size at weld toe is about 0.8 mm

- **tr2**: dense mesh, smallest element size at weld toe is about 0.6 mm with 9 layers for the chord
- **tr3**: very dense mesh, smallest element size at weld toe is about 0.6 mm with 12 layers for the chord.

The smallest element size for the ground model is smaller than that of sharp weld toe model to sufficiently catch the curved profile feature for ground weld toe. For both models, the analyses were performed under linear elastic condition with Young's modulus equal to 205000 MPa and Poisson ratio equal to 0.3.

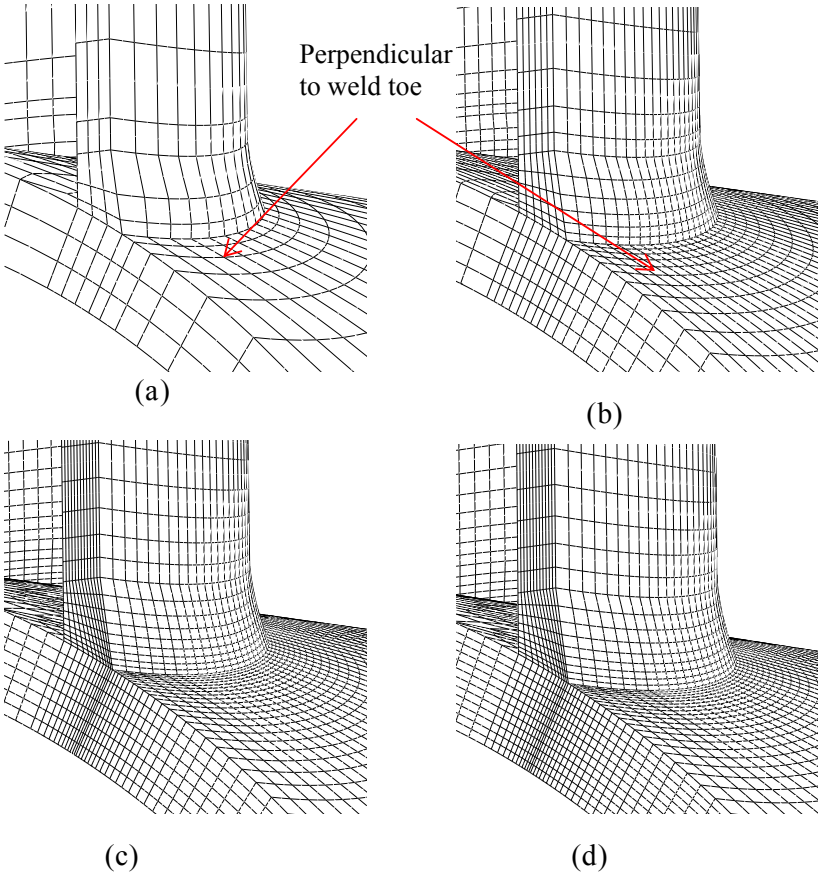

Figure 5.7 Different mesh schemes for sharp weld toe model: (a) t-base; (b)t1; (c)t2; (d) t3

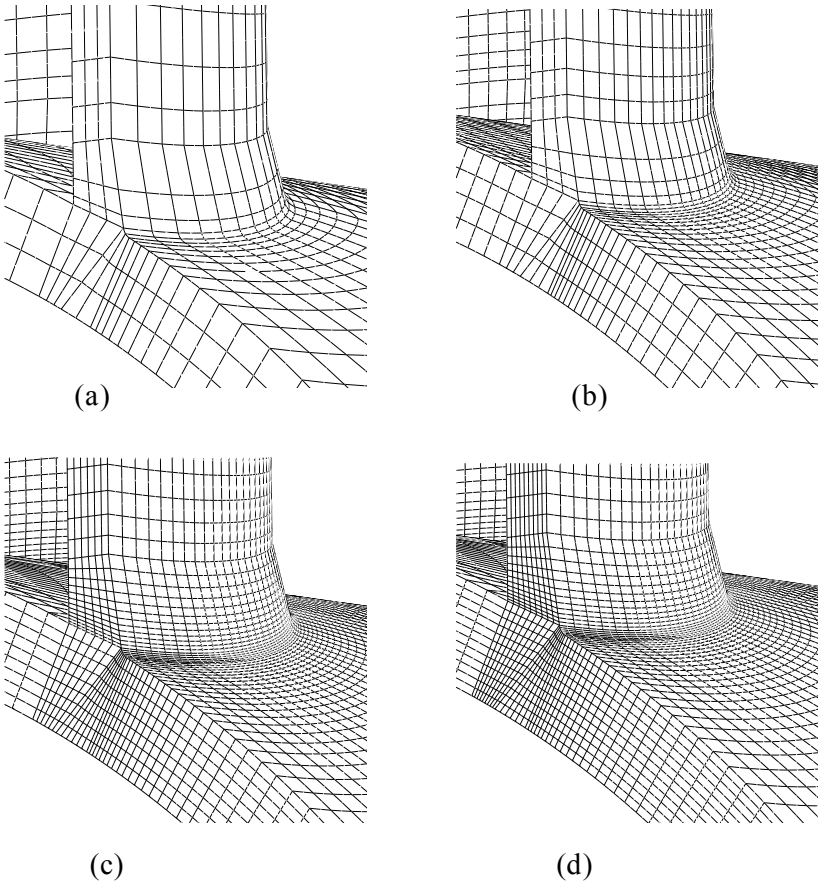

Figure 5.8 Different mesh schemes for ground weld toe model: (a) tr-base; (b)tr1; (c)tr2; (d) tr3

5.5.1.2 FE results

Sensitivity due to post processing

Unique nodal values in Abaqus result file are utilized for determination of hot spot stress/strain. It was noticed that stress and strain are element based values; the accurate result is at the integration point. The nodal value is computed based on mapping (sometimes also called extrapolation) using shape function. For a common node shared by a few elements the averaging method, called 'smoothening', needs to be applied. In this study, different smoothening methods available in Abaqus CAE (SIMULIA, 2007) were tested for sensitivity study. It was found the difference is insignificant for the adopted mesh scheme. A typical comparison is shown in Figure 5.9 (a), in which different nodal stress (maximum principal stress) along the

extrapolation path of the coarse sharp weld toe model t-base are plotted together. It can be seen the largest difference of the nodal stress occurred at sharp weld toe, the theoretically singularity point, which should be ignored. The other values are in close agreement. In the study, the reduced integration element (C3D20R) with the default post processing in Abaqus CAE (SIMULIA, 2007), the stress invariant calculated before averaging, are adopted.

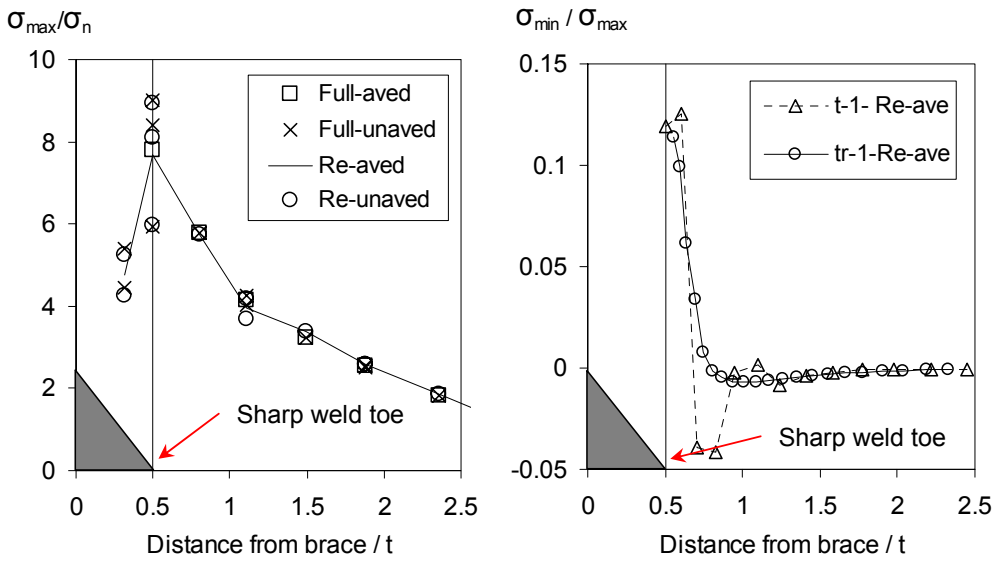

Figure 5.9 Comparison of FE surface stresses at chord saddle extrapolation path for the T joint with different post processing and element integration schemes: (a) normalized max principal stress; (b) ratio of min principal stress to max principle stress. The sharp weld toe is 0.5t away from brace wall, and the notations are:

Full-aved is the full integration element with the stress invariant calculated before averaging smoothening;

Full-unaved is with the stress invariant calculated after averaging;

Re-aved is reduced element with stress invariant calculated before averaging; and

Re-unaved is reduced element with stress invariant calculated after averaging.

Further check for the minimum principal stress is done, as shown in Figure 5.9 (b) for model t1 and tr1 on the same extrapolation path. The minimum principal stress is supposed to be zero theoretically due to the bi-stress status on the surface. Although

the errors associated with solid element is not completely eliminated as discussed by Soh (1997), it can be seen they are located very close to the weld toe and the peak notch stress. The stress values at the sampling points are with small errors, less than 1%.

Comparison of the results

For all the models, the largest stress occurs at saddle point. On the chord saddle path, the maximum principal stress is perpendicular to the weld toe intersection line, so the maximum principal stress is also the normal stress. The surface nodal stress value is used directly for hot spot stress computation. The stress contours and the normalized surface maximum stresses are shown in Figure 5.10. The comparison of two models is plotted in Figure 5.11. The hot spot stress concentration factors (SCFs) computed according to three different definitions is shown in Table 5.4 and Table 5.5.

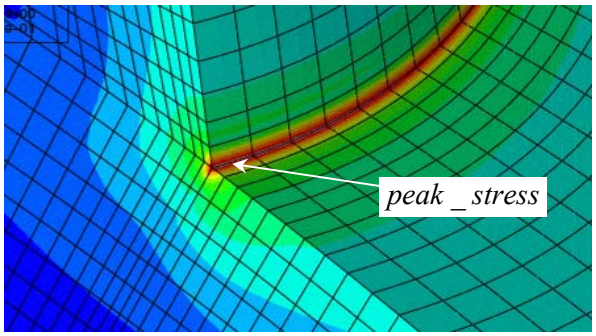

(a)

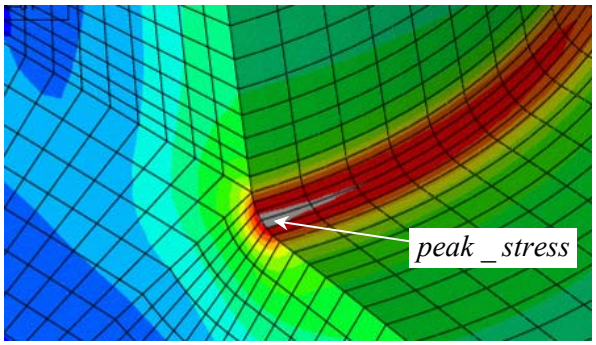

(b)

Figure 5.10 to be continued

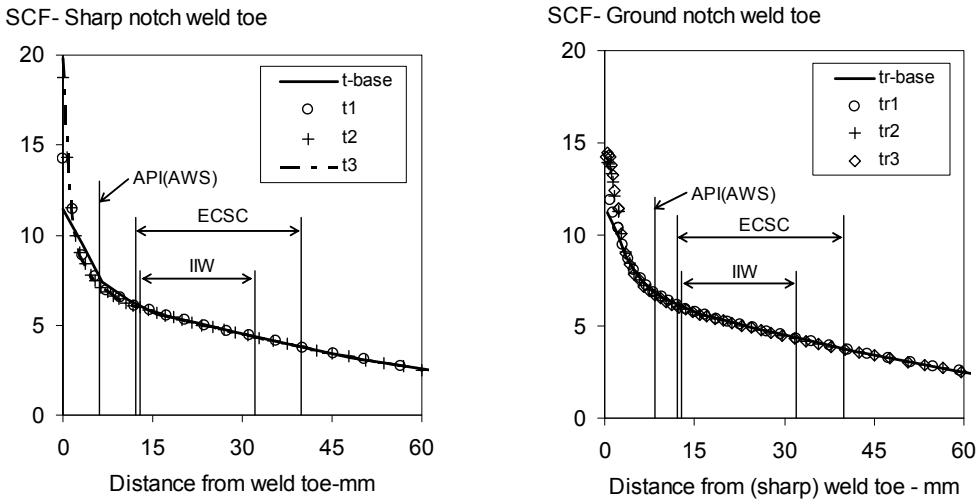

Figure 5.10 Surface stress distribution: (a) contour plot for sharp weld toe; (b) contour plot for ground weld toe with radius =0.15t 4.8mm; (c) distribution along chord saddle for sharp weld toe; (d) distribution for ground weld toe, the distance is from nominal sharp weld toe, same as in Figure 5.2

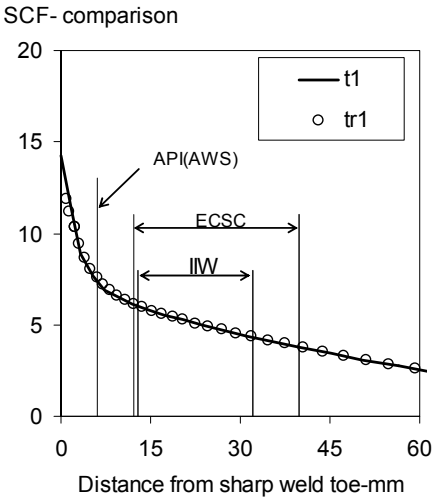

Figure 5.11 Comparison of surface stress for sharp weld toe-t1 and ground weld toe-tr1

The through thickness normal stress distribution is also computed and plotted in the Figure 5.12 and Figure 5.13, the degree of bending stress (DOB) is worked out according to the two methods introduced above. The results are shown in Table 5.6 and Table 5.7 for sharp and ground model respectively.

Table 5.4 SCF result- sharp notch weld toe for as-welded condition

		t-base	t1	t2	t3	Max. dif - FE*	Aver age-FE	Aver age-Test
Actual stress	API	7.68	7.39	7.24	7.18	0.50	7.37	-
Extrapolation method	ECSC	7.24	7.07	7.06	7.04	0.20	7.10	7.15
	IIW	7.24	7.11	7.06	7.05	0.19	7.12	-
Linearization	Through thickness ($\sigma_m + \sigma_b$)	7.15	7.35	7.51	7.51	0.36	7.38	-

Table 5.5 SCF result- weld toe radius ρ = 4.8mm (0.15T) for ground condition

		tr-base	tr1	tr2	tr3	Max. dif - FE[a]	Aver age-FE	Aver age-Test
Actual stress	API	6.90	6.86	6.73	6.70	0.20	6.80	-
Extrapolation method	ECSC	7.22	7.21	7.09	7.08	0.14	7.15	7.04
	IIW	7.26	7.22	7.10	7.08	0.18	7.16	-
Linearization	Through thickness ($\sigma_m + \sigma_b$)	7.55	7.59	7.58	7.59	0.04	7.58	-

[a] The difference between the largest and the smallest FE results.

Table 5.6 Degree of bending - sharp weld toe model

		t-base	t1	t2	t3	Average
Actual stress	API	0.79	0.81	0.81	0.82	0.81
Extrapolation method	ECSC	0.85	0.86	0.86	0.87	0.86
	IIW	0.85	0.86	0.87	0.87	0.86
Linearization	Through thickness	0.86	0.85	0.85	0.85	0.85

Table 5.7 Degree of bending - ground weld toe model

		tr-base	tr1	tr2	tr3	Average
Actual stress	API	0.82	0.82	0.83	0.83	0.82
Extrapolation method	ECSC	0.85	0.85	0.86	0.86	0.86
	IIW	0.85	0.86	0.87	0.87	0.86
Linearization	Through thickness	0.85	0.84	0.84	0.84	0.84

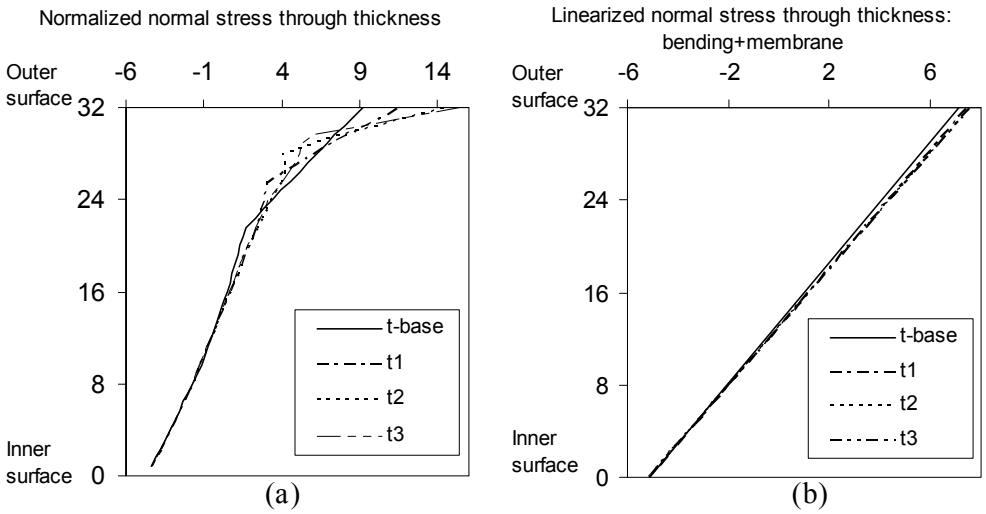

Figure 5.12 Through thickness stress distribution for sharp weld toe model: (a) normal stress distribution; (b) bending stress and membrane components by linearization

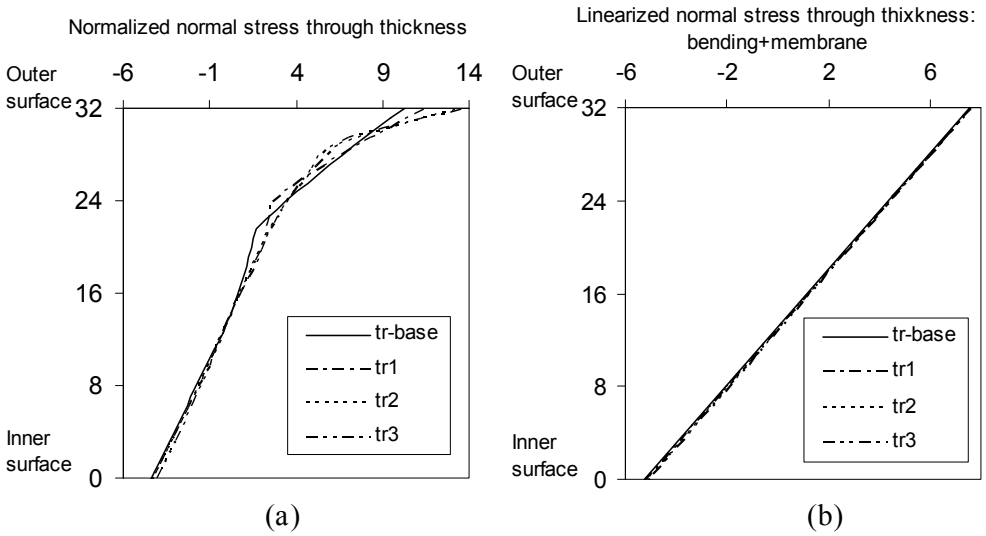

Figure 5.13 Through thickness stress distribution for ground weld toe model: (a) normal stress distribution; (b) bending stress and membrane components by linearization

5.5.1.3 Discussion of the FE results and conclusion

From Figure 5.10 it can be seen that the surface stress in hot spot region for sharp weld toe is more mesh sensitive than that for ground weld toe because of the singularity of sharp notch at weld toe. Comparing the SCFs as shown in Table 5.4 and Table 5.5, the extrapolation method, either ECSC or IIW approach, is preferred, since it is relatively insensitive to the mesh density. The two extrapolation approaches

generated almost the same SCFs, which are insensitive to the geometrical notch conditions of weld toe. For ground weld toe, the extrapolation was made up to the location of initial sharp weld toe. This is considered to be more reasonable, because the largest surface notch stress occurs at the mid of the notch, as shown in Figure 5.11, very close to the sharp weld toe.

Relatively, the API (AWS) approach is with slightly higher variation of SCFs for the sharp weld toe model, showing the influence of singularity of sharp notch. The notch effect is supposed to be partially reflected in the API hot spot stress SCF: the averaged FE result of sharp notch is 1.084 times of ground notch. Using the X curve of API RP2A (API, 2000) for controlled weld profile joints:

$$\Delta\sigma_l^{4.38} \cdot N = A \qquad (5.7)$$

For sharp weld toe and ground weld toe, the fatigue life improvement could be calculated as:

$$\left(\frac{SCF_s}{SCF_g}\right)^{4.38} = \frac{N_g}{N_s} = \left(\frac{7.37}{6.80}\right)^{4.38} = 1.43$$

which is close to the fatigue test results of 1.5 times improvement under lab air condition (Dijkstra and Noordhoek, 1985).

As compared with the experimental measurement, the FE results of medium density mesh t1 can be found suitable for sharp weld toe model, which is to simulate as-welded condition. The smallest element size of t1 mesh in the hot spot region is 6.5 mm, about 20% of chord wall thickness. As an optimized value, this proportion will be kept in further parametric study. For ground weld toe model, the basic tr-base model is sufficient to model the radiused notch.

The results of DOBs, as presented in Table 5.6 and Figure 5.8, show that the extrapolation approach is close to the linearization method, while the API hot spot

stress is relatively with smaller magnitude. Figure 5.12 and Figure 5.13 show that although the distribution of through thickness stress is influenced by the mesh density, the linearization result is not.

Further parametric study has been carried out with variation of three parameters:

- weld toe radius, from 3.6mm to 9mm, based on ground model with H1 and H2 equal to 24mm and 20mm respectively;
- weld leg length H1, from 22mm to 32 mm, based on sharp weld toe model; and
- weld height H2, from 18mm to 28mm, based on sharp weld toe model

The mesh density is similar to t1 and tr1. The result, as shown in Figure 5.14, reveals that

- The extrapolation approach generates stable geometric stress irrespective of weld toe notch radius, while the API hot spot stress is able to reflect the notch effect;
- For all three types of hot spot stress at chord, the weld leg length H1 is more influential than weld height H2;
- For ground weld toe model, the extrapolated geometric stress is higher than API hot spot stress, while for sharp weld toe model the trend is opposite.
- With reasonable variation of local macroscopic parameters H1, H2 and ρ, the maximum difference of 3D FE hot spot stress results are around 10% of the average values.

The DOBs do not show much variation with the change of local weld parameters. Finally, the results of hot spot stress and degree of bending are summarized and compared with hand calculation result by empirical formulas as shown in Table 5.8 and Table 5.9. It can be seen Kellogg formula as recommended in RP2A (API, 2000)

underestimate the hot spot stress significantly. The Efthymiou formula (BSi, 2007) gives very close results to both FE analysis and test measurement. The formula for DOB was generated through shell element FE analysis (Connolly et al., 1990) and gives satisfactory prediction.

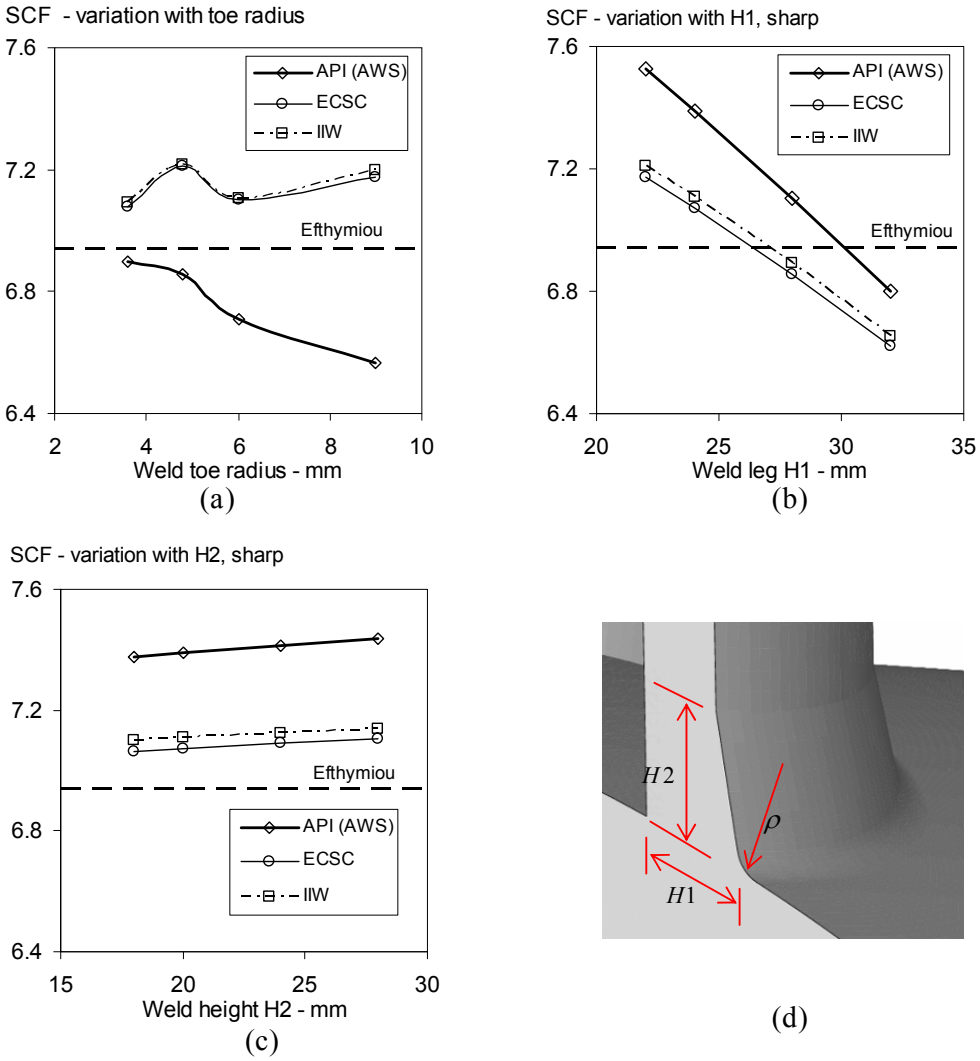

Figure 5.14 FE hot spot stress SCFs with different local parameters: (a) ground weld toe, H1=24, H2=20; (b) sharp weld toe, H2=20; (c) sharp weld toe, H1=24; (d) notation

Table 5.8 Comparison of SCFs

	Empirical formula		FE analysis		Test	
	Kellogg	Efthymiou	sharp	ground	as-welded	ground
API	4.59	-	6.80~7.52	6.57~6.90	-	-
ECSC	-	6.94	6.62~7.17	7.08~7.17	7.15	7.04

Table 5.9 Comparison of DOBs

Empirical formula	FE analysis	
Connolly[a]	Extrapolation	Linearization
0.82	0.86	0.85

[a] reference Connolly et al (1990)

Through the case study, the mesh adequacy and local parametric sensitivity have been presented. It can be concluded as follows:

- The mesh scheme using quadratic solid element with reduced integration is suitable for hot spot stress computation. The smallest element size in the hot spot region at 20% of chord wall thickness is sufficient.
- With the adopted modeling and meshing schemes, the geometric notch effect can be reflected on the API hot spot stress. When used to correlate the fatigue test results under air laboratory condition, the API hot spot stress prediction can be used to explain the fatigue life improvement due to grinding.
- The geometric stress defined by linear extrapolation is insensitive to the geometric notch effect, and is more consistent with through thickness stress result than API hot spot stress.
- For β ratio at mid range as analyzed, the local macroscopic parameters of weld profile will not affect the geometric stress SCF significantly, except for the weld leg length, H1 in Figure 5.2, which may cause 10% fluctuation of FE result. This is consistent with the experimental observation (Dijkstra and Back, 1980; Dijkstra and Noordhoek, 1985) that the weld leg length is an influencing parameter for the geometric stress. The prediction of Efthymiou formula, which uses ECSC definition, is in very good agreement with the FE and test results. From Figure 5.14 (b), the Efthymiou model was deduced to have weld leg length between 1.75 and 2 times the brace thickness.

5.5.2 Case study II: X-joint with β =1

When the β ratio is approaching one, the fluctuation of SCF will be large, as reported by Wylde and McDonald (1980) and Wordsworth (1987). In the document prepared by Lloyd's register (HSE, 1997), the issue was discussed again and the solution for the joints with β=1 is using the 'cut-back' angle and modified diameter ratio β', as shown in Figure 5.15. However, it is found the cut back angle and modified diameter ratio β' are difficult to determine in real application. In most cases, the weld profile for β=1 is with certain degree of convexity as shown in Figure 5.16 (a). In this study for the X joint with β=1(MSL, 1997), a more straightforward parameter termed as 'convexity' is defined as shown in Figure 5.16 (b), together with the weld leg H1 and height H2 to describe the weld geometry of joints with large diameter ratios. The study focused on the geometric parametric study.

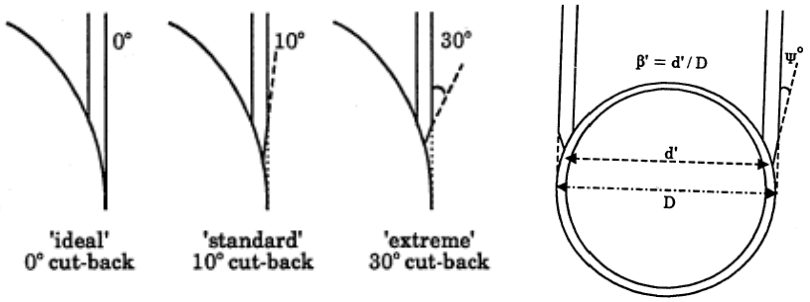

Figure 5.15 Additional parameters for joints with β=1, extracted from HSE (1997)

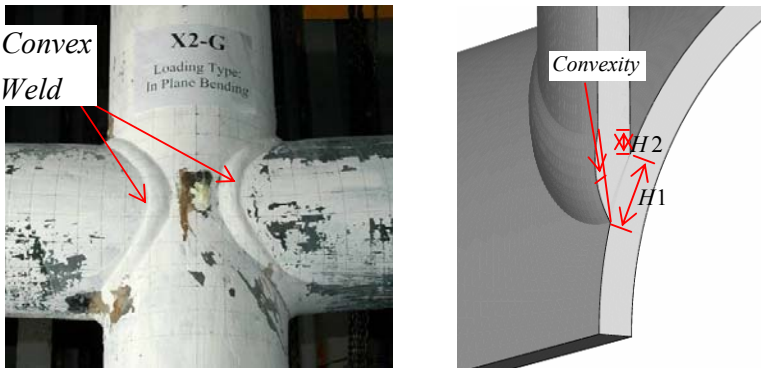

(a) (b)

Figure 5.16 X joint with equal diameters, β=1: (a) real specimen tested in NUS; (b) FE model with definitions of local parameters

5.5.2.1 Modeling

The X-joint configuration follows record of the specimen DT3 in MSL (1997). Table 5.1 and Table 5.10 present the global and local parameters used in 3D FE analysis. Parametric study was performed on the weld leg length H1 and the convexity. The mesh density and element type follow the conclusion in the above case study for the T- joint. Sharp weld toe is adopted to simulate the as-welded condition. Brace axial tensile load was imposed on the one-eighth model due to symmetry. Figure 5.17 illustrates the model with the variation of weld geometry.

Table 5.10 Local weld profile parameters for X joint, DT3, with $\beta=1$

	H1	H2	Convexity
Sharp weld toe, As-welded	24 ~ 36 mm (1.5t ~ 2.25t)	8.3 mm (0.5t)	0.1 ~ 8 mm (0 ~ 0.5t)

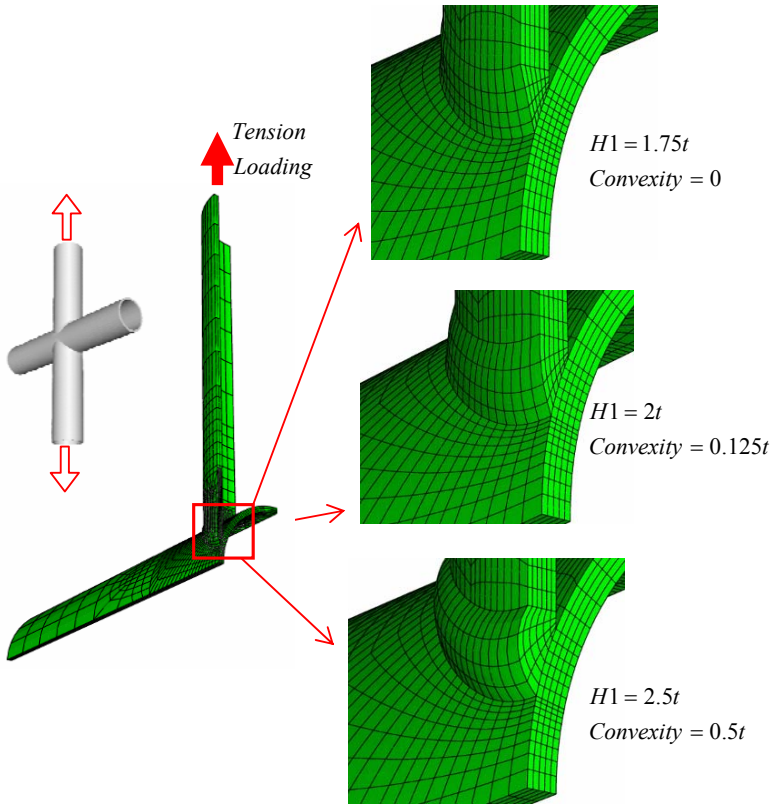

Figure 5.17 Typical FE modeling of X joint, DT3 with β=1, with different weld profiles under brace tension

5.5.2.2 FE results and discussion

The hot spot stress SCFs are calculated according to different definitions as introduced previously and plotted in Figure 5.18. It could be seen that for all SCFs the weld leg length H1 influences the results tremendously with same trend: the shortest leg leads to highest hot spot stress. For ECSC definition, the smallest SCF is 2.63 and the largest is 6.07; the difference is more than 130%. Meanwhile, the influence of convexity is relatively smaller, around 10~15%.

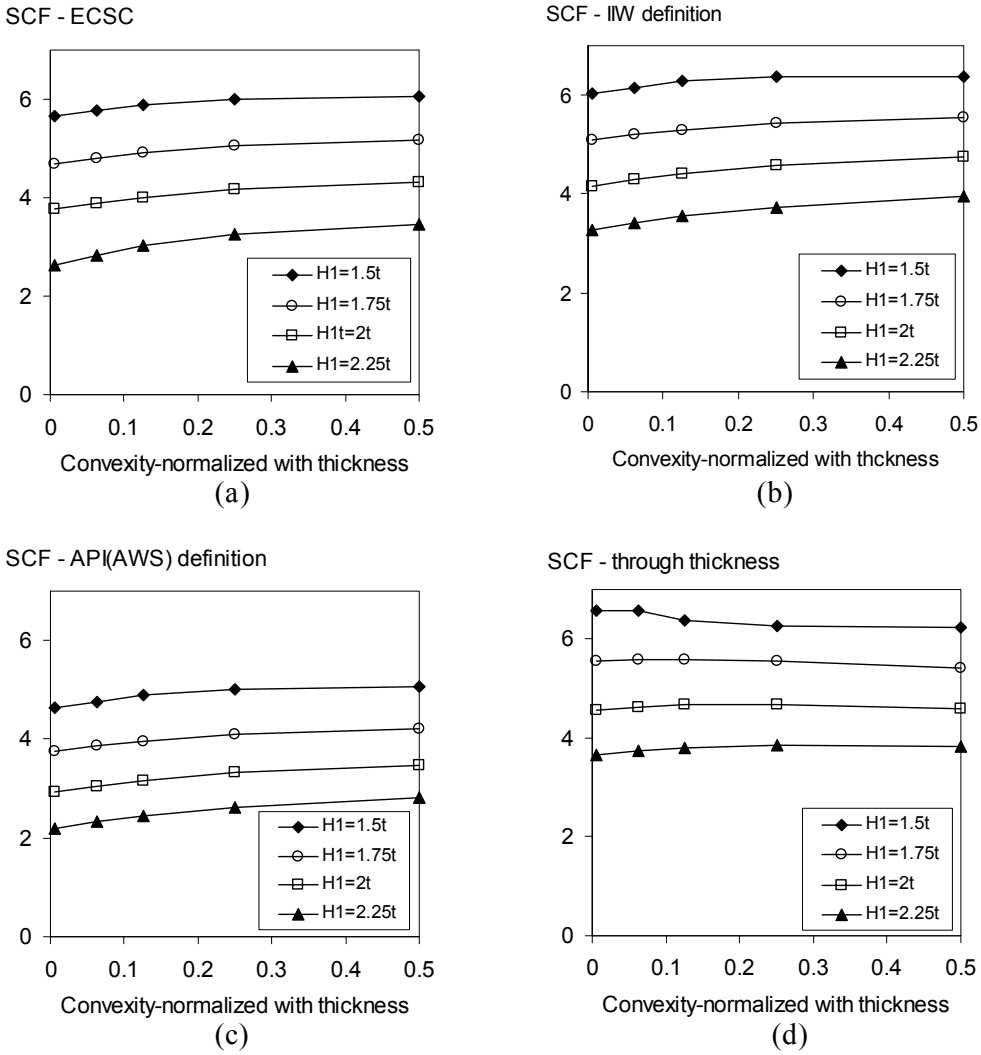

Figure 5.18 Variations of SCFs due to weld geometry for DT3 with β=1 based on different hot spot stress definitions: (a) ECSC geometric stress; (b)IIW; (c)API (AWS); (d) structural stress

Table 5.11 shows the degree of bending stress (DOB) results, which are obtained from linearization of through thickness stress. It can be seen that the DOB was also changing significantly with the variation of the weld leg length, while the change caused by the variation of the convexity is relatively insignificant. On the contrary to the bending stress, the membrane stress is maintained at a constant level as shown Table 5.12. Thus, it can be concluded that the variation of hot spot stress is due to fluctuation of the local bending action, which is varying with different weld leg length. The constant membrane stress may represent the equilibrium from a slightly larger scale, somehow a coincidence to the ring model in determining the ultimate strength.

Table 5.11 Degree of bending (DOB), DT3

H1 \Convexity	0	0.0625t	0.125t	0.25t	0.5t
1.50t	0.56	0.57	0.57	0.58	0.58
1.75t	0.48	0.48	0.49	0.50	0.51
2t	0.36	0.38	0.39	0.40	0.41
2.25t	0.20	0.22	0.24	0.27	0.29

Table 5.12 Normalized membrane stress on the cross section of chord saddle

H1 \Convexity	0	0.0625t	0.125t	0.25t	0.5t
1.50t	2.89	2.85	2.75	2.66	2.60
1.75t	2.91	2.87	2.84	2.76	2.65
2t	2.92	2.89	2.86	2.80	2.70
2.25t	2.92	2.90	2.88	2.82	2.74

Further parametric study of weld leg length has been carried out on the loading case of out-plane bending, Figure 5.19. Similar trend of constant membrane stress was observed as shown in Figure 5.20. As compared with the prediction of Efthymiou formula, the model with weld leg length around 1.75~2 times brace wall thickness generates close results in both loading cases.

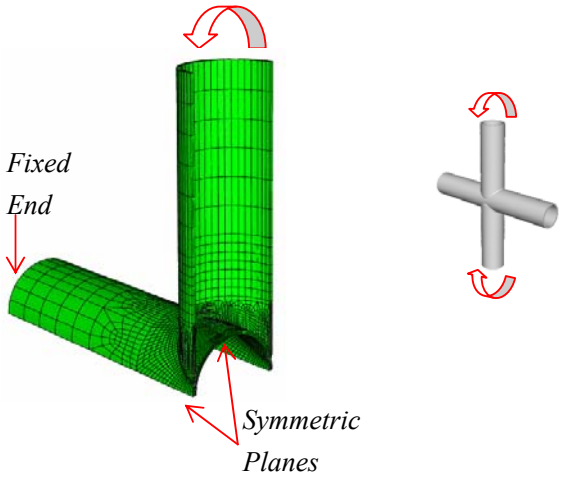

Figure 5.19 Typical FE modeling of DT3 with β=1, under out-plane bending

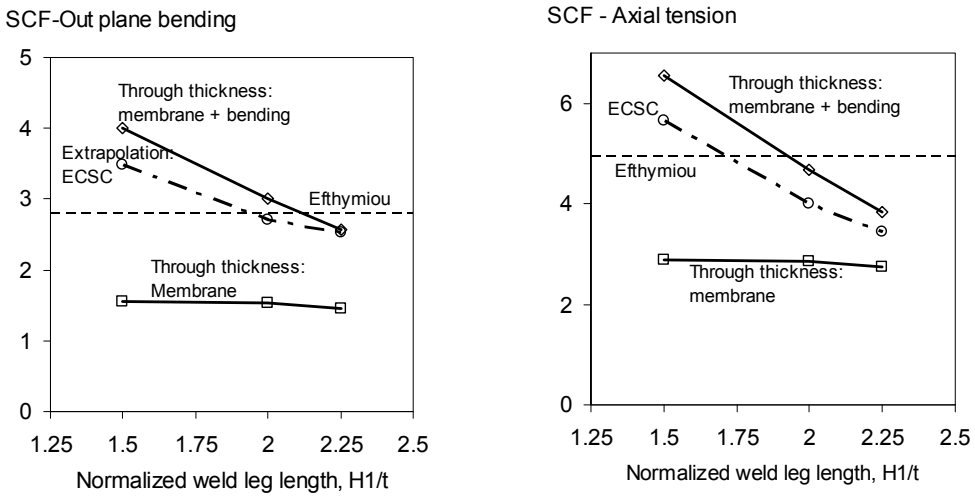

(a) (b)

Figure 5.20 Comparison of SCF results of DT3: similar trend of membrane stress development for out-plane bending and axial tension

At this point, it is felt necessary and interesting to look into the SCF correction due to the variation of weld leg length proposed by Marshall (2005), Eq. (5.8), which is based on Efthymiou formula (ECSC definition):

$$SCF_{corr} = 1 - (H_1 - L\ ) / L_{mp} \qquad (5.8)$$

where: SCF_{corr} is the correction factor applied to Efthymiou SCF

H_1 is the actual weld leg length as shown in Figure 5.2

L is the basic nominal weld leg length, Figure 5.21, which is used by PMBSHELL and Efthymiou to generated formula for SCF computation

L_{mp} is the moment persistence length (from nominal toe to reversal of shell moment, using initial slope), calculated as Eq. (5.9), in which R is the radius of chord.

$$L_{mp} = (0.42 - 0.28\beta)R \qquad (5.9)$$

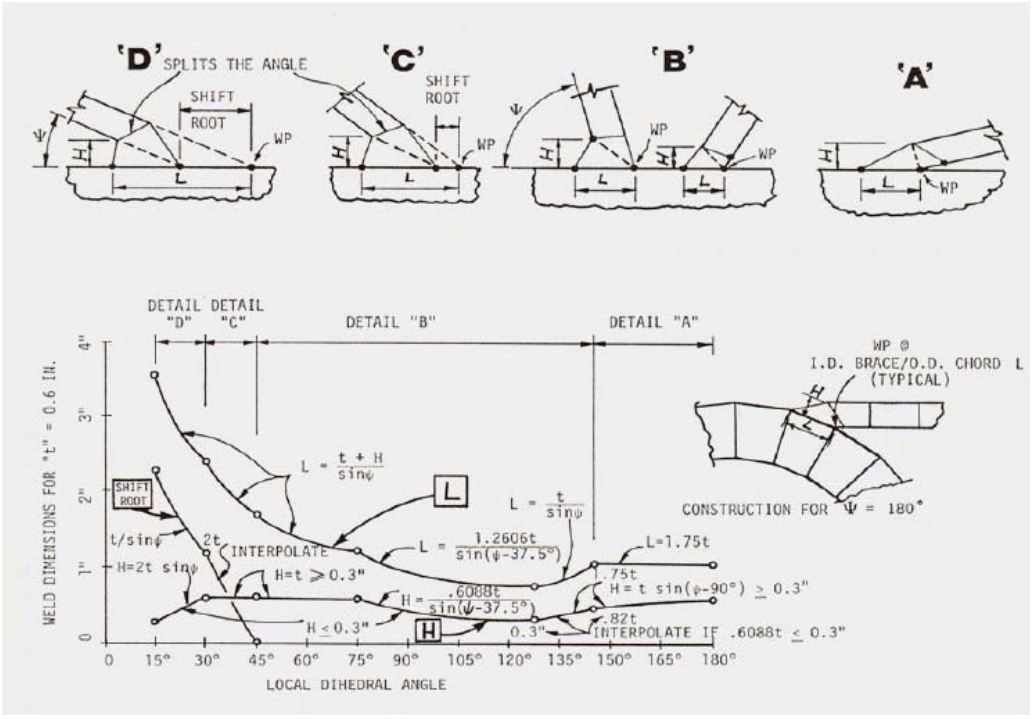

Figure 5.21 Basic nominal weld leg length, extracted from Marshall (2005)

The comparison of the results is shown in Figure 5.22 for the two cases studied. In case-I the agreement is amazingly good, the difference is within 1%. In case-II, the agreement is not that good as case-I but within acceptable range, the difference is around 5% to 15% for axial tension and out of plane bending respectively.

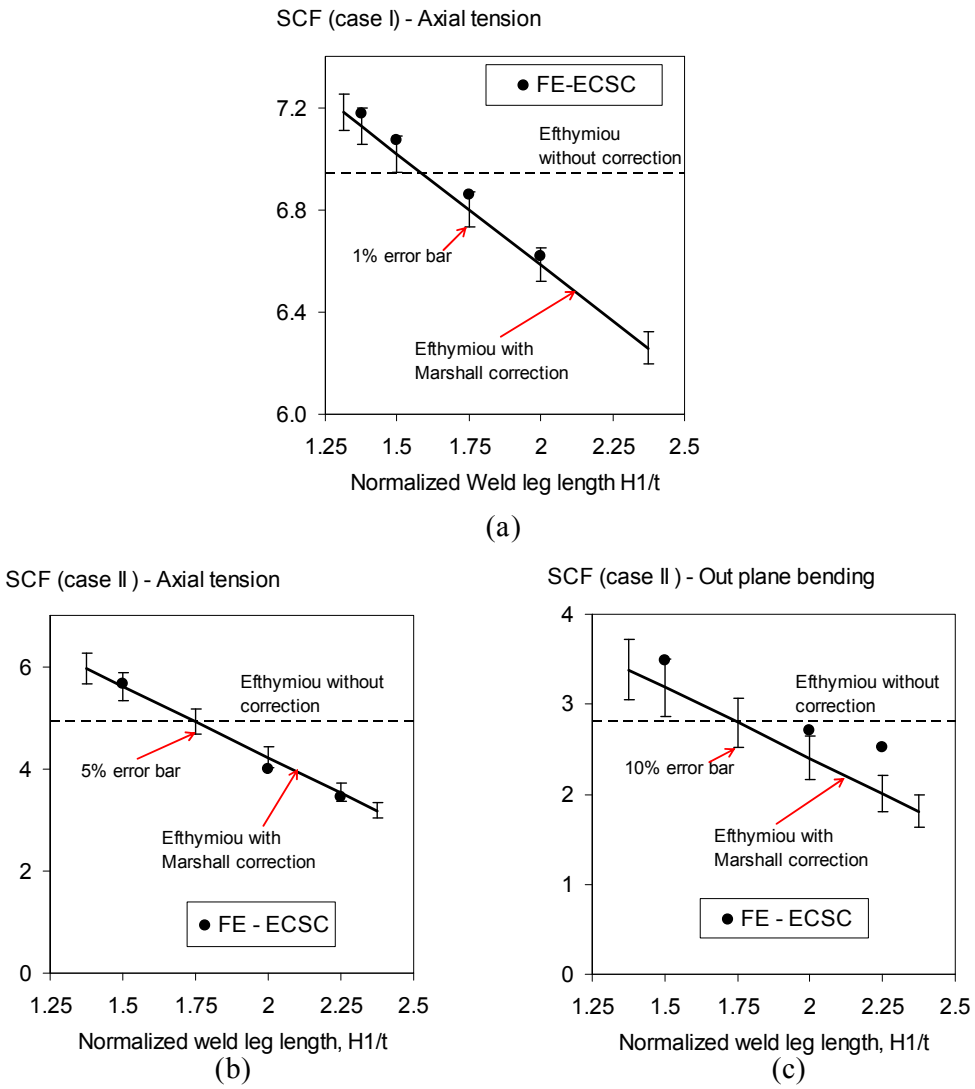

Figure 5.22 Comparison for geometric stress: (a) T joint of case-I under brace tension; (b) X joint of case-II under brace tension; (c) X joint of case-II under out-plane bending

According to Marshall (1992), computer program PMBSHELL, which was used to generate the Efthymiou equations, adopted 3D solid elements to model the weld and curved shell elements to model the chord and brace. The good agreement of case-I demonstrates that for joints with β at mid range, the chord could be reasonably represented by shell. This is consistent with the conclusion of Healy and Buitrago (1994), in which two tubular T-joints with mid β range were studied using PMBSHELL and Abaqus respectively and similar good agreement was also achieved.

However, when the β approaches unity, the stress/strain field for the hot spot region becomes more complex and the influence from weld geometry is more significant, using solid element with convex weld profile is deemed more appropriate. Overall, the SCF results from either FE analysis or the prediction by equations (5.8) and (5.9) sufficiently reflect the fact that increase of weld leg length causes decrease of geometric stress by reducing the bending stress component, supporting the claim by de Back (1987).

5.6 Conclusion

In this chapter, current practice of stress analysis adopted in fatigue design and assessment for tubular joints are reviewed and exercised. Two methods – FE analysis and empirical formula are deployed to determine the hot spot stress SCFs with different definitions. The findings and conclusions can be summarized as:

- For finite element method, the sensitivity caused by mesh size and weld geometry are studied adequately. A suitable smallest element size in the hot spot region is around 20% of the wall thickness is recommended as a rule of thumb. For mid range β, the variation of geometric stress caused by weld leg length is around 10%. But for β=1 joints, the variation can be more than 130%.
- From the FE results, it is seen that the geometric stress (ECSC definition) is not affected by the weld toe notch and the influence from weld geometry is insignificant, while API (AWS) hot spot stress can reflect the weld toe geometric notch effect to a certain degree.
- Comparison between FE results and the prediction using Efthymiou formula with correction factor proposed by Marshall (2005) shows the agreement is fairly satisfactory. The fluctuation of geometric stress is mainly caused by variation of bending stress component, which can be confirmed to be due to

the variation of weld leg length. Meanwhile, the weld bead profile as defined by the parameter convexity would also cause variation of geometric stress, but not so significant as that by weld leg length.

Chapter 6

Reduction of stress concentration of tubular X-joint with chord with fully infilled grout

6.1 Introduction

Similar to the tubular members, tubular joints could also be strengthened by grouting method. Currently there are two grouting schemes available in offshore industry for tubular joints, namely the single skin grouting and the double skin grouting as introduced in Chapter 2. Similar to conventional as-welded tubular joints, the design for grouted tubular joints can be governed by either static strength or fatigue performance. Therefore, the strengthening or enhancement effect of grouted tubular joints should also be evaluated in these two aspects. In this thesis, the fatigue aspect of the single skin (fully infilled) grouted joints is addressed.

6.1.1 Provisions in design codes for fatigue assessment of grouted joints

Current design codes like ISO19902 (BSi, 2007) and RP C-203 (DNV, 2008) have partially covered the design aspects for grouted tubular joints. For fatigue analysis, the codes indicate that it shall be treated as simple joints, implying using the same hot spot stress and S-N curves like T (based on 32 mm chord wall thickness) or T'(based

on 16mm chord wall thickness) for conventional un-grouted joints are applicable for grouted joints also. For hot spot stress SCF calculation using recommended formulae like Efthymiou equations, the chord thickness of grouted joints for γ ratio computation should be the equivalent chord wall thickness, T_e, given by equations (6.1) and (6.2) for single skin and double skin respectively (BSi, 2007).

$$T_e = (5D + 134T)/144 \qquad (6.1)$$

$$T_e = T + 0.45T_p \qquad (6.2)$$

where, T is chord thickness and T_p is thickness of insert pile.

RP C-203 (DNV, 2008) and ISO 19902 (BSi, 2007) indicate that *joints with high β or low γ ratios gain little benefit from grouting. Although fully substantiated evidence is not available, the benefits of grouting should be neglected for joints with β > 0.9 or γ < 12.0, unless documented otherwise. A minimum SCF value of 1.5 is recommended for all locations*. Both codes also mention that the SCF for grouted joints appear load level dependant.

American design code RP2A (API, 2000) does not explicitly provide design guide for grouted tubular joints for fatigue assessment, but implicitly indicates in the commentary part that *the recommended Kellogg formula (empirical formula for hot spot stress SCF calculation) has provision for grouted joints, but caution is needed when applied for grouted joints*. Similarly, this indication implies that the approach of hot spot stress with coupled S-N curve is applicable for grouted joints.

6.1.2 Literature review

Little work has been published with regards to the fatigue behavior of grouted tubular joints. Summaries of some major research programs in the past decades can be found in two references by BOMEL (1995,a) and UEG (1985). It can be seen two kinds of research have been conducted in recent decades for the fatigue assessment of grouted

tubular joints: one is focusing on the reduction of hot spot stress due to the presence of grout in the chord member with static load on the brace, and another is the fatigue tests with cyclic loads on the brace. In addition to the two references, the author conducted literature review based on available documentations. A brief introduction of the review is presented below, some of which can also be found in the two references above.

6.1.2.1 Reduction of hot spot stress SCF

DNV (VERITEIC, 1984) reported measured SCFs for double skin grouted X- and T-joints. As compared with un-grouted joints, the reduction of SCF is significant. It also reported the phenomenon of load dependency of measured SCFs for grouted joints. In some occasions, the initial SCF at very low load is larger than later at higher load level.

Marshall (UEG, 1985) proposed an effective chord wall thickness when calculating the SCF of grouted joints using formula with γ value modified as:

$$T_e = \frac{(T^3 + T_P^3)^{1/2}}{T} \leq 2T \qquad (6.3)$$

UEG (1985) indicated that Tebbett published experimental results about the SCF reduction for grouted joints under tension, compression, in-plane and out-plane bending respectively without detailed data.

MSL (1997) reported the results of a joint industry project on numerical and experimental SCF determinations of 5 grouted T-joints and 7 grouted DT- (X-) joints under in-plane, out-plane bending and axial load. All the joints were single skin (with fully infilled) grouted for the chord member. This was so far the most complete and detailed report in the open publication for single skin grouted joints. Lalani et al (1996), Partiman et al (1997) and Morahan and Lalani (2002) presented the test results respectively with comparisons with FE results. The measured SCFs for all the

joints were quite stable at different load level within elastic range, and no load dependency was observed.

6.1.2.2 Fatigue tests for grouted joints

DNV (VERITEIC, 1984) tested four double skin grouted tubular joints under cyclic loading. In all cases the fatigue lives were beyond the expectation. However, the method of strain gauging is different from current ECSC recommendation, and the load dependency of SCF with its impact for fatigue damage was not clearly explained in the report, so that the fatigue test results were not fully acceptable (BOMEL, 1995,a). Nevertheless, this reference is considered as a research and development proposal, which *summarizes the need for development work in the area of double skin grout reinforced tubular joints and the benefits that can be derived from these joints* (UEG, 1985).

UEG (1985) reported that Billington presented outline details of fatigue tests on DT- (X-) joints carried out as part of the research at Wimpey. It stated that the fatigue lives of grouted joints fell on the safe side of the appropriate S-N curve, and would appear that normal S-N curves for as-weld tubular joints could be used as a design basis for grouted joints with reduced SCF. Unfortunately, no further details of the tests could be found.

Marshall (1992) presented the results for the fatigue tests of double skin grouted K-joints. Both tension and compression loads were applied in measuring the hot spot stress SCF; the reduction of SCF under compression was more significant than under tension. Fatigue test results expressed in terms of hot spot stress range for grouted joints were within the same scatter band as the un-grouted joints, used for generating AWS X curve. The results support the recommendation of design code that the same X curve can be used for grouted joints.

Baker Jardine (HSE, 1993) reported experimental measurement for SCFs of two repaired and single skin grouted tubular T-joints with β=0.5 and γ=14.28 under axial, in-plane and out-plane bending. The joints later underwent fatigue test of axial loading to failure. In contrast with the fatigue test results presented above, the fatigue lives were below the mean value of S-N T curve of 32mm thickness, inconsistent with the recommendations of the design codes.

6.1.3 Summary of Literature Review

Through literature review it can be seen that the proof is insufficient to support the claim that same S-N curve is applicable for both conventional un-stiffened and grouted tubular joints. Hence, it is not surprising that the provisions and coverage in current design codes for grouted joints are not comprehensive. Furthermore, there are a few unanswered questions with regards to the application of hot spot stress S-N approach to grouted joints:

- The reduction and redistribution of hot spot stress/strain of grouted tubular joints; and
- The thickness effect for grouted joints - a critical adjustment for the predicted fatigue life using hot spot stress S-N approach.

Therefore, it is crucial to further investigate the fatigue performance of grouted tubular joints to refine the design recommendation, and then the grouting method can be applied in practice with more confidence.

6.2 Research on grouted tubular joints in NUS

Since 2006, series of test programs, listed as follows and shown in Figure 6.1, for grouted tubular joints have been initiated and planned in NUS: The first two items were completed at the completion of this thesis.

- Static test of single skin grouted X-joints subjected to in-plane bending.

- Static tests of both single skin and double skin grouted X-joints subjected to axial tension and compression;
- Fatigue tests of single skin grouted X-joints subjected to axial tension and compression.

(a) (b)

Figure 6.1 Research for grouted tubular joints conducted in NUS: (a) grouting the cross joint; (b) in-plane bending test

The main purpose of static tests is to observe the behavior of grouted joints subjected to static brace loading, and understand the interaction mechanism between the grout and the steel chord member. For fatigue analysis, the study begins with the application of hot spot stress. Accurate estimation of hot spot stress is decisive for an appropriate fatigue design. It was found the predicted SCF_g by means of equivalent thickness method with Efthymiou equation was inaccurate as compared with experimental measurement. It was expected that through the comparison of measured hot spot stress SCF with FE SCF, the FE model can be calibrated, so that parametric study using FE models can be conducted. The reduction and redistribution of stress of hot spot region due to the presence of grout in the chord can be studied using FE calibrated models.

The following Section 6.3 reports the details of measuring the hot spot strain/stress during the static tests, and Section 6.4 reports the subsequent parametric study to generate design curves for hot spot stress reduction factors for X-joints.

6.3 Experimental investigation for hot spot stress of X-joints with grout-infilled chord subjected to in-plane bending

6.3.1 Specimens and test set-up

Two pairs of X-joints, with grouted and as-welded condition as reference, and with the geometric parameters given in Table 6.1 were tested in the Structural Engineering Laboratory of NUS using 1000 tonne Instron test rig. The test rig set-up is shown in Figure 6.1 (b). Displacement controlled static load were applied to the specimens as shown in Figure 6.1 (b) to failure. In linear elastic stage, hot spot strain was measured and hot spot stress SCFs were derived based on measurement. Comparison was done to find the reduction factor for the joint in as-welded and grouted conditions.

Table 6.1 Parameters for the X joints tested under in-plane bending

	X-joint configuration, all the dimensions are in mm, f_y =240 MPa									Grout property	
Specimen	D	d	T	t	β	γ	τ	L	l	E (GPa)	strength (MPa)
X1	508	406	15.9	22	0.8	15.97	1.38	2500	1600	no fill	no fill
X1-G	508	406	15.9	22	0.8	15.97	1.38	2500	1600	70	210
X2	406	406	22	22	1	9.23	1	2500	1600	no fill	no fill
X2-G	406	406	22	22	1	9.23	1	2500	1600	70	210

The grout material indicated in Table 6.1 is Densit's Ducorit D4. The specimens were made by external contractor and the casting was done in the Structural Engineering Laboratory of NUS. The grouted specimens were cast in vertical stand-up position, and were initially flooded with water to simulate the flooding condition

before casting. The water was displaced out from top when the grout was pumped from the inlet at bottom as shown in. Figure 6.1 (a). The grouted specimens were cured more than 28 days before testing.

Based on preliminary FE analysis, normal stress - the surface stress perpendicular to the weld toe, was considered as more reasonable than maximum principal stress for hot spot stress calculation. Strip gauge, as shown in Figure 6.2 (a), was adopted for hot spot strain measurement. The strain gauge positions are illustrated in Figure 6.2 (b) (c), in which the angle between the paths is based on the projection on the plane at the center of chord member. A total of eight extrapolation paths around the brace-chord intersection were adopted for measuring the hot spot strain. Paths 1 to 6 are on the chord and paths 7 to 8 are on the brace. Each path has 2 strip gauges, with each strip gauge consisting of five 1 mm long single gauges spaced 2mm apart, Figure 6.2.

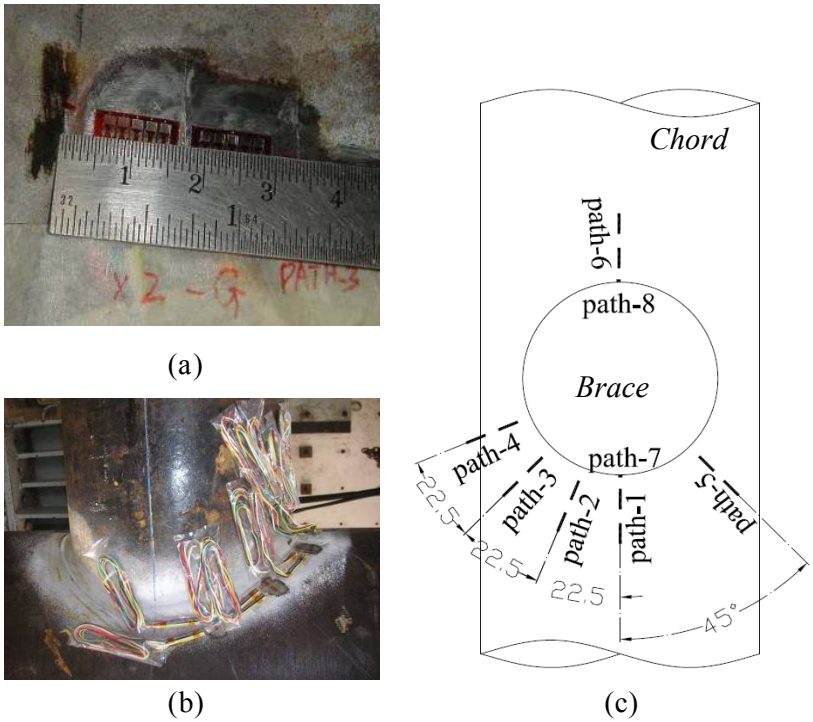

Figure 6.2 Strain gauges for X joints tested in NUS under in-plane bending (a) 1mm strip gauge used; (b) over view of strain gauges at hot spot region; (c) notation for extrapolation path

To be compatible with ISO 19902 (BSi, 2007), the ECSC approach was decided to apply in the experiment. It is noted that ISO 19902 (BSi, 2007) does not specify the extrapolation positions for the path in between the crown and saddle positions; and for in-plane bending, the largest hot spot stress may occur at intermediate positions. In this investigation, for intermediate paths the second extrapolation positions are determined by interpolation between the crown and saddle, as indicated in Table 6.2.

Table 6.2 Distance of extrapolation points away from weld toe (mm)

	path-1,chord crown		path-2, chord, 22.5^0		pathe-3,chord, 45^0		path-4,chord, 67.5^0	
Specimen	1^{st}point	2^{nd} point	1^{st} point	2^{nd} point	1^{st}point	2^{nd} point	1^{st} point	2^{nd} point
X1/X1-G	13.4	26.1	13.4	25.1	13.4	24.1	13.4	23.1
X2/X2-G	13.4	26.7	13.4	24.5	13.4	22.2	13.4	20.0

6.3.2 Test procedures

All specimens underwent two rounds of pre-loads before they were loaded to failure. The pre-load level was judged based on the occurrence of first yield of the strain gauge reading closest to the weld toe. Loading rate was kept at 0.2 mm/minute for a full static load test. The strain gauge readings were recorded every 30 seconds. The hot spot strain measured in all three rounds showed stable and consistent slope in linear elastic range, so that no further shake down pre-load cycle was performed due to tight testing schedule.

6.3.3 Experimental results

As mentioned above, for all the 4 specimens, the gradient of strain gauge readings of pre-load and final full-load showed no significant difference within linear elastic range, except that the yield point changed, which was always slightly above the previous round of pre-load level. Typical strain recordings are shown in Figure 6.16 (b). According to the discussion in Chapter 5, hot spot stress is basically a linear

elastic stress concept. The determination of hot spot stress and corresponding stress concentration factor (SCF) needs to be conducted within the elastic range. Presented below are some selected indicative data extracted from the test result database and plotted in different combinations for comparison.

6.3.3.1 Linearity check by strain measurement

In Figure 6.3 some strain gauge readings versus the global loads are plotted. It was observed that the yield point appears at load level of 140KN for X1, 150KN for X1-G, 180KN for X2, and 190KN for X2-G respectively. The development of local strain in grouted specimens is similar to that of un-grouted specimens, consistent with the FEA results as shown in Figure 6.12. The non-linearity due to the contact action between the infilled grout and chord is insignificant.

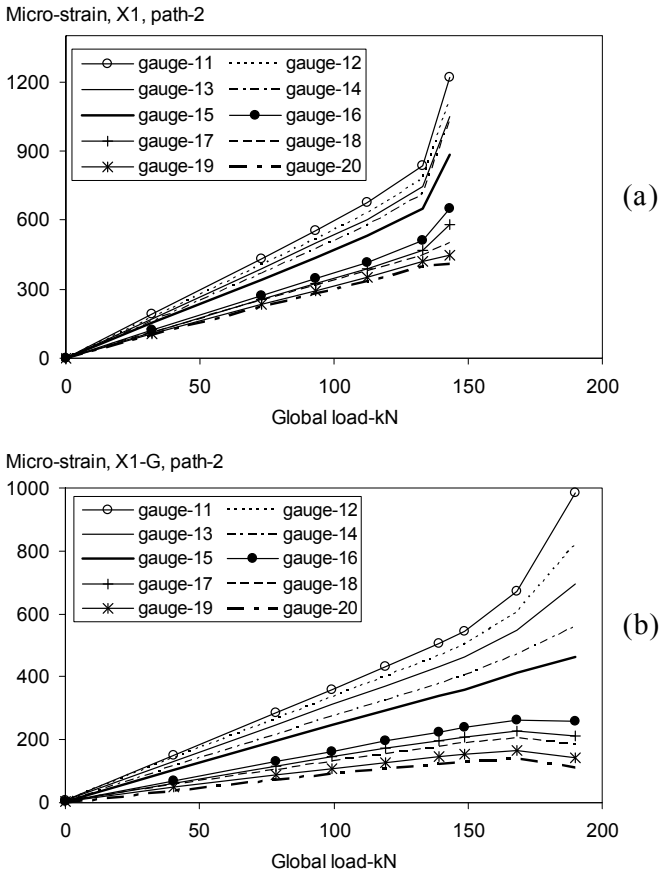

Figure 6.3 to be continued

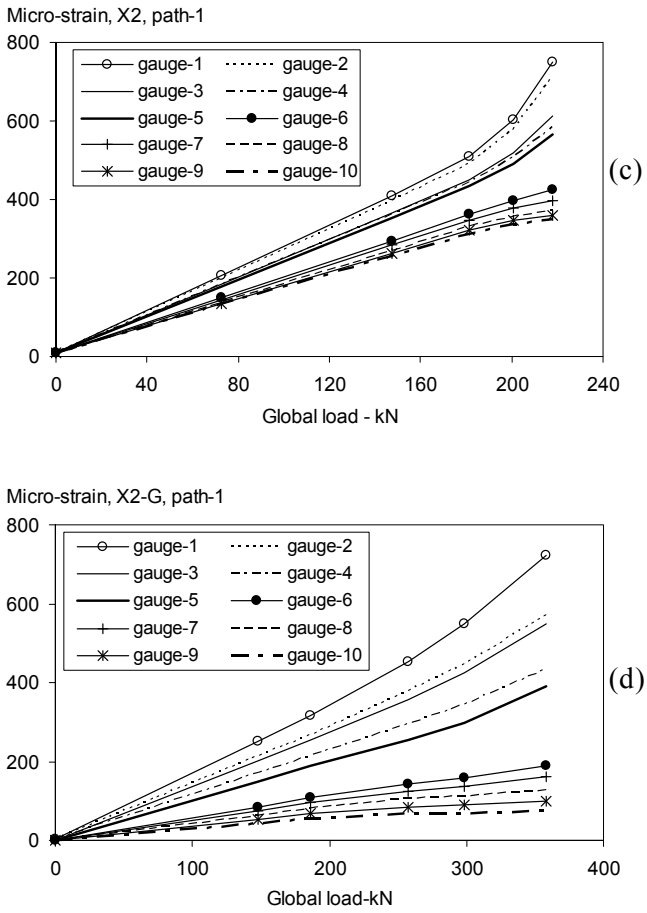

Figure 6.3 Linearity check for (a) X1, path-2; (b) X1-G, path-2; (c) X2, path-1; (d) X2-G, path-2

6.3.3.2 Symmetry check by strain measurement

To check the symmetry of test condition, path-3 and path-5 were put on the symmetric locations with each other. The readings at the same load level are plotted in Figure 6.4 together with FEA results for comparison. For X1-G, path-11 is the additional path on the chord at 45 degree. It can be observed that the overall symmetry of the test condition was satisfactory, and also in close agreement with FEA results.

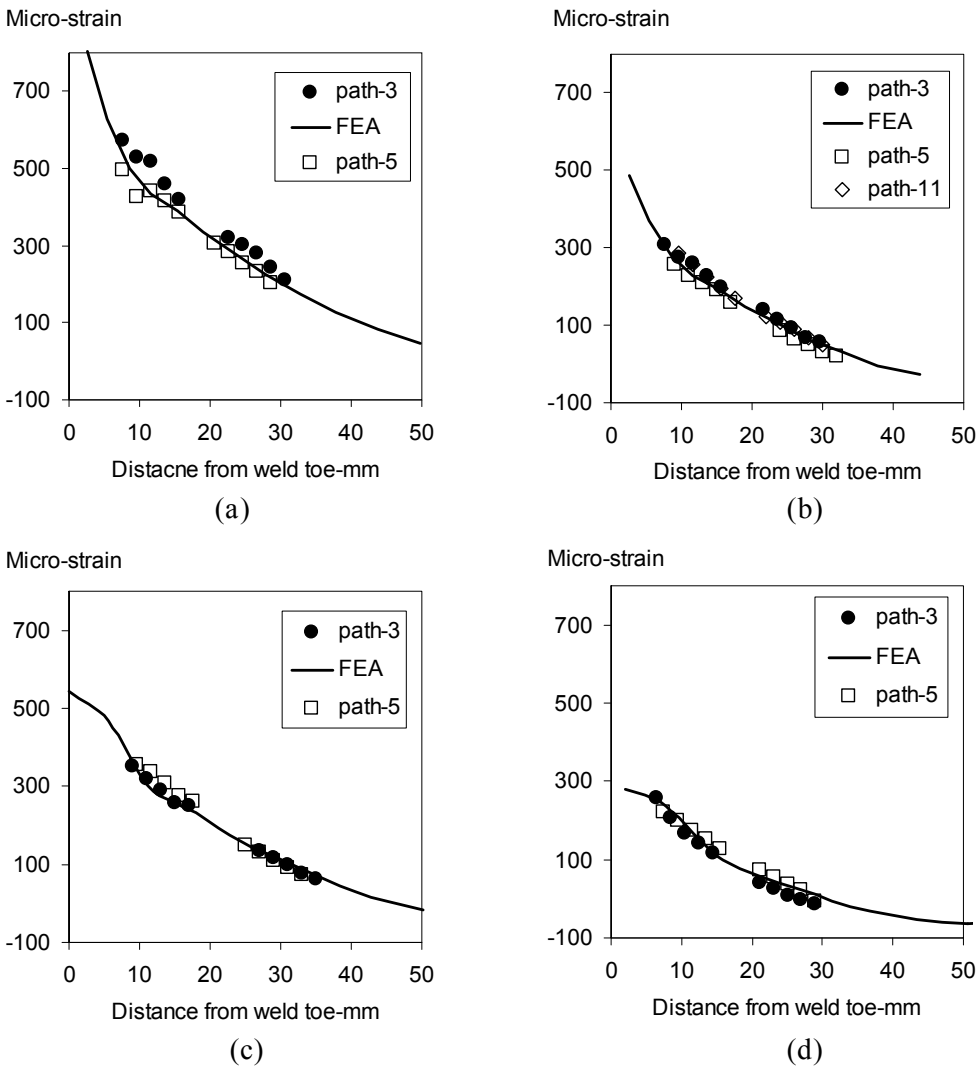

Figure 6.4 Comparison of normal strain measurement for the path at 45^0: (a) X1; (b)X1-G; (c)X2; (d)X2-G

6.3.3.3 Load dependency check for measured SNCF

The hot spot strain is obtained through linear extrapolation following ECSC approach as introduced in Chapter 5. The strain concentration factor SNCF is the ratio between hot spot strain and nominal strain, which is calculated using nominal stress divided by Young's modulus. The measured SNCF for the 4 specimens at different load levels are shown in Table 6.3. It could be seen that the load dependency of SNCF is insignificant. There is very minor increasing trend of measured SNCF with the rising of load level for both un-grouted and grouted joints. This is postulated to be due to

undue release of residual stress: insufficient shake down cycles performed, leading to early occurrence of yield as discussed later. In Table 6.3 the bolder numbers are selected for conversion to SCFs.

Table 6.3 Measured SNCFs

Specimen	load level - kN	SNCF			
		path-1,chord crown, 0 degree	path-2, chord, 22.5 degree	path-3,chord, 45 degree	path-4,chord 67.5 degree
X1	85	3.45	3.57	3.66	2.96
	105.1	**3.60**	**3.74**	**3.79**	**3.02**
	124.2	3.73	3.86	3.91	3.05
	FEA	3.87	3.87	3.87	2.38
X1G	83.6	2.48	2.60	2.19	1.33
	124.2	**2.53**	**2.64**	**2.20**	**1.36**
	153.9	2.59	2.67	2.24	1.38
	FEA	2.35	2.48	2.11	1.22
X2	72.6	1.90	1.96	1.99	1.63
	147.6	**1.86**	**1.94**	**1.94**	**1.57**
	181.3	1.87	1.95	1.95	1.57
	FEA	1.70	1.88	1.91	1.68
X2G	97.3	1.05	1.34	0.90	0.24
	186.6	**1.06**	**1.35**	**0.89**	**0.22**
	257.8	1.07	1.56	0.91	0.23
	FEA	1.01	1.22	0.82	0.41

6.3.4 Finite element analysis

6.3.4.1 Modeling

The finite element models were constructed according to the geometric dimensions shown in Table 6.1. Certain parametric study was performed for the variation of weld profile. It was confirmed again that the SCF results is sensitive to the weld leg length. The model with closest dimensions to actual weld profile generates best simulation result. 20-noded 3-D solid element with reduced integration (C3D20R) was used for

the steel section and weld. Both 20-noded and 8-noded 3-D solid elements with reduced integration (C3D20R and C3D8R) were used for the in-filled grout for contact sensitive study. For steel and weld, the same elastic and plastic material property was specified, with Young's modulus E_s=205000 MPa, yield stress f_y=240 MPa and Poisson's ratio=0.3. For grout, elastic material property was specified, with Young's modulus E_g=70000 MPa and Poisson's ratio= 0.19. Due to symmetry, only quarter model is built, as shown in Figure 6.5. Weld profile was according to the measurement of actual specimen.

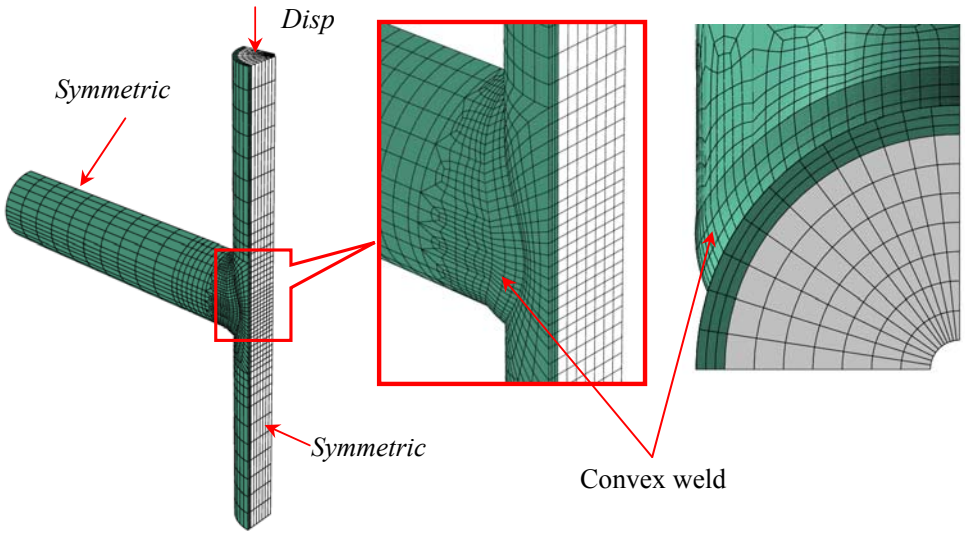

Figure 6.5 Boundary conditions and quarter model for in-plane bending for X2G: convex weld profile, weld leg length=1.69t, convexity=2mm

Through preliminary analysis it was found the stress level the grout had experienced was lower than the nominal yield stress, hence the grout can be set as linear elastic material in FE analysis for hot spot stress computation for the efficiency of computation. The finding was confirmed by the inspection of open-up specimens after tests as shown in Figure 6.6, the open-up of X1-G. It can be seen that no sign of crushing for the grout; and also no visible gap in between: the grout was tightly fit into the chord, indicating good casting quality achieved and insignificant grout

shrinkage occurred in such a confined environment. The only gap found was due to pull-out action of in-plane bending. The situation is similar to those in Chapter 4 for the grouted tubular member.

Figure 6.6 Open-up of the grouted specimen after test

Based on the understanding as discussed in Chapter 4 that the adhesive bonding effect on the interface between D4 grout and steel is insignificant, and the interaction specified as 'surface-to-surface hard contact' in Abaqus is deemed appropriate for grouted tubular joints. The internal surface of the chord is assigned as 'master surface' and the surface of the grout is assigned as 'slave surface' for specifying the contact pair. Small sliding and small deformation were assumed.

6.3.4.2 Sensitivity study for FE analysis

It was found in preliminary FE analysis that the hot spot stress SCF results were sensitive to the mesh configuration of grout due to the contact analysis. This is because the accuracy of FEA solution for contact problem is relying on the computation of contact traction on the contacted surfaces. The contact traction can be resolved into contact pressure in normal direction and frictional shear in the tangential

direction. The frictional shear is calculated based on Coulomb's law as introduced in Chapters 3, Eq. (3.2), by multiplying the frictional coefficient to the contact pressure. Hence, the accuracy of contact pressure determines the accuracy of contact traction. In Abaqus, the contact pressure is calculated according to the gap between the contact surfaces. Whether the gap is open or closed initially is judged by the distance between the nodes of each contact pair on the contact surfaces. This judgment relies on the functions of auto searching and forming contact pairs, and will be influenced by the difference in mesh configuration of the contact surfaces as indicated in Abaqus manual (SIMULIA, 2007). The best mesh scheme is to have two identical meshes for the contacted surfaces - the so called matching mesh as used in Chapters 3 and 4, so that the searching and forming contact pair is with best precision and the initial distance judgment is almost exact.

It was also noted that Abaqus (SIMULIA, 2007) provides three numerical algorithms for enforcing the constraint function in normal direction namely direct method, augmented Largrangian method and penalty method. By comparing the same mesh configuration with the three algorithms, it was found that the differences of SCF results were insignificant: smaller than 0.5%. Direct method with the best accuracy as indicated in Abaqus manual with related calibration is the default selection, and augmented Largrange method provides better convergence. In this study, when direct method sometimes encountered non-convergence, especially for large γ ratio for β=1 joints during parametric study, the algorithm was changed to augmented Largrange method.

For hot spot stress computation, it is not expected but without surprise to find that the SCF results are sensitive to the different grout mesh scheme, because the contact zone with high contact pressure was near or inside hot spot region. So the sensitivity

study was carried out. The intention was to firstly eliminate the sensitivity induced by mesh configuration, and then study the influence from variation of material properties, so that the optimized FE model can be decided and calibrated with test results for further parametric study.

Sensitivities of grout mesh configuration and shrinkage gap

The mesh scheme for the steel tubular joint follows the recommendation in Chapter 5 for hot spot stress computation. Three layer solid quadratic elements with minimum size about 20% of chord thickness at weld toe were used for the chord, which means the grout also need to adopt solid quadratic element for forming matching mesh. The matching mesh for grout is generated using the sweep function in software Patran. The sweep is done based on the same surface mesh as for the chord. In order to avoid irregularly shaped or distorted elements, the central core of the grout is removed. The removed volume is small, equivalent to about 1% of total infilled grout, and is believed not to marginal change in stiffness. Typical match meshes are shown in Figure 6.7 (b).

However, it was found for contact analysis using quadratic element meshes that the computation is very expensive, typical running time for an analysis using HP work station 6200 with 4G RAM is over 6 hours. Therefore, the mesh for grout was tested with dense linear element mesh. Extensive analyses of different mesh schemes were performed on the model of X2G. Three typical cases listed in Table 6.4 are selected to present the mesh sensitivity results, and the mesh schemes are shown in Figure 6.7.

In addition to mesh scheme, it was found grout shrinkage will also cause unstable SNCF/SCF results, leading to load dependency phenomenon. In order to differentiate these two different sources of sensitivities - one is the numerical sensitivity and the other is physical sensitivity, more cases with intentionally built gaps as shown in

Figure 6.8 were analyzed. Listed in Table 6.4 are 3 typical cases selected to present the SCF results by FE simulation. In Table 6.4, the first three cases, case-1 to case-3, are for numerical sensitivity study for grout mesh configuration, while the last three cases, case-3 to case-5, are for physically shrinkage gap sensitivity study. In all the cases in Table 6.4 the mesh for steel joint was kept the same.

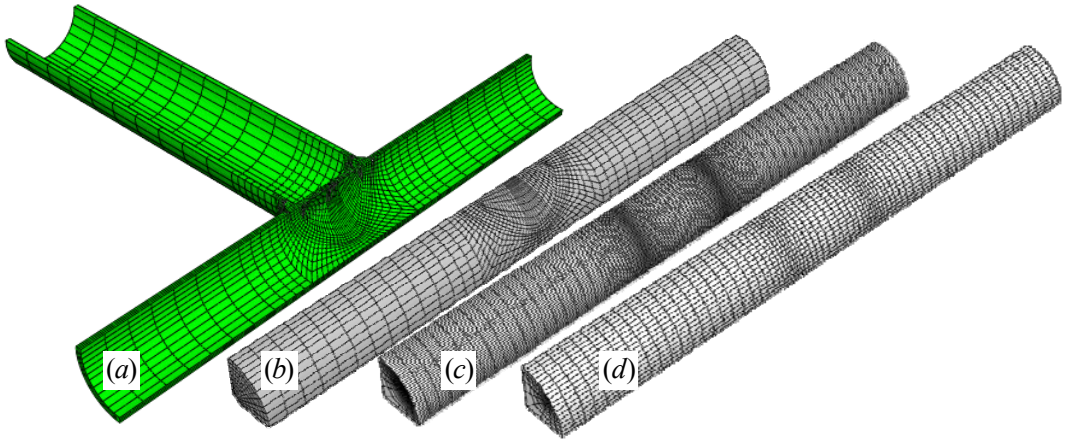

Figure 6.7 Mesh schemes used for sensitivity study for X2G: (a) steel joint; (b) grout using matching mesh, quadratic elements; (c) grout using dense unmatched mesh, linear elements; (d) grout using medium unmatched mesh, linear elements

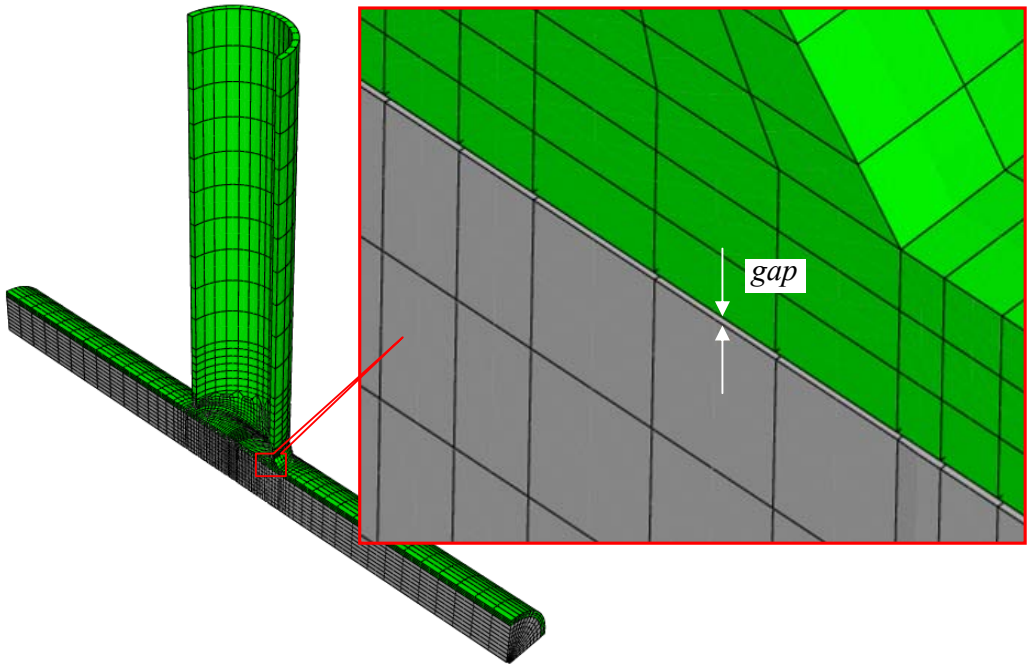

Figure 6.8 Modeling of the shrinkage gap between grout and internal surface of chord

Table 6.4 Cases of sensitivity study for X2G

	case-1	**case-2**	**case-3**	**case-4**	**case-5**
Grout mesh	Dissimilar medium mesh for grout, linear solid element; physically no gap initially	Dissimilar dense mesh for grout, linear solid element; physically no gap initially	Matching mesh for grout, quadratic element, physically no gap initially	Matching mesh for grout, quadratic element, 0.1 mm gap initially	Matching mesh for grout, quadratic element, 1 mm gap initially

Figure 6.9 shows the FE SNCFs at chord crown, path-1, versus applied load. The test results are also plotted for comparison. The extrapolation of SNCF followed ECSC definition. From Figure 6.9 it can be seen that case-3 is in close agreement with the test result. In Figure 6.9 (a) for first three cases, the dissimilar mesh causes the contact action progressively to effect. This is because the contact pressure is calculated based on the gap distance between the nodes of contact pairs, and the dissimilar mesh caused inexact judgment of the distance despite the geometry used to build mesh is without gap. Dense mesh improves the result slightly, but matching mesh solves the problem completely. For the second three cases, as shown in Figure 6.9 (b), it is quite obvious that the gap size has its influence on calculated result, when the gap is one millimeter almost no contact effect was triggered. With a small 0.1 mm gap, the load dependency is caught by simulation with significance.

Similar sensitivity study was also performed on X1G, and similar FE results were obtained that the SCF/SNCF result is sensitive to the grout mesh and the gap size. Compared with test result, it is with confidence to conclude that there is no shrinkage gap for the specimen tested. It is also found that for FE study the generated mesh needs high accuracy for the coordinates of nodes. The minimum accuracy is at least 0.01mm for the nodes on the contact surfaces for an appropriate representation of curved surface for gap size calculation.

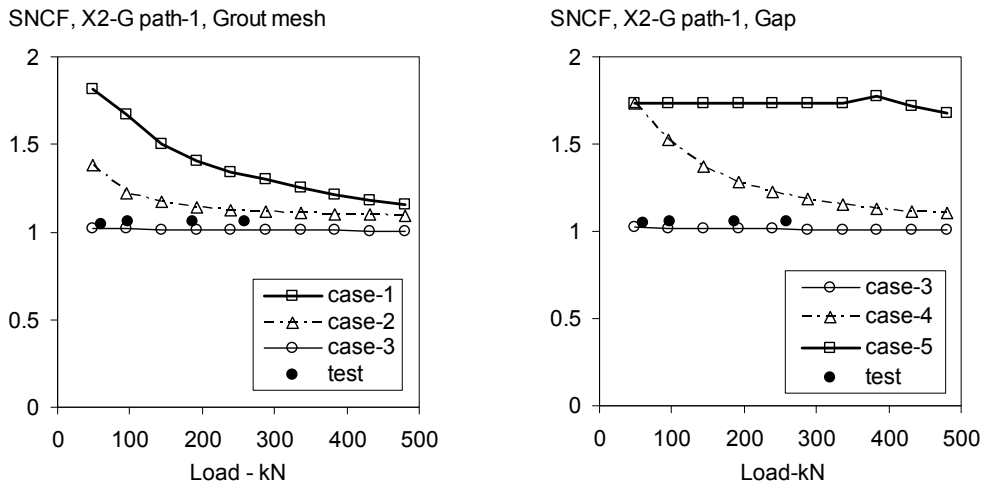

(a) (b)

Figure 6.9 Comparison of strain concentration factors (SNCF) for sensitivity study due to contact effect: (a) sensitivity due to different grout mesh scheme; (b) sensitivity due to different gap magnitude assigned between grout and internal surface of steel chord

Sensitivity of grout material property

The next sensitivity study was performed on two other concerned material parameters: the frictional coefficient μ and the Young's modulus of grout. By using the same mesh scheme as case-3, the two parameters are varied as shown in Table 6.5 to simulate different grout materials that could possibly be used.

The computed SNCFs at chord crown are plotted in Figure 6.10. It could be seen that the influences of frictional coefficient and elastic modulus are insignificant. The fluctuation caused by frictional coefficient is within 3% and the variation induced by Young's modulus is around 10%. The result shows high strength D4 grout could be replaced by slightly lower grade S5 or even normal grade 40 concrete if shrinkage (creep) performance of S5 and G40 is similar to D4.

Table 6.5 Cases of different friction coefficients and Young modulus for X2G

	case-6	**case -7**	**case -8**	**case -9**
Grout property	Matching mesh, no initial gap. **μ=0, E=70GPa (grout D4)**	Matching mesh, no initial gap. **μ=0.6, E=70GPa (grout D4)**	Matching mesh, no initial gap. **μ=0.3, E=42GPa (grout S5)**	Matching mesh, no initial gap. **μ=0.3, E=30GPa(G40 concrete)**

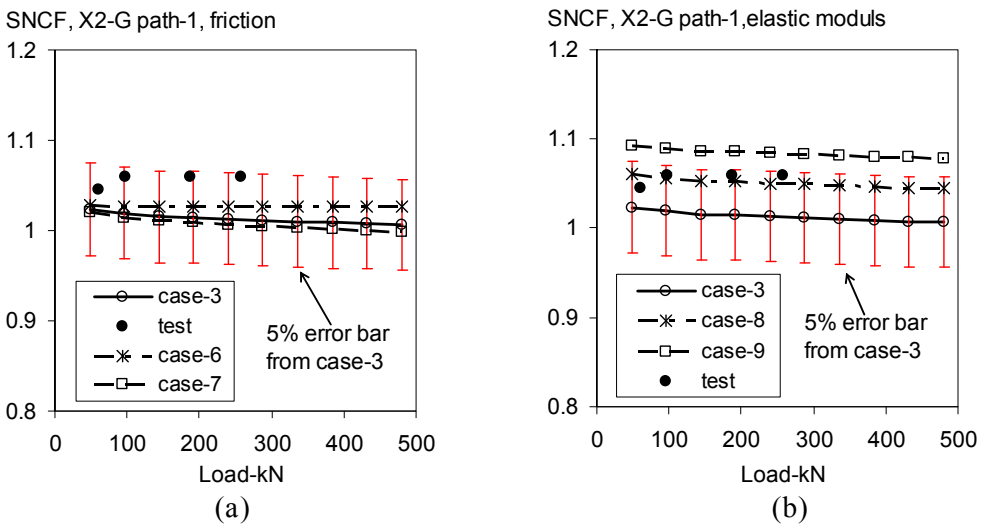

Figure 6.10 Sensitivity study for X2G with different grout material: (a) different friction coefficients; (b) different Young's modulus

From the results of sensitivity study as shown, it is found case-3 is close to the real situation, and this model is selected for further comparison with results of experimental measurement and in un-grouted conditions for FE model calibration and SCF reduction factor. More result comparisons are reported as follows.

6.3.4.3 Calibration of FE models

Typical stress contour plots for the two pairs of X joints are shown in Figure 6.11. The largest stress occurred in between the chord and saddle for in-plane bending. In grouted condition, the hot spot is slightly shifted to the chord crown for X2G.

Figure 6.12 and Figure 6.13 show the surface tensile stress distribution along the extrapolation path-1. Note that although ISO19902 (BSi, 2007) recommend maximum principal stress for geometric stress computation, but the normal stress seems suitable for hot spot stress extrapolation for grouted joints. It could be seen that for hot spot locations at chord crown and saddle, the un-grouted joints have maximum principal stress coinciding exactly with the normal stress on the extrapolation path. However, for grouted joints the maximum stress change direction within the hot spot region due to the constraints effect to the chord ovalization provided by infilled grout. For both

grouted joints, the direction of maximum principal deviates from the initial direction, as the distance further away from the weld toe As shown in Figure 6.12 and Figure 6.13, for the second extrapolation point, it is the mid principal stress that coincides with the normal stress. In experimental measurement, the direction of maximum principal stress needs to be checked for extrapolation, otherwise un-conservative extrapolation SCF will be generated if just using the maximum principal stress of rosette gauge.

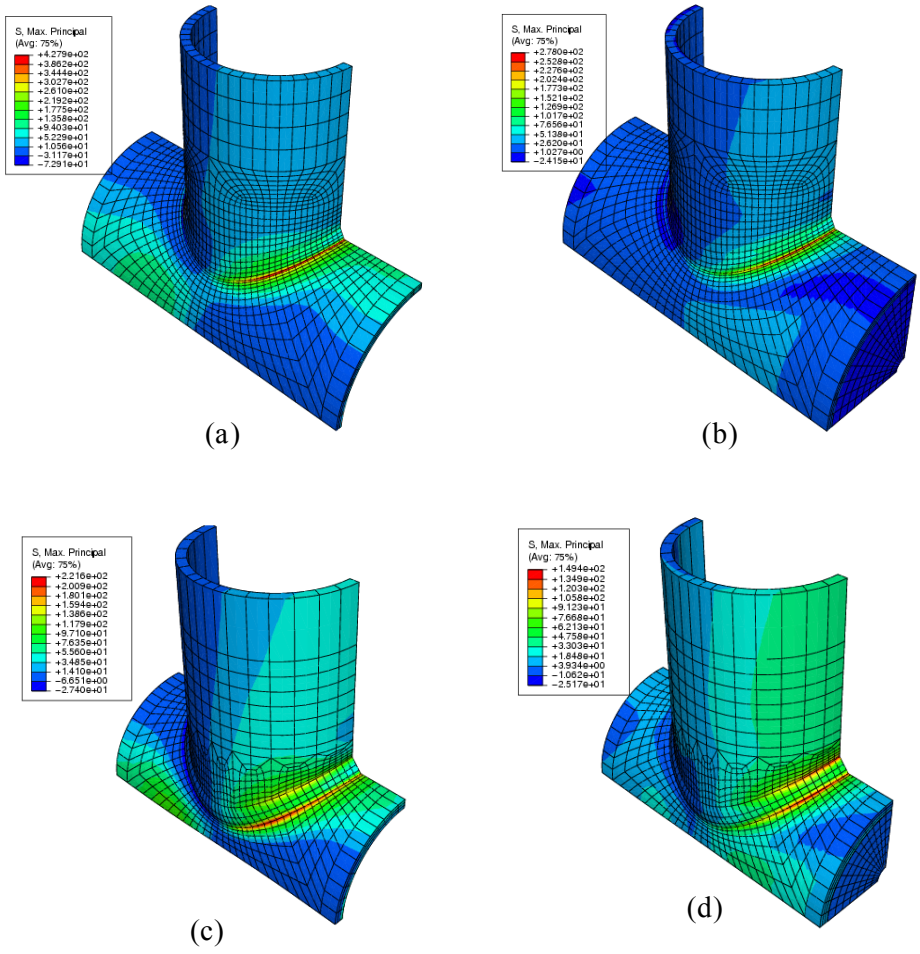

Figure 6.11 Stress contour plots, tensile stress, load=192kN, (a) X1; (b) X1G; (c) X2; (d) X2G

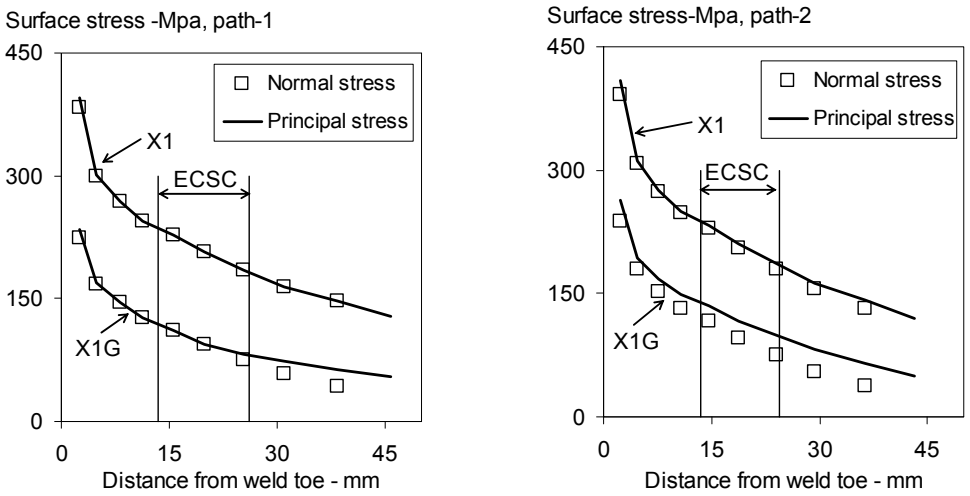

Figure 6.12 Surface stress distribution along extrapolation path for X1 and X1-G, load =192 kN: (a) path-1, chord crown; (b) path-2, intermediary, 22.5^0

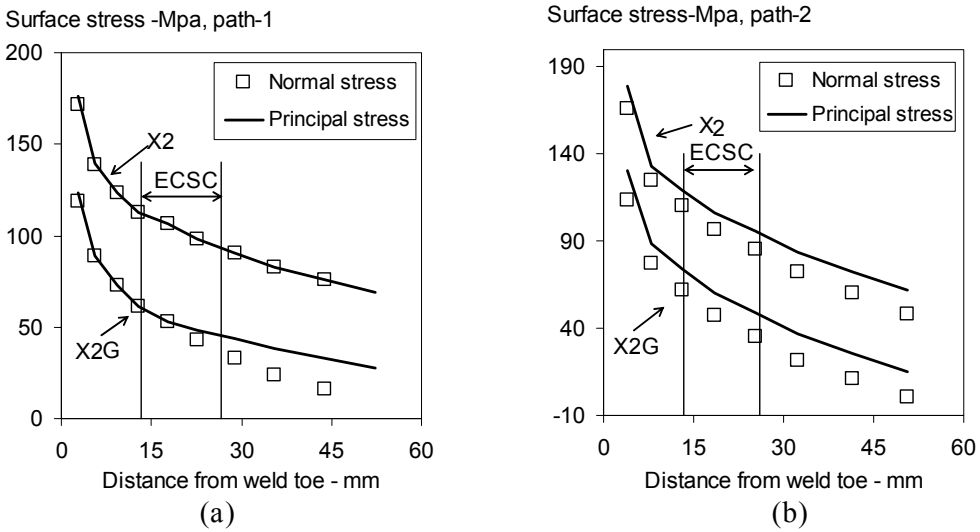

Figure 6.13 Surface stress distribution along extrapolation path for X2 and X2-G, load=192kN: (a) path-1, chord crown; (b) path-2, intermediary, 22.5^0

For the intermediate extrapolation path, the maximum principal stress is changing direction, so that the maximum principal stress at two extrapolation points should not be used directly for extrapolation. If the six components of the Cauchy stress are extrapolated and then combined to determine the maximum principal stress as specified in the ISO 19902 (BSi, 2007), the procedure is only suitable for finite element method, but not applicable for experimental measuring using Rosette strain

gauge. The normal stress, in this case, can be applied, and is consistent with the fracture mechanics analysis for mode I dominating fatigue cracking.

In reality, the structure is subjected to combined loading cases, and the normal stress can be superimposed logically. However, usually this is not the case for maximum principal stress. It needs to be checked for the direction before performing superposition, unless all the six components of Cauchy stress is extrapolated and then combined again. The procedure is rather tedious and theoretically unsound.

The normal stress/strain on the surface extrapolation path is changing direction. To obtain appropriate normal stress/strain result from computed FE models, the following transformation formula in basic elasticity theory is applied (Ugural and S.K.Fenster, 1995):

For Cauchy stress, $[\sigma]=\begin{bmatrix}\sigma_{11} & \sigma_{12} & \sigma_{13}\\ \sigma_{21} & \sigma_{22} & \sigma_{23}\\ \sigma_{31} & \sigma_{32} & \sigma_{33}\end{bmatrix}$, the normal stress in any direction is:

$$\sigma_{nor} = \sigma_{11}l^2 + \sigma_{22}m^2 + \sigma_{33}n^2 + 2(\tau_{12}l\cdot m + \tau_{23}m\cdot n + \tau_{13}l\cdot n) \qquad (6.4)$$

where, *l, m, n* are the directional cosine in a Cartesian coordinate system:

cos(n,x) = l

cos(n,y) = m

cos(n,z) = n

The directional angle for directional cosine is calculated through the node coordinate on the extrapolation path. Note that is why the surface radial mesh is intentionally built perpendicular to the weld toe. For strain transformation, the same formula is applicable by just replacing the stress with the strain.

For the four models, paths 1 to 4 are of major interest, as they are in tension side of the chord, the most critical locations for in-plane bending. The comparisons are conducted for the four paths as shown below.

Comparison for strain reduction due to grouting

Typical strain results for the same path subjected to same load level are shown in Figure 6.14. It can be seen that the reduction effect is quite significant. However, the percentage of reduction is decreasing for the locations approaching the weld toe position due to notch effect. The FE results are in close agreement with the test result. Compared with preliminary FE results, as reported in Choo et al.(2007), the FE improves accuracy due to proper modeling of weld profile, especially for X2G.

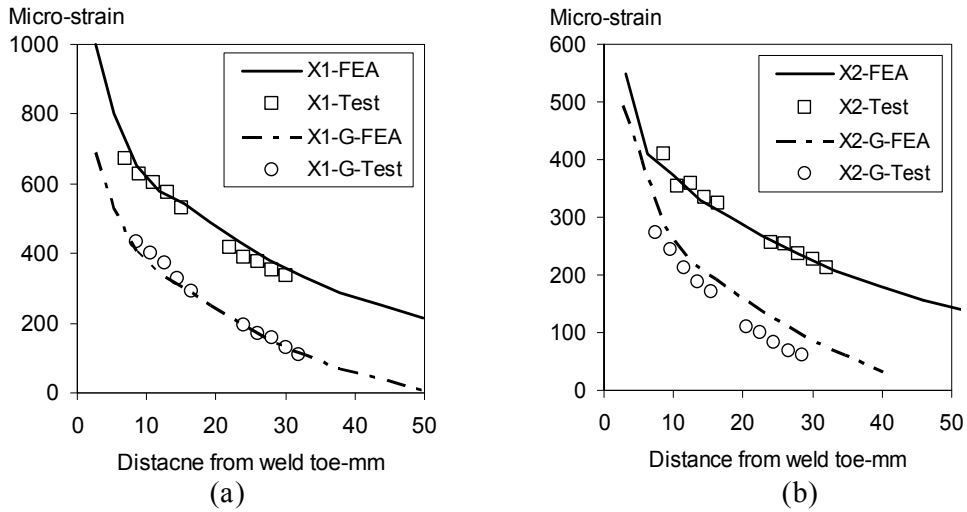

Figure 6.14 Comparison of reduction of strain at path-2 under the same loading level: (a) load level:120 kN for X1 and X1-G; (b) load level 147 kN for X2 and X2-G

Experimental SCFs determined from measured SNCFs

At the surface of tubular joints, every point is in bi-stress status with the third direction stress equal to zero, the so called plane stress condition. The following formula (Berge, 2004) from elasticity analysis should apply for converting SNCF to SCF, (6.5).

$$S_{hs} = E \times \varepsilon_{hs} \frac{1 + \nu \dfrac{\varepsilon_y}{\varepsilon_{hs}}}{1 - \nu^2} \qquad (6.5)$$

where, ε_{hs} is hot spot strain in the normal direction;

ε_y is the strain perpendicular to the normal hot spot strain ε_{hs};

ν is the Poisson ratio, taken 0.3 for steel; and

E is the young modulus of steel, taken 205000 Mpa.

The ratio of SCF to SNCF equals to $\frac{1+\nu\frac{\varepsilon_y}{\varepsilon_{hs}}}{1-\nu^2}$. From FE analysis, this value for un-grouted joints stays around 1.2, consistent with literature (HSE, 1997). For grouted joints X1-G and X2-G, this value is slightly higher than the corresponding un-grouted joints at chord crown due to the constraint of chord ovalisation imposed by infilled grout. The ratio to convert the experimental SNCF to SCF is listed in Table 6.6, and the converted results are shown in Table 6.7 together with the reduction factor.

Table 6.6 Ratios of SCF/SNCF from FE analysis to covert measured SNCF to SCF

Degree of intersect	X1	X1G	X2	X2G
0.0	1.19	1.28	1.21	1.31
22.5	1.23	1.25	1.15	1.17
45.0	1.22	1.22	1.17	1.20
67.5	1.23	1.19	1.05	1.12
90.0	-1.19	1.11	0.50	1.03
112.5	1.23	1.23	1.07	1.06
135.0	1.24	1.15	1.17	1.12
157.5	1.27	1.11	1.15	0.98
180.0	1.23	1.08	1.20	0.99

The overall SCF distributions around the brace-chord intersection are plotted in Figure 6.15. Due to symmetry, only half specimens are plotted. It could be seen that the tensile FE SCF results are in close agreement with experimental results. Hence, the models are calibrated satisfactory. The compression SCFs can be reasonably represented by FE result. The distribution of SCF for un-grouted joints are almost anti-symmetric for tensile and compression, indicating the stress induced by chord

load is insignificant, the test set up can reasonably represent in-plane bending. For grouted joints, the stress reduction for compression is more significant than tension due to the infilled grout.

Table 6.7 Summary of stress concentration and reduction factors

Specimen	SCF	path-1, chord, crown	path-2, chord, 22.5^0	path-3, chord, 45^0	path-4, chord, 67.5^0
X1	SCF -test	4.46	4.77	4.76	3.76
	SCF -FEA	4.63	4.78	4.72	2.
X1-G	SCF -test	3.11	3.24	2.71	1.66
	SCF -FEA	3.01	3.12	2.59	1.48
Reduction[a]	RF -test	0.71	0.71	0.59	0.45
	RF -FEA	0.67	0.67	0.57	0.54
X2	SCF -test	2.26	2.23	2.27	1.65
	SCF -FEA	2.06	2.16	2.23	1.77
X2-G	SCF -test	1.44	1.57	1.07	0.27
	SCF -FEA	1.33	1.43	0.98	0.46
Reduction[a]	RF -test	0.64	0.70	0.47	0.16
	RF -FEA	0.60	0.65	0.43	0.24

[a] Reduction factor is the ratio of the pair of SCFs as defined in Eq. 6.6 on P173

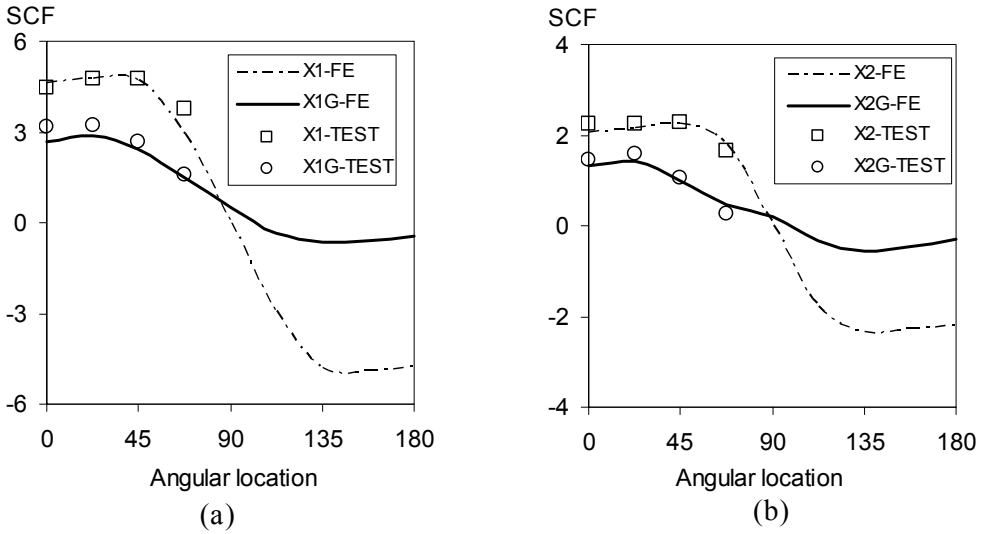

Figure 6.15 Overall distribution of SCFs on the chord surface: (a) X1 and X1G; (b) X2 and X2G. The notation of degree location follows Figure 6.2, the zero and 180 degrees are the chord crowns

Efthymiou SCFs and DOBs

SCF results from Efthymiou formulae are compared with FE and test results as shown in the Table 6.8 for joint X2. It can be seen that for X2 with the correction formula Eq. (5.8) and (5.9) using actual weld leg length, the prediction using Efthymiou formula is satisfactory. For X2-G, the thickness correction are following equation (6.1). The prediction is conservative. The degree of bending stress (DOB) is determined from FE results as shown in Table 6.9.

Table 6.8 Comparison of prediction of SCFs at chord crown

Joints	FE (40mm weld leg)	Test	Efthymiou (33mm weld leg)	With weld leg correction (40mm weld leg)
SCF-X2	2.06	2.26	2.95	2.56
SCF-X2G	1.33	1.44	2.55 (T'=1.57T, for γ, Eq. (6.1))	2.21
			2.37 (T'=2T for γ)	2.05

Table 6.9 DOBs at chord crown based on through thickness stress

X1	X1-G	X2	X2-G
0.71	0.86	0.66	0.81

6.3.5 Discussion

It has been shown that the FE results are in close agreement with the test results. The 'hard contact' mechanism in Abaqus/Standard is thus demonstrated to be suitable for simulating the interaction between the grout and steel tube, and the matching mesh scheme performs well, although, computationally it is expensive.

During the tests, the shake down of residual stress phenomenon was observed. The pre-loads generated different first yield load level. Figure 6.16 shows typical strain gauge readings versus the external loads. In Figure 6.16 (a), the occurrence of yielding was much earlier than FEA prediction due to the residual stress in the actual

joints. However, the residual stress can be released through pre-load as shown in Figure 6.16 (b). The non-linearity of hot spot stress is predominantly caused by the material yielding, similar to that of un-grouted (as-welded) joints.

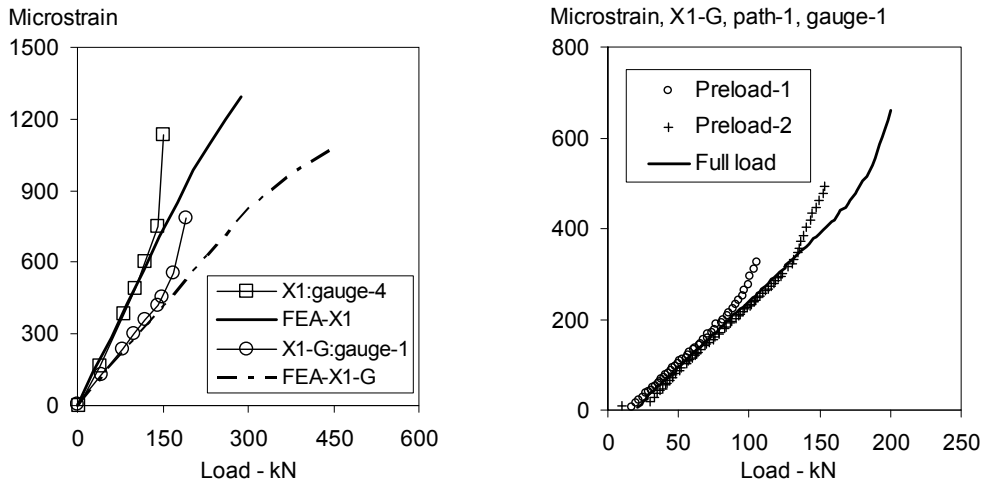

Figure 6.16 Strain reading comparison: (a) yield occurrence earlier than FEA prediction; (b) yield occurrence later than previous preload – shake down effect

From the observation during the static test, it can be postulated that the response of single skin grouted joint subjected to fatigue cyclic loading will be similar to the conventional un-grouted joint. When subjected to same brace load, the fatigue life of grouted joint is likely to be extended due to the reduction of hot spot stress.

Another interesting phenomenon is that due to the presence of infilled grout, the ovalization of chord is reduced. However, this does not mean the reduction of degree of bending stress. As shown in Table 6.9, under in-plane bending the DOB is even raised up for grouted joint, which is beneficial for fatigue resistance.

6.4 Finite element parametric study

Based on above satisfactory calibration of finite element models, further finite element parametric study was carried out to investigate the reduction of hot spot stress of infilled grouted X-joints with different geometric parameters and subjected to

different brace loading conditions. It is expected to generate design curves through FE parametric study, since compared with experimental work the finite element simulation is inexpensive. Similar mesh scheme was adopted and Patran command language (PCL) was used to develop a systematic mesh generating code.

6.4.1 Loading modes and hot spot locations

Three brace loading conditions - axial tension, in-plane bending and out-of-plane bending were studied. The loading modes adopted are consistent with the suggestions of current code ISO19902 (BSi, 2007). For X-joints the assumptions are:

- axial forces on braces are assumed to be balanced;
- SCFs in X-joints are not sensitive to the sign of the in-plane bending moment;
- Out-of-plane bending moments on braces are assumed to be balanced.

As mentioned in the ISO19902 (BSi, 2007), *these recommendations are based on the assumption that, in a well-brace structure, the response of primary joints is usually governed by axial forces; bending and shear due to frame action are of secondary importance. Hence the (normal components of) axial forces in the braces at a joint should be approximately balanced so that shear remains small. In-plane bending and out-of-plane bending moments can be significant when they are caused by direct wave action (as opposed to frame action) and for secondary braces*.

Through preliminary study and literature review, it was found the hot spot stress at chord side is usually more critical than that of brace side. The assessment of chord hot spot stress concentration factor is thus of higher priority. Four locations of the X-joints were selected for assessment of SCFs and the associated reduction factor in both un-grouted and chord grout-infilled conditions, which is consistent with ISO19902 (BSi, 2007) and the provisions of Efthymiou formulae:

- Chord saddle when subjected to brace axial tension;

- Chord crown when subjected to brace axial tension;
- Chord saddle when subjected to brace out-of-plane bending; and
- Chord crown when subjected to brace in-plane bending.

Through systematic parametric study, it was found for chord infilled (single skin grouted) X-joints within normal geometric range that:

- the hot spot locations do not shift significantly from the original location in as-welded (un-grouted) condition;
- chord side is more critical than brace side even with chord infilled grout; and
- SCFs of tension are more critical than compression.

For brace bending load, the tensile SCFs were decided to report to comply with the code of ISO19902 (BSi, 2007) – A.16.10.2.4 (page 452). Similar to as-welded joints, for grouted joints under in-plane bending, the hot spot is in-between the chord crown and saddle with the highest SCF at similar magnitude to that of chord crown as shown in the above section 6.3 for the tests conducted. The design code in this case uses chord crown as the reference location for superposing the hot spot stress considering real combined loading condition, and as introduced certain degree of safety factor was built in the Efthymiou formula to account for this effect. This study follows the same treatment of using chord crown to evaluate the hot spot stress and reduction factor for in-plane bending.

6.4.2 Joint configurations

The non-dimensional geometric parameters of the X-joints studied are $\alpha = 12$, $0.3 \le \beta \le 1$, $9 \le \gamma \le 28$ and $\tau = 0.5 \& 1$. Table 6.10 shows the particular geometric parameters for every joint studied. It is noted that for joint design, the design codes recommend chord wall thickness ratio at $12 \le \gamma \le 28$ to be considered as a normal joint. For joints PX19 and PX23 in Table 6.10, the γ ratio is 9.23, and should be

considered as thick wall joints usually. So these two joints are not included in design curves. The joints with asteroid (*) are additional verification cases with different τ ratio to check the accuracy of interpolation for τ between 0.5 and 1, and are not included in the design curves derivation.

Table 6.10 Geometric parameters of X joints in parametric studies

No.	**α**	**β**	**γ**	**τ**	Chord diameter-**D**(mm)	Brace diameter-**d**(mm)	Chord wall thickness-**T**(mm)	Brace wall thickness-**t**(mm)
PX1	12	0.79	11.64	1	512	406	22	22
PX2	12	0.79	16.00	1	512	406	16	16
PX3	12	0.79	23.27	1	512	406	11	11
PX4	12	0.79	11.64	0.5	512	406	22	11
PX5	12	0.79	16.00	0.5	512	406	16	8
PX6	12	0.79	23.27	0.5	512	406	11	5.5
PX7	12	0.53	12.20	1	610	324	25	25
PX8	12	0.53	19.06	1	610	324	16	16
PX9	12	0.53	24.40	1	610	324	12.5	12.5
PX10	12	0.53	13.86	0.5	610	324	22	11
PX11	12	0.53	19.06	0.5	610	324	16	8
PX12	12	0.53	24.40	0.5	610	324	12.5	6.25
PX13	12	0.30	11.43	0.5	914	273	40	20
PX14*	12	0.30	14.28	0.6875	914	273	32	22
PX14	12	0.30	14.28	1	914	273	32	32
PX15	12	0.30	28.56	1	914	273	16	16
PX16*	12	0.30	11.43	0.7	914	273	40	28
PX16	12	0.30	11.43	1	914	273	40	40
PX17	12	0.30	14.28	0.5	914	273	32	16
PX18*	12	0.30	28.56	0.75	914	273	16	12
PX18	12	0.30	28.56	0.5	914	273	16	8
PX19	12	1.00	9.23	1	406	406	22	22
PX20	12	1.00	12.69	1	406	406	16	16
PX21	12	1.00	14.28	1	914	914	32	32
PX22	12	1.00	28.56	1	914	914	16	16
PX23	12	1.00	9.23	0.5	406	406	22	11
PX24	12	1.00	12.69	0.5	406	406	16	8
PX25	12	1.00	14.28	0.5	914	914	32	16
PX26	12	1.00	28.56	0.5	914	914	16	8

* The additional verification case of different tau ratio

It has been shown in Chapter 5 that hot spot stress is influenced by the weld geometry. For a normal joint with mid β range the weld leg on the chord side will cause about 10% variation of hot spot stress SCF, while for joints with β=1 the

variation could be more than 100%. In this study the X-joints with β=1 are included for completeness and the hot spot stress reduction factors were calculated based on the same joint mesh with the same weld geometry. Figure 6.17 shows the weld geometry used in the FE study. Particularly,

- the weld geometry for β <1 joints follows the profiles for generating Efthymiou formulae as introduced by Marshall (2005), which is also in compliance with AWS rules (API, 2000), as shown in Figure 6.17 (a);
- the weld profile at chord saddles for β=1 joints follows the observation of real specimens tested with reasonable weld leg length and convexity. The relative length of weld leg, H1, is longer for small diameter joints and shorter for larger diameter joints considering the actual welding conditions.
- the weld leg height H2 for all the joints is based on the real cutting profile as shown in Figure 6.17. The convex is for joints with β=1 only, and is adjusted to make the joints with β=1 have similar convexity.

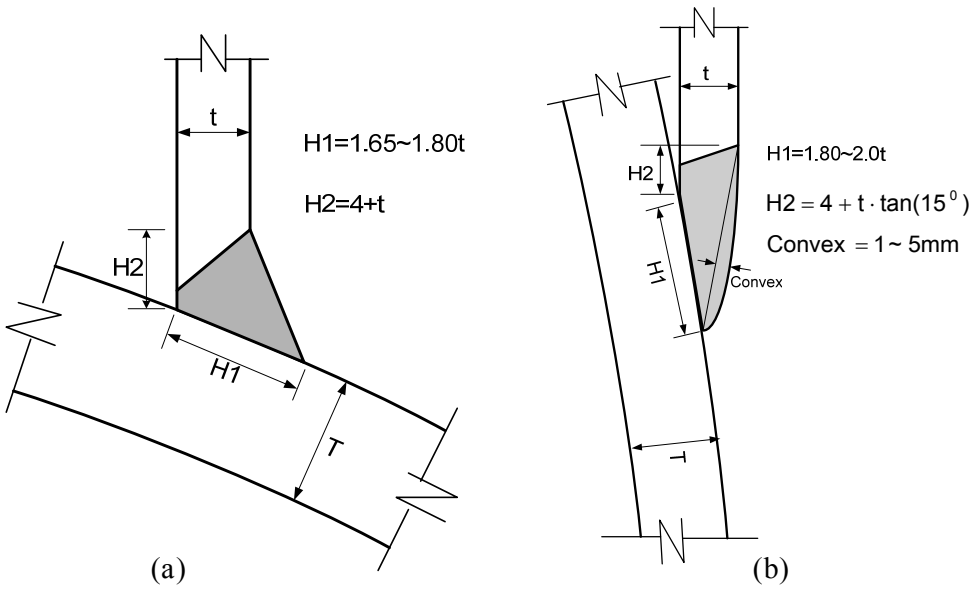

Figure 6.17 Weld geometry used in FE parametric study: (a) for β<1; (b) for β=1 at chord saddle

6.4.3 Boundary conditions

Due to the symmetry of loading and geometry (without imperfection), one eighth and quarter models were used for brace axial loading and bending respectively as shown Figure 6.18. For brace axial tensile loading, negative pressure load was applied on the brace; for in-plane bending, displacement load is applied on the chord end which is similar to the test condition conducted in NUS; and for out-of-plane bending, moment load was applied on the brace end. The loading was applied to 40% of the strength design load for as-welded (empty) joint for both as-welded and infilled grouted joints. The design load was calculated using design formulae in ISO19902 (BSi, 2007) assuming material strength is 355MPa. Figure 6.18 illustrates the details. For both grouted and un-grouted joints, same boundary condition is applied.

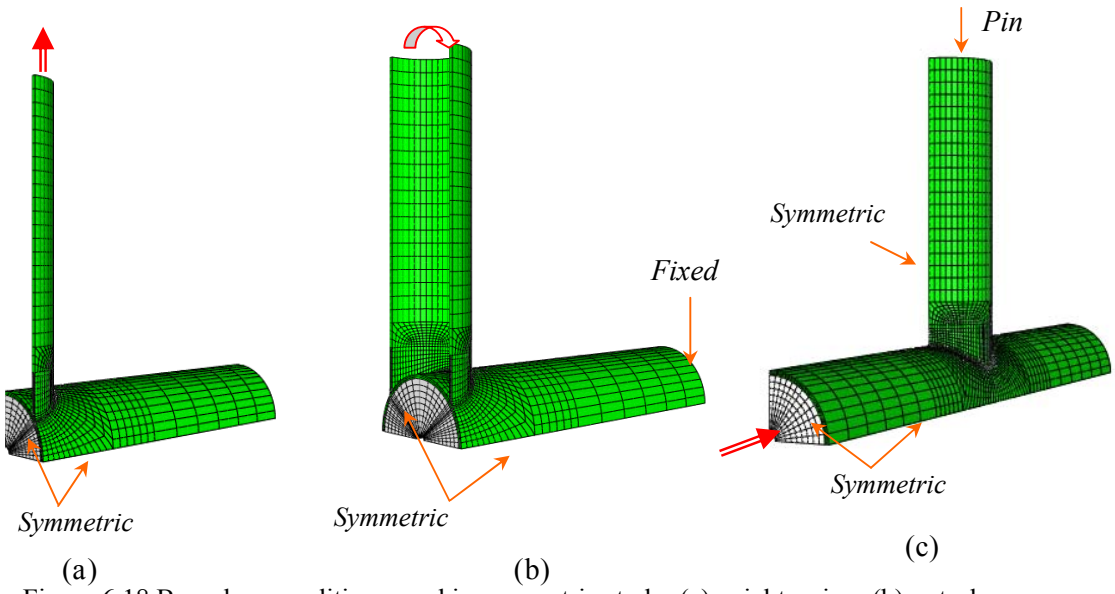

Figure 6.18 Boundary conditions used in parametric study: (a) axial tension; (b) out-plane bending; (c) in-plane bending

6.4.4 Material properties

Linear elastic material property was assigned to both steel and grout. The Young's modulus for steel is 205,000 MPa, and for grout is 70, 000 MPa. The Poisson ratio for steel is 0.3 and for grout is 0.19. The grout material property follows Densit Ducorit

D4. It has been shown in the above section that the stress level for grout in infilled X-joint under in-plane bending is very low, and if replaced with normal G40 concrete the strengthening effect for hot spot stress reduction is similar, provided there is no shrinkage. Similar effect is observed for axial tension and out-of-plane bending also, as there is no global bending effect for X-joints. Hence, the derived hot spot stress reduction curves are also applicable for other type of high strength infilled grout, if the shrinkage is similar to that of Densit Ducorit D4.

6.4.5 FE analysis

The analysis was performed using Abaqus 6.7.1/standard on HP work station 6200 with ram memory of 4G. A total of 152 analysis were conducted including both as-welded and grouted joints. For grouted joints, the bending model (quarter model) took the longest running time. A typical bending analysis for grouted joint was around 8 hours. The post-processing was carried out using Abaqus 6.7.1/CAE. Based on calibration and sensitivity analysis in Chapter 5, nodal stress/strain values were extracted for hot spot stress calculation. ECSC definition was adopted for extrapolation so that the results are in compliance with ISO19920.

6.4.6 FE results

The hot spot stress result obtained through FE analysis was converted to stress concentration factor. For every joint configuration, the grouted SCF was divided by as-welded SCF and the ratio is the reduction factor. Meanwhile the degree of bending at hot spot location was also worked out using linearization of through thickness stress. For all the grouted joints, the FE SCFs show constant values despite varying load applied. It is confirmed through FE simulation that the contact action does not change the linearity of SCF in tensile condition. Note as codified in ISO19920 for fatigue assessment as the tension SCF is more critical than compressive condition.

Hence, using tension SCF for fatigue assessment will be conservative and consistent with the linearity requirement for damage calculation.

For comparison and examining existing method recommended, the SCF and DOB were also calculated using available empirical equations. For SCF, the Efthymiou formulae was adopted, and for DOB for X-joints the formula generated by Connolly et al.(1990) is used. The detailed DOB results are presented in Chapter 7.

6.4.6.1 Axial tension

For brace axial tension, the critical hot spot stress occurs at chord saddle for both as-welded and grouted joints. The SCFs at chord saddle of as-welded joints obtained from FE analysis is compared with the prediction by Efthymiou formulae as shown in Figure 6.19, (a). It could be seen the results is in very good agreement. For certain results of equal brace and chord diameters with β=1, the match is with slightly large deviation due to influence of weld geometry as introduced and discussed in Chapter 5. The SCFs for as-welded joints is with a very large range, the maximum SCF is about 40. Figure 6.19, (b) shows the strengthening effect of infilled grout. It could be seen the SCF at chord saddle is significantly reduced - the effect is tremendous, especially for large as-welded SCFs. For joints with β=1 the strengthening effect is not very significant.

The SCFs at chord crown is plotted in Figure 6.20. Compared with the results of chord saddle, the SCFs at chord crown show large disagreement with Efthymiou prediction Figure 6.20 (a). The reason is that the chord crown SCF of Efthymiou equation under axial forces was derived from the corresponding SCF for T/Y-joints by suppressing beam bending of the chord, not from direct FE results like those for chord saddle. The accuracy of this equation was not supported by the test results and not recommended in the current code (BSi, 2007). However, compared with chord

saddle, the SCF of as-welded joint is significantly less critical. The comparison generally shows the Efthymiou equation is conservative. For completeness of design consideration, the Efthymiou is still acceptable, and in real situation of combined loads it is useful. The grouted SCFs at chord crown do not show consistent reduction or increment, Figure 6.20 (b), but the SCFs are relatively in a small range, less critical than those for chord saddle.

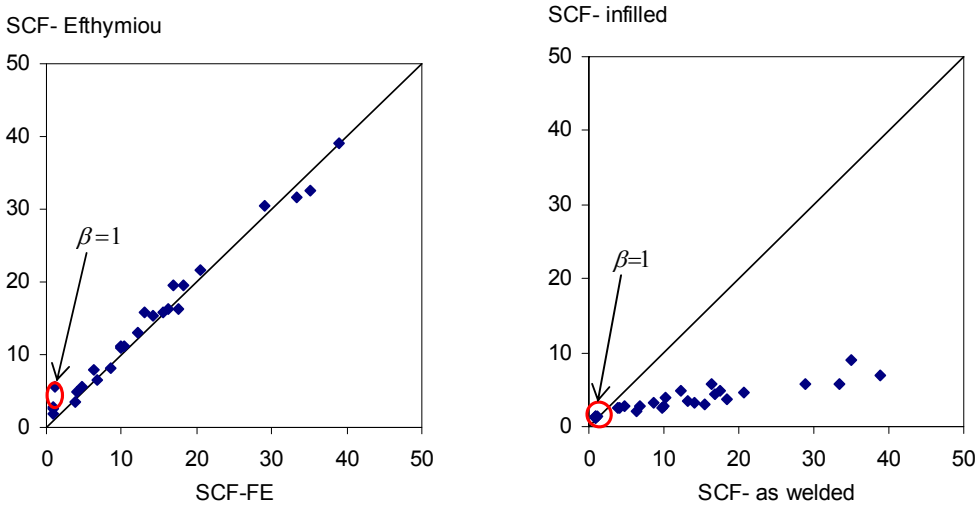

Figure 6.19 SCFs of as-welded and grouted joints at chord saddle under brace tension load: (a) FE vs Efthymiou for as welded (b) FE results for as-welded vs infill grouted

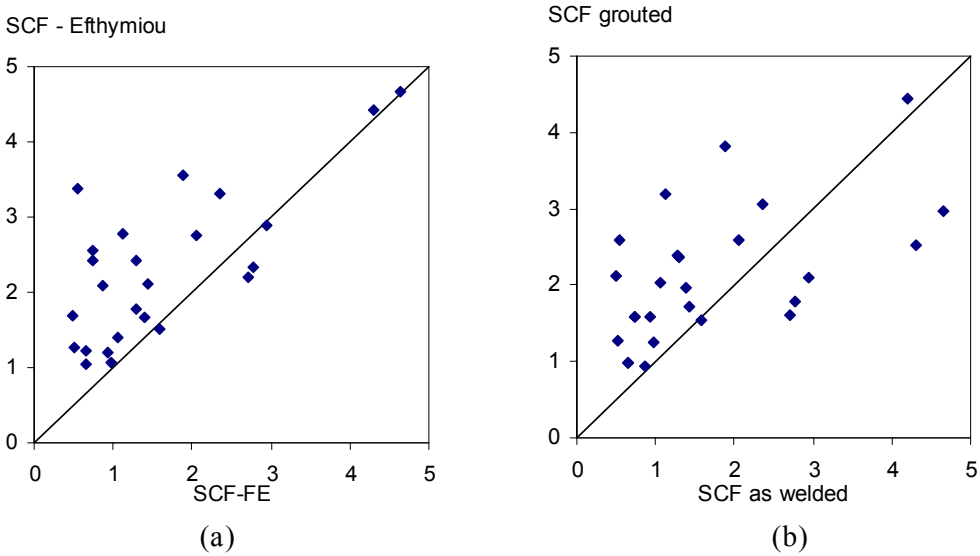

Figure 6.20 SCFs of as-welded and grouted joints at chord crown under brace tension load: (a) FE vs Efthymiou for as welded (b) FE results for as-welded vs infill grouted

6.4.6.2 Out plane bending

Figure 6.21 shows the SCFs at chord saddle (tension side) under out-of-plane bending load case. Similar to the axial tension, the FE result is satisfactorily matching the Efthymiou prediction, and the SCFs of grouted joints showed significant reduction. For the joints of equal brace and chord diameters, the strengthening effect is relatively small.

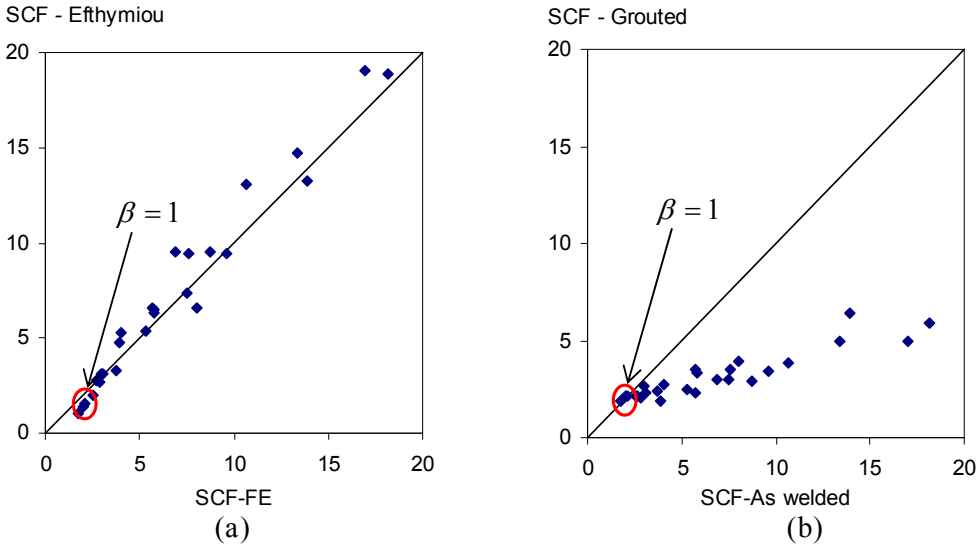

Figure 6.21 SCFs of as-welded and grouted joints at chord saddle under out-plane bending: (a) FE vs Efthymiou for as welded (b) FE results for as-welded vs infill grouted

6.4.6.3 In plane bending

Figure 6.22 shows the SCFs at chord crown under brace in-plane bending. It could be seen that the prediction of Efthymiou is on the conservative side for as-welded joint. This is because the maximum hot spot stress occurs at a location in-between the crown and saddle and the Efthymiou equation intentionally takes this into account to build in certain safety factor in generating the equations. For grouted joints the SCFs are generally reduced to a certain degree but not as significant as for axial tension and out-plane bending. For joints with equal brace and chord diameters (β=1) and large γ ratio, the strengthening effect is insignificant.

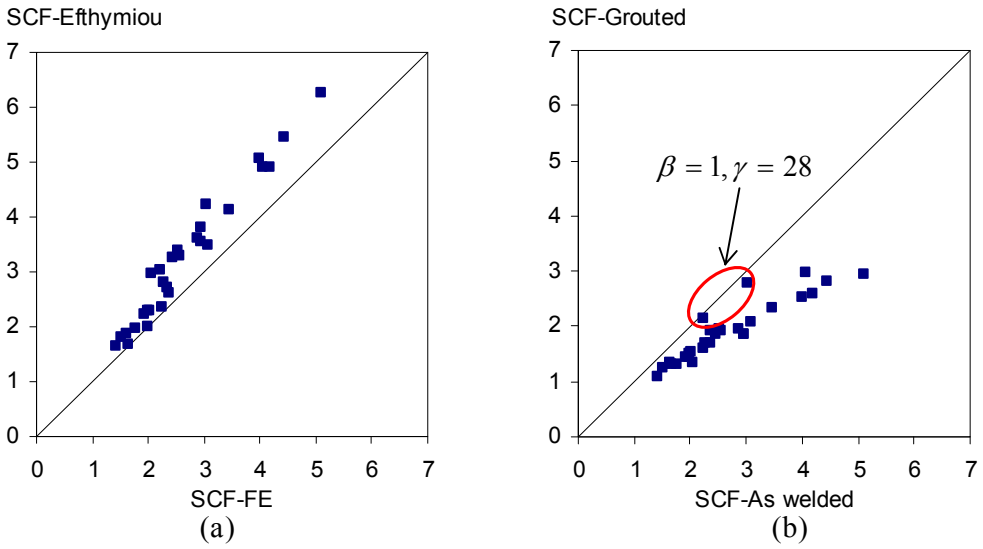

Figure 6.22 SCFs of as-welded and grouted joints at chord crown under brace in-plane bending load: (a) FE vs Efthymiou for as welded (b) FE results for as-welded vs infill grouted

6.4.7 Reduction factor in terms of proposed design chart

In order to facilitate design practice, the reduction factor:

$$RF = \frac{SCF_g}{SCF_{as}} \qquad (6.6)$$

is expressed in terms of charts as shown from Figure 6.23 to Figure 6.26. The charts were made based on the FE results using curve fitting function in Excel software, which is based on 3rd order polynomial. The SCF of grouted joints can be easily determined using Efthymiou formula of as-welded joint (attached in the Appendix) multiplied by the reduction factor from the design chart. The validate range is: $0.3 \le \beta \le 1$, $9 \le \gamma \le 28$ and $0.5 \le \tau \le 1$ for right angle X joints. The chart given is based on either $\tau = 1$ or $\tau = 0.5$, for the thickness ratio in-between, interpolation is required.

It is noticed that current design also provides the equivalent chord wall thickness to plug in Efthymiou formula for computing SCFs for grouted joints. Through systematic parametric study, it was found this method is rather inaccurate as

compared with FE results, while the proposed design charts give much better estimation. Figure 6.27 shows the comparisons. It can be seen that except for very few noise caused by joints with $\beta = 1$, the general agreement of proposed chart is significantly better than the recommendation of current design code ISO19902, which uses equivalent chord wall thickness.

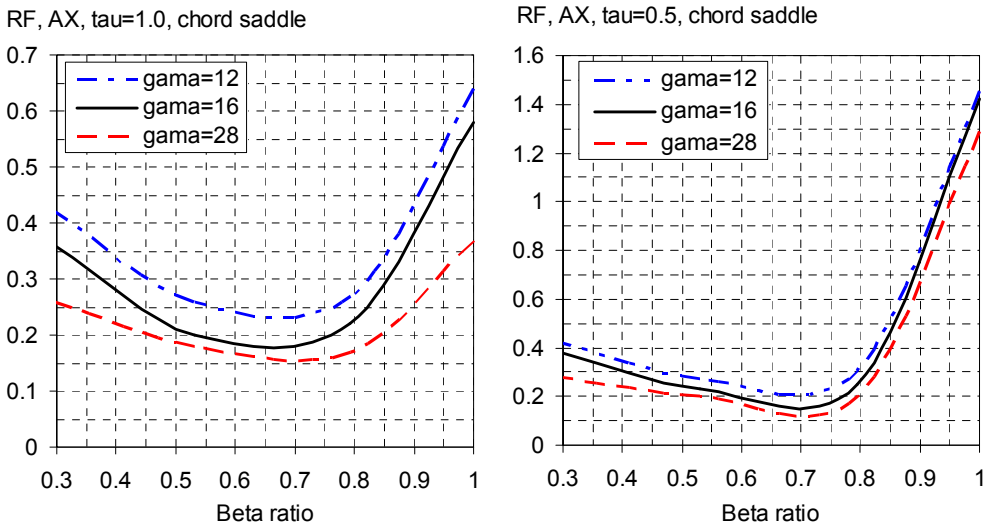

Figure 6.23 Proposed design charts for reduction factor at chord saddle of right angle X-joints under axial tension: (a) $\tau = 1$; (b) $\tau = 0.5$

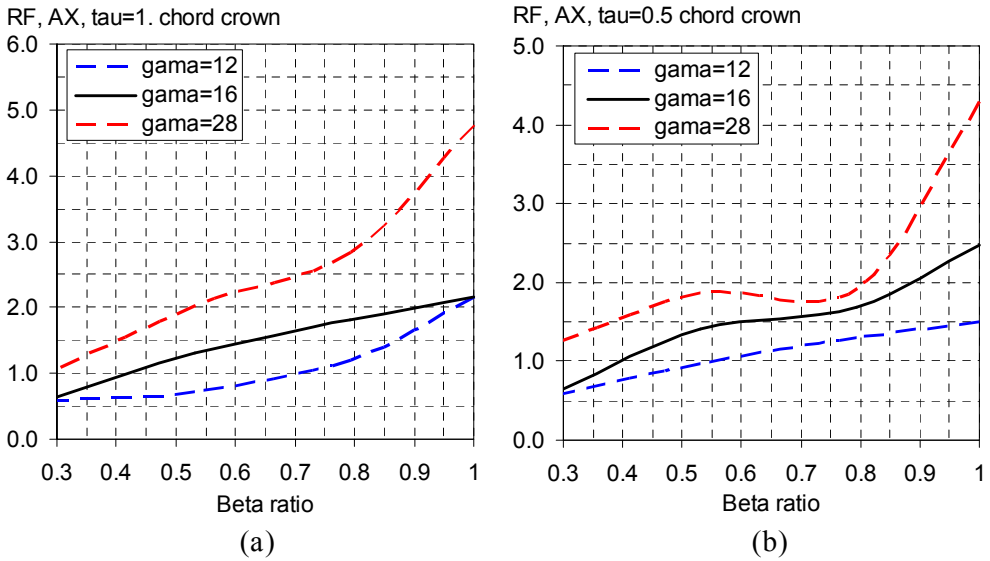

Figure 6.24 Proposed design charts for reduction factor at chord crown of right angle X-joints under axial tension: (a) $\tau = 1$; (b) $\tau = 0.5$

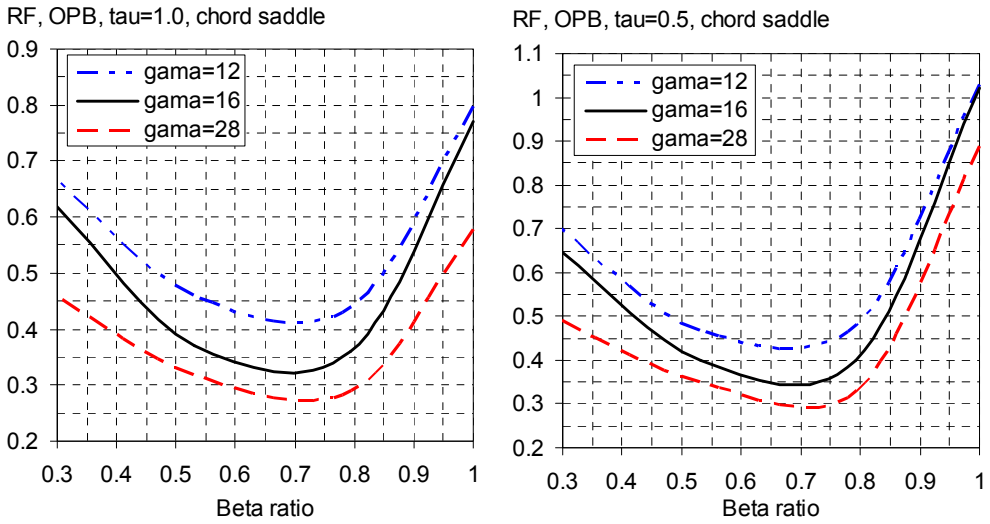

(a) (b)

Figure 6.25 Proposed design charts for reduction factor at chord saddle of right angle X-joints under out-plane bending: (a) $\tau = 1$; (b) $\tau = 0.5$

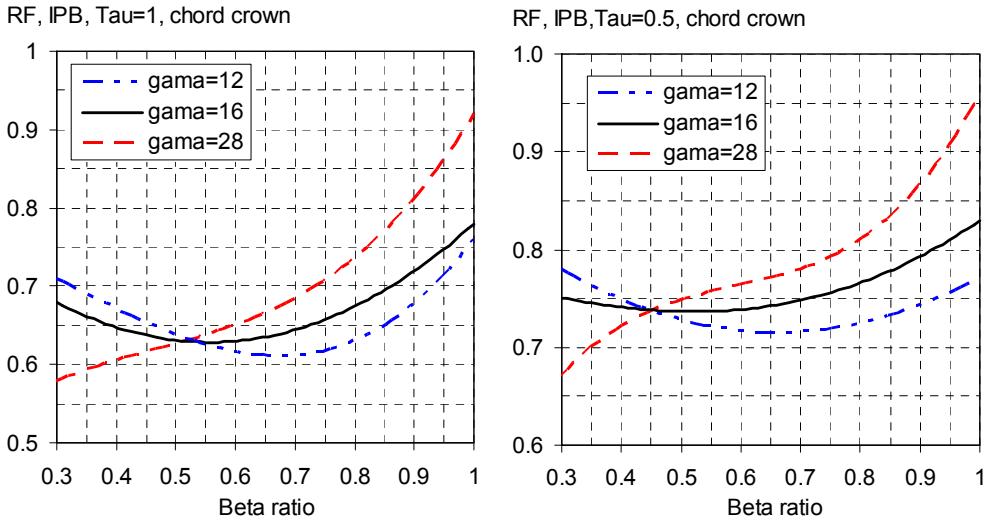

(a) (b)

Figure 6.26 Proposed design charts for reduction factor at chord crown of right angle X-joints under in-plane bending: (a) $\tau = 1$; (b) $\tau = 0.5$

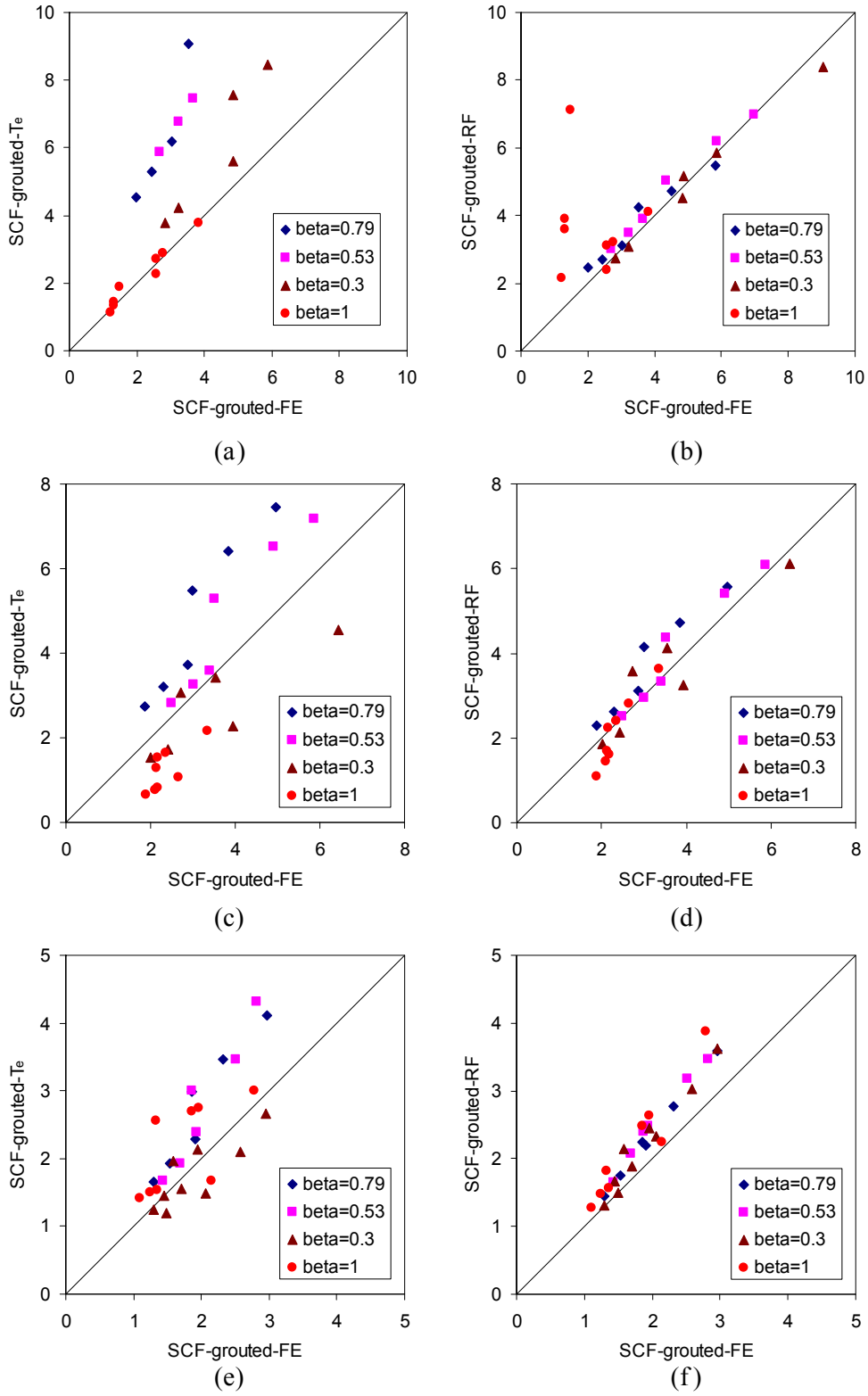

Figure 6.27 Comparison of SCFs of chord saddle for grouted joints determined according to: (a) equivalent thickness, axial tension; (b) proposed design chart, axial tension; (c) equivalent thickness, out-plane bending; (d) proposed design chart, out-plane bending; (e) equivalent thickness, in-plane bending; (f) proposed design chart, in-plane bending

6.5 Experimental verification for proposed design charts

Further experimental verification for the proposed design charts for reduction factor of infilled grouted X-joints was carried out. The test program consisted of five pairs of X-joints statically loaded in axial tension in the brace. Table 6.11 shows the parameters of the specimens with β = 0.7 and 1.0, γ = 13, 20 and 29, and τ=1. The specimens were fabricated by P.T. McDermott and grouted in NUS with high strength grout Ducorit D4. Due to symmetry of loading and geometry, there were four chord saddles of hot spot for each joint. Each hot spot region was instrumented with strip gauges for hot spot strain measurement. Figure 6.28 shows the test set up and instrumentation. The strain concentration factor (SNCF) was converted to stress concentration factors (SCF or SCF_g).

Table 6.12 shows the measured stress concentration factors. It can be seen the measured SCFs are with certain degree of scatter due to the irregular weld geometry and minor eccentric load. For joints with β=1, the scatters are larger than the others as expected. The averaged values were used for comparison and generation of reduction factors. For un-grouted joints, the average SCFs were in satisfactory agreement with those using Efthymiou equation. For grouted joints, the predicted reduction factor using the present proposed charts were in good agreement with test results as shown in Figure 6.29, while those using equivalent thickness method were diverging from the test results significantly, especially for the joints with $\beta = 0.7$.

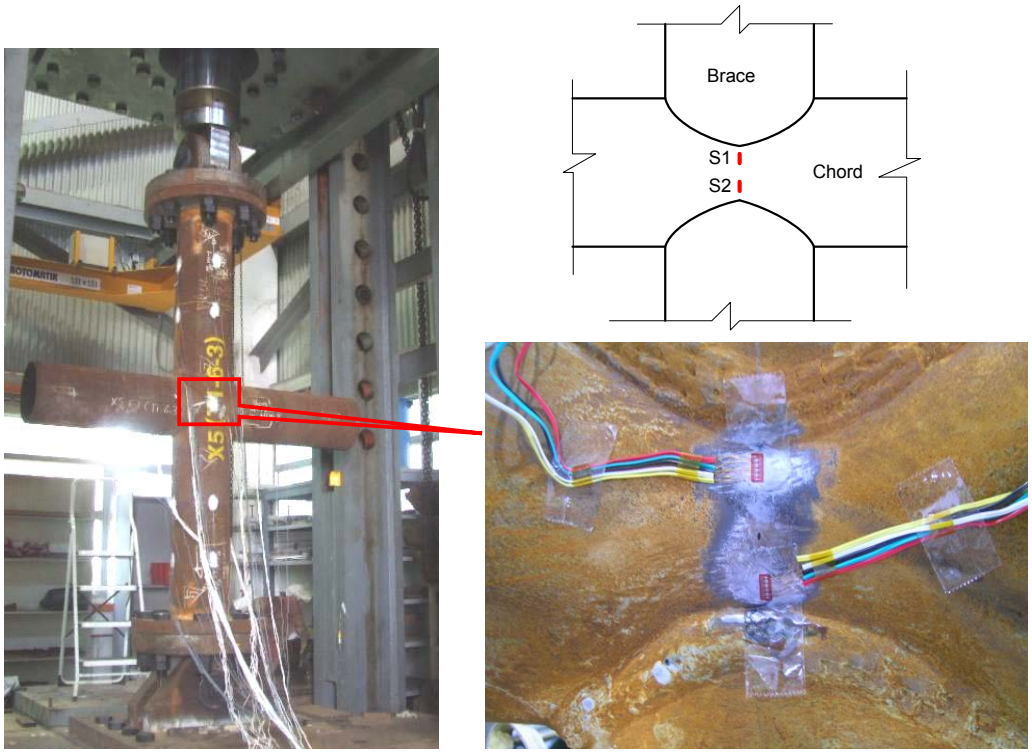

Figure 6.28 Set up and instrumentation of X joint under axial tension

Table 6.11 Parameters for the X joints tested under axial tension

	X-joint configuration, all the dimensions are in mm, f_y =355 MPa									Grout: D4	
Specimen	d_0	d_1	t_0	t_1	β	γ	τ	l_0	l_1	E (GPa)	strength (MPa)
X3	324	324	12.5	12.5	1.0	12.95	1.0	1950	970	no fill	no fill
X3G	324	324	12.5	12.5	1.0	12.95	1.0	1950	970	70	210
X4	324	219	12.5	12.5	0.7	12.95	1.0	1950	650	no fill	no fill
X4G	324	219	12.5	12.5	0.7	12.95	1.0	1950	650	70	210
X5	324	324	8.0	8.0	1.0	20.25	1.0	1950	970	no fill	no fill
X5G	324	324	8.0	8.0	1.0	20.25	1.0	1950	970	70	210
X6	324	219	8.0	8.0	0.7	20.25	1.0	1950	650	no fill	no fill
X6G	324	219	8.0	12.5	0.7	20.25	1.0	1950	650	70	210
X7	457	324	8.0	8.0	0.7	28.55	1.0	2740	970	no fill	no fill
X7G	457	324	8.0	8.0	0.7	28.55	1.0	2740	970	70	210

Table 6.12 Measured stress concentration factors

Specimens	SCF1	SCF2	SCF3	SCF4	Ave-test	Efthymiou	RF-test
X3	4.13	6.27	9.23	5.35	6.24	5.01	-
X3G	3.51	4.92	3.83	3.23	3.87	-	0.62
X4	19.00	25.17	16.85	12.92	18.48	20.52	-
X4G	7.25	3.56	8.10	3.69	5.65	-	0.31
X5	4.76	9.53	5.35	-	6.55	7.84	-
X5G	2.21	4.32	3.66	-	3.40	-	0.52
X6	32.51	49.62	26.37	40.76	37.31	32.09	-
X6G	5.85	8.70	7.59	5.72	6.97	-	0.19
X7	45.92	52.78	40.84	42.66	45.55	43.99	-
X7G	7.17	6.81	5.90	6.86	6.68	-	0.15

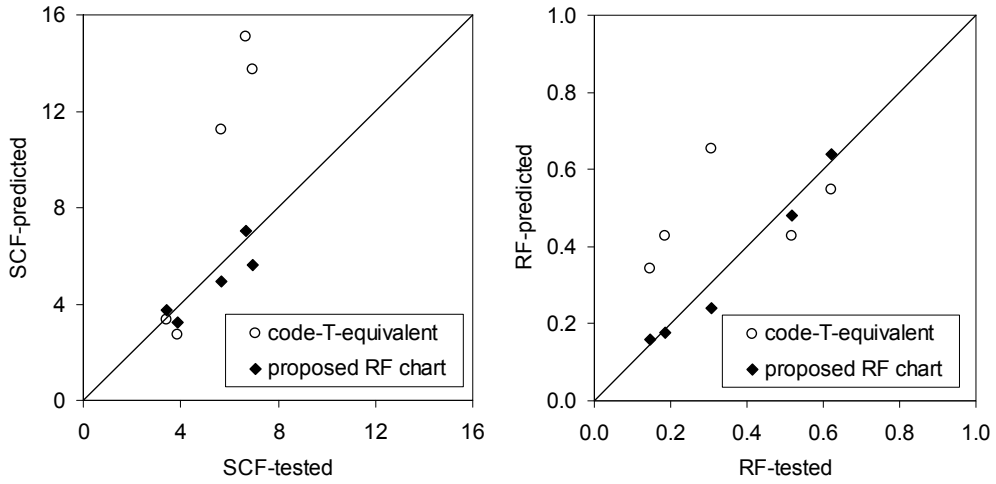

(a) (b)

Figure 6.29 Comparison of experimental results of grouted X joints: (a) SCFs; (b) reduction factors

6.6 Conclusion

From physical model tests to systematic finite element study, a series of comprehensive investigations of hot spot strain/stress of X-joints with chord infilled grout have been carried out. In compliance with current design codes for conservative consideration, the stress/strain concentration factor at chord tensile side, which is more critical than the compressive side, was thoroughly studied. Generally, the SCF

was found significantly reduced due to the presence of infilled grout in the chord, indicating the fatigue strength could be improved. A set of design charts of reduction factors were proposed for calculating the hot spot stress concentration factor SCF_g of X-joints with chords fully grouted. The proposed design charts coupled with Efthymiou formulae are convenient for use and generate much more accurate results than the equivalent thickness method in current design code. Particularly, it is with a degree of confidence to conclude as follows:

- Through experimental investigation the linearity of stress concentration factor of infilled grouted X-joints were found similar to that of un-grouted joints, the load dependency of tension SCF_g is insignificant, implying the hot spot stress S-N approach may be applicable for infilled grouted joints.
- Detailed finite element analysis shows for X-joints with chord fully infilled that the contact action will not cause non-linear response with the material property still in elastic range, supporting the experimental evidence and the record in documentation (MSL, 1997).
- The shrinkage of grout material used (Densit ducorit D4) was found insignificant with both physical inspection and finite element simulation proofs.
- Grout material sensitivity study shows the Young's modulus of infilled grout will not influence the SCFs of X-joint significantly. This is promising for using lighter weight cementious material as infilled grout if the shrinkage performance is similar to the D4 grout.
- Except for a few joints with β=1, the SCFs of as-welded joint predicted by Efthymiou formulae are generally in very good agreement with finite element results and test results. For grouted joint, the FE results were in good

agreement with test results also, providing solid calibration foundation for parametric study.

- Through systematic FE parametric study, a set of design charts of SCF reduction factor was developed, which was further experimentally verified to be more accurate than the equivalent thickness method and convenient to apply for fully grouted X-joints.

Chapter 7

Fracture mechanics analysis for fatigue of tubular joints with fully grouted chord

7.1 Introduction

Infilling the chord member of as-welded tubular joint with cementitious grout, as detailed in Chapter 6, can be a convenient and cost effective method to strengthen joints in offshore tubular structures. Consistent with the conclusions in Chapter 6, the published results (HSE, 1993; BOMEL, 1995; M.Lalani et al., 1996; MSL, 1997; Partiman et al., 1997; Morahan and Lalani, 2002; MSL, 2004) indicate that the hot spot stress concentration factor (SCF) of a grouted joint is significantly smaller than that of the original as-welded joint. Current design codes, like ISO19902 (BSi, 2007) and DnV RP C-203 (DNV, 2008), recognize this fact and implicitly assume the S-N curve of as-welded joints is also applicable for grouted joints. However, experimental evidence in the published literature to support this assumption is insufficient. To-date, limited fatigue tests of grouted tubular joints are reported (BOMEL, 1995,a), and the data do not provide a definite trend.

Two summary reports by BOMEL (BOMEL, 1995,a) and UEG (UEG, 1985) record several fatigue tests of grouted tubular joints with improved fatigue lives but some detailed joint data and test conditions are not reported. In contrast, Baker Jardine (HSE, 1993) presents detailed information about measured SCFs and fatigue

lives of two weld repaired and infilled grouted tubular T-joints (T208G and T215G). The geometric parameters of the two joints are the same and listed in Table 7.1. In the static tests, the SCFs for the grouted T-joint are found to reduce significantly, as shown in Figure 7.122, but in the fatigue tests the fatigue lives for the grouted joints are considerably less than that predicted by the mean S-N curve of as-welded joints, as shown in Figure 7.1. In terms of hot spot stress, the fatigue test results failed to demonstrate the degree of fatigue life enhancement expected for grouted joints according to the design codes (BSi, 2007; DNV, 2008). This is qualitatively speculated to be due to additional residual stress induced by weld repair (HSE, 1993). However, this speculation is inconsistent with the conclusion made by Tubby and Wylde (1989) and lacks of experimental evidence. Tubby and Wylde (1989) show that weld repair for tubular joints will not reduce the fatigue strength: the difference in fatigue lives between the weld repaired tubular joint and original as-welded joint is marginal. As recorded in the HSE report for the two weld repaired joints (HSE, 1993), the weld repair work is carried out following normal procedure in the industry. The measured SCFs after repair in both grouted and as-welded conditions do not show unusual trends (as plotted in Figure 7.12), and the observed fatigue failure mode and crack development (from initiation to propagation) are also similar to those of as-welded joints. It is felt the qualitative speculation is inadequate to explain the observed fatigue test results.

Table 7.1 Geometric parameters for the T joints

Joints [a]	Chord diameter - D (mm)	Chord thickness - T (mm)	Brace diameter-d (mm)	Brace thickness - t (mm)	α (2L/D)
T208(G)/T211/T215(G)	914	32	457	16	5
B3 (Calibration case)	914	32	457	16	8.53

[a] G indicates grouted

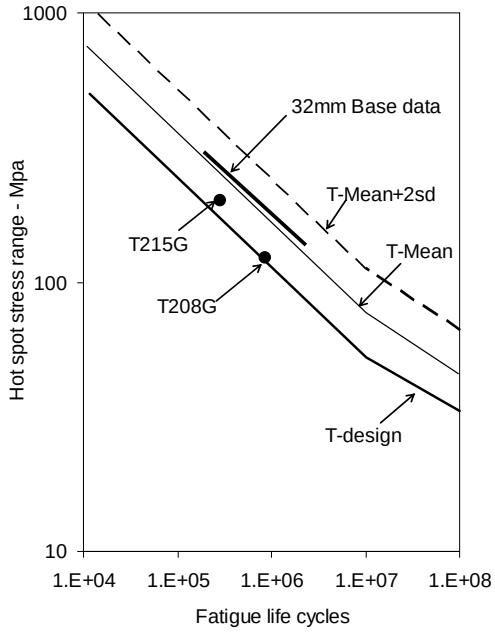

Figure 7.1 Fatigue test results of grouted T joints, adapted from HSE (1993). T curve is the design curve adopted in DNV(2008), ABS(2003) and HSE (1999) for 32mm thick tubular joints based on fatigue test results of as-welded joints. Two times standard deviation is assumed for design

In order to obtain a better understanding of the fatigue mechanism of grouted tubular joints, comprehensive fracture mechanics study is carried out on the grouted T-joints (T208G/T215G) in this thesis. In this study, which is based on the experimental evidence as mentioned above, the weld repaired joint is treated similarly as as-welded joint without consideration of the influence of residual stress (Bowness and Lee, 1995; 1998; Lee and Bowness, 2002), but with the focus on the geometric effect. The stress intensity factors (SIFs) for both grouted and as-welded conditions are determined by numerical method and then by engineering formulae in the design codes (BSI, 1993; 2005). The computed results are consistent and strongly support the fatigue test results as reported by Baker Jardine (HSE, 1993). It is shown that the presence of infilled grout in the chord member significantly alter the through thickness stress distribution at hot spot region, which can be characterized by the parameter, degree of bending (DOB) as defined in Chapter 5, Eq.(5.5) for fracture

mechanics analysis. For tubular joints with weld toe fatigue cracking and subjected to same amount of hot spot stress, lower DOB (larger portion of membrane stress) leads to larger SIF. In other words, hot spot stress with lower DOB is more fatigue damaging than that with higher DOB. The revealed mechanism for grouted joint is that the presence of infilled grout in the chord member reduces not only the SCF but also the DOB, which results in shorter fatigue life in terms of hot spot stress. Therefore, for practical fatigue assessment of grouted joints using hot spot stress approach, it is essential to consider the effect of DOB.

7.2 Stress intensity factor for fatigue assessment

As mentioned in Chapter 2, in fracture mechanics the fatigue mechanism is based on the fatigue crack propagation Paris law, equation (2.2), in which the propagation rate of fatigue crack is correlated to the range of SIF, ΔK. K is a field parameter characterizing the stress/strain field around crack tip, while ΔK is regarded as fatigue crack driving force. K can be expressed in a general form, as in Eq.(7.1), related to remote stress (external load):

$$K = Y \cdot \sigma \sqrt{\pi \cdot a} \qquad (7.1)$$

where, a is the crack depth as shown in Figure 7.2,

Y is the shape factor depending on the geometry of the structure and configuration of the crack, and also termed as normalized SIF.

σ is the remote stress, and can be either hot spot stress σ_{hss}, as defined in Chapter 5, or nominal stress σ_n, as defined in Eq.(2.5) and (2.6).

Fracture mechanics method ignores the fatigue crack initiation life, which may be acceptable for welded joints, since there are initial defects formed along weld toe, such as undercut, slag, intrusions or micro-cracks (Berge, 1985; HSE, 1999). Successful applications of fracture mechanics method to assess the fatigue

performance of welded tubular joints are reported in the literature (Berge et al., 1989; 1994; HSE, 1998). In many applications, for simplification and ease of study, welded T-butt joint is considered to be representative of tubular joints in a local sense. However, attention should be paid to the different load shedding effects. Load shedding is the load path alteration and stress redistribution caused by fatigue crack propagation. Compared with T-butt joint, tubular joint is with more significant load shedding effect due to its special structural configuration (Berge et al., 1994). The different load shedding effects result in different relative crack propagation life as illustrated in Figure 7.3. Ideally, the load shedding effect should be included in the shape factor *Y*.

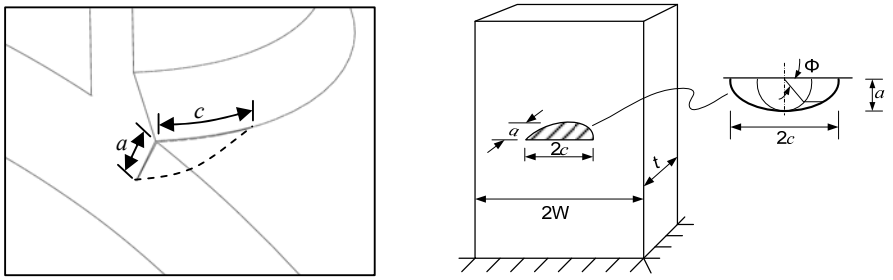

(a) (b)

Figure 7.2 Surface cracks: (a) fatigue crack at weld toe of a tubular joint (half model); (b) surface crack in a plate

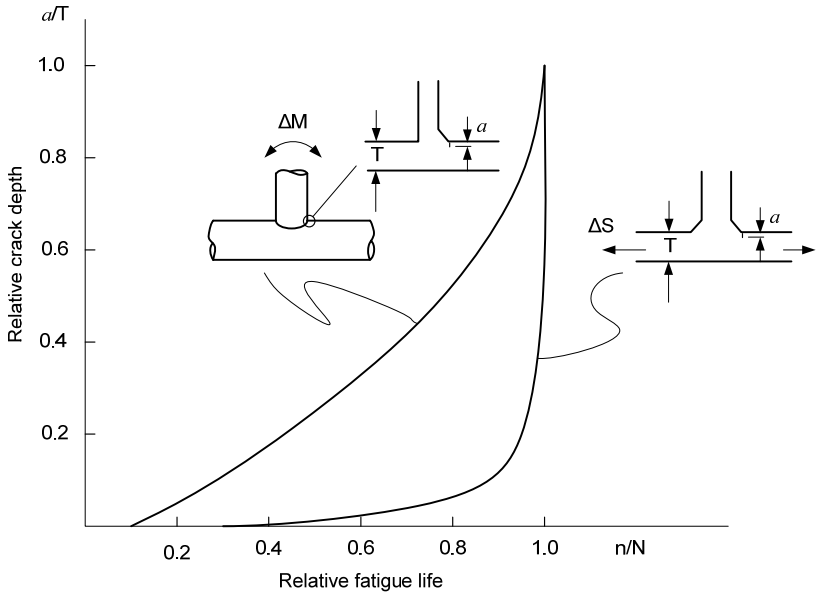

Figure 7.3 Comparison of relative fatigue lives, adapted from Berge et al.(1994)

7.3 Determining SIF by numerical method

Numerical method (also called computational fracture mechanics) was applied in this study using the finite element (FE) software Abaqus/Standard 6.7-1 (SIMULIA, 2007). The SIF computed using cracked 3D FE model is considered to be the highly accurate for tubular joints, because the determination is strictly in accordance with the definition of SIF in fracture mechanics, and the load shedding effect is explicitly taken into account by modeling crack in the geometry.

7.3.1 SIF in computational fracture mechanics

In computational fracture mechanics two methods are frequently used to determine SIF, namely the displacement extrapolation method and the J integral method. The displacement extrapolation method uses the displacement field behind the crack tip for calculation. For mode I fracture under plane strain condition, the SIF expression is:

$$K_I = \lim_{r \to 0} \left[\frac{E u_y}{4(1-\nu^2)} \sqrt{\frac{2\pi}{r}} \right] \quad (\theta = \pi) \tag{7.2}$$

where, K_I is the mode I SIF, E is the Young's modulus, v is the Poisson ratio, u_y is the displacement of crack surface as defined in Figure 7.4, and r is the distance from crack tip following Figure 7.4.

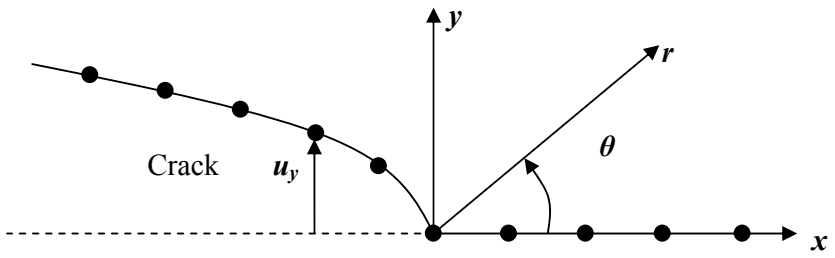

Figure 7.4 Local coordinate system for displacement field at crack tip in an FE model, adapted from Anderson (2004)

The J integral method converts *J* integral into *K* under linear elastic condition. For mode I fracture under plane strain condition, the conversion follows (7.3):

$$J = (1-\nu^2)K_I^2 / E \qquad (7.3)$$

Under mixed mode loading, the relationship between *J* integral and SIF is

$$J = (K_I^2 + K_{II}^2)/\overline{E} + K_{III}^2 / 2G \qquad (7.4)$$

where, $\overline{E} = E$ for plane stress and $\overline{E} = E/(1-\nu^2)$ for plane strain conditions;

$G = E/[2(1+\nu)]$;

K_{II} is mode II SIF and K_{III} is mode III SIF.

J integral is determined by domain integration in Abaqus (SIMULIA, 2007), which then uses a special interaction integral method to extract SIFs according to Eq. (7.4). The mathematical details can be found in Abaqus theory manual (SIMULIA, 2007).

Under cyclic fatigue loading, the crack emanated from weld toe for tubular joints is simplified as standard elliptical surface crack, which is characterized by crack depth *a* and crack length 2*c* as defined in Figure 7.2. The surface crack will propagate in the both directions of depth and surface length simultaneously. In the study, the focus is on the deepest crack at saddle with mode I only, because the fatigue life for tubular joint is determined on the cycles of first through-wall cracking, and mode I is dominant (Bowness and Lee, 1998). Plane strain condition for the plane of deepest crack is assumed to be consistent with published literature (Bowness and Lee, 1995; HSE, 2000).

7.3.2 Calibration and optimization of cracked FE model of an as-welded tubular T joint

Detailed computational fracture mechanics studies (Tan et al., 1990; Anderson, 2004)

suggest using quadratic solid element for computing SIFs for 3D FE model, and indicate that the shape and size of the elements in critical region with high stress gradient will influence the computed result. For tubular joints, the stress/strain field of the hot spot region, where fatigue crack locates, is with large magnitude and associated gradient. Close to the crack tip it is singularity dominant. Potentially, the FE result will be unstable and mesh sensitive. In order to achieve reliable computational results within appropriate timeframe, the FE model needs to be calibrated and the mesh to be optimized. A tubular T-joint B3 with similar geometrical parameters in the literature (Delft et al., 1986; Bowness and Lee, 1995; BOMEL, 1995,b; Bowness and Lee, 1998) is selected for calibration and optimization. The geometric parameters of B3 are listed in Table 7.1. It can be seen that except for α ratio all the parameters of B3 are the same as those of the grouted joints, T208G/T215G. The crack configuration of B3 follows crack-2 in Table 7.2 with three depths, which are taken from reference (Bowness and Lee, 1998) based on experimental observation. It is noted at these depths the weld toe notch effect is insignificant to the SIF results. Both cracked and un-cracked FE models for B3 are built and analyzed with different mesh schemes.

Table 7.2 Crack aspect ratios studied

crack-1[a]		crack-2[b]	
a / T	*a* / c	*a* / T	*a* / c
0.1	0.08	-	-
0.3	0.07	0.203	0.43
0.5	0.09	0.447	0.314
0.7	0.11	0.756	0.24

[a] Reference (HSE, 1993)
[b] Reference (Bowness and Lee, 1998)

7.3.2.1 Modelling of cracked T-joint

For tubular joints, due to the complexity of its geometry, satisfactory 3D FE modeling

for weld toe cracking is scarce in the literature. Bowness and Lee (1995) report successful attempts to model weld toe crack using 20-node solid elements with fully compatible mesh according to the real crack shape. Cao et al (1998) introduce similar method to model a cracked Y-joint with straight and perpendicular crack.

In this study, straight and perpendicular surface crack with sharp weld toe is modeled using 20 node solid element with fully compatible mesh. The modeling procedure generally follows that of Bowness and Lee (1995). Figure 7.5 illustrates the procedure. The basic crack block is generated by the software FEA Crack (Quest-reliability-LLc) based on a T-butt joint with weld toe crack. The cracked T-butt model is then mapped to form a tubular T-joint.

Due to the symmetries of the structure and loading condition, the quarter model as shown in Figure 7.5 (e) is analyzed assuming the crack to appear on the both chord saddle points. The boundary condition is pin at the chord ends with negative pressure load on the brace. Linear elastic property with Young's modulus 205,000 MPa and Poisson's ratio 0.3 are assumed for both steel and weld.

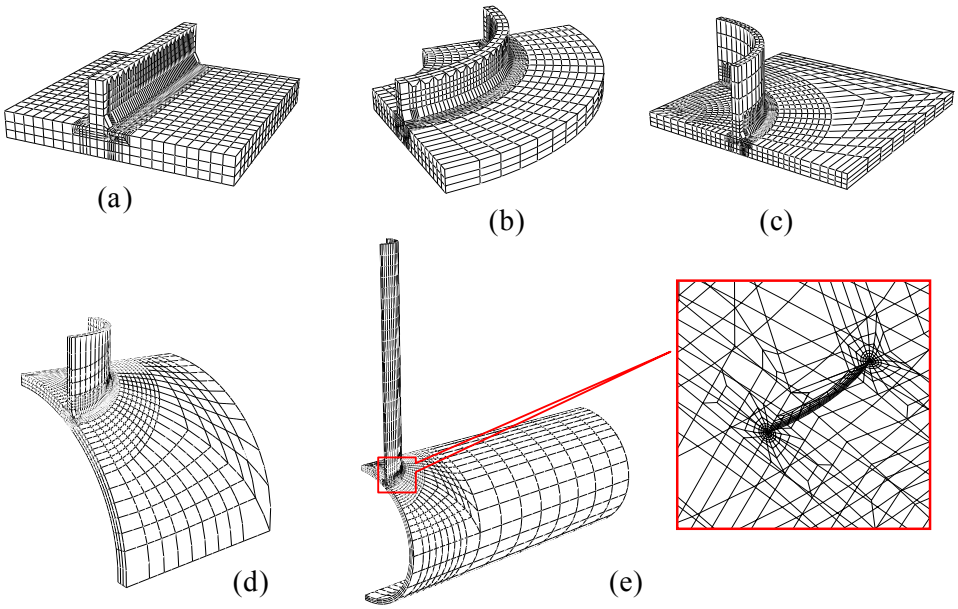

Figure 7.5 Procedure to generate a cracked tubular joint with weld toe cracking: (a) cracked T-butt joint generated by FEA crack (Quest-reliability-LLc); (b) mapping -1; (c) building mesh in Patran (MSC., 2005); (d) mapping-2; (e) building mesh in Patran (MSC., 2005)

7.3.2.2 Convergence study

In order to check the effects of mesh refinement, element integration scheme and solution technique on the accuracy of SIF, a series of convergence study are performed on the model with shallow crack. The mesh refinement scheme is carried out in two aspects, as shown Figure 7.6: one is with more rings within a fixed radius from crack tip; the other is 3 times refinement along the whole crack front. The element integration scheme is examined by assigning the elements of the crack block with either full or reduced integration, while the global element type is always using reduced integration for efficient computation.

For displacement extrapolation method, the SIFs are calculated based on Eq.(7.2) using nodal displacement values extracted from Abaqus result files. Because of the non-symmetric deformation for the crack, the nodes of the far side under the weld toe are taken for calculation as shown in Figure 7.7. For the J integral method, the SIFs are obtained through post-processing function in Abaqus (SIMULIA, 2007). All the SIFs are then normalized with nominal stress in the brace using Eq. (7.1) to determine the shape factor Y.

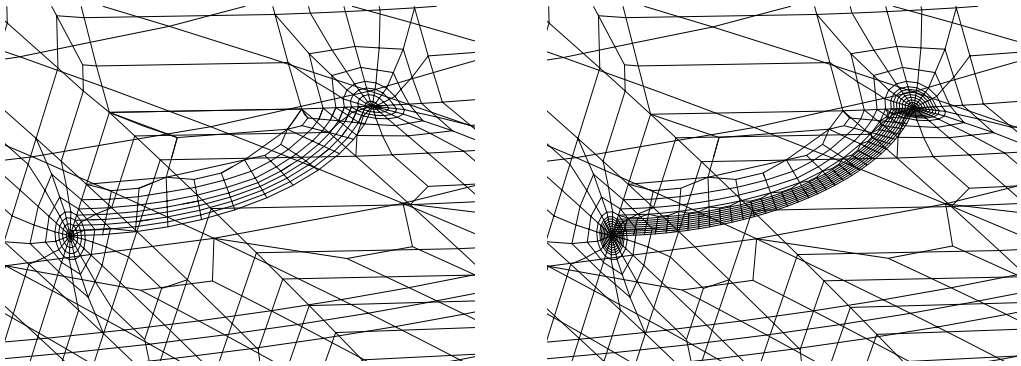

(a) (b)

Figure 7.6 Mesh refinement schemes for crack: (a) 4 rings; (b) dense - 8 rings (with 3 times refinement along crack front)

Figure 7.8 shows the comparison of shape factor Y. It can be seen that the results

of each model are quite close to each other with an average value around 4.9. For displacement extrapolation method, the dense model with reduced integration element is relatively stable and converges quickly. For J-integral method, dense mesh model tends to generate slightly higher results and is relatively insensitive to the element integration scheme. Comparatively, J-integral method shows better convergence and consistency. Considering both computational accuracy and efficiency, the model with 8 rings with reduced integration element using J integral method is preferred as an optimized choice.

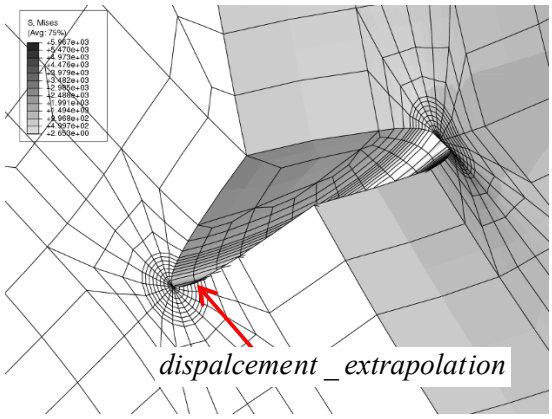

Figure 7.7 Deformed crack in FE analysis (exaggerated 20 times)

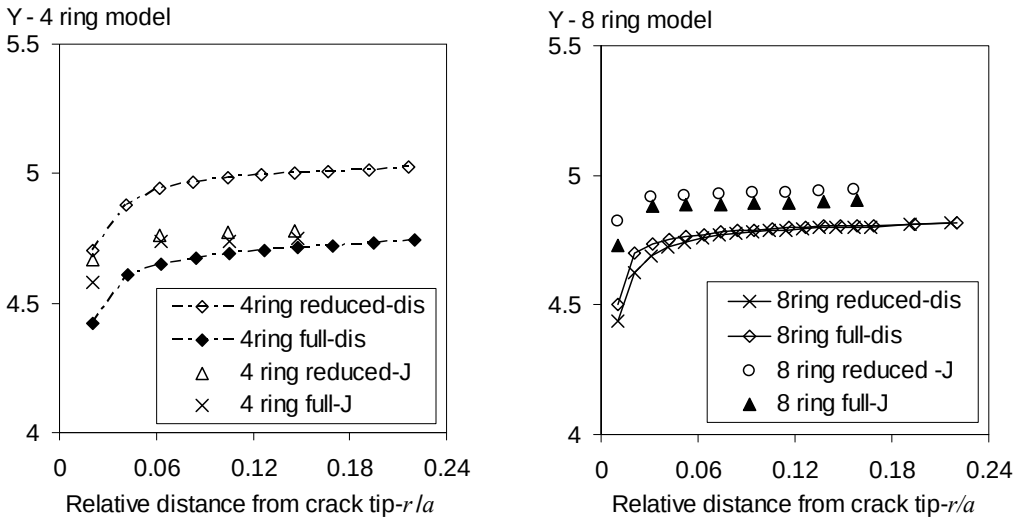

(a) (b)

Figure 7.8 (to be continued)

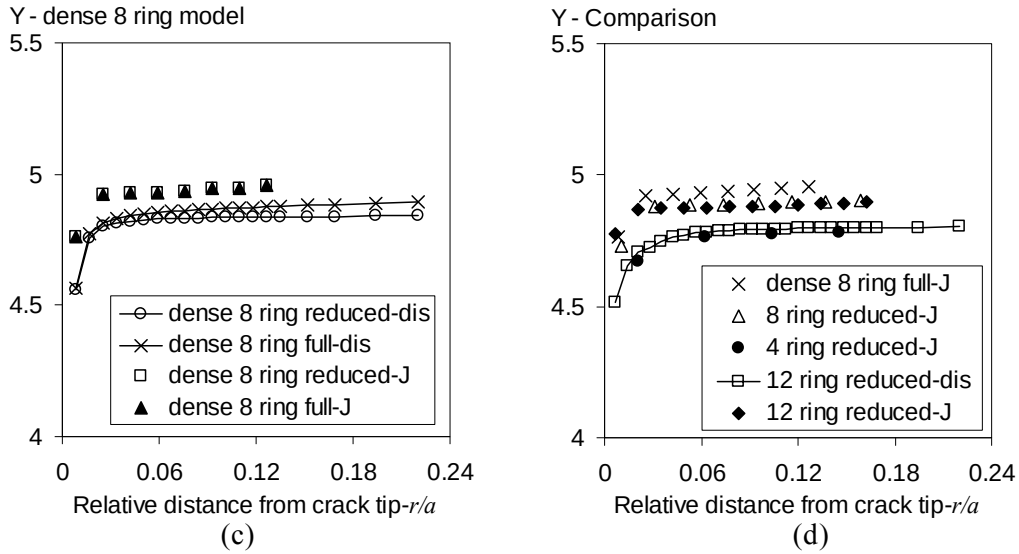

Figure 7.8 Convergence study of shape factor Y for B3 with shallow crack: (a) 4 ring model; (b) 8 ring model; (c) dense 8 ring model with 3 time refinement along crack front; (d) overall comparison

7.3.2.3 Calibration with previous results in the literature

For calibrating the shape factor Y, which is based on the 8 ring model using J integral method and denoted as NUS-calibration, this is plotted in Figure 7.9 together with the published results (Bowness and Lee, 1995; Bowness and Lee, 1998). It can be seen that the agreement is good: the calibration result is within the middle band between the upper and lower bounds of the reference results.

Further calibration is extended to un-cracked model to compare the hot spot stress SCF. The un-cracked model is generated using the node equivalence function in Patran (MSC., 2005) software by merging the nodes of crack surfaces. As shown in Table 7.3 good agreement is also achieved. Through the above comparisons, it is reasonable to conclude that:

- the SIFs determined from the J integral method based on domain integration embedded in Abaqus (SIMULIA, 2007) are in good agreement with those using the displacement extrapolation method;

- the FE results of SIF for the as-welded tubular joint fit the previous results very well, showing good correlation with the adopted mesh scheme;
- other related key issues, including boundary conditions and weld geometry, etc are also calibrated.
- as an optimized option, the 8 ring model with reduced integration element using J integral method is suitable for the study of the cracked grouted joint.

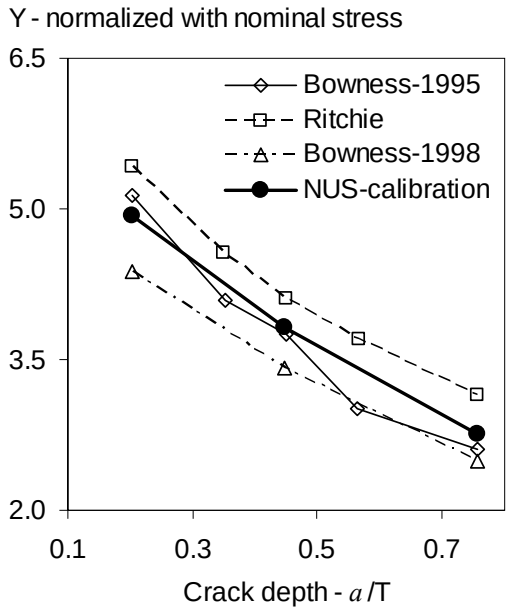

Figure 7.9 Comparison of shape factor Y of B3 with previous results in the literature for calibration

Table 7.3 Comparison of SCFs at chord saddle for un-cracked B3 model for calibration

Joint	Experiment[a]	Bowness[b]	**NUS calibration**	Efthymiou
B3	6.96	6.58	**6.74**	7.15

[a] References (Dijkstra and Noordhoek, 1985; Bowness and Lee, 1995)
[b] Reference (Bowness and Lee, 1995)

7.3.3 FE analysis for the grouted T-joint subjected to fatigue loading

The FE analysis is further performed on the grouted joint T208G/T215G as reported by Baker Jardine (HSE, 1993).

7.3.3.1 Modeling

Both cracked and un-cracked models are generated according to the geometric parameters in Table 7.1 and Table 7.2.

For un-cracked models, in addition to the above-mentioned mesh scheme of merging nodes on the crack block, another normal mesh scheme as shown in Figure 7.10 (b) is also generated and analyzed to test the sensitivity. The maximum difference of SCFs and DOBs for both grouted and un-grouted conditions caused by different mesh schemes is insignificant, which is less than 5%. For the merging-nodes mesh, due to the refinement at the crack end on the surface, the notch stress at the crack end is amplified, but the extrapolated hot spot stress is not much affected. It is found that the major influence of hot spot stress is from the weld leg length, regardless of the grouted or as-welded conditions. It is consistent with the understanding of positional issue for geometrical stress raised by Dijkstra and Noordhoek (1985) and de Back (1987) through experimental observation for as-welded joints.

The grout is meshed with the 'matching mesh' scheme, which means the contact pair nodes on the interface have exactly the same coordinates as shown in Figure 7.10 and Figure 7.11, to ensure the contact action is appropriately simulated (SIMULIA, 2007). 20-node solid elements with reduced integration are also employed. The center core with a radius of 10% of the grout cylinder is removed as shown in Figure 7.11, to eliminate the distorted finite elements. The influence of the removal to global stiffness is negligible, as only 1% volume is removed. The grout is assumed to be linear elastic with Young's modulus 30,000 MPa and Poisson's ratio 0.2. Surface-to-surface 'hard contact' algorithm in Abaqus/Standard (SIMULIA, 2007) is specified to simulate the interaction. The grout is assumed to fit tightly into the chord without gap, and no

adhesive bond is modeled for the steel-grout interface. Standard Coulomb friction model (SIMULIA, 2007) is assumed with frictional coefficient equal to 0.3. Symmetric condition, including joint geometry, cracks, and loading condition are assumed as previous, so that a quarter model is analyzed. The symmetric cracks are consistent with the experimental observation that in many occasions cracking is balanced on both saddle positions (HSE, 1993).

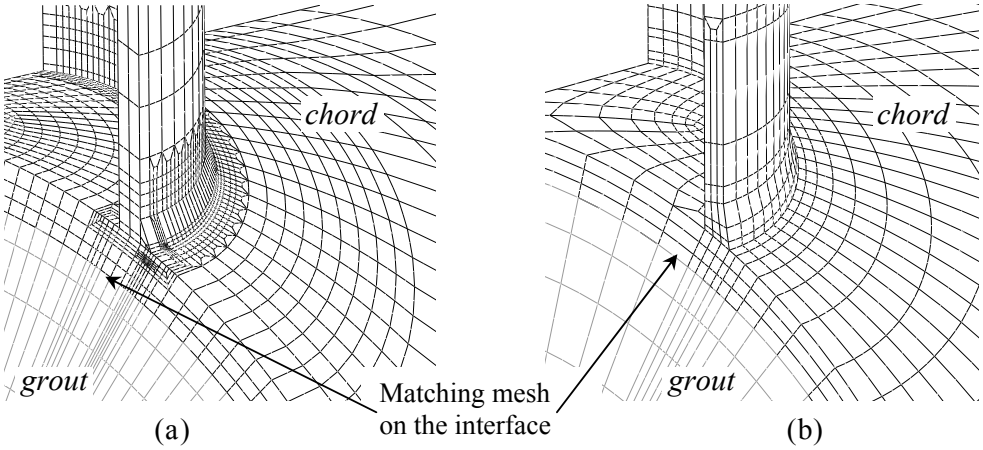

Figure 7.10 Two mesh schemes for the grouted joint in uncracked condition for determination of SCF: (a) merged nodes of crack block; (b) conventional mesh

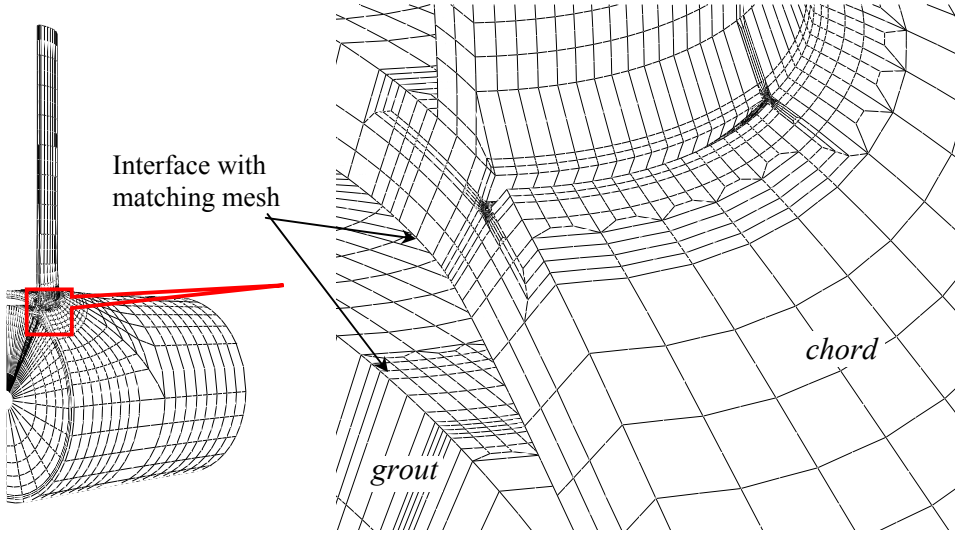

Figure 7.11 Deformed, grouted and cracked FE model: crack-1 with a/t=0.3 (extravagant 100 times)

For cracked models, two crack configurations as shown in Table 7.2 are studied. Crack-1 corresponds to the grouted joint taken from the HSE report (HSE, 1993); crack-2 corresponds to the as-welded joint in the reference (Bowness and Lee, 1998). It can be seen crack-1 was relatively longer and narrower. This is due to the difference in stress distribution. As shown in Figure 7.12, the grouted joint is with more even stress distribution along the welded brace-chord intersection.

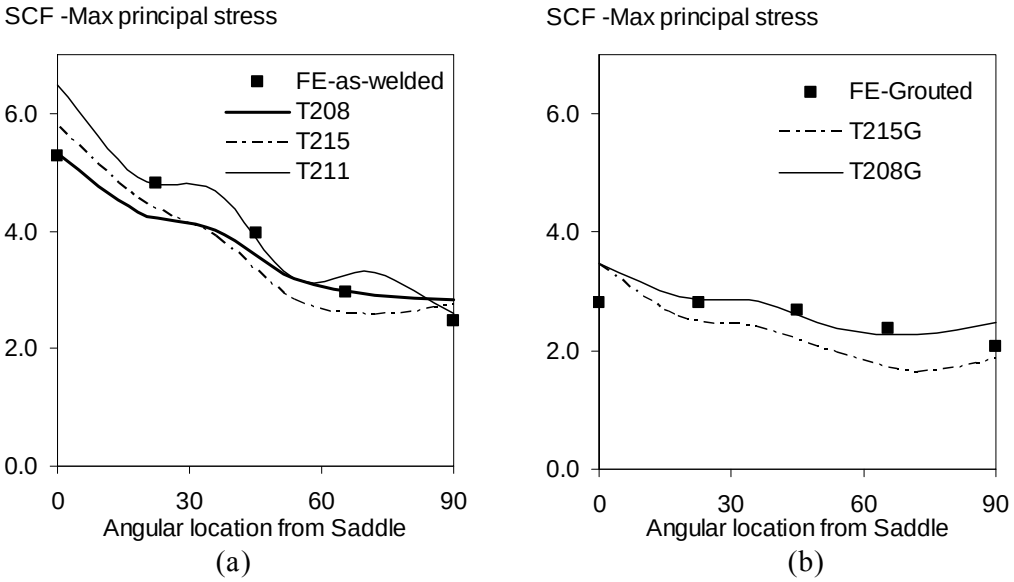

Figure 7.12 Hot spot stress SCFs for uncracked models under axial tension: (a) As-welded, T211 is the T joint with same geometric parameters in the UKOSRP research program; (b) infill grouted

7.3.3.2 FE results

It is noted that contact analysis is a highly non-linear procedure. Similar sensitivity study as in Chapter 6 was also conducted in this case. It is found both SCF and SIF are insensitive to the load level of imposed tension on the brace. The non-linearity due to contact action between the infilled grout and chord inner surface is insignificant under both cracked and un-cracked conditions, implying the grouted joint may be treated similarly as as-welded joint (at least in pulsating tensile cyclic loading

condition). The detailed FE results are presented below.

SCFs for un-cracked model

Figure 7.12 shows the computed FE SCF results and the comparison with the experimental measurements. The presented results are from the model converted from cracked model by merging the crack surface nodes. The hot spot SCF is based on the ECSC definition using maximum principal stress for extrapolation. The reduction factor obtained from FE results based on chord saddle SCFs is 0.54, lower than 0.6 in the report (HSE, 1993). The DOBs obtained by linearization of through thickness stress at hot spot are 0.82 and 0.7 for as-welded and grouted joint respectively. The un-cracked results are summarized in Table 7.4. For as-welded joints, the experimental SCF results exhibit a reasonable scatter band. The FE SCF at saddle is at the lower bound probably due to the perfect model and weld profile assumed in the FE model. For grouted model, the FE results shows slightly better stress reduction and more even stress distribution. This may also be due to the perfect condition assumed for the grouted joint. It is reasonable to expect that minor shrinkage may have occurred in the grout of the actual specimens. As indicated in Chapter 6: **6.3.4.2**, minor shrinkage gap at the grout-steel interface will cause a reduction in strengthening effect, and the stress reduction will be less than the perfect condition. In general, the FE results reasonably agree with the experimental results. It is considered acceptable for mechanism study with perfect conditions assumed.

Table 7.4 Summary of results for un-cracked model

Joints	SCF-FE	Reduction factor - FE	SCF-test	Reduction factor - test	DOB-FE
T208G/T215G	2.8	0.54	3.4	0.6	0.7
T208/T215	5.27		5.3-6.5		0.82

SIFs for cracked models

The SIF results are normalized with both nominal stress and hot spot stress with the shape factors denoted as Y and Y_{hss} respectively. The comparisons together with the calibration case are shown in Figure 7.13. Figure 7.13 (a) and (b) are for crack-1 in grouted and crack-2 in as-welded conditions to simulate the test situations. Figure 7.13 (c) and (d) are for crack-2 in both as-welded and grouted conditions to show the change of crack driving force when the chord of a cracked as-welded joint is infilled with grout.

Figure 7.13 (a) shows in terms of nominal stress, the shape factor Y of as-welded joint is larger than that of grouted joint. When the crack grows deeper, the difference becomes smaller. On the other hand, Figure 7.13 (b) shows that in terms of hot spot stress the shape factor Y_{hss} of grouted joint is significantly larger than that of as-welded joint, which explains why the fatigue lives of grouted joints (T208G and T215G) are shorter than the prediction by mean S-N curve of as-welded joints. Figure 7.13 (b) also shows that in terms of hot spot stress, the as-welded joints with different SCFs but similar DOBs (the DOB for B3 is 0.84) will have similar shape factors Y_{hss}, demonstrating the validity of hot spot stress S-N curve for as-welded joints. Figure 7.13 (b) strongly supports the fatigue test result of the grouted joint shown in Figure 7.2. Note that the real specimens (T208G and T215G) may have experienced larger hot spot stress range than that predicted by FE model due to the perfect condition assumed, as observed in Figure 7.12.

Figure 7.13 (c) shows that a significant reduction in crack driving force will occur, if a fatigue damaged as-welded joint is infill grouted, in terms of nominal stress (subjected to same brace load). However, if expressed in terms of hot spot stress, the opposite trend, as shown in Figure 7.13 (d), will occur.

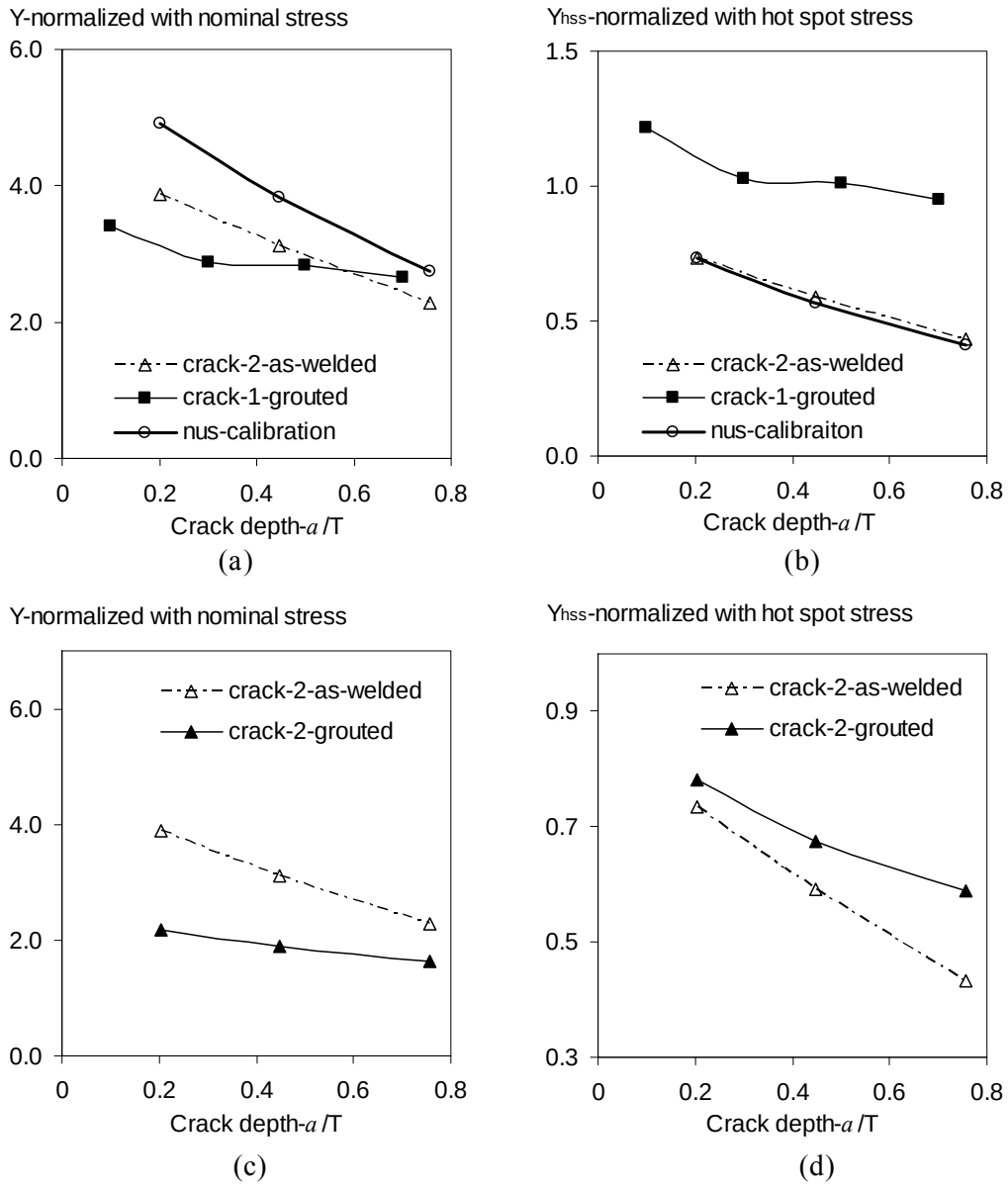

Figure 7.13 Comparison of shape factors: (a) Ys of the joints; (b) Y_{hss}s of the joints; (c) Y of crack-2; (d) Y_{hss} of crack-2

7.4. Determining SIF using engineering formula

In practice, SIF is often determined by empirical formula based on the Newman-Raju solution in Eq.(7.5) (Newman and Raju, 1981).

$$K_I = (\sigma_m + H\sigma_b) \cdot F \cdot \sqrt{\pi a / Q} \qquad (7.5)$$

where σ_m and σ_b are the membrane and bending components of the through thickness stress for a plate; for a tubular joint the linearized stress as illustrated in chapter 5, Eqs.(5.2) and (5.3), can be applied.

H, Q and *F* are functions of crack depth, plate thickness and elliptical angle (Anderson, 2004).

Eq. (7.5) reveals the different contributions of membrane and bending stresses to SIF, providing a strong basis for discussion on the influence of degree of bending (DOB) to fatigue strength.

7.4.1 SIF derived from hot spot stress and degree of bending

The design codes for fatigue and fracture (BSI, 1993; BSI, 2005; Hobbacher, 2005) recommend equation Eq.(7.6) to calculate SIF for welded T-butt joints, which is originally proposed by Maddox (Maddox, 1974):

$$K = (M_{km} Y_m \sigma_m + M_{kb} Y_b \sigma_b]\sqrt{\pi \cdot a} / \phi \qquad (7.6)$$

where, Y_m and Y_b are geometry factors based on the plain plate solution of Newman and Raju, Eq. (7.5)(Newman and Raju, 1981),

M_{km} and M_{kb} are magnification factors on membrane and bending stresses due to the weld toe notch stress concentration, and

Φ is the elliptical integral angle of the surface crack, Figure 7.2.

The solution of M_{km} and M_{kb} in the design codes (BSI, 1993; Hobbacher, 2005) is from Maddox (1974) by 2D FE solution. BS7910 (BSI, 2005) also includes additional results by Bowness and Lee (Bowness and Lee, 2000) using 3D FE results.

Hot spot stress is always implicitly assumed to be equal to through thickness structural stress as illustrated in Chapter 5, Eq. (5.4), according to the codes (BSI, 1993; Niemi, 1995; BSI, 2005; Hobbacher, 2005; Niemi et al., 2007). By using DOB the membrane stresses σ_m and bending stress σ_b can be determined. The SIF is then

expressed as Eq.(7.7) (BSI, 2005):

$$K = \sigma_{hss}[M_{km}Y_m(1-DOB) + M_{kb}Y_bDOB]\sqrt{\pi \cdot a}/\phi \qquad (7.7)$$

For the deepest point of semi-ellipse crack, ϕ equals to π/2, which can be included in Y_m and Y_b, so that SIF can be simplified as Eq.(7.8):

$$K = \sigma_{hss}[M_{km}Y_m(1-DOB) + M_{kb}Y_bDOB]\sqrt{\pi \cdot a} \qquad (7.8)$$

Eq. (7.8) is derived from welded plate (T-butt) joint. When used for tubular joints, the T-butt joint is considered as unfolded tubular joint. BS7910 (BSI, 2005) recommends 2D solution for tubular joint and indicates the SIF results will be conservative due to the different load shedding effects for T-butt joint and tubular joint. Aaghaakouchak et al. (1989) propose a simplified model by a hinge analogy to account for load shedding of tubular joint. In the model the membrane stress σ_m is assumed to be unaffected by the crack propagation, while the bending stress range σ_b is assumed to decrease linearly with crack depth, the virtual changing bending stress, denoted as σ_b', is expressed as:

$$\sigma_b' = \sigma_b(1-a/t) \qquad (7.9)$$

Hence, if the load shedding effect is considered for tubular joints, the SIF becomes:

$$K = \sigma_{hss}[M_{km}Y_m(1-DOB) + M_{kb}Y_bDOB(1-a/t)]\sqrt{\pi \cdot a} \qquad (7.10)$$

7.4.2 Comparison of SIF results

In the study, both Eq. (7.8) and Eq.(7.10) are employed to determine the SIF, the geometry factor Y_m and Y_b are obtained using Newman-Raju solution Eq.6 by setting the W and t, as shown in Figure 7.2 (b), equal to the circumference of the brace (1500mm) and chord wall thickness (32mm) respectively. The weld toe notch magnification factors M_{km} and M_{kb} are calculated using 2D solutions in the design

codes(BSI, 2005; Hobbacher, 2005). The SCFs and DOBs used for both grouted and as-welded joints are from the FE analyses of un-cracked models.

Table 7.5 and Table 7.6 show the results of shape factors normalized with hot spot stress. Y_{hss} denotes without load shedding following Eq. (7.8), and Y'_{hss} denotes with load shedding model using Eq. (7.10). It can be seen that the trend of the SIFs predicted by formula are consistent with FE results for both grouted and as-welded joints, and the results of shallow crack without load shedding are very close to the numerical model. Consistent with BS7910 (BSI, 2005), without load shedding the prediction is conservative, while with load shedding the prediction under-estimates the SIF up to 20%.

Table 7.5 Comparison of shape factor Y_{hss} for crack-2 in as-welded condition (T208/T215)

a / c	*a*/T	SCF	DOB	Y_{hss}-FE	Y_{hss} -Eq. (7.8)	Difference from FE	Y'_{hss} -Eq. (7.10)	Difference from FE
0.43	0.203	5.27	0.82	0.74	0.76	3.9%	0.64	-12.4%
0.314	0.447			0.59	0.68	15.5%	0.47	-19.8%
0.24	0.756			0.43	0.57	31.3%	0.36	-16.0%

Table 7.6 Comparison of shape factor Y_{hss} for crack-1 in grouted condition (T208G/T211G)

a / c	*a* / T	SCF	DOB	Y_{hss}-FE	Y_{hss} -Eq. (7.8)	Difference from FE	Y'_{hss} -Eq. (7.10)	Difference from FE
0.08	0.10	2.80	0.70	1.22	1.19	-2.5%	1.11	-8.5%
0.07	0.30			1.03	1.05	2.3%	0.86	-16.4%
0.09	0.50			1.01	1.15	13.5%	0.85	-16.6%
0.11	0.70			0.95	1.19	24.8%	0.83	-12.4%

7.5. Discussion on the influence of DOB to fatigue life

From the comparison of SIF results as shown in Table 7.5 and Table 7.6, the effect of DOB can be seen clearly: a lower DOB is associated with larger shape factor Y_{hss}. More precisely, to compare the stress fields entering into the computation in FE study, the normalized and linearized through thickness stresses on the plane of deepest crack

at the location of 0.4T away from weld toe are extracted from the 3D FE models and plotted in Figure 7.14. It can be seen that when normalized with hot spot stress, the grouted joint experienced more critical tensile (membrane) action under both cracked and un-cracked conditions, consistent with the observation for the effect of DOB.

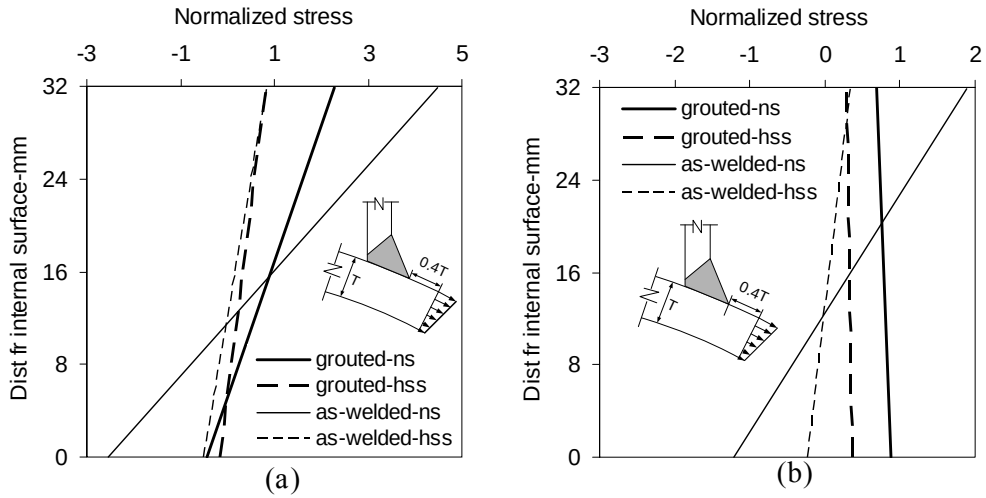

Figure 7.14 Linearized through thickness stress of T208(G)/T215(G) at 0.4T away from weld toe: (a) uncracked model; (b) cracked model with crack depth *a*/T=0.5. ns denotes normalized with nominal stress, hss denotes normalized with hot spot stress

The SIF results obtained support the fatigue test result, which suggests that in terms of hot spot stress, the fatigue strength of grouted joint will be lower than that of as-welded joint. The S-N curves used for as-welded tubular joints, e.g. T curve for 32mm thickness and T' curve for 16mm thickness, are not applicable for grouted joints of the same thickness due to different DOBs associated with the joint behavior.

Similar findings for the effect of DOB of tubular joints are also reported in the literature. Berge (1994; Boge et al., 2007) shows that a shift in DOB by 15% will result in a shift in fatigue life by a factor of two. Lee and Bowness (2002) indicate the average DOB of 16mm thick T-joint in the HSE database (HSE, 1999), which is used for producing T' curve, is 0.81, and incorporation of DOB yields effective improvements in the fatigue life prediction. However, the effect of DOB is ignored in

current design codes for as-welded joints, which can be one of the many sources for the scatter of fatigue data.

For tubular joints with chord fully infilled with grout, it is crucial to include the effect of DOB in the fatigue assessment by the hot spot stress approach. If the DOB is lowered considerably e.g. from 0.82 to 0.7 as shown in this case, shorter fatigue life than the mean S-N curve (or lower safety margin) is expected.

7.6 DOB for X-joint with fully grouted chord

It has been shown the application of fracture mechanics method to analyze the fatigue performance of tubular joints. However, it is not practical to replace the hot spot stress S-N approach as recommended in the current design codes with the fracture mechanics method. A realistic treatment for grouted tubular joint is to include the DOB together with the hot spot stress.

For as-welded tubular joints, there have been proposals in the documentation for calculating DOBs (Connolly et al., 1990; Chang and Dover, 1999). For infilled grouted joints, similar parametric FE studies have been carried out in NUS for grouted X-joints as detailed in Chapter 6. The joint configurations studied in Chapter 6 for hot spot stress computation were studied again for DOB. Consistently, the four load cases for hot spot stress assessment were studied:

- Chord saddle under brace axial tension;
- Chord saddle under out-of-plane bending;
- Chord crown under brace axial tension;
- Chord crown under in-plane bending;

As introduced in Chapter 5, there are the two methods: through-thickness linearization, Eq. (5.2) and (5.3) and surface extrapolation, Eq. (5.6) to determine DOB, which were compared again here for more joint configurations. Interestingly,

DOB results were found very close to each other: the difference is less than 3%, and in good agreement with the prediction by empirical formula proposed by Chang and Dover (1999). The results reported below are from through thickness linearization. Figure 7.15 shows the change of DOB due to infilled grout. It could be seen that for axial tension, the reduction of DOB at chord saddle is significant, while at chord crown DOB is increased. For both in-plane and out-plane bending cases the change of DOB is not that significant as the axial tension.

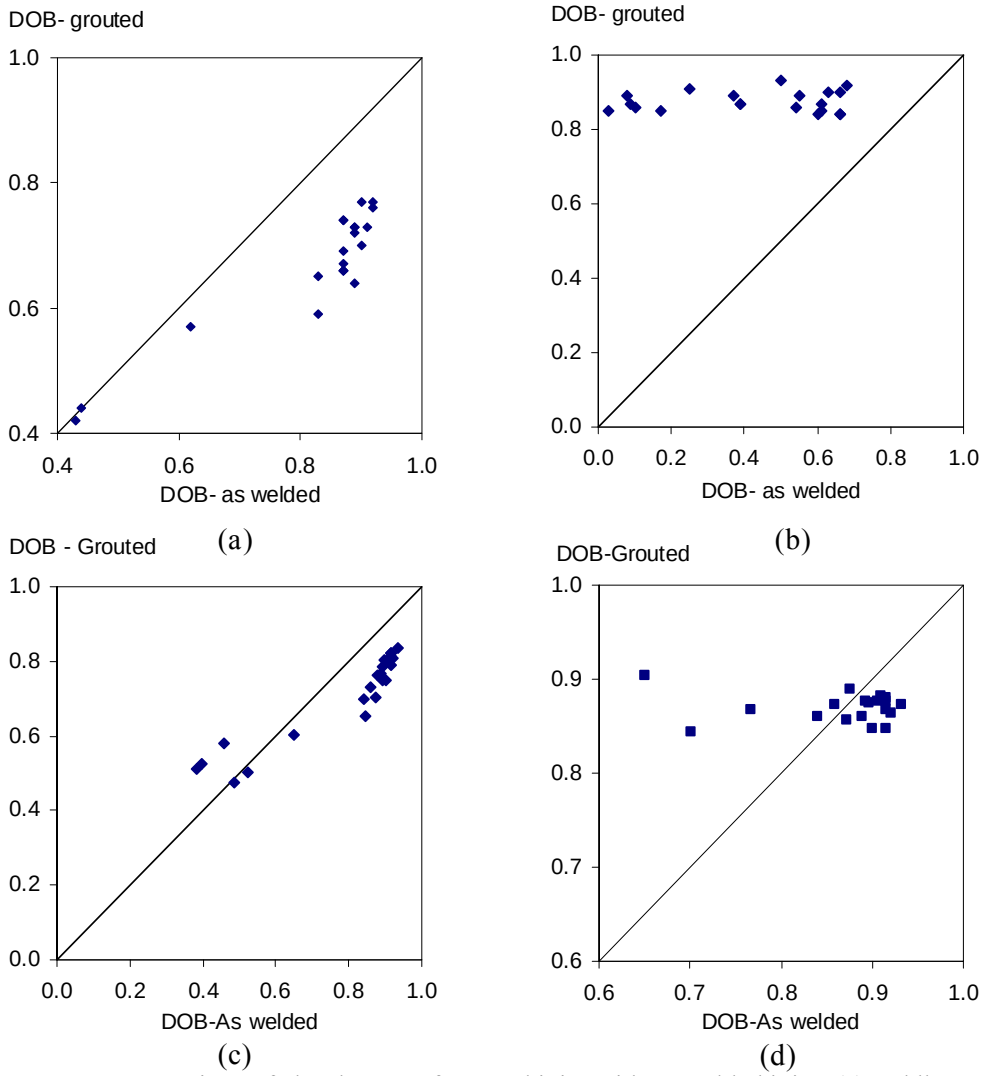

Figure 7.15 Comparison of chord DOB of grouted joint with as-welded joint: (a) saddle under axial tension; (b) crown under axial tension; (c) saddle under out plane bending; (d) crown under in plane bending

In order to facilitate the practical design and analysis, the DOB results are expressed in charts as shown in Figure 7.16 to Figure 7.19. With DOBs of grouted joints known, it is convenient to perform quick judgment whether the fatigue life of grouted joint assessed by current S-N curves, like T or T', is conservative or not. Or it is not difficult to carry out fracture mechanics analysis following BS7910 (BSI, 2005), as what has been shown in **7.4.1**.

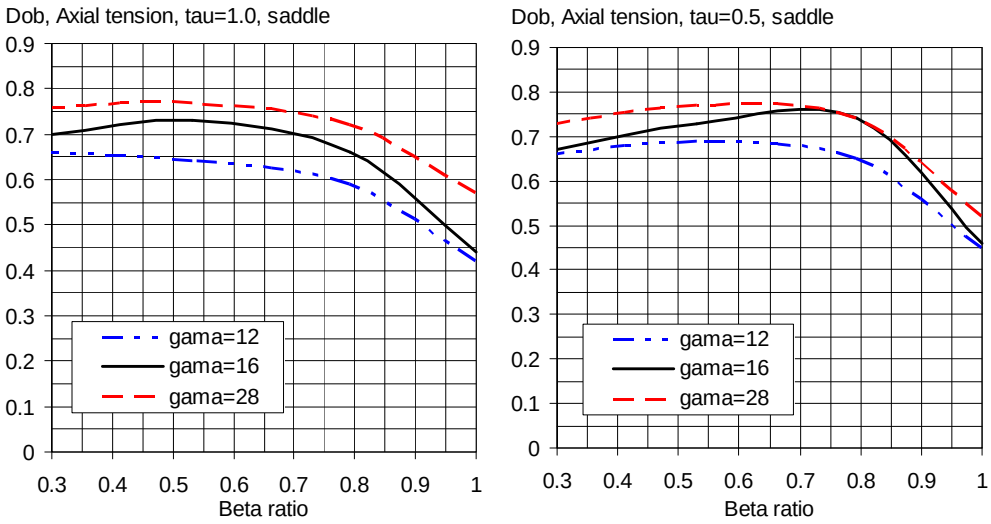

Figure 7.16 DOB for X joint at chord saddle under brace tension, (a) $\tau = 1$; (b) $\tau = 0.5$

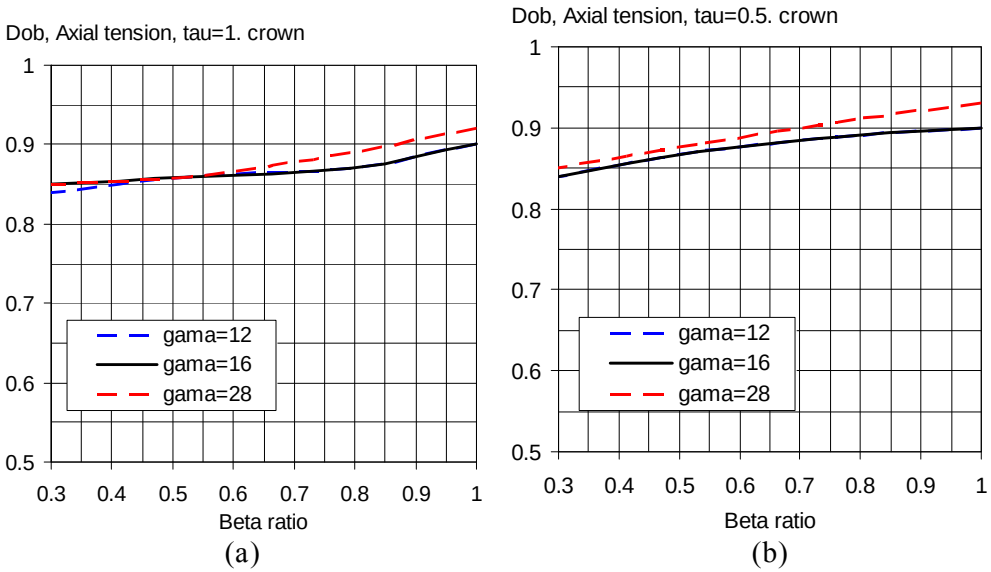

Figure 7.17 DOB for X joint at chord crown under brace tension, (a) $\tau = 1$; (b) $\tau = 0.5$

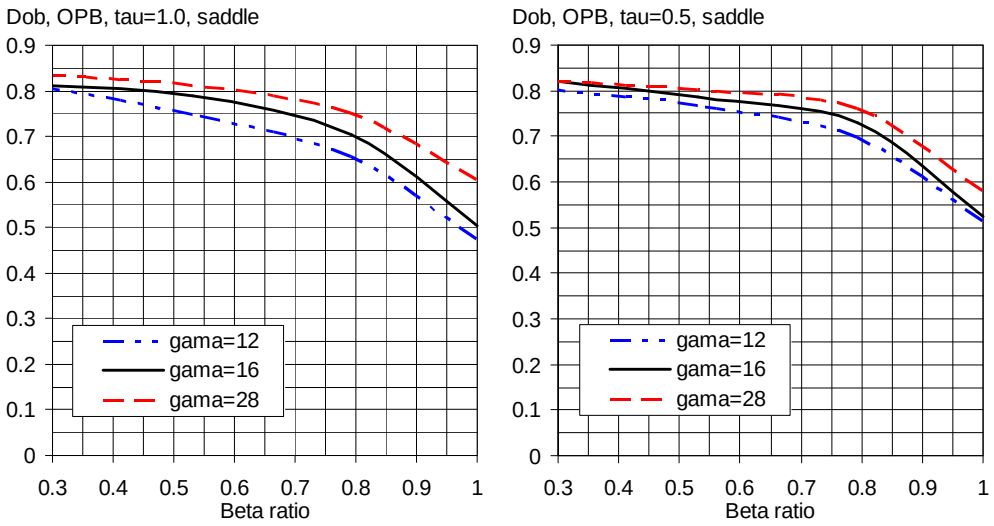

Figure 7.18 DOB for X joint at chord saddle under brace out-plane bending, (a) $\tau = 1$; (b) $\tau = 0.5$

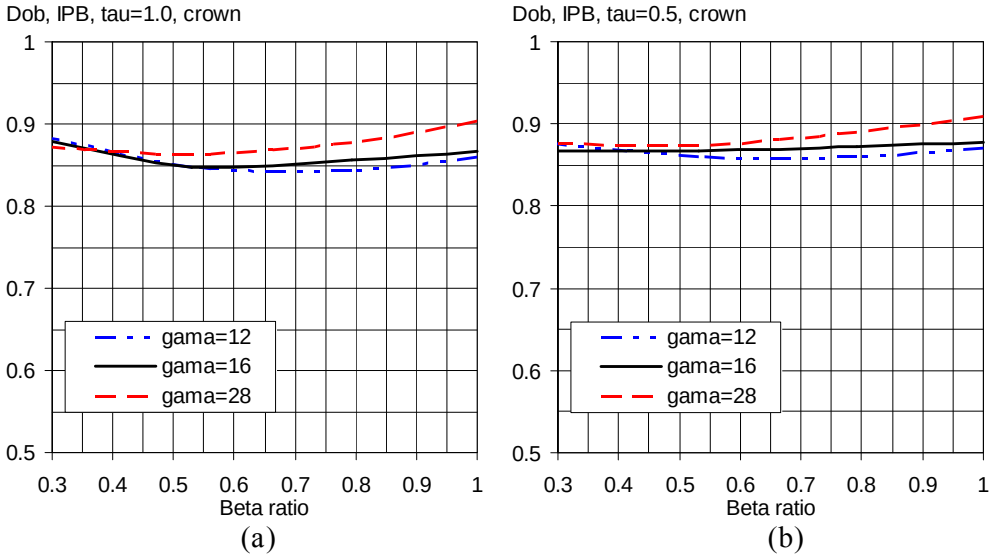

Figure 7.19 DOB for X joint at chord crown under brace in-plane bending, (a) $\tau = 1$; (b) $\tau = 0.5$

7.7 Conclusions

Stress intensity factors for a grouted tubular joint determined both numerically and empirically are consistent and strongly supportive of the reported fatigue test results. The following conclusions can be drawn:

- In terms of nominal stress, or a joint subjected to the same brace load, the fatigue life of tubular joint with chord fully infilled with grout will be improved as compared with the original as-welded joint.
- However, in terms of hot spot stress, the fatigue strength of grouted joint may be lower than that of as-welded joint, because when normalized with hot spot stress, the shape factor, Y_{hss}, of grouted joint is higher than that of original as-welded joint due to the reduction in DOB caused by the presence of infilled grout in the chord.
- For grouted tubular joints it is essential to include the effect of DOB in practical design and analysis. For certain configurations of the grouted joints as considered here, the DOB are significantly different from the original as-welded condition. Direct application of hot spot stress S-N curve of as-welded tubular joints to grouted joints will be un-conservative.
- As a complementary part to the reduction of SCF of grouted X-joints, a series of design charts of DOBs were produced for better estimation of fatigue life of X-joints with fully infilling grouted chord.

Chapter 8

Conclusions and recommendation for future work

8.1 Conclusions from present research

From numerical simulation to experimental investigation, the application of grouting in tubular structures has been examined from the viewpoints of structural analysis and design. Certain topics with insufficient coverage in current design codes have been reviewed and investigated, and a number of supplementary proposals have been made in the previous chapters. The final conclusions are summarised in the following sub-sections.

8.1.1 Partially grout infilled tubular members

It is possible to utilize partial grouting method to strengthen a tubular member with certain load transfer mechanism through the proposed scheme of stiffening plates, which is particularly useful to solve local buckling problem for tubular member under strong compressive action. It is encouraging to find that the proposed stiffening plates, or ring stiffeners, can also be utilized as mechanical aids for partial grouting to enhance the member strength. The strengthening effect is found to be significant.

For structural design, the adhesive bond at the interface between the grout and steel is observed to play an insignificant role in the load transfer mechanism for partial infilled grouting for tubular member, and is recommended to be ignored.

The proposed design equation in this thesis based on contact and bearing mechanisms for stiffening plates is found to provide good prediction of the member strength. When compared with the present experimental results, the prediction given by the proposed equation is on the conservative side with acceptable safety margin.

According to the contact - bearing strengthening mechanism as observed in the present study, high strength grout like Ducorit D4, provides reliable strengthening, and is recommended for field implementation.

8.1.2 Fatigue assessment of tubular joint with fully grouted chord

It is confirmed in this study that infilling the chord member of tubular joint can reduce the hot spot stress concentration factor (SCF) significantly. For grout infilled X joints, the SCF remains constant with the variation of external load applied. The shake down phenomenon of grouted X joint is similar to that of as-welded (un-grouted) joint. Therefore, the fatigue assessment for variable amplitude fatigue load for as-welded joint is applicable for grout infilled joint.

For X joints, a series of design charts for reduction factors have been derived and are proposed to facilitate design calculation. It is shown that it can be used together with the Efthymiou equation to generate accurate SCFs for grouted X joints. For axial loading and out of plane bending, the reduction at chord saddle may become uncertain when the brace diameter equals to chord diameter (β=1). This can be attributed to strong influence of inherent uncertainty of weld profile for β=1 case.

Due to the presence of grout inside the chord member, the SCF is reduced but the degree of bending stress (DOB) is also altered. For brace axial tension, infilled T and X joints will have smaller DOBs than the corresponding as-welded joints, leading to lower fatigue strength in terms of hot spot stress (geometrical stress) range. Through application of computational fracture mechanics, this experimental evidence is

verified in this thesis. Hence, it is essential to include the DOBs in dealing with fatigue problem of grouted joints. A series of design charts of DOBs for grouted tubular X joints are proposed to satisfy the design needs.

8.2 Major findings and contributions

As mentioned, this study is to supplement the insufficient coverage in current design code and practice for grouted member and tubular joints. The aim has been achieved in general, and the major findings and contributions are listed in Table 8.1 below:

Table 8.1 Major findings and contributions from the thesis

Topics	Issues	Current code and practice	After the present research
Partially grout infilled tubular members	Applicability of partial grouting	Not available	• Applicable with contributions from mechanical aids, ring stiffener and chamfer; • Design equation proposed
	Local buckling of existing member	Welding additional member or replacement	Application of partial grouting
	Adhesive bonding on steel-grout interface	Arguable, not clear	Confirmed that under partial grouting the adhesive bond is insignificant
	High strength grout Ducorit D4	Constitutive modelling not available	Successful application of concrete damaged plasticity model in Abaqus using proposed stress – strain curve with damage parameter
Fatigue assessment for fully grout infilled tubular joints	Fatigue assessment method	Inconsistent statement in current design codes	Present method applicable due to: • independency of SCFs of grouted joints to applied load • Similar shake down effect of grouted joint to empty joint
	Reduction factor of SCF	Inaccurate	Charts proposed for grouted X joints with accurate prediction
	Fracture mechanics method	Unclear	• Successful application of computational fracture mechanics to verify the experimental evidence of DOB; • DOB charts for grouted X joints proposed

8.3 Recommendation for Future work

It is understood that although the present investigation has found solutions to the studied problems, further research work needs be carried out. Meanwhile new problems related to the subjects have been encountered during the study, and will need to be solved in future work.

8.3.1 Partial infilled grouting for tubular members

The identified future work for this topic is listed as follows:

8.3.1.1 Constitutive modelling for high strength grout

It is noticed that concrete damaged plasticity model embedded in Abaqus provide a solution to for high strength grout like Ducorit D4. However, associated with this model there are a few parameters difficult to determine due to the limitation of current test equipment in NUS. The simulations conducted in this thesis, as presented in Chapter 4, utilized default value in Abaqus. It is possible to further study the influence of these parameters, and then decide the best combination for particular cementious material, like D4, S5, etc.

Furthermore, it is possible to generate specific constitutive model for high strength grout, as the small scale column stub test provided very good test result for calibration.

8.3.1.2 Quantifying strengthening effect of ring stiffener

It has been demonstrated that the ring stiffener, which exists widely in fixed jacket platforms, can be utilized as mechanical aids for partial grouting strengthening method. The utilization of existing parts in the frame would lead to significant reduction or even exclusion of additional weld for applying partial grouting method.

The proposed equation is most suitable for stiffening plates based on shear mechanism. When applied for ring stiffener, it will generate overestimated prediction

as exhibited in the small scale test results. It is essential to proceed with further study to quantify the contact – bearing effect with ring stiffeners. The work can be done by means of both FE simulation and physical tests.

8.3.2 Fatigue assessment for grouted tubular joints

With regards to fatigue assessment, a few problems have been identified. Some of them are related to fundamentals of basic approaches to fatigue problem for tubular joint. Further studies as listed below are considered essential.

8.3.2.1 Large scatter of SCF values for joints with equal brace and chord diameters

It has been verified by means of both FE analysis and test measurement that the SCFs for the joint with equal brace and chord diameters (β=1) joints are with large scatter, because of the inherent uncertainty of weld profile influencing the SCF values significantly for this type of joints. However, it is also interesting to find that the membrane stress component remains almost constant. The questions associated with this phenomenon are:

- how to deal with the large scatters;
- and whether the fatigue life is dominant by the mean value or the worst value, or the membrane component of the hot spot stress.

For the first question, it may be possible to carry out statistics or reliability study. The scatters can be expressed as the difference between the real (or simulated) value and the Efthymiou prediction. For the second question, the best answer is, of course, from the fatigue test results. From preliminary literature review, the information is found to be insufficient. Additional tests with focus on this joint type (both in as-welded and grouted conditions) may be carried out, because there are large amount of X joint with equal brace and chord diameter in existing fixed platform. It is

understood that the two questions are closely related to each other, if there is answer to the second, then the first one will be easy to handle.

8.3.2.2 Proposed fatigue tests for grouted tubular joints

It is clear that infill grouting for the chord member would significantly reduce SCFs. Meanwhile, the DOBs will also be altered due to infill grouting. The study using fracture mechanics indicates lower DOB lead to shorter fatigue life, which requires the hot spot stress S-N curve for tubular joint should be further sorted by DOB. However, the influence of DOB is ignored by current design codes. For X joints under brace axial tension, the reduction of SCF and DOB happens simultaneously after the joint is infill grouted. To answer the questions:

- which factor is dominant? and
- how significant the result will be by ignoring DOB?

experimental evidence is needed obviously. It is possible to carry out the fatigue tests for grouted tubular joints in the structural lab of NUS using 200 T dynamic test rig as shown Figure 8.1. The detailed proposal is attached in Appendix.

.

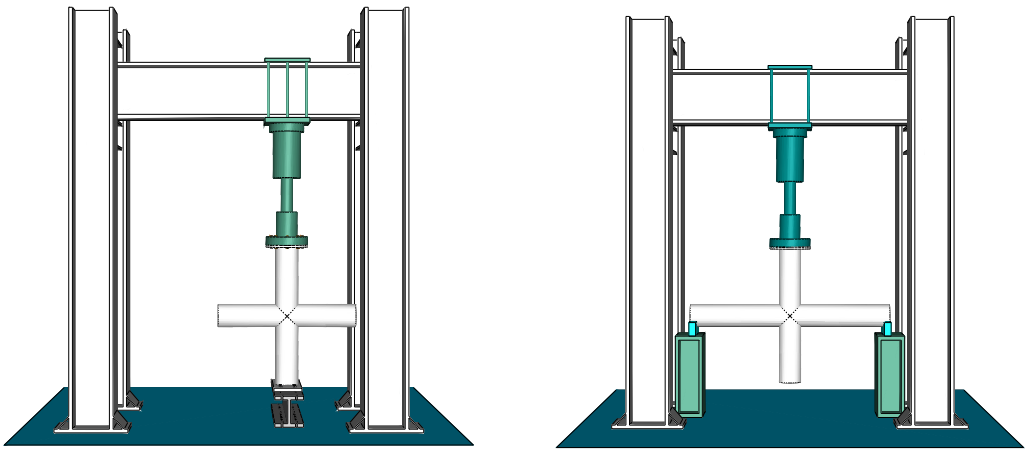

Figure 8.1 Proposed fatigue test set-up in NUS: (a) brace axial loading; (b) in-plane bending

It is understood that the recommended S-N curves in current design codes are based on the fatigue test results for decades. It is a culmination of tens or hundreds of selected data base. Large amount of tests may be needed to sufficiently proof and generate the S-N curve for grouted joints.

For infill grouting of an existing joint in aging platform, fracture mechanics method as demonstrated in previous chapter is necessary to apply to evaluate the strengthening effect and plan for inspection schedule.

8.3.3 Other related topics

In addition, it may be necessary to carry out other related topics as listed below:

- failure assessment by means of failure assessment diagram (FAD) method using the cracked model. The FAD method is widely adopted in current design codes. When applied on grouted tubular joints, certain issues need to be solved like the demarcation between plastic failure and brittle fracture, effect of residual stress induced by welding process, and proportional loading, etc.
- reliability study using stochastic model for the investigation of fatigue of grouted joints. The stochastic model studies the uncertainty, which is an important concern for practical application for an empirical engineering model. If more refined deterministic model is proposed for fatigue of tubular joints, like inclusion of DOB, it is essential to evaluate its impact on safety margin.

Reference

Aaghaakouchak A., G.Glinka and S.Dharmavasan (1989). A load shedding model for fracture mechanics analysis of fatigue cracks in tubular joints. 8th International conference on offshore mechanics and arctic engineering.

ABS (2003). Guide for the fatigue assessment of offshore structures. Houston, USA, American Bureau of Shipping.

Anderson T. L. (2004). Fracture mechanics: fundamentals and applications, CRC.

API (2000). RP 2A-WSD Recommended Practice for Planning, Designing and Constructing Fixed Offshore Platforms - Working Stress Design.

AWS (1994). Structural Welding Code-steel. ANSI/AWS D1.1-94.

Back J. d. (1987). The design aspects and fatigue behaviours of tubular joints. Steel in Marine Structures. C. Noordhoek and J. d. Back. Amsterdam, Netherland, Elsevier.

Bathe K. J. (1996). Finite Element Procedures, PRENTICE HALL.

Berge S. (1985). On the effect of plate thickness in fatigue of welds. Engineering Fracture Mechanics 21(2).

Berge S., O. I. Eide and P. Tubby (1989). Fatigue strength of tubular joints - some unresolved problems. International Conference on Offshore Mechanics and Arctic Engineering (OMAE 1989).

Berge S., J. Haswell and K. Engesvik (1994). Fracture mechanics analysis of tubular joint tests degree of bending effects. International Conference on Offshore Mechanics and Arctic Engineering (OMAE 1994).

Berge, S. (2004). Fatigue and Fracture Design of Marine Structures II Fatigue Design of Welded Structures.

Boge F., T. K. Helland and S. Berge (2007). Low cycle fatigue of T-tubular joints with out-of-plane bending loading. OMAE2007, San Diego, California

BOMEL (1995,a). Design and reassessment of tubular joints for offshore structures, chapter 5: fatigue life assessment S-N approach. C6060R09.07 REV B

BOMEL (1995,b). Design and reassessment of tubular joints in offshore structures, chapter 6: fatigue and fracture mechanics approach. C6060RIO.12 REV A.

Bowness D. and M. M. K. Lee (1995). The development of an accurate model for the fatigue assessment of doubly curved cracks in tubular joints. International Journal of Fracture(73).

Bowness D. and M. M. K. Lee (1998). Fatigue crack curvature under the weld toe in an offshore tubular joint. International Journal of Fatigue 20(6).

Bowness D. and M. M. K. Lee (2000). Weld toe magnification factors for semi-elliptical cracks in T-butt joints - comparison with existing solutions. International Journal of Fatigue 22(5).

BSI (1993). BS 7608:1993 Code of practice for Fatigue design and assessment of steel structures, British Standards.

BSI (2005). BS 7910:2005 Guide to methods for assessing the acceptability of flaws in metallic structures, British Standards.

BSi (2007). Petroleum and natural gas industries — Fixed steel offshore structures BS EN ISO 19902:2007.

BSI (2008). Fatigue — Design procedure for welded hollow-section joints — Recommendations. BS ISO 14347:2008.

BSI (2009). Eurocode 3: Design of steel structures — Part 1-9: Fatigue. BS EN 1993-1-9:2005.

Cao J. J., G. J. Yanga, J. A. Packer and F. M. Burdekin (1998). Crack modelling in FE analysis of circular tubular joints. Engineering Fracture Mechanics 61.

Chakrabarty J. (2006). Theory of plasticity Amsterdam; Boston; Oxford, Elsevier Butterworth-Heinemann.

Chang E. and W. D. Dover (1999). Parametric equations to predict stress distributions along the intersection of tubular X and DT-joints. International Journal of Fatigue 21(6).

Choo Y. S., X. D. Qian, J. Y. R. Liew and J. Wardenier (2003). Static strength of thick-walled X-joints-part I: New approach in strength definition. Journal of Constructional Steel Research 59.

Choo Y. S., W. Shen and J. Gronbech (2007). Hot Spot Stress for As-welded and Grouted Tubular X-joints Subjected to In-Plane Bending. 11th International Conference of the Jack-up Platform. London, England.

Connolly M. P., A. K. Hellier, W. D. Dover and J. Sutomo (1990). A parametric study of the ratio of bending to membrane stress in tubular Y- and T-joints. International. Journal of Fatigue 12 No 1.

Cook R. D. (1994). Finite Element Modelling for Stress Analysis, JOHN WILEY &SONS, INC.

Delft D. R. V. v., D. D. O and H. H. Snijder (1986). The calculation of fatigue crack growth in welded tubular joints using fracture mechanics OTC 5352. The 18th Annual Offshore Technology Conference. Houston Texas.

Dier A. F. (2004). Assessment of repair techniques for ageing or damaged structures Project #502. DOC REF C357R001 Rev 1, MSL limited.

Dijkstra O. D. and d. Back (1980). Fatigue strength of tubular T- and X-joints. 12th Annual Offshore Technology Conference. OTC3699 Houston Tex. USA..

Dijkstra O. D. and C. Noordhoek (1985). The Effect of Grinding and a Special Weld Profile on the Fatigue Behavior of Large-Scal Tubular Joints. 17th Annual OTC 4866. Huston, Texas.

DNV (2005). DNV-RP-C203 Fatigue design of offshore steel structures. RECOMMENDED PRACTICE DET NORSKE VERITAS DNV-RP-C203.

DNV (2006). Feasibility study for NRA platform jacket leg segment E4-B2T3 strengthening (conceptual design pahse). DNV/ SPR20060106.

DNV (2008). Recommended practice Det Norske Veritas DNV-RP-C203 Fatigue design of offshore steel structures, DET NORSKE VERITAS.

DNV (2008). Strengthening of NRA platform project – finite element analysis for ultimate capacities of three selected joints (pre-grouted and post-grouted).

Dunne F. and N. Petrinic (2005). Computational Plasticity, Oxford University Press.

Elnashai, A. S. and W. Aritenang (1991). Nonlinear modelling of weld-beaded composite tubular connections. Engineering Structures 13(1).

Energo Engineering, I. (2006). Assessment of fixed offshore platform performance in hurricanes Andrew, Lili and Ivan. MMS Project No.: 549 Energo Engineering Project No.: E05114.

Energo Engineering, I. (2007). Assessment of fixed offshore platform performance in hurricanes Katrina and Rita. MMS Project No.: 578 Energo Engineering Project No.: E06117.

Engesvik K. M. and T. Moan (1983). Probabilistic analysis of the uncertainty in the fatigue capacity of welded-joints. Engineering Fracture Mechanics 18(4).

Etterdal B., D. Askheim, H. Grigorian and R. Gladso (2001). Strengthening of Offshore steel Components Using High-Strength Grout: Component Testing and Analytical Methods. OTC13192. Offshore Technology Conference 2001. Houston Texas USA.

Etterdal B. and I. Scherf (2001). Strengthening of Ekofisk Platforms to Ensure Continued and Safe Operation. Offshore Technology Conference 2001, Houston.

Gibstein M. B. (1987). Stress concentration in tubular K-joints with diameter ratio equal to one. Steel in marine structures. C. Noordhoek and J. d. Back. Delft, Netherland, Elsevier.

Gotoh K. and S. Berge (2004). Low cycle fatigue strength of X65 pipeline girth welds. International Pipeline Conference, Calgary, Alberta, Canada.

Grundy P. (1994). Incremental collapse of hollow sections. Tubular structures VI. P. Grundy, A. Holgate and G. B. Wong. Rotterdam, Balkema.

Grundy P. and G. T. Kwong (1994). Shakedown analysis of tubular structures. Tubular Structures VI. P. Grundy, A. Holgate and G. B. Wong. Rotterdsm, Ba/kerns.

Gurney T. R. (1968). Fatigue of welded structures, Cambridge at the university press.

H.Shakir-Khalil and N. K. A. Hassan (1994). Push out resistance of concrete-filled tubes. Rotterdam, Balkema.

Han L. H., G. H. Yao and X. L. Zhao (2005). Tests and calculations for hollow structural steel (HSS) stub columns filled with self-consolidating concrete (SCC). Journal of Constructional Steel Research 61(9).

Harwood R. G. and E. P. Shuttleworth (1988). Grouted and mechanical strengthenign and repair of tubular offshore structures. OTH 88 283 (Wimpey Offshore Engineers & Constructors Ltd).

Healy, B. E. and J.Buitrago (1994). Extrapolation procedures for determining SCFs in mid-surface tubular joint models. TubularStructures VI, Balkama, Rotterdam, A.A. BALKEMA.

Hobbacher, A. (2005). Recommendations for fatigue design of welded joints and components IIW document XIII-1965-03 / XV-1127-03, International Institute of Welding.

HSE (1993). Fatigue life enhancement of tubular joints by grout injection OTH 92 368 Health & Safety Executive.

HSE (1997). Stress concentration factors for simple tubular joints - Assessment of existing and development of new parametric formulae OTH 354, Health & Safety Executive.

HSE (1998). A review of fatigue crack growth rates in air and seawater. OTH 511, Health & Safety Executive.

HSE (1999). Background to New Fatigue Guidance for Steel Joints and Connections in Offshore Structures OTH 92390, Health & Safety Executive.

HSE (2000). Fracture mechanics assessment of fatigue cracks in offshore tubular structures OTR 2000/077, Health & Safety Executive.

HSE (2000). OTO 1999081, Ultimate strength performance of offshore structural framing, Health & Safety Executive.

HSE (2001). Comparison of fatigue provisions in codes and standards, OTR 2001/083, Health & Safety Executive.

Krahl, N. W. and D. I. Karsan (1985). Axial strength of grouted pile-to-sleeve connections, Journal of Structural Engineering-Asce 111(4 April).

Kwong, G. T. and P. Grundy (1994). Capacity of CHS YT-joints under high amplitude cyclic load. Tubular Structures VI. P. Grundy, A. Holgate and G. B. Wong. Rotterdam, Balkema.

Lee, M. M. K. (1999). "Strength, stress and fracture analyses of offshore tubular joints using finite elements." Journal of Constructional Steel Research 51

Lee, M. M. K. and D. Bowness (2002). Estimation of stress intensity factor solutions for weld toe cracks in offshore tubular joints. International Journal of Fatigue 24.

Lee, M. M. K. and D. Bowness (2002). Fatigue life prediction of offshore tubular joints using fracture mechanics. Fatigue & Fracture of Engineering Materials & Structures 25(11).

Liang, C. and J. W. Hutchinson (1993). Mechanics of the fibre push out test. Mechanics of Materials 14(3): 207-221.

Liew, J. Y. R. and D. X. Xiong (2009). Effect of preload on the axial capacity of concrete-filled composite columns. Journal of Constructional Steel Research 65(3).

Lubliner, J., J. Oliver, S. Oller and E. Onate (1989). A plastic-damage model for concrete. International Journal of Solids and Structures 25(3): 299-326.

M.Lalani, D.J.Morahan, R. J. v. Foeken and J.Wardenier (1996). Fatigue behaviour and ultimate capacity of grouted tubular joints. Tubular Structures VII, Balkema Rotterdam.

Maddox S. J. (1974). "Assessing the significance of flaws in welds subjects to fatigue." Welding J, Res Suppl, 1974, 53 (9), 401s-409s.

Marshall P. W. (1992). Design of Welded Tubular Connections - Basis and Use of AWS Code Provisions, ELSEVIER.

Marshall P. W. (2005). New API Fatigue Provisions. The fifteenth (2005) International Offshore and Polar Engineering Conference, Seoul Korea.

Morahan D. J. and M. Lalani (2002). Fatigue and ultimate limit state of grouted tubular joints. 21st International Conference on Offshore Mechanics and Arctic Engineering, OMAE'02, Oslo, Norway.

MSC (2005). Patran 2005 User's Guides & Reference Manuals.

MSC, S. (2005). Patran 2005 User's Guides & Reference Manuals.

MSL (1997). Development of grouted tubular joint technology for offshore strengthening and repair. DOC REF C14100R020 Rev 2 JUNE 1997, MSL Engineering Limited.

MSL (2004). Assessment of repair techniques for ageing or damaged structures Project #502. DOC REF C357R001 Rev 1 NOV 2004, MSL Engineering Limited.

MSL, E. L. and A. F. Dier (2004). Assessment of repair techniques for aging or damaged structures, Project #502. DOC REF C357R001 Rev 1(MMS Project Number 502).

Newman J. and I. S. Raju (1981). An empirical stress-intensity factor equation for the surface crack. Engineering Fracture Mechanics 15(1-2).

Niemi E. (1995). Stress Determination for Fatigue Analysis of Welded Components. IIS/IIW-1221-93, The Internaitonal Institute of Welding.

Niem, E., W. Frickke and S. J. Maddox (2007). Fatigue Analysis of Welded Components, Wood head publishing limited.

O'Shea M. D. and R. Q. Bridge (2002). Closure to "Design of circular thin-walled concrete filled steel tubes by Martin D. O'Shea, M.ASCE and Russell Q. Bridge, F.ASCE." Journal of Structural Engineering-Asce 128(1): 134-135.

O'Shea, M. D. and R. Q. Bridge (2000). Design of circular thin-walled concrete filled steel tubes. Journal of Structural Engineering-Asce 126(11).

Paris P. C. and F. Erdogan (1960). A Critical Analysis of Crack Propagation Laws. Journal of Basic Engineering 85.

Parsanejad S. and P. Gusheh (1992). Behavior of partially grout-filled damaged tubular members. Journal of Structural Engineering-Asce 118(11).

Partiman G., J. Wardenier, A. Romdjn and R. J. v. Foeken (1997). Numerical SCF-Analyses of Grouted Tubular T- and X-Joints. The Seventh (1997) International Offshore and Polar Engineering Conference, Honolulu, USA, The International Society of Offshore and Polar Engineers.

Qian, X. D. (2005). Static strength of thick-walled CHS joints and global frame behavior. Civil Engineering, National University of Singapore. PhD.

Quest-reliability-LLc FEA Creak manual 2.8.

Radaj D., C. M. Sonsino and W. Fricke (2006). Fatigue assessment of welded joints by local approaches, Wood Publishing and Maney Publishing,CRC Press.

Radaj D., C. M. Sonsinob and W. Frickec (2009). Recent developments in local concepts of fatigue assessment of welded joints, International Journal of Fatigue 2(31).

Sele A. and M. Skjolde (1993). Design Provisions for Grouted Construction, Th Annual Offshore Technology Conference. Houston, Texas USA. OTC 7150

Shanmugam N. E. and B. Lakshmi (2001). State of the art report on steel-concrete composite columns. Journal of Constructional Steel Research 57(10).

SIMULIA (2007). Abaqus 6.7-1 Analysis manual, theory manual.

Skallerud B. and J. Amdahl (2002). Nonlinear Analysis of Offshore Structures. RESEARCH STUDIES PRESS LTD.

SOH, A. K. (1997). An improved procedure for the determination of hot spot stress in tubular joints. Fatigue & Fracture of Engineering Materials & Structures 20(12).

Tan P. W., I. S. Raju, K. N. Shivakumar and J. J.C. Newman (1990). Evaluation of finite-element models and stress intensity factors for surface cracks emanating from stress concentrations. Surface crack growth: Model, Experiments and Structures ASTM STP 1060, Philadelphia.

Tandon G. P. and N. J. Pagano (1998). Micromechanical analysis of the fiber push-out and re-push test. Composites Science and Technology 58.

Timoshenko, S. P. and J. M. Gere (1963). Theory of Elastic Stability, McGRAW-HILL book company.

Tubby, P. J. and J. G. Wylde (1989). The fatigue performance of tubular joints containing weld repairs. The third international symposium on tubular structures. E. Niemi and P. Makelainen. Lappeenranta Finland, Elsevier.

Tveiten, B. W. and T. Moan (2000). Determination of structural stress for fatigue assessment of welded aluminum ship details. Marine Structures 13: 189-212.

UEG (1985). Design of tubular joints for offshore structures, UEG Publication UR33.

Ugural, A. C. and S.K.Fenster (1995). Advanced Strength and Applied Elasticity. Englewood Cliffs New Jersey 07632, PTR Prentice Hall.

Vanwingerde A. M., A. P. Jeffrey and J. Wardenier (1995). Criteria for the fatigue assessment of hollow structural section connection. Journal of Constructional Steel Research 35(1).

Vanwingerde A. M., J. A. Packer and J. Wardenier (1996). New guidelines for fatigue design of HSS connections. Journal of Structural Engineering-Asce 122(2).

VERITEIC (1984). Double skin grout reinforced tubular joints - final report. VERITEC REPORT NO. 84-3564, VERITEC marine technology consultants.

Waalen, J. and S. Berge (2005). Low cycle fatigue of T-tubular joints with in-plane bending loading. OMAE2005. Halkidiki, Greece

Wardenier, J. (2002). Hollow sections in structural applicaitons, Bouwen met Staal.

Wardenier, J., Y. Kurobane, J. A. Packer, D. Dutta and N. Yeomans (1991). Design Guide for Circular Hollow Section (CHS) Joints under Predominantly Static Loading, Verlag TUV Rheinland GmbH Koln.

Wordsworth, A. C. (1987). Aspects of the stress concentration factors at tubular joints. Steel in Marine Structures. C. Noordhoek and J. d. Back. Delft, The Netherlands.

Wylde, J. G. (1983). Fatigue tests on welded tubular T-joints with equal brace and chord diameters, OTC 4527. 15th annual offshore technology conference. Houston, Texas: 133-142.

Wylde, J. G. and A. McDonald (1980). The influence of joint dimensions on the fatigue-strength of welded tubular joints. International Journal of Fatigue 2(1).

Zhao, X. L., L. W. Tong and X. Y. Wang "CFDST stub columns subjected to large deformation axial loading." Engineering Structures 32(3): 692-703.

Zienkiewicz, O. C. (1971). The finite element method in engineering science. LONDON, McGRAW-HILL.

Appendix 1

Details of fully infilling grouted tubular specimen with stiffening plates-G1

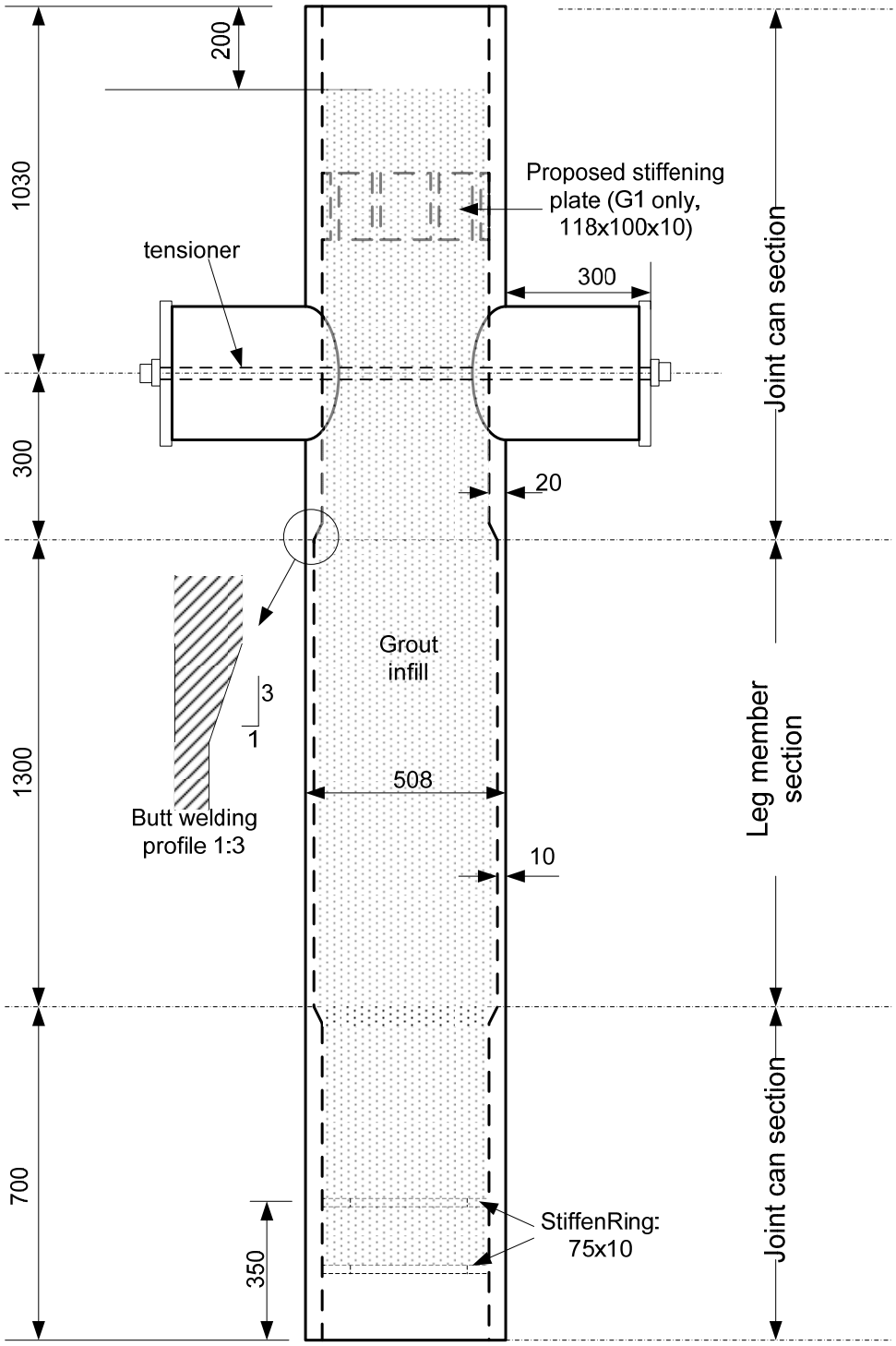

Appendix 2

Standard Operating Procedure for Mixing D4

1.0 Pre Mixing Considerations

- Ensure that the correct equipment for mixing Ducorit is available as detailed in this procedure.
- The ratio of Ducorit to water shall be tightly controlled and mixed according to specifications.
- It is imperative that a timer is used to ensure the mixing time is accurate.

Figure A2-1 5L ToniMIX

For amounts less than 25 kg it is recommended to use the above mixer or similar.

For 25 kg up to 1 ton it is recommended to use a paddle pan mixer Equipped with 4 arms close adjusted to bottom plate and side wall as shown in Figure A2-2. The paddle pan mixer must be in good condition with the arms well maintained and set as close as possible to bottom plate and side wall. (Max 8mm gap). Please note that if the rotation speed is increased then the mixing time may be reduced in certain circumstances.

Table A2-1 Examples of Mixer Sizes and Recommended Batch Sizes

Tank Capacity (Litres)	*Tank Diameter (cm)*	*Rotation Speed (rpm)*	*Motor Power Rating (kW)*	*Recommended D4 Batch Size*
140	*75*	*34*	*3.0*	*50*
325	*100*	*32*	*5.5*	*250*
800	*150*	*35*	*22.0*	*100*

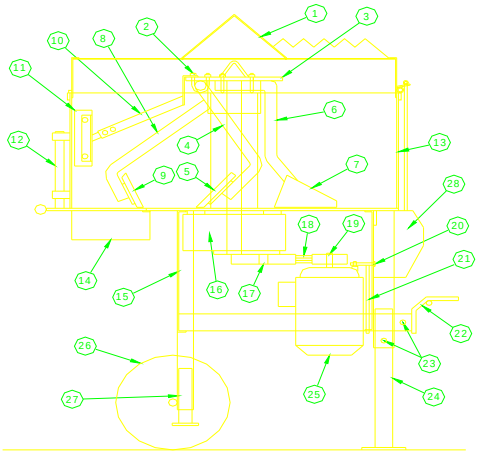

Figure A2-2 Paddle Pan Mixer for 25kg – 1 Ton Batches

2.0 Standard Mixing Procedure for D4

2.1 Use the following scale to get the exact amount of Ducorit D4 and water. The right amount of water in D4 is 7.5% measured by weight i.e.

1000kg Ducorit D4 = (1000/100)*7.5 = 75L of water
25kg Ducorit D4 = (25/100)*7.5 = 1.875L of water
10kg Ducorit D4 = (10/100)*7.5 = 0.75L of water

2.2 Empty the Ducorit into the mixer and start the mixer.

2.3 Empty the exact quantity of water into the mixer and start the timer.

2.4 Mix for 10 minutes. **NOTE**: It is important that the Ducorit D4 is mixed for the full 10 minutes as the mix often changes in viscosity between the 9 and 10 minutes.

2.5 In the 11th minute the mix is discharged from mixer and a new mix is commenced.

3.0 Standard Mixing Procedure for D4 with Steel Fibres

3.1 Empty the Ducorit into the mixer and start the mixer.

3.2 Empty the steel fibres very slowly into the tank and make sure the fibres are well distributed the full 360 degrees in the tank while the paddle pan rotates.

3.3 Empty the exact quantity of water into the mixer and start the timer.

3.4 Mix for 10 minutes. **NOTE**: It is important that the Ducorit D4 is mixed for the full 10 minutes as the mix often changes in viscosity between the 9 and 10 minutes.

3.5 In the 11th minute the mix is discharged from mixer and a new mix is commenced.

Appendix 3

Details of small scaled column stub

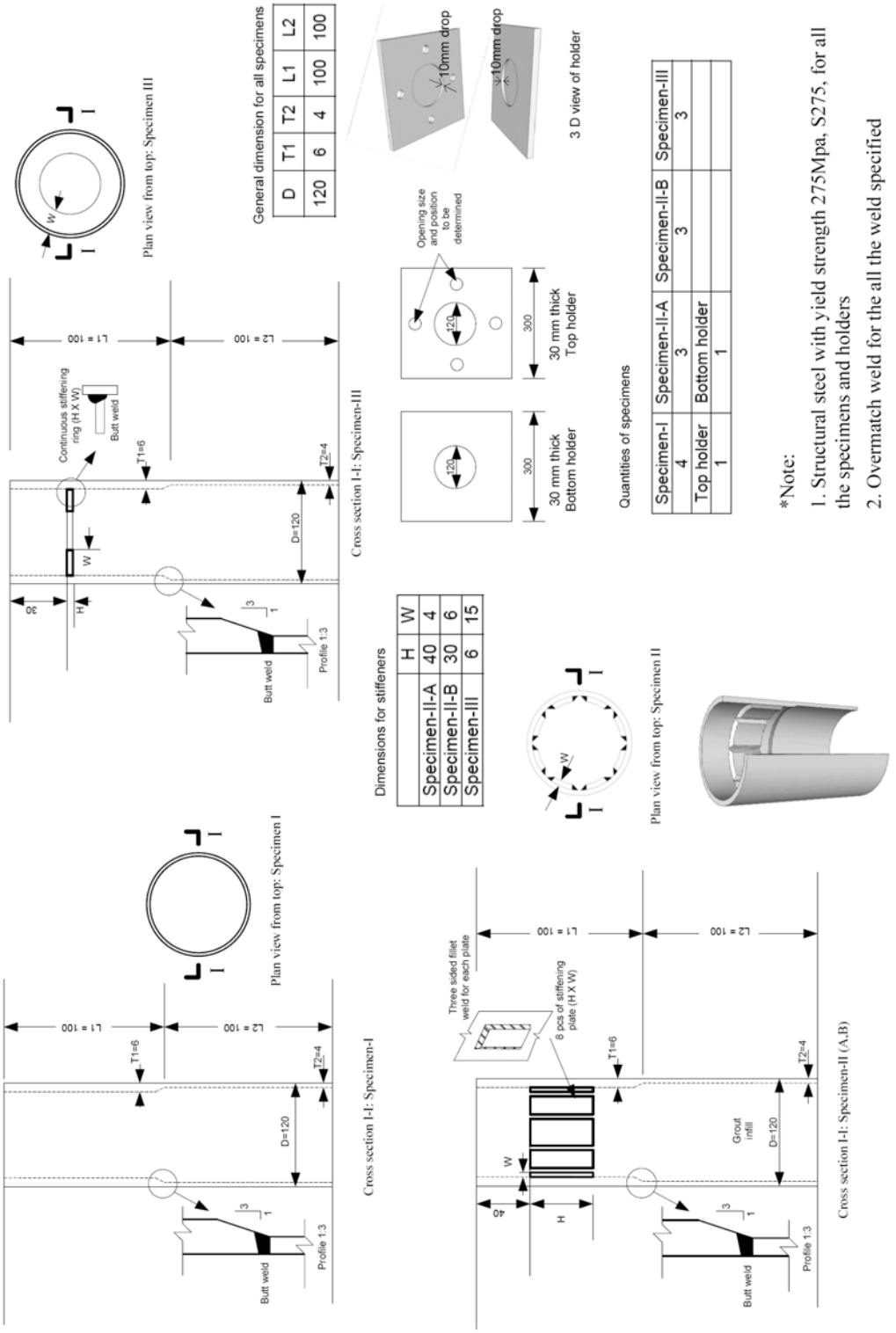

Appendix 4

Efthymiou equations for SCFs of X joints

Brace axial load

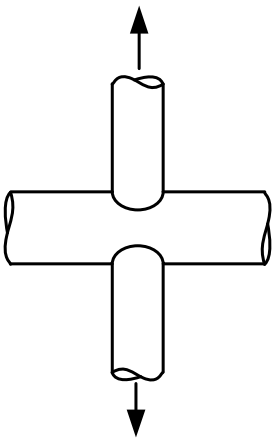

Chord saddle:

$C_{CS} = C_{X1}$ $\quad C_{X1} = 3,87\gamma\tau\beta\left(1,10-\beta^{1,8}\right)\sin^{1,7}\theta$

Chord crown:

$C_{CC} = C_{X2}$ $\quad C_{X2} = \gamma^{0,2}\tau\left[2,65+5\left(\beta-0,65\right)^2\right]-3\,\tau\beta\sin\theta$

Brace saddle:

$C_{BS} = C_{X3}$ $\quad C_{X3} = 1+1,9\gamma\tau^{0,5}\beta^{0,9}\left(1,09-\beta^{1,7}\right)\sin^{2,5}\theta$

Brace crown:

$C_{BC} = C_{X4}$ $\quad C_{X4} = 3+\gamma^{1,2}\left[0,12\exp\left(-4\beta\right)+0,011\beta^2-0,045\right]$

Brace in plane bending

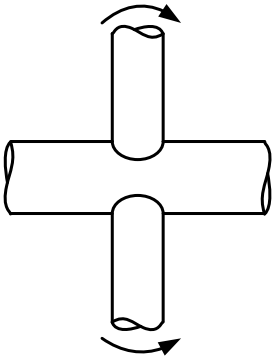

Chord crown:

$C_{CC} = C_{T8}$ $\quad C_{T8} = 1,45\beta\tau^{0,85}\gamma^{(1-0,68\beta)}\sin^{0,7}\theta$

Brace crown:

$C_{BC} = C_{T9}$ $\quad C_{T9} = 1+0,65\beta\tau^{0,4}\gamma^{(1,09-0,77\beta)}\sin^{(0,06\gamma-1,16)}\theta$

Brace out plane bending

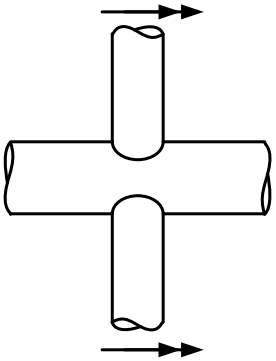

Chord saddle:

$C_{CS} = C_{X5}$ $\quad C_{X5} = \gamma\ \tau\ \beta\left(1,56-1,34\beta^4\right)\sin^{1,6}\theta$

Brace saddle:

$C_{BS} = C_{X6}$ $\quad C_{X6} = \tau^{-0,54}\gamma^{-0,05}\left(0,99-0,47\beta+0,08\beta^4\right)\times C_{X5}$

Appendix 5

Proposed fatigue test for grouted tubular X joints in NUS

1. Introduction

According to the research evidence of hot spot stress concentration factors (SCFs) for as-welded (un-grouted) and grouted tubular X-joints so far, it can be concluded that infilling grouting for the chord member would significantly reduce SCFs. This implies that the fatigue strength of grouted joint would be improved based on hot spot stress S-N approach recommended in current design codes. Meanwhile, the study by fracture mechanics method indicates the fatigue strength of tubular joint is also closely related to degree of bending component of hot spot stress (DOB), which is ignored in current design codes. The studies in NUS show that the infilling grouted joint will have DOB varied together with the reduction of SCFs, and the trend and significance of variation are dependent on loading mode. From fracture mechanics point of view, lower DOB leads to shorter fatigue life with the same amount of hot spot stress range applied. For grouted X joints under brace axial tension, the reduction of SCF and DOB happens simultaneously. The following questions arise naturally:

- which factor is dominant for fatigue life, reduction of SCF or DOB? and
- how significant the result will be by ignoring DOB?

To answer the above questions, experimental evidence is needed obviously. As shown in Table B, the variation of DOB due to infilling grout in the chord member is considered as significant for X joints. Hence, the fatigue tests of grouted X joints are proposed here. It is expected to provide experimental evidence to complement the design codes, so that the design and analysis for fatigue of fully grouted tubular joints can be done with more confidence.

2. Initial sizing of the specimen

The proposal was made based on the existing testing facilities in the structural lab of NUS. The fatigue tests can be conducted on 200T Instron test rig, Figure A5-1, (the cyclic dynamic loading capacity is limited to 100T with Max. frequency about 0.5 Hz). Brace axial loading and in plane bending can be performed as shown in Chapter 8. Considering the space constraints (Figure A5-3) and loading capacity of the test rig, the following X joint configurations are proposed subject to the availability of the material, shown in Table A5-1 and Figure A5-2 below. The sizing is based on the preliminary prediction of SCFs and DOBs, which are shown in Table A5-2.

Table A5-1 X joint configurations for fatigue tests

	α	β	γ	τ	T-mm	t-mm	D-mm	d-mm	l-mm	L-mm
FX-1	12	0.70	14.28	1	16	16	457	319.9	911.5	2400
FX-2	12	0.88	16.24	1	12.5	12.5	406	355.25	937	2400

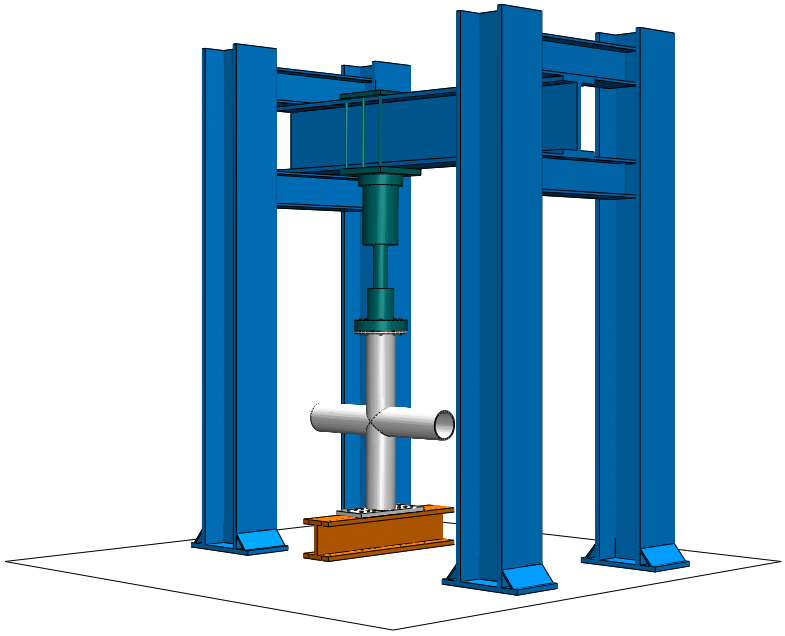

Figure A5-1 set up for axial loading fatigue tests on 200T Instron test rig

Table A5-2 Preliminary prediction of SCFs and DOBs

Joints	Loading mode	SCF		DOB	
		As-welded	grouted	As-welded	grouted
FX-1	Axial tension	22.20	4.44	0.87	0.67
FX-2	Axial tension	17.25	6.04	0.81	0.57

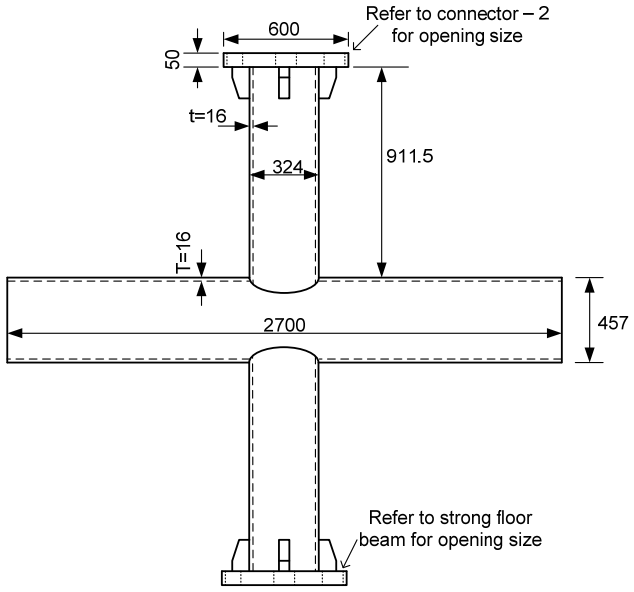

(a)

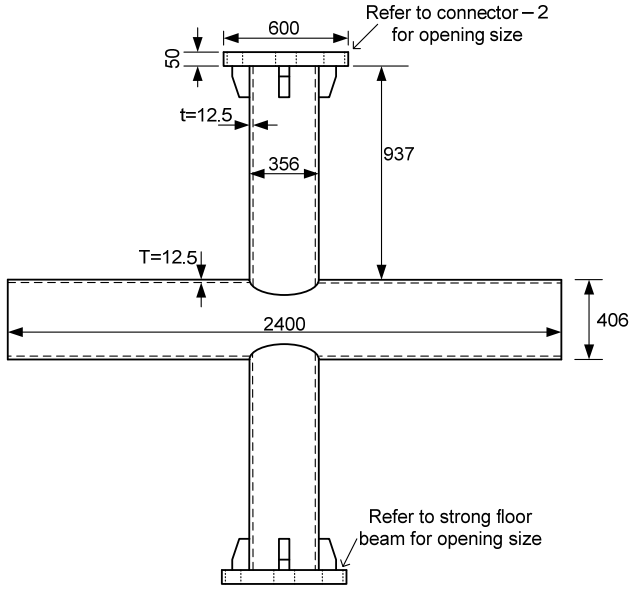

(b)

Figure A5-2 Detailed dimensions of the specimens: (a) FX-1; (b) FX-2

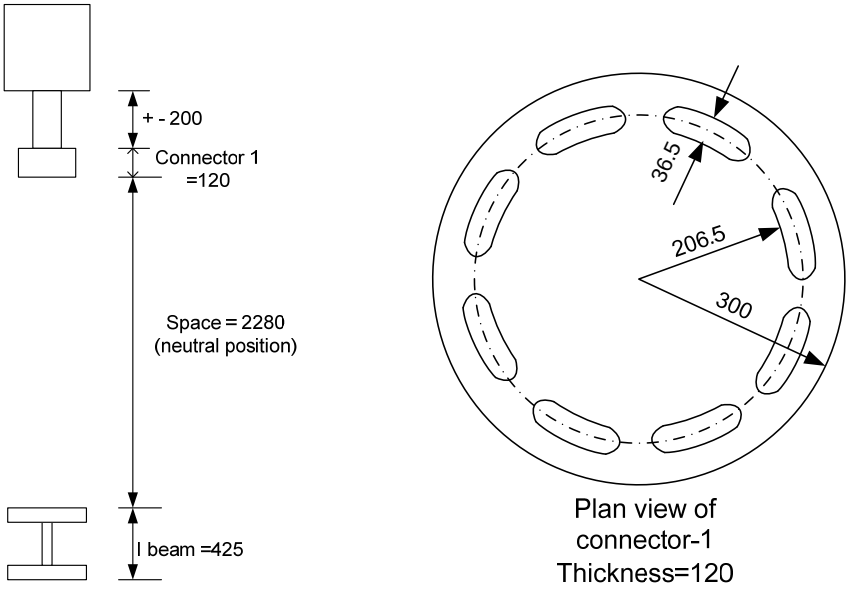

Figure A5-3 Space constraints of the test rig and details of the connectors

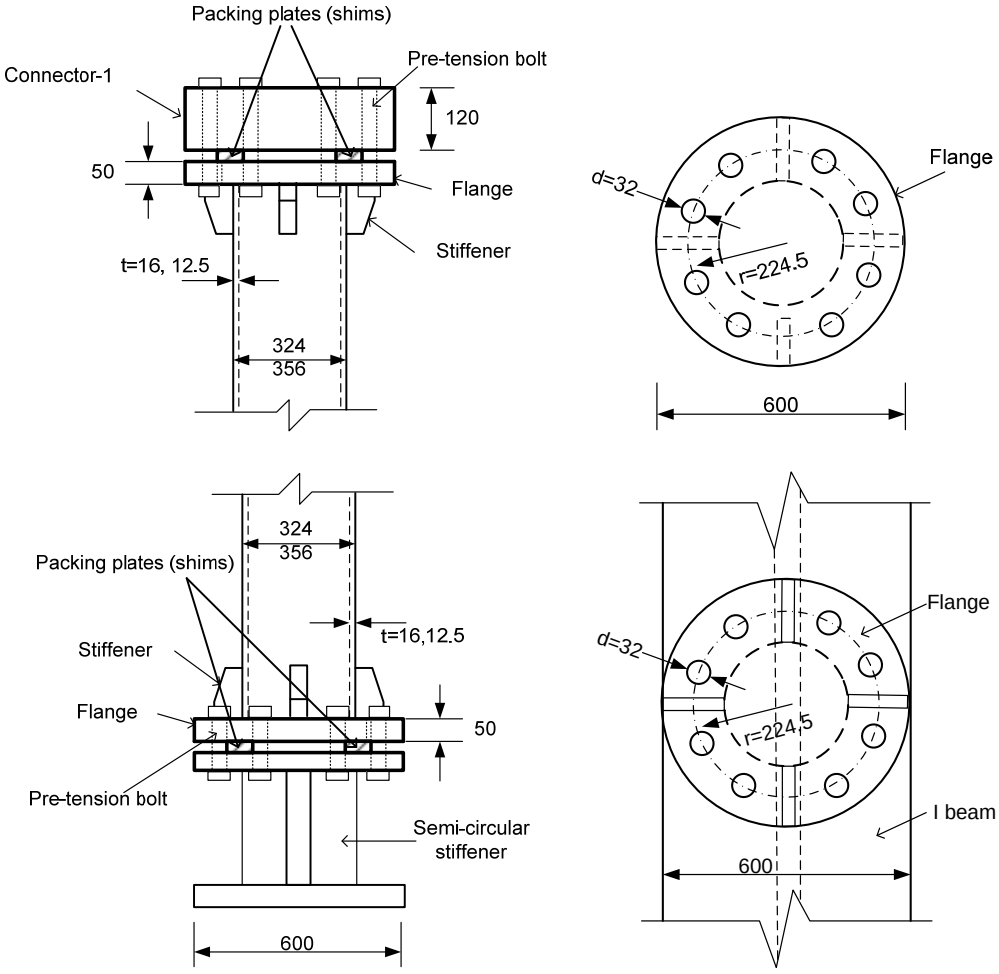

Figure A5-4 Connection details

3. Loading cases

It can be seen from Table A5-2 that due to infilled grouting, both SCFs and DOBs of the joints are altered significantly and variation is depending on the loading mode. Their influences to fatigue strength can be examined through testing with different load cases.

Constant amplitude cyclic fatigue load with ratio equal to 0.1 is suggested, shown in Table A5-3. For each load case, minimum two load levels are proposed, so that they should experience:

- Same nominal stress range; and
- Same hot spot stress range

This arrangement is to check:

- whether the infill grouted joint will have longer fatigue life;
- whether the same hot spot stress S-N curve for empty joint, like T' curve, is applicable for grouted joints

Table A5-3 Proposed testing load cases

Joints	Load-case	Joint status	Loading mode: axial tension, R = 0.1			Quantity
			Max. tensile load from actuator-kN	Nominal stress range-Mpa	Hot spot stress range-Mpa	
FX-1	FX-1-E-1	As-welded	585	38	851	1
	FX-1-G-1	grouted	585	38	170	2
	FX-1-E-2	As-welded	205	13	298	1
	FX-1-G-2	grouted	1024	67	298	2
FX-2	FX-2-E-1	As-welded	670	50	859	1
	FX-2-G-1	grouted	670	50	301	1
	FX-2-E-2	As-welded	149	10	179	1
	FX-2-G-2	grouted	391	29	175	1

The arrangement covers two beta ratios and two thicknesses of chord wall. The beta ratio is close to 0.9 for FX-2. This is to catch certain degree of implicit and inherent characteristics associated with large beta ratio for X–joint, as it is understood in reality a very large portion of X-joint is with equal brace chord diameter (beta=1). However, it has been noticed there is inherent uncertainty for hot spot stress SCF of beta=1 X-joints, which is extremely sensitive to the weld profile. This arrangement is trying to reduce the forecast scatters of the result by using such large beta ratio joint for approximation.

Considering the scatters of fatigue tests, certain degree of repeat is essential. As shown in Table A5-3, totally 10 specimens may be needed. Table D shows the length of pipes needed for fabrication of joints without considering the wastage.

Table A5-4 Pipe length estimated to fabricate the joints (without wastage)

Pipe for chord, D=457mm,T=16mm	15m
Pipe for brace, d=324mm, t=16mm	12m
Pipe for chord, D=406mm, T=12.5mm	10m
Pipe for brace, d=356mm, t=12.5mm	9m

4. Discussion

1. The connection details are tentatively arranged as shown in Figure A5-4, further details for the shims and the pre-stress level for the bolts are needed. Assume Max. brace tensile load 1000kN is taken by 6 bolts (d = 30mm), the nominal stress in the bolt is:

$$\left(1000000 \Big/ 8\right) \Big/ \left(\frac{1}{4} \times 3.14 \times 25^2\right) = 255 Mpa$$

Assume grade 8.8 high tensile bolt is used, the suggested pre-tension load at 70% of the yield stress is:

$$0.7 \times 800 \times 0.8 = 448 Mpa$$

Hence, it is sufficient to avoid fatigue of bolts, if pre-tension installation is adopted.

2. The short brace, less than three times brace diameter, might lead to possible end effect.
3. local stiffener at brace end, is it necessary? Refer to Figure E, similar SCF about 4 will be generated according to FEA result. This amount is close to the SCF of grouted joint, Table A5-2

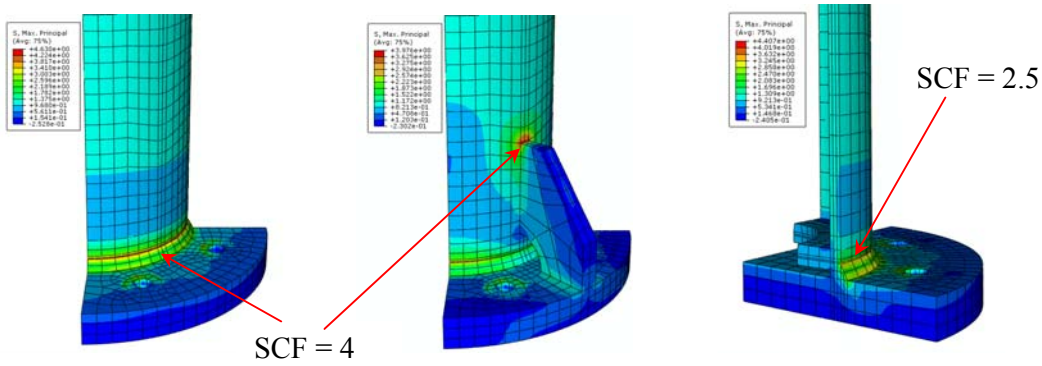

Figure A5-5 Different designs for brace end flange